ABSTRACT

Title of Dissertation: A SEARCH FOR SQUARKS AND GLUINOS USING THE JETS AND MISSING ENERGY SIGNATURE AT DØ

Adam Leonard Lyon, Doctor of Philosophy, 1997

Dissertation directed by: Professor Nicholas J. Hadley
Department of Physics

This thesis reports on a search for evidence of production and decay of squarks ($\tilde{q}$) and gluinos ($\tilde{g}$) of Minimal Supergravity (mSUGRA) in $p\bar{p}$ collisions at a center of mass energy of 1.8 TeV using the DØ detector at the Fermi National Accelerator Laboratory. Data corresponding to 79.2 ± 4.2 pb^{-1} were examined for events with large missing transverse energy ($\not\!\!E_T$), three or more jets, high energy leading jet, and the absence of isolated leptons. Since no events were observed in excess of Standard Model background predictions, limits are placed in the mSUGRA M_0 – $M_{1/2}$ plane for fixed parameters $\tan\beta = 2$, $A_0 = 0$, and $\mu < 0$. The excluded region includes all mSUGRA models with $m_{\tilde{q}} < 250$ GeV/c^2. For small M_0, gluinos with mass less than 300 GeV/c^2 are excluded. If squarks and gluinos have the same mass, that common mass must be greater than 260 GeV/c^2.

A SEARCH FOR SQUARKS AND GLUINOS USING THE JETS AND MISSING ENERGY SIGNATURE AT DØ

by

Adam Leonard Lyon

Dissertation submitted to the Faculty of the Graduate School of the
University of Maryland at College Park in partial fulfillment
of the requirements for the degree of
Doctor of Philosophy
1997

Advisory Committee:

Professor Nicholas J. Hadley, Chair
Professor Sarah Eno
Professor Abolhassan Jawahery
Professor Alice Mignerey
Professor Rabindra Mohapatra

DEDICATION

To my parents, Frannie and Martin Lyon

ACKNOWLEDGEMENTS

At the Academy Awards and similar extravaganzas, there are always the long winded acceptance speeches giving thanks to those unfamiliar but obviously special people who helped the recipient to the heights he or she just reached. Since I am quite confident that no Oscar will come my way, I am taking full advantage of this opportunity to express my gratitude to the people who have helped me achieve this point. Apologies for the long windedness and to those who I will not list by name.

First of all, those outside of high energy physics probably do not realize the extent to which running a particle physics experiment is a huge team effort. The DØ experiment is made up of nearly 400 especially talented collaborators. Though this thesis carries my name alone, it would not have been possible to write without their contributions to DØ. Several require special mention. I was incredibly fortunate to have Nick Hadley for my advisor. I forgive him for shipping me out to Fermilab where the day after I arrived the temperature dropped to -27° F with -80° wind chills. He always tells others that since I come from North Carolina, he expected that I would have called him from the road stating that although my hands were frozen to the steering wheel, I would not be stopping until I arrived back in the warm South. Though starting my car in the cold the next morning was indeed painful (for me as well as the car), in fact I knew that Fermilab was the place for me to be, and with his guidance my career as a high energy physicist would get off to the best start possible. Though extremely busy leading DØ's discovery of the top quark and serving on a myriad of committees, Nick always had time to answer my questions, give excellent advice, and provide appropriate uplifting speeches when I was buried in the quagmires of the analysis. He is an all around good guy and a good friend.

Marc Paterno is another good friend. It was Marc and I who did the analysis for this thesis. I started learning about this stuff by helping him finish his analysis and thesis three years ago. He has very kindly reciprocated my long hours helping him during those days by putting in long hours in the past year with this analysis. Though my sense of

humor has perhaps become a bit more warped in the process (and his too), it has been a true pleasure working with him. Whether it's Bayesian statistics or C++ programming, Marc is one of those people with a far reaching vision. I have benefitted much from our collaboration.

Along with Marc, I had frequent advice from Joey Thompson, Bill Cobau, and Doug Norman who always happily answered my questions and gave me good ideas to try. It's been fun to watch Joey's son Jed, a frequent visitor to the trailers, grow up. Fortunately, he quickly outgrew his passion for pressing the bright yellow reset buttons on our workstations.

When I started at DØ, the New Phenomena group was expertly lead by Dave Cutts and Wyatt Merritt, who, along with Nick, always tried to make sure that the analysis stayed on track. Special thanks are due to Wyatt and Amber Boehnlein for fending off the "Toppies" and fighting hard to keep my analysis trigger unprescaled (Amber has also been a great source of information on triggers and exploding transparency pen stain removal). Wyatt and Nick now have the daunting task of leading the effort to write the Run II software in C++. I have complete confidence that they will pull it off. A little more than a year ago, Wyatt and Dave left the NP group to the good hands of Sarah Eno and John Hobbs, and they appropriately pushed this analysis to completion. Their advice and good humor have always been a great help. I also very much appreciate the advice and patience from my editorial board, made up of Jim Linnemann, Paul Padley, Heidi Schellman, and Gordon Watts. Their very thorough scrutiny greatly improved and strengthened the analysis. I also thank Nick, Sarah, Hassan Jawahery, Alice Mignerey, and Rabindra Mohapatra for serving on my dissertation committee.

Along with Nick and Sarah, the Maryland High Energy group consists of a great group of people. I am especially grateful to Sally Megonigal for handling all of the administrative stuff for us far away graduate students and for waging battle with the Maryland bursar's and travel offices.

The first year of graduate school at the University of Maryland was really, really hard. Although misery loves company, I think the real reason why most of the graduate

students in my class got along so well is because they are all extremely friendly people. Since leaving for Fermilab, I've been very fortunate to have kept in touch with Kirk Burrows, Tina Chen, Susan and Sham Chotoo, Zoa Conner, Gregg Harry, and Gayatri and Rana Hasan. They are all really good friends. Special thanks to Kirk and Gregg for giving me a place to stay during my visits to College Park.

Thanks go to the physics department at North Carolina State for giving me the preparation to tackle graduate school at Maryland. I am especially grateful to Dr. Patty who headed the very successful and extremely friendly department and to Dr. Tilley, my undergraduate advisor. One of the sophomore lab classes at NCSU involved making a little cloud chamber. Though the many tracks we saw were mostly due to the high levels of radon in the bricks of the physics building, it was a cool experiment and sparked my interest in particle physics.

Working summers at Wandel and Goltermann during high school and undergraduate years started my work with computers by writing database programs. Though FilePro programming has long been a useless skill, I learned so much from my time there. Special thanks to Carol Johnson who looked after me like a mom and to Bert Kuthe who, even with Germany and investors breathing fire at him, always kept up his good nature and made working for him fun.

I am grateful to many others at Fermilab, North Carolina, and elsewhere for reasons too lengthy to list here: David Chappel, Gervasio Gomez, Marc Johnson, Jean Mielke, Sonya Misra, all of the Paternos, Mike (if I could only write lengthy e-mails as interesting as his) and Theresa Rubes, and Peter Tamburello.

I was fortunate to have several relatives living near College Park. It was always fun meeting my Aunt Marion in Baltimore every few months. We would meet for lunch at the Linwood, which she claimed was "half way" between D.C. and Baltimore (the restaurant was in reality well north of Baltimore!). Seeing her and my aunt and uncle and cousins in Columbia was always worth the trips.

Finally, I am deeply indebted to my parents, brother, and grandparents for all of their encouragement and support. They are some of the only people outside of physics who

do not laugh hysterically when I mention that my work involves searching for particles called squarks. My Mom really wanted me to go into HEP since she thought it was really neat; she is one of the most creative and forward thinking people that I know. Though neither of my parents are scientists, I can see in them where I got my interest in science. I cannot think of words to thank them enough for all they have given me. I love them very much.

And lastly (yes, I can hear the music playing meaning that my acknowledgments have gone on too long; just a few more lines), it may seem silly to thank the US Department of Energy and the other funding agencies that support DØ and Fermilab, but without them none of this would have been possible. It good that there are those in government that feel that, like art and the humanities, support of basic science is worthwhile, if not important. Regardless of what the bureaucrats say, basic science is done to learn more about our environment, our universe, and ultimately about ourselves. Whenever I got buried in debugging some obscure piece of code or sitting around at 3am in the control room waiting for the beam to be fixed, I could remind myself why this stuff is so interesting and exciting. We can actually take smallest bits of matter known to man and smash them into each other and see what happens. It is incredible that we really are asking the fundamental and basic questions about how our universe works and even more incredible that we are beginning to learn the answers.

TABLE OF CONTENTS

LIST OF TABLES

LIST OF FIGURES

Chapter 1

Introduction

We are always asking questions. "What is everything made of?" is an ancient one. The answer has evolved from the realm of the Greek philosophers to the particle and high energy physicists of today. The answer itself is now expressed with the Standard Model, a theory that describes what are believed to be the fundamental units of matter and the nature of their interactions.

The Standard Model is a remarkable achievement of modern physics. Indeed, there has not been an experiment yet that has been able to disprove any of its many predictions. The Standard Model, however, is a complicated theory and contains some inconsistencies leading to the belief that it is really only a part of some grand theory. Extensions to the Standard Model try to fix the inconsistencies and add some simplicity and "beauty" to the model. One such extension is Supersymmetry. Supersymmetry predicts the existence of additional particles beyond what the Standard Model alone describes. The topic of this thesis is a search for two of these additional particles predicted by Supersymmetry, namely the squarks and gluinos.

Chapter 2 starts with a review of the Standard Model and a discussion of some of its problems. The difficulties lead to the formulation of Supersymmetry. What Supersymmetry is and how it fixes some of the problems are explained. Supergravity, the particular Supersymmetry model used in this search, is presented followed by a brief listing of some other Supersymmetry models that have recently become popular. If squarks and gluinos do exist, what evidence would they leave in a detector? That question is answered in

Chapter 3, which describes the characteristics of the signal and the overall strategy of the search. Previous experimental searches for squarks and gluinos are also briefly reviewed. Chapter 4 covers the apparatus used for this experiment, namely the Tevatron collider and the DØ detector at the Fermi National Accelerator Laboratory located near Chicago, Illinois. Those detector systems of particular importance to this analysis will be explored in some detail. Algorithms and procedures for identifying particles and measuring the characteristics of events are briefly explained in Chapter 5.

The analysis itself is discussed in Chapter 6, which describes the event selection criteria used to select squark and gluino candidates and reject background events, the collider data passing the selection requirements, and the background estimates with the methods used to calculate them. Chapter 7 discusses the sensitivity of the analysis to the signal and gives the results. Finally, Chapter 8 offers a summary of the analysis and what may be expected for the future. Many chapters end with a short summary that is written in a (hopefully) more accessible manner. The result of the analysis, a limit in the Supergravity $M_0 - M_{1/2}$ plane, is shown in Figure 7.7 on page 184.

Chapter 2

The Theories

2.1 The Standard Model

The Standard Model (SM)[1–3] accurately predicts all observed phenomena at distances smaller than the diameter of the atomic nucleus ($\sim 10^{-15}$ m). It is one of the must successful theories ever invented.

2.1.1 Fundamental Particles

There are two basic types of particles in the Standard Model, fermions and bosons. The fermions have spin 1/2 and are the building blocks of matter. Fermions adhere to the Pauli Exclusion Principle: only one fermion can occupy a particular quantum state. The fundamental bosons are either spin 0 or spin 1 particles and are thought of as the force carriers.

Some characteristics of the SM fermions are shown in Table 2.1. They can be further broken down into the categories of quarks and leptons. Quarks are the constituents of protons and neutrons and are affected by the strong force which holds the protons and neutrons together in nuclei. The quarks have fractional charge: the up, charm, and top quarks have electrical charge 2/3 e (-1 e is the electron charge), and the down, strange, and bottom quarks have charge $-1/3$ e. The quarks make up particles called hadrons. Hadrons with three constituent quarks (such as protons and neutrons) are called baryons, and those with a quark and an antiquark are mesons. An important

Generation	Particle	Name	Mass (MeV/c^2)	Charge (e)
	Quarks (spin 1/2)			
1	d	Down	∼7.5	$-1/3$
	u	Up	∼4.2	$2/3$
2	s	Strange	∼150	$-1/3$
	c	Charm	∼1100	$2/3$
3	b	Bottom	∼4200	$-1/3$
	t	Top	172,000	$2/3$
	Leptons (spin 1/2)			
1	e	Electron	0.511	-1
	ν_e	Electron neutrino	< 15 eV	0
2	μ	Muon	105	-1
	ν_μ	Muon neutrino	< 0.17	0
3	τ	Tau	1777	-1
	ν_τ	Tau neutrino[a]	< 24	0

Particle	Name	Mass (GeV/c^2)	Charge (e)	Force
Gauge Bosons (spin 1)				
γ	Photon	0	0	Electromagnetic
g	Gluon	0	0	Strong
W	W	80.2	1	Weak
Z	Z	91.2	0	Weak
Fundamental Scalar (spin 0)				
H	Higgs[b]	?	?	Couples to matter

[a] The tau neutrino has not been directly observed yet.

[b] The Higgs boson is only predicted; not yet observed.

Table 2.1: Particles of the Standard Model.[4]

theoretical advancement was the realization[5] that quarks must have color charge in addition to electric charge, since without color quarks in some hadrons appear to occupy the same quantum state (since they are fermions, that is not allowed). Color charge has three "polarities" represented by the primary colors, red, green, and blue. There are also anticolors for the antiquarks. Mixtures of a color and its anticolor or of the three separate colors or anticolors are referred to as colorless. As discussed below, individual free quarks with color are not observed, and the quarks seem to be confined inside colorless mesons and baryons. The type of quark (up, down, charm, etc.) is referred to as the quark flavor. The top quark, the last SM particle to be discovered, was finally observed in 1995 with the DØ and CDF detectors at Fermilab.[6,7]

Leptons are particles that are unaffected by the strong force. For each charged lepton, there is a neutrino that is electrically neutral. Unlike charged particles that interact electromagnetically, neutrinos are only affected by the weak force; the force responsible for nuclear decay. As the name suggests, the weak force is the weakest of the three interactions described by the SM (in the small distance regime gravity has virtually no effect and is not addressed by the SM) and so neutrinos are virtually undetectable directly. Their existence can be inferred by looking for imbalances in events where momentum is conserved. Experiments have put constraints on the masses of the neutrinos such that they are presumed to be massless and therefore must always travel at the speed of light. The possibility of massive neutrinos, however, is still one of the important questions in particle physics and the subject of much study.

A common feature of the quarks and leptons is that they can be grouped into three generations. Each generation of quarks has one charge $+2/3$ e quark (up type) and one charge $-1/3$ e quark (down type). Each generation of leptons has a negatively charged particle (electron type) and a massless neutrino. As seen in Table 2.1, the second generation contains heavier particles than the first and similar for the third. The particles of the heavier generations are unstable and ultimately decay down to the first generation or to photons. Only particles of the first generation make up matter in the everyday world, while particles of the second and third generations can be produced with cosmic

rays and in high energy particle colliders. In fact, even when only the up, down, and strange quarks were known, the existence of the charm quark was theoretically required in order to explain the observed suppression of flavor changing neutral weak interactions, and the third generation was needed to introduce CP violation into the SM. Aside for this fact that three generations are needed to make the SM theory work correctly, the second and third generations appear to play no role in the everyday world. Experiments at CERN's LEP e^+e^- collider have shown that there are no more than three light or massless neutrinos,[8] strongly suggesting that there are only three generations.

2.1.2 Fundamental Interactions

When fermions interact by the electromagnetic, strong, or weak force, the interaction is thought of as being transmitted between the particles by a spin one gauge boson. The gauge bosons of the standard model are shown in the lower part of Table 2.1. They represent some quantized state of the field of that interaction (i.e. the photon is the quantization of the electromagnetic field). For example, the scattering of two electrons is depicted as one electron emitting a photon which is absorbed by the other electron. For a brief instant, there are three particles present, the two electrons and the photon, representing more energy than is available in the initial or final states. This situation is allowed, because some energy can be "borrowed" for a very short time as stipulated by the Heisenberg uncertainty principle. The photon is virtual; it only lives for the brief amount of time it takes to carry out the interaction.

The gauge bosons couple to the fermions with a strength appropriate with the force. For example, photons do not couple at all to the neutral neutrinos, since neutrinos are unaffected by the electromagnetic force.* As discussed below, the strengths of the couplings are not constant, but in fact change for different energy scales.

The strong force is mediated by the gluon. The gluon is massless and electrically neutral, but does carry color charge. While the quark is characterized by one "polarity"

*Photons do couple to some electrically neutral particles. For example, the π^0 meson is neutral but does interact electromagnetically since its constituent quarks have electric charge. The π^0 can, in fact, decay to two photons.

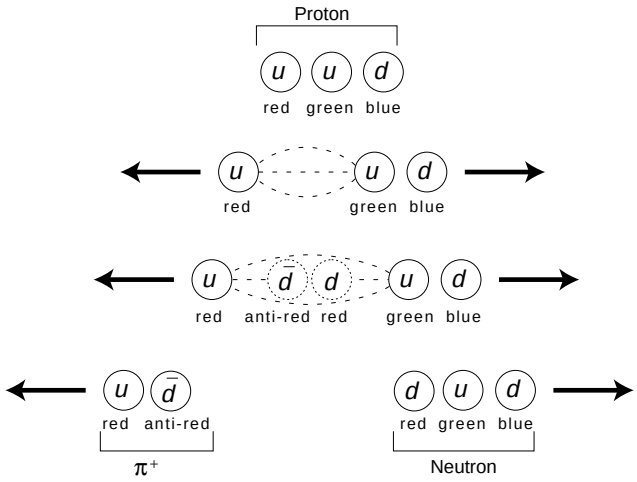

Figure 2.1: An example of Hadronization. Remove one of the up quarks from the proton and what remains are not free quarks, but a π^+ meson and a neutron. The color charge of the quarks are also shown. Note that all of the hadrons in the initial and final states are colorless.

of color (red, green, blue, antired, antigreen, or antiblue), the gluon must carry two polarities (a color and an anticolor) since it may be exchanged between two quarks that are interacting via the strong force. The fact that the gluon carries the charge of the strong force implies that it can interact with itself, corresponding to self interacting loop diagrams. The photon does not have this ability, since it is electrically neutral.

As mentioned, the quarks and gluons are never observed as free particles. That is because the strength of the strong force increases with increasing distance. For example, if the quarks making up a proton are close together, they feel little from the strong force and just "rattle around" inside the proton (this phenomenon, called asymptotic freedom, is described in more detail in Section 2.1.3). If one quark begins escaping from the others, it starts feeling the strong force pulling it back towards the other quarks. The force will increase with the distance between them. This effect is opposite to gravity and the electromagnetic force which weaken as distance is increased.

If a quark within a proton is given a big enough kick so that it cannot stay inside (possibly due to a collision at high energy with another quark), the quark may leave the proton, but the potential energy of the strong force will be so great that a new quark-antiquark pair will appear out of the vacuum, one to bind with the leaving quark

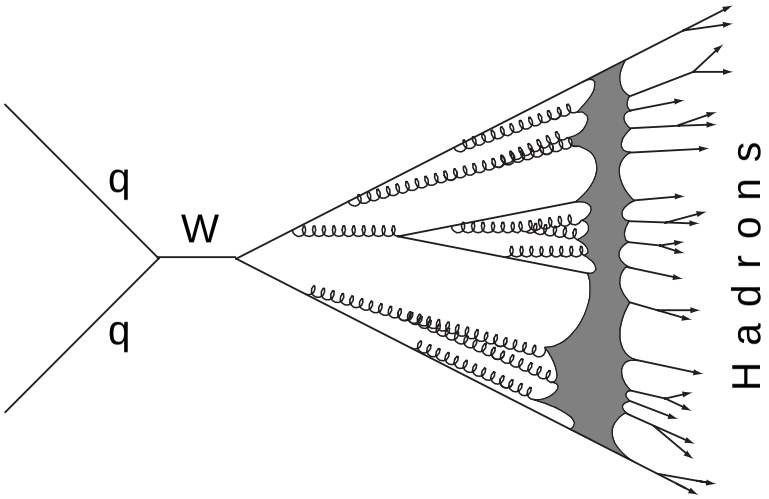

Figure 2.2: Cartoon of hadronization. Two high energy quarks on the left are shown annihilating into a W boson. The W then decays into two high energy quarks which hadronize by emitting many gluons (curly lines) that decay to more quarks. The grey region is where the quarks form hadrons, the particles that are observed in a detector. The direction of the cartoon lines do not represent actual particle directions. The final hadrons, in fact, will be collimated along the direction of their parent quarks or gluons forming jets. There will be at least two jets from the two quarks that decayed from the W. Hard gluons decayed from those quarks may also produce jets (final state radiation). The jets will be balanced in the event if the incident quarks have the same energy (if not, the jets will balance only in azimuthal angle). For example, if two jets are produced and the W is not boosted, the jets will have the same energy and will appear back to back.

forming a meson and another to stay with the proton remnants. In the end, all that one observes are colorless hadrons. This process is called hadronization or fragmentation and is not that well understood. An example is depicted in Figure 2.1. Since energy must be conserved, the energy of the system is decreased by the energy it takes to create the new quarks. High energy quarks will produce many new quarks and antiquarks as they escape as shown in Figure 2.2. Therefore in a detector, a high energy quark is seen as a spray or jet of collimated hadrons moving along the direction of the original quark. The particles within the jet have little momentum transverse to the jet direction, regardless of the energy of the original quark.

The weak force is carried by the weak gauge bosons: the charged W boson and the neutral Z. Unlike the gluons and photons, the W and Z are quite heavy ($\sim$100 GeV/c^2), which implies that the weak force only acts over short distances. It is difficult to form a

picture of the effects of the weak interaction, since it does not attract or repel particles like the other forces. Rather, the weak force is the cause of beta–decay of nuclei, allowing neutrons to transmute into protons and vice-versa. All particles may be affected by the weak force.

2.1.3 Gauge Theories and the Electroweak Force

The Standard Model is comprised of two separate theories, quantum chromodynamics (QCD) and electroweak. Electroweak unifies the electromagnetic force, described by quantum electrodynamics (QED), with the weak force. All of these theories are gauge theories in that they involve fields (mathematical constructs that represent the particles and interactions) that are invariant under a change of phase or gauge. For example, if the phase of the electron field of QED is changed arbitrarily, the resulting physics is not altered so long as the field for the photon is also changed in the appropriate manner. In fact, for spin 1/2 fields to be invariant under change of gauge, there must be a massless spin 1 boson (the photon for QED). This rule would seem to be violated by the weak force with its massive gauge bosons, but there is a fix discussed below.

The manner in which the gauge enters the theory characterizes the interaction. For instance, QED involves phase factors of $e^{i\phi(x)}$, which are members of the symmetry group $U(1)$ – unitary transformations in one dimension. For the weak force, it is convenient to group the particles into doublets,

$$\begin{pmatrix} \nu_e \\ e \end{pmatrix}, \begin{pmatrix} \nu_\mu \\ \mu \end{pmatrix}, \begin{pmatrix} \nu_\tau \\ \tau \end{pmatrix}, \begin{pmatrix} d \\ u \end{pmatrix}, \begin{pmatrix} s \\ c \end{pmatrix}, \text{ and } \begin{pmatrix} b \\ t \end{pmatrix}. \tag{2.1}$$

Instead of using a field for every particle, there is a two-component field for each doublet. The gauge transformations are now quite complicated since matrices are involved, and, in fact, the transformations can cause a particle to transform into its doublet partner. Such transformations belong to the $SU(2)_L$ symmetry group (the L subscript indicates that the weak interactions only affect particles in left handed helicity states). For the theory to be gauge invariant, there must be three massless gauge bosons, W^+, W^-, and the W^0 (note these massless bosons are not the same as the massive W and Z bosons described in

Section 2.1.2; at least not yet). At this stage, the electromagnetic force can be combined with the weak force by adding in the $U(1)$ group and its gauge boson, the massless and neutral B^0 which will eventually become part of the photon. This $SU(2)_L \times U(1)$ theory with the massless gauge bosons does not reflect the fact that electromagnetism and the weak forces are separate in the everyday world, and that the W and Z weak gauge bosons have mass. Therefore, the symmetry must be broken in some way.

The Higgs mechanism provides the method for spontaneously breaking electroweak symmetry by forcing one to choose a vacuum expectation value (vev) for a Higgs field. The results are that the W^+, W^-, and the neutral Z (a mixture of the W^0 and the B^0) acquire mass. The photon (a different mixture of the W^0 and the B^0 bosons) remains massless. The price one pays is the introduction of a new field representing a scalar (spin zero) particle, the Higgs boson, and a new parameter in the model, θ_W, the mixing angle for relating the Z and γ to the W^0 and B^0. The scalar Higgs couples to any particle with mass: the heavier the mass, the stronger the coupling. The triumph of the Higgs mechanism is the prediction of the masses of the W and Z weak bosons. These particles were discovered at CERN with the UA1 and UA2 detectors in the late 1980's. Their masses were measured to be right at the SM prediction. This strong evidence for the validity of the Higgs Mechanism is the only evidence, for the Higgs particle has never been observed in an experiment.

2.1.4 Running Coupling Strengths and GUTs

Although in the everyday world the weak and electromagnetic forces are separate to first order, above the weak energy scale, $\mathcal{O}(M_W)$, these forces are unified into the electroweak force. There are still two coupling strengths for the interaction (one for the $SU(2)_L$ part which is mediated by the W^+, W^-, and W^0 bosons, and another for the $U(1)$ part mediated by the B^0). QCD also has an $SU(3)$ symmetry involving the color charge with its own coupling strength (there are eight generators of the $SU(3)$ symmetry resulting in eight two–color combinations that can be carried by gluons). Note that that phrase "coupling constant" has been avoided since the couplings are indeed not constant. They

change with the energy scale (the scale of the momentum transfer between the two interacting particles) and thus are "running constants." This phenomenon is due to higher order effects of virtual bosons spontaneously forming loops of fermion–antifermion pairs and fermion–antifermion pairs appearing and disappearing from the vacuum. Indeed, the picture that a proton is composed of three quarks is simplistic. The three valence quarks are constantly exchanging gluons, which may transform into quark–antiquark pairs (sea quarks) and back into gluons again. In fact, about half of the momentum of a moving proton is carried by gluons. For QCD, the coupling strength decreases with increasing momentum transfer (shorter distances). That is why when quarks within a nucleon are probed with high energy electrons, the quarks appear to be free. This effect is asymptotic freedom. The quarks and gluons within protons are collectively called partons.

The root cause of the running coupling strengths has to do with the fact that the higher order effects can cause some calculations to result in infinities. The infinities can be absorbed into quantities that cannot be directly measured and are safely "swept under the rug" or renormalized, making the theories calculable again. The price one pays is an additional term that must be added to the coupling strengths that is dependent on the energy scale. The renormalized quantities are the running constants.

A goal of particle physicists is to invent a theory where all of the symmetries of the Standard Model can be expressed by one symmetry, and consequently, all of the forces are unified into one force. Such theories are called Grand Unified Theories (GUTs). If the running coupling strengths are extrapolated to huge energy scales, they appear to converge at a scale of $M_{GUT} \sim 10^{16}$ GeV (though not all three at the same point, see Section 2.2.3 and Figure 2.6a). This convergence may be a hint that GUT theories are valid. One also presumes that gravity can be unified at the Planck scale, $M_{PL} \sim G_N^{-1} \sim 10^{19}$ GeV, where G_N is Newton's constant. Below those scales the grand symmetry is broken at some point, yielding the particles and interactions observed presently.

A high energy physicist's dream is the ability to probe physics at huge energy scales. The Tevatron collider at Fermilab produces interactions with momentum transfers near the weak scale $\mathcal{O}(100$ GeV). The now defunct SSC would have been able to probe the

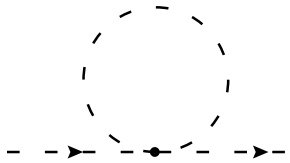

Figure 2.3: Self interaction diagram of fundamental scalars. This diagram is quadratically divergent.

TeV scale, and the soon to be completed LHC collider at CERN will get close to that. Directly probing anywhere near the GUT or Planck scale does not seem remotely possible with current technology. Instead, the predicted effects of the different GUT theories on weak scale physics (new particles and interactions) are the subject of searches. So far, no new particles or unexpected interactions have been observed beyond what are included in the SM. Though some proposed GUT models have been ruled out or severely constrained with experiments, it is still unknown what kind of GUT model is correct, let alone if GUTs are indeed the right description of physics at high energy scales.

2.1.5 Problems with the Standard Model

The SM is extremely successful in predicting the phenomena of the subatomic realm. Some aspects of the SM, however, are worrisome. Although the masses of the W and Z bosons are predicted with the Higgs mechanism, the SM gives no hint as to the masses of the quarks and leptons. They are input into the model by hand. And though the Higgs Mechanism seems to work, it was added in an ad hoc manner; the SM does not predict electroweak symmetry breaking (EWSB) by itself. This deficiency is addressed by some GUT models that have EWSB built into them.

There is a more serious problem. The scalar Higgs boson is a special kind of particle in that it gives mass to the fermions. Since the Higgs itself is massive, it can be involved in self-interaction loop processes as shown in Figure 2.3. Unlike similar diagrams for gluons, self interaction loop diagrams for fundamental scalar particles involve integrals that are quadratically divergent. When such an integral involved in calculating the Higgs mass is integrated over all momenta, an infinity results that cannot be renormalized away. A nonrenormalizable theory is a disaster, so there must be something that alleviates the

quadratic divergence. One can imagine cutting off the integral at some energy scale where new physics becomes important, M_X, which is likely near the GUT scale. The mass parameter of the Higgs from EWSB runs[†] from an energy scale at Q_1 down to a lower energy scale of Q_2 according to,

$$M^2(Q_2) = M^2(Q_1) + Cg^2\left(Q_2^2 - Q_1^2\right) + g^2 R + \mathcal{O}(g^4) \tag{2.2}$$

where C is a dimensionless constant, g is a coupling strength, and R is some parameter that grows at worst logarithmically as $Q_1 - Q_2 \to \infty$. The running of the Higgs mass from the high scale M_X down to the weak scale M_W is thus given by,

$$M_H^2(M_W) \sim M_H^2(M_X) - Cg^2 M_X^2 \tag{2.3}$$

where $M_X \approx \mathcal{O}(M_{GUT}) \gg M_W$. Since the Higgs mass at the weak scale is supposed to be on the order of M_W (that is the scale where EWSB takes place), the terms on the right hand side of Equation (2.3) must be tuned to a precision of $\sim 10^{-26}$ in each order of perturbation theory. A tuning to that degree would be an incredible feat of nature and is unnatural. This difficulty is called the fine tuning problem. A related question is the hierarchy problem: why do the coupling constants of the SM appear to converge at such a huge energy scale ($M_X \gg M_W$)? Nothing in the SM can answer these questions, thus providing the expectation that there must be some theory beyond the Standard Model.

2.1.6 Beyond the Standard Model[9, 10]

Theorists have introduced two schemes for eliminating the quadratic divergence of the Higgs mass. One solution involves treating the Higgs not as a fundamental particle, but comprised of fermions. Some force must keep the constituent fermions confined within the Higgs, similar to how the strong force confines the quarks within a hadron. Like QCD, the theory of this new interaction would be renormalizable, thus alleviating the quadratic

[†]A mass *parameter* is a parameter of the theory, like a coupling strength, and for some particles runs with the energy scale. The actual mass of the particle that one measures is the pole mass and does not change with energy scale. The pole mass for the Higgs can be calculated within the theory by solving the one loop diagram discussed here and involves the running mass parameter. If one could solve to all orders of perturbation theory, the dependence on the energy scale would cancel out completely.

divergences. Keeping with the strong force similarity, this new force is called Technicolor (recent reviews can be found in References 11 and 12), which introduces its own color charge that is carried by the constituent fermions called techniquarks. Technicolor theories predict the existence of technipions and technirhos, particles made up of techniquark pairs. No such particles have been observed and severe constraints can be placed on the validity of this theory. Though Technicolor can alleviate the fine tuning problem, it has nothing to do with unification of forces and does not address the hierarchy question.

A variation of Technicolor, compositeness, posits that none of the SM particles are fundamental, but are, in fact, made up of preons. If compositness is reality, then the cross section (reaction rates) for some processes would be different than what the SM predicts. No such significant deviations have been observed. Compositness also suffers from the same deficiency as Technicolor in that it cannot address the hierarchy problem and is constrained by experiments.

The second scheme for eliminating quadratic divergences is Supersymmetry, which adds fermions and scalar particles to the Standard Model to introduce new loop diagrams that cancel out the quadratic divergent loops. Models of Supersymmetry may be based on GUTs that build in EWSB and provide relations between the weak scale and the GUT scale, addressing the hierarchy problem. Described in this thesis is a search for two of the particles that Supersymmetry predicts, and so Supersymmetry is explored in some detail in subsequent sections of this chapter.

2.2 Supersymmetry

Supersymmetry (SUSY)[10, 13–15] is a theory that cancels the quadratic divergence from the fundamental scalar Higgs particle by adding new particles to the Standard Model. First, a simple SUSY model is presented to explain how the cancellation is achieved. More realistic SUSY models will then be explored.

2.2.1 Basics of SUSY

A simple supersymmetric model is one by Wess and Zumino[15–18] and shows the basic features of SUSY. This theory involves two real scalar fields (A and B) representing spin zero bosons like the Higgs, and a two degree of freedom spinor field (ψ) representing a Majorana (particle and anitparticle are one and the same) spin-1/2 fermion. The Wess and Zumino lagrangian describing the theory is,

$$\begin{aligned}\mathcal{L} = &\frac{1}{2}(\partial_\mu A)^2 + \frac{1}{2}(\partial_\mu B)^2 + \frac{i}{2}\bar{\psi}\not{\partial}\,\psi - \frac{1}{2}m\bar{\psi}\psi - \frac{1}{2}m^2A^2 - \frac{1}{2}m^2B^2 \\ &+ mgA(A^2+B^2) - \frac{1}{2}g^2(A^2+B^2)^2 - ig\bar{\psi}A\psi + ig\bar{\psi}\gamma_5 B\psi\end{aligned} \tag{2.4}$$

where the three particles have the same mass m and same coupling constant g (a circled number will be used later to refer to the term underneath it). The A, B, and ψ fields can undergo certain transformations. Transformations are written as,

$$A \to A' = A + \delta A = A + \bar{\alpha}QA \tag{2.5}$$

where α is the constant parameter of the transformation and Q is the transformation generator. Wess and Zumino define supersymmetric transformations for the scalar fields to be,

$$\delta A = i\bar{\alpha}\gamma^5\psi \qquad\qquad \delta B = -\bar{\alpha}\psi \tag{2.6}$$

and for the fermion field,

$$\delta\psi = F\alpha - iG\gamma^5\alpha + (\not{\partial}\,\gamma^5 A)\alpha + i(\not{\partial}\,B)\alpha \tag{2.7}$$

where $F = mA - g(A^2 - B^2)$ and $G = mB - 2gAB$.

With some work,[18] one can show that the lagrangian of Equation (2.4) is invariant under the Wess and Zumino transformations. That is if the transformed fields are plugged into the lagrangian, it changes at most by a total derivative and thus the resulting physics remains unaltered. The transformations of Equation (2.6) and (2.7) are called supersymmetric, because boson transformations involve the fermion field and the fermion transformation involves the boson fields. This "Supersymmetry" relates the bosons to the fermion and vice-versa.

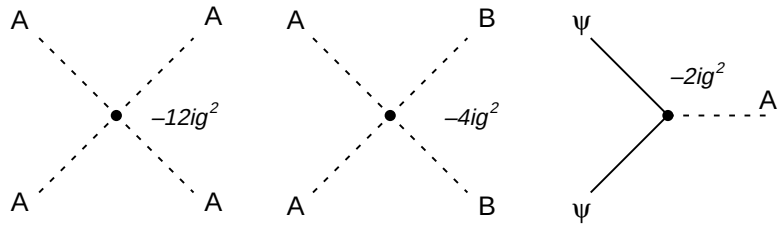

Figure 2.4: Interactions involving the A scalar particle. The vertex factors are shown with each interaction.

Using Equation (2.5), one can identify the transformation generator, Q, in Equation (2.6) and (2.7). Q appears to be an operator that transforms a fermion field into a scalar boson field and vice-versa, altering the spin of the particle by $\pm 1/2$. The anticommutation relation for Q is,

$$\left\{Q_a, \bar{Q}_b\right\} = 2(\gamma_\mu P^\mu)_{ab} \tag{2.8}$$

where P^μ represents the translation generators of the Poincaré group (Lorentz boosts and rotations). The a, b subscripts are components of the spinor fields. Since the transformations are involved with space–time transformations, Supersymmetry is a space–time symmetry. This distinction is important, since it differs from the internal symmetries of particles, such as electric and color charge, lepton number, and baryon number. The Wess and Zumino supersymmetric generator acting on a field will only change the spin; the particle retains its mass, charge, and its other internal quantum numbers. For the lagrangian to be invariant under the transformations, one particle is needed for each degree of freedom of its partner, so the two scalar bosons are the super-partners of the fermion and vice-versa.

The interaction terms marked ① and ② in the Lagrangian (Equation (2.4)) describe how the A scalar particle interacts with the B and the ψ. These terms are expanded below,

$$\mathcal{L} = \ldots - \frac{1}{2}g^2(A^4 + 2A^2B^2 + B^4) - ig\bar{\psi}A\psi + \ldots \tag{2.9}$$

and predict the interactions shown in Figure 2.4 (the B^4 term is ignored for this discussion). With these interactions, the self interacting one loop diagrams for the A can be

drawn as in Figure 2.5. Diagrams (3), (4), and (5) are separately quadratically divergent, but when their amplitudes are added together, the quadratic divergent terms cancel,[18] leaving a logarithmically divergent term that can be renormalized. The self interaction diagrams for the B cancel in a similar manner.

Supersymmetry eliminates the quadratic divergences by introducing new particles so that each fermion is paired with two scalar particles causing the divergences to cancel. Clearly, the Wess and Zumino theory is not realistic, since all of the particles must have the same mass. If that were the case, then SUSY could be ruled out immediately, since a scalar electron with the electron's mass has not been observed. Supersymmetry must be broken so that there can be mass splitting between the SUSY partner particles. A splitting is allowed because the quadratic divergences do not have to cancel exactly. The fine tuning problem is still alleviated so long as masses are not more than $\sim$1 TeV apart (see Section 3.6 for some constraints on the splittings). The Wess and Zumino model is too simplistic for the real world, but it shows the basic characteristics of SUSY models. The basis of the model used for this search is the Minimal Supersymmetric Standard Model.

2.2.2 Minimal Supersymmetric Standard Model

The Minimal Supersymmetric Standard Model[19–22] (MSSM) is a scheme for introducing Supersymmetry to the Standard Model that adds the fewest new particles. Each SM particle receives supersymmetric partners or sparticles, one for each degree of freedom. These additions reflect $N = 1$ Supersymmetry, where N is the number of supersymmetric generators (Q in the previous section) that alter spin by 1/2 unit. One can conceive of $N \geq 2$ models, but one gets into trouble in relating fermions with different helicities incompatible with the left–handed weak interactions.

The particle content of the MSSM is shown in Table 2.2. The particles and sparticles form supermultiplets, similar in spirit to the doublets of electroweak theory in Equation (2.1). There are two kinds of supermultiplets. A chiral supermultiplet contains a chiral fermion (fermions that couple differently to the weak gauge bosons depending on

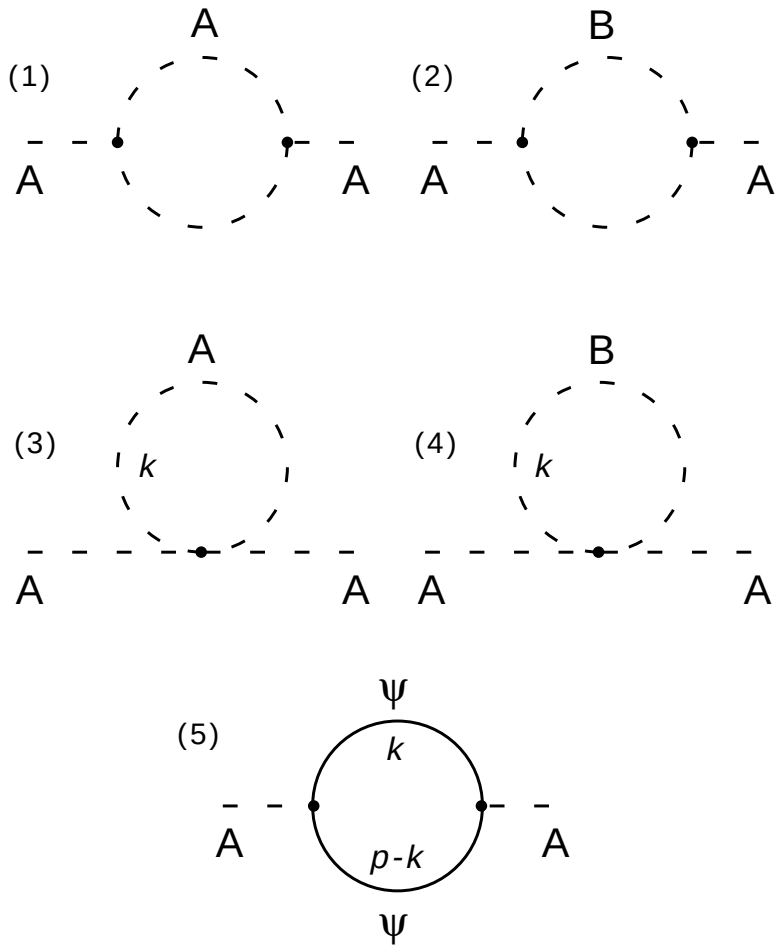

Figure 2.5: Self interaction loop corrections for the A scalar particle.

Particle			Sparticle		
Fermion (spin 1/2)	Lepton	ℓ	*Sfermion (spin 0)*	Slepton	$\tilde{\ell}_L$, $\tilde{\ell}_R$ (only $\tilde{\nu}_L$)
	Quark	q		Squark	$\tilde{q}_L$, $\tilde{q}_R$ ($\tilde{b}_{1,2}$, $\tilde{t}_{1,2}$)
(spin 1)	Gluon	g	*(spin 1/2)*	Gluino	$\tilde{g}$
Gauge Boson (spin 1)	Photon	γ	*Gaugino (spin 1/2)*	Photino	$\tilde{\gamma}$ → Neutralino $\tilde{\chi}^0_{1,2,3,4}$
	Z boson	Z		Zino	$\tilde{Z}$ → Neutralino $\tilde{\chi}^0_{1,2,3,4}$
Higgs Boson (spin 0)	light Higgs	h	*Higgsino (spin 1/2)*	Higgsino	$\tilde{h}$ → Neutralino $\tilde{\chi}^0_{1,2,3,4}$
	heavy Higgs	H		Higgsino	$\tilde{H}$ → Neutralino $\tilde{\chi}^0_{1,2,3,4}$
	Pseudoscalar Higgs	A		Higgsino	$\tilde{A}$ → Neutralino $\tilde{\chi}^0_{1,2,3,4}$
Gauge Boson (spin 1)	W boson	$W^\pm$	*Gaugino (spin 1/2)*	Wino	$\widetilde{W}^\pm$ → Chargino $\tilde{\chi}^\pm_{1,2}$
Higgs Boson (spin 0)	Charged Higgs	$H^\pm$	*Higgsino (spin 1/2)*	Higgsino	$\tilde{H}^\pm$ → Chargino $\tilde{\chi}^\pm_{1,2}$
(spin 2)	Graviton	G	*(spin 3/2)*	Gravitino	$\widetilde{G}$

Table 2.2: Particle content of the MSSM. The mixings are explained in the text.

their helicity state) and two spin zero scalars. The vector supermultiplet consists of a spin-1 vector boson and a fermion. These supermultiplets hold a Standard Model particle and its partner(s).

As shown in Table 2.2, each charged lepton receives two spin zero *sleptons*, since fermions have two degrees of freedom. Each neutrino is paired with only one *sneutrino*, since neutrinos have only one helicity state. The quarks are similar to the leptons and receive two scalar *squarks* each. The squarks and sleptons are labeled left and right handed. Since these particles are scalars, the labels reflect how they couple to the partners of the weak gauge bosons instead of denoting helicity. The massless spin 1 gluon has 16 degrees of freedom (2 helicity states $\times$ 8 color) and is associated with the massive spin 1/2 gluino, also with 16 degrees of freedom.

The partners of the gauge and Higgs bosons are more complicated. For the MSSM, two Higgs doublets are required in order to give mass to the up type and down type quarks (in the SM, the single Higgs field and its conjugate fulfill this role, but in the MSSM

conjugate fields cannot be used[23]). Consequently, five Higgs particles exist: two charged scalars ($H^{\pm}$), two neutral scalars (h and H) and one neutral pseudoscalar (A) as shown in Table 2.2. Since there are two Higgs doublets, there are two vacuum expectation values ($< v_1 >$ and $< v_2 >$). The vevs are constrained so that $< v_{SM} >^2 = < v_1 >^2 + < v_2 >^2$, where $< v_{SM} >$ is the vev of the single Higgs field in the SM. The ratio of the two Higgs doublet vevs is still undetermined, however, and is denoted by the parameter $\tan\beta = < v_2 > / < v_1 >$. There is also a free Higgsino mass parameter, μ.

The Z, photon, and neutral Higgses add up to eight degrees of freedom (three helicity states for the Z, two for the γ, and one each for h, H, and A). Their partners, the zino, photino, and Higgsinos, respectively, mix to form four, neutral, spin 1/2 *neutralinos*, where $M_{\tilde{\chi}_1^0} < M_{\tilde{\chi}_2^0} < M_{\tilde{\chi}_3^0} < M_{\tilde{\chi}_4^0}$. The SUSY partners of the W boson (two charges $\times$ three helicities = six d.o.f.) and the charged Higgses (two charges $\times$ one helicity) mix to form two charged spin 1/2 *charginos* which have eight d.o.f. The couplings of the scalar squarks and sleptons to the charginos and neutralinos depend on the chargino/neutralino "gauge content." The parameters $\tan\beta$ and μ determine what fraction of the chargino and neutralino mixtures are higgsino and wino/zino/photino. Since the right handed SUSY scalars only couple to the Higgsino part, the branching fractions of the charginos and neutralinos depend heavily on $\tan\beta$ and μ.

Since Supersymmetry commutes with the $SU(3)_C \times SU(2)_L \times U(1)$ symmetries of the SM, the gauge interactions of the sparticles are the same as their partner SM particles with the same coupling strengths, although the difference in spins must be taken into account. For example, if the chargino is mostly wino, it will decay to quarks and leptons with the same branching fractions as a SM W boson. If it is mostly higgsino, it will decay like a Higgs.

The MSSM also introduces a new multiplicative quantum number, R – Parity. R – Parity is defined to be,

$$R = (-1)^{3(B-L)+2S} \tag{2.10}$$

where B is the particle's baryon number, L is the lepton number and S is the spin. According to this definition, R – Parity is $+1$ for SM particles and -1 for their sparticle

partners. In the analysis described here, R – Parity is assumed to be conserved. Although R – Parity conservation is not required by any model, its violation implies that lepton and baryon number conservation are violated as well.

In R – Parity conserving SUSY, sparticles are always produced in pairs, and each decay of a sparticle yields another sparticle. Consequently, the lightest supersymmetric particle (LSP) must be stable. R – Parity conservation is theoretically favored, since it does not allow sparticles to play intermediate roles in processes that involve only SM particles, and so the predictions of the SM remain unaltered. Fast proton decay is also prohibited.

The stable LSP is generally assumed[24] to be the lightest neutralino, $\tilde{\chi}_1^0$. It must be neutral since charged LSPs would have been seen in atomic physics. The LSP only interacts weakly, like neutrinos, producing missing energy (imbalanced events) in a detector which can be used as an experimental signature for SUSY. It is also a candidate for cold (nonrelativistic) dark matter.

2.2.3 GUT Frameworks for the MSSM

Although the MSSM allows one to add the fewest number of new particles to the SM, it unfortunately leads to an enormous number of new parameters. The MSSM gives no prediction on the masses of the sparticles (of course, they must be heavier than their partners or else they would have been observed already). The mixing angles are also completely unknown. With > 100 parameters that must be input by hand, the MSSM is a cumbersome theory to use in systematic searches for sparticles.

The usual method for reducing the number of independent parameters is to work within the framework of a Grand Unified Theory (GUT). In fact, the MSSM gives a hint that a GUT with SUSY particles may be the correct description of physics at high energy scales, since the additional particles of the MSSM cause the running coupling strengths to converge at the same point as shown in Figure 2.6. A "GUT inspired MSSM" relies on some symmetry at a high energy scale to give relations between some of the sparticle masses. For example, with such models the masses of the squarks are degenerate except

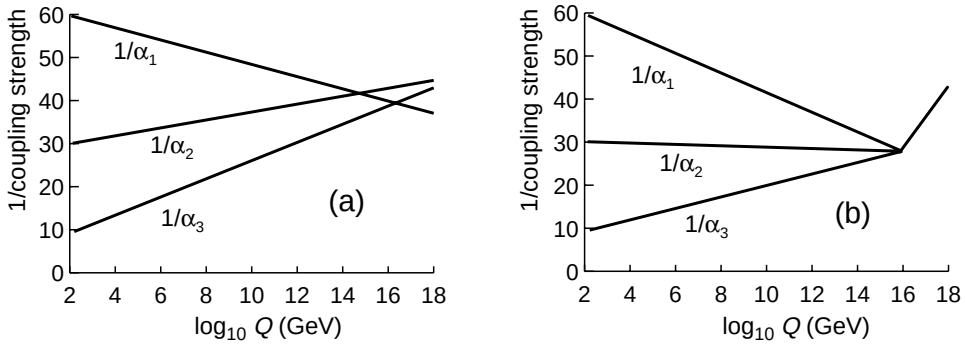

Figure 2.6: Evolutions of the coupling constants. Shown are the evolutions of the $U(1)$ (α_1), $SU(2)$ (α_2), and $SU(3)$ (α_3) coupling constants with the energy scale. Plot (a) shows the evolution in the Standard Model. Plot (b) is the evolution within the MSSM. The addition of the sparticles changes the running of the coupling strengths so that they all converge at the same point, suggesting that the interactions arise from a single grand unified force.

for the scalar top.[‡] In GUT models, the gauginos are mass degenerate at the GUT scale, and so their masses are related at the weak scale (i.e. typically, $\tilde{\chi}_1^{\pm} \approx \tilde{\chi}_2^0 \approx 2\tilde{\chi}_1^0$). Although such relations are helpful, one still must input by hand the degenerate squark mass, masses for the sleptons, $\tan\beta$, μ, and so on.

The DØ experiment has performed many searches within the framework of the GUT inspired MSSM. As shall be seen, the decays of squarks and gluinos are highly dependent on the parameters of the model, and so it is advantageous to use a framework with the least number of free parameters and most predictive power possible.

2.3 Minimal Supergravity

Minimal Low Energy Supergravity[23, 25–28] (mSUGRA) is a model that not only unifies the strong, weak, and electromagnetic forces, but also includes gravity at some large energy scale M_X. Typically, M_X is the GUT scale (10^{16} GeV) or the Planck scale (10^{19} GeV). At M_X, the mass parameters (see footnote on page 13 for the difference between mass parameters and the measured mass) for the gauginos are degenerate as for any GUT model, and in the simplest supergravity models, the inclusion of gravity means that all

[‡]Because the top quark is so heavy, the left and right top squarks can mix into a light scalar top ($\tilde{t}_1$) and a heavier one ($\tilde{t}_2$), as shown in Table 2.2.

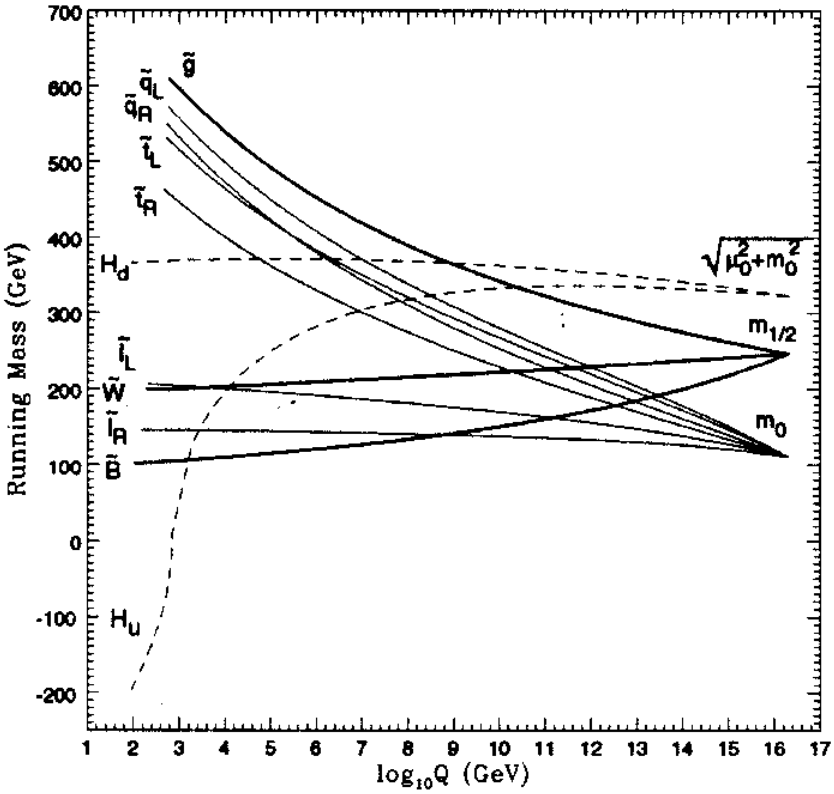

Figure 2.7: Evolution of sparticle mass parameters in Minimal Supergravity. This plot shows the mass parameters of various sparticles vs. energy scale (Q). Note that the gauginos are in states before electroweak symmetry breaking ($\widetilde{W}$ and $\widetilde{B}$). The Higgs mass parameter running negative is the originator of EWSB. These evolutions shown are for a particular choice of the model parameters. Choosing M_0, $M_{1/2}$, and the other parameters differently will result in different evolutions. There are some with Higgs masses that stay positive, meaning EWSB is not predicted by those models.

of the SUSY scalars also share a common mass parameter. The only parameters needed to describe mSUGRA models are then as follows:

- M_0, the common mass parameter for all scalar sparticles at the M_X scale.
- $M_{1/2}$, the common mass parameter for all gauginos at the M_X scale.
- $\tan\beta$, the ratio of the vacuum expectation values of the two Higgs doublets.
- sign(μ), the sign of the Higgsino mass parameter.
- A_0, a common trilinear coupling constant in the lagrangian (for searches at the Tevatron, A_0 only affects scalar top mixing).

Along with A_0 there is a bilinear coupling constant, B_0, but it is recast into $\tan\beta$ and μ. Only the sign of μ is needed, because its magnitude is constrained to yield the correct Z mass by electroweak symmetry breaking.

Given the mSUGRA parameters and masses of the SM particles, masses and mixing angles for the sparticles can be determined at the weak scale by solving the renormalization group equations (RGEs) of the model and evaluating loop diagrams. The evolutions of the sparticle mass parameters are shown in Figure 2.7. For many choices of the mSUGRA parameters, a Higgs mass parameter starts positive at M_X and, as the energy scale is decreased, runs negative, thus breaking electroweak symmetry. For the SM, the negative Higgs mass parameter must be put in by hand. The prediction of EWSB is one of the features of mSUGRA that makes these models favored among many SUSY phenomenologists.

Describing masses of the sparticles with just M_0 and $M_{1/2}$ is convenient, but one loses the physical aspect of the model. The correspondences of squark and gluino masses to M_0 and $M_{1/2}$ are shown in Figure 2.8.[§] In mSUGRA, the squark masses are not quite degenerate. While the masses of the scalar up, down, charm, and strange (both left and right varieties) are typically within 1 GeV/c^2 of each other, the scalar bottom can sometimes mix its left and right states into lighter and heavier mass eigenstates.

[§] All of the contours were determined with code within the `isajet` Monte Carlo event generator.[29]

The lighter sbottom is not more than 15 GeV/c^2 less than the four other squarks. The squark mass contours shown in the figure are an average of the masses for left and right squarks excluding scalar tops. Similar plots of mass contours for some other sparticles are shown in Figure 2.9. The values of the other model parameters are $\tan\beta = 2$, $A_0 = 0$, and $\mu < 0$. For small M_0 and $M_{1/2}$, electroweak symmetry breaking does not occur in mSUGRA, and so that region can be ruled out immediately. There are also points where the electron sneutrino is lighter than $\tilde{\chi}_1^0$ and thus becomes the LSP. Cosmological considerations disfavor a sneutrino LSP, but aside from that, there is no evidence why that situation cannot occur.

2.4 Other SUSY Models

Of course, one would like to experimentally test the validity of all SUSY models, but the details of squark and gluino decays are highly model dependent. Therefore, Monte Carlo simulations must be performed for each model to be tested. For models with many parameters, this task is prohibitive. The mSUGRA framework requires a minimum of free parameters and is used for the analysis described here. Aside from the fact that mSUGRA is a "nice" model in that it has few parameters, includes gravity, and predicts EWSB in many cases, there is no evidence that mSUGRA is the true, correct model of SUSY, assuming that SUSY itself is correct in the first place. As Monte Carlos become faster, however, more models will be able to be tested on a reasonable time scale.

Some new models have surfaced recently that are different from mSUGRA in an attempt to explain one event[30] collected by CDF, the other collider experiment at the Tevatron. The event has an electron, a positron, two photons, and is quite imbalanced (remember that LSPs give rise to imbalanced events). No similar event has been observed at DØ. The SM does not predict the occurrence of such an imbalanced $ee\gamma\gamma$ event. It also turns out that mSUGRA does not predict a significant rate for SUSY processes ending up with photons in the final state. Other models, called "Gauge Mediated SUSY" which involve how Supersymmetry is broken, explain how such an event could result from SUSY.

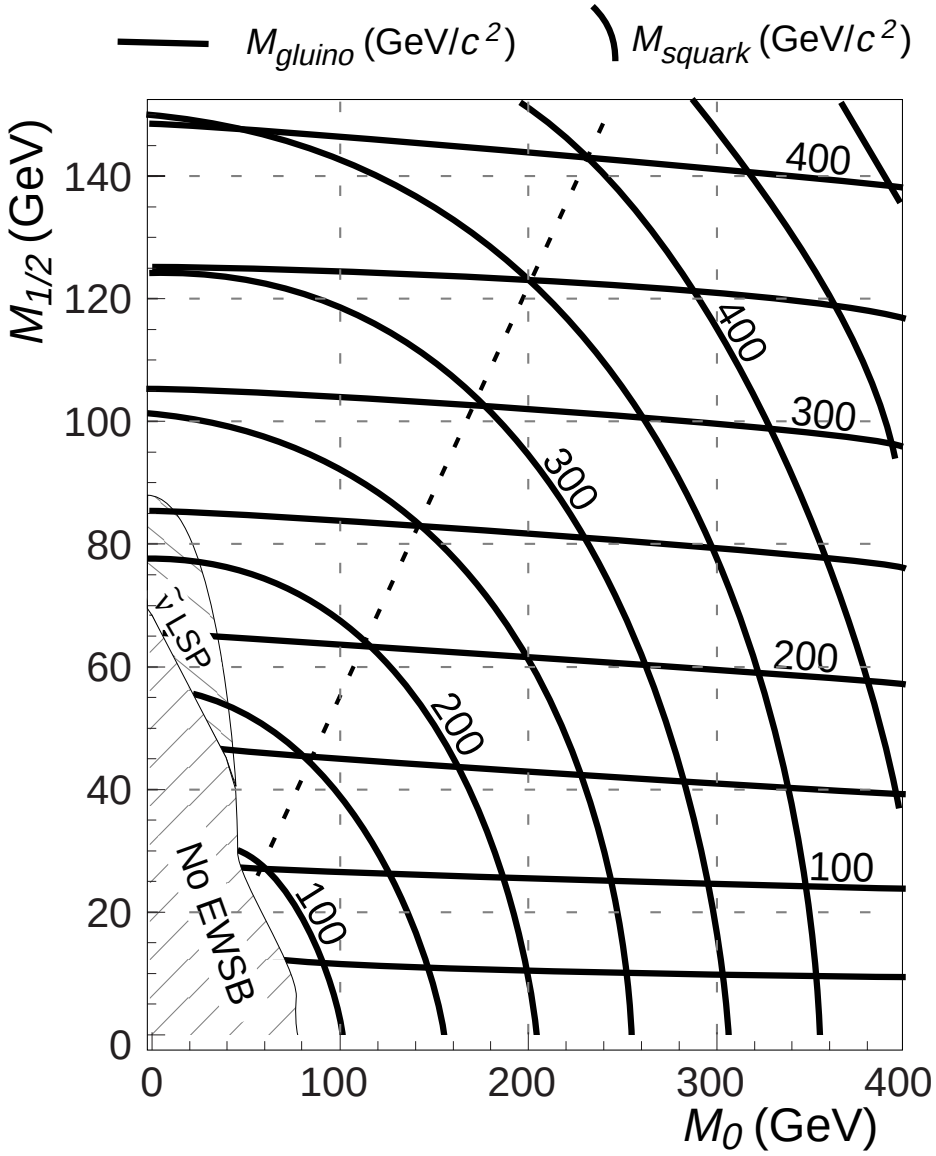

Figure 2.8: Mass contours of squarks and gluinos on the M_0 – $M_{1/2}$ plane. The nearly horizontal lines are gluino mass contours, and the lines forming the radial patterns are squark mass contours. The diagonal dashed line marks where squarks and gluinos have equal mass. The lower hashed region is where mSUGRA does not produce electroweak symmetry breaking. The upper hashed region is where the sneutrino is the LSP. These contours are valid for parameters $\tan\beta = 2$, $A_0 = 0$, and $\mu < 0$.

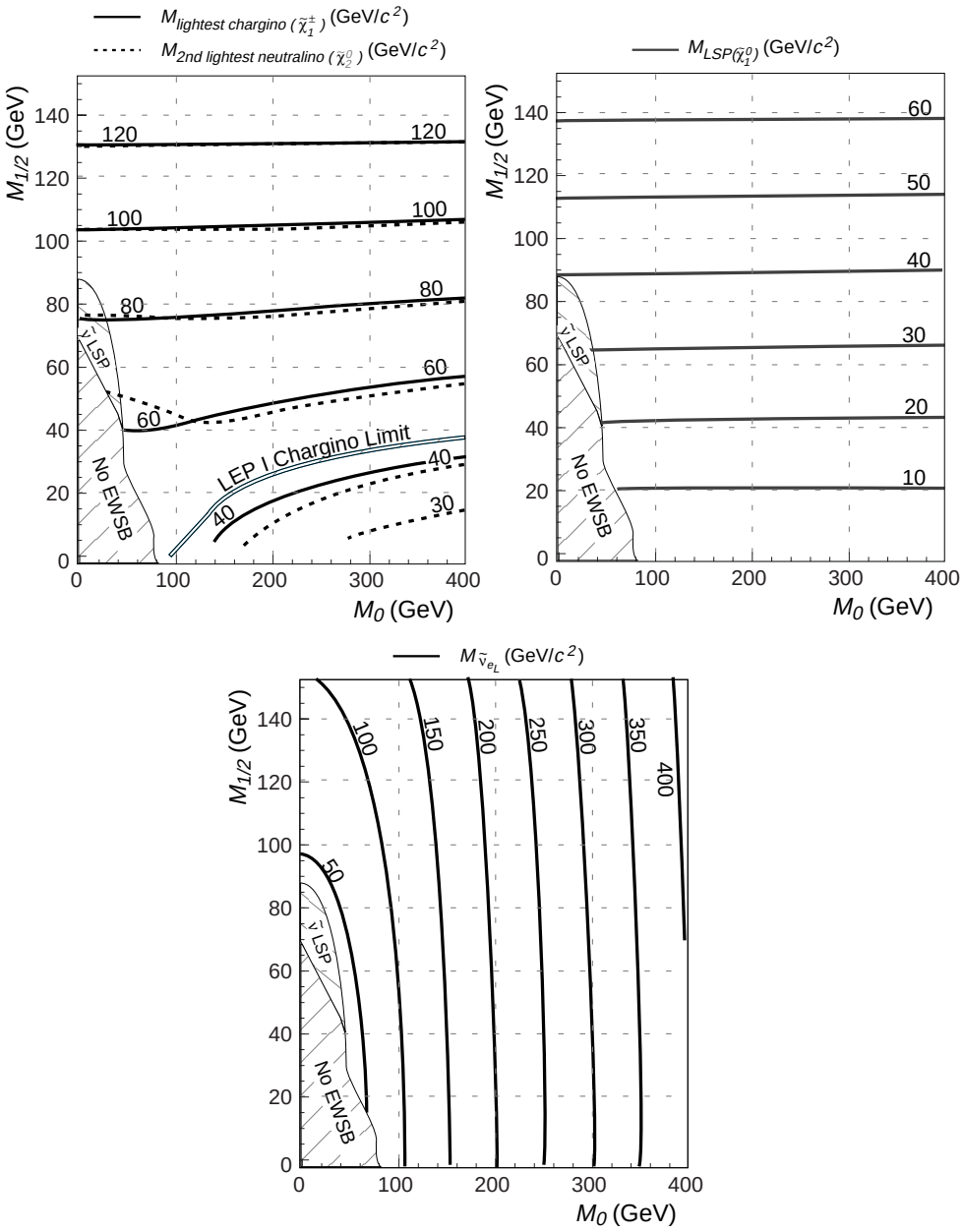

Figure 2.9: Contours of other sparticle masses on the M_0 – $M_{1/2}$ plane. These contours are valid for parameters $\tan\beta = 2$, $A_0 = 0$, and $\mu < 0$. Note that the mass contours for the scalar electron are nearly the same as the sneutrino contours shown.

There are two types of Gauge Mediated SUSY models,[21, 31, 32] those where the LSP is the $\tilde{\chi}_1^0$ and those where the LSP is the gravitino ($\widetilde{G}$), the SUSY partner of the graviton (the spin 2 graviton carries the gravitational interaction and has never been observed). In the $\tilde{\chi}_1^0$ LSP type model, the $\tilde{\chi}_2^0$ is mostly photino and the $\tilde{\chi}_1^0$ is mostly higgsino so that the decay $\tilde{\chi}_2^0 \rightarrow \gamma\tilde{\chi}_1^0$ occurs often. If the $\widetilde{G}$ is the LSP, then photons are produced when the $\tilde{\chi}_1^0$ radiatively decays via $\tilde{\chi}_1^0 \rightarrow \gamma\widetilde{G}$. Both models predict that imbalanced events with two photons should occur more often than what the SM predicts and should be observable in the data sets at CDF and DØ. Searches have been performed and no such excess has been found aside for the one event at CDF, so severe constraints can be placed on these models.

Forming conclusions on the basis of only one event is always a bit dangerous, since the measurements may be fluctuations. Nevertheless, the new SUSY models are interesting in their own right, and, if nothing else, serve as a reminder that there are other possibilities than mSUGRA.

2.5 Summary

The fundamental constituents of matter are described by the Standard Model (SM), a theory that has been used with great success to explain the sub-atomic and sub-nuclear regime. Although there has been no experiment that conclusively disputes the Standard Model, the theory has some internal problems and cannot predict some basic, fundamental parameters of nature. Thus, many believe that the SM is not a final theory but is part of some grander theory of nature. Supersymmetry theories (SUSY) are such extensions to the SM. SUSY predicts that there should be more particles beyond those of the SM, and so many experiments have been performed to search for these "sparticles". The search described here is for two sparticles called squarks and gluinos.

Although it eliminates a nagging problem with the SM, SUSY alone is also a complicated theory with more than one hundred free parameters. Therefore, many types of models have been introduced to make SUSY tractable. One such model is Minimal Super-

gravity (mSUGRA) that only has four free parameters and a free sign. The mSUGRA framework will be used for this search.

Chapter 3

The Strategy of the Search

The Tevatron at the Fermi National Accelerator Laboratory (Fermilab) is the highest energy collider in the world, colliding protons and antiprotons at a center of mass energy of 1.8 TeV. This machine at the "energy frontier" is the best place to search for direct production of new particles not yet observed. This analysis involves searching for squarks and gluinos of the mSUGRA model described in the previous chapter. The strategy of the search is now discussed.

3.1 Production of Squarks and Gluinos

Since squarks and gluinos will be produced through the strong interaction at the Tevatron, the production cross sections* may be large and will only depend on the masses of the squarks and gluinos themselves. Some examples of production diagrams[33] are shown in Figure 3.1. Since R – Parity is assumed to be conserved, squarks and gluinos are always produced in pairs. The protons and antiprotons of the Tevatron collide at very high energy (center of mass energy of 1.8 TeV), so the collisions actually involve individual quarks and gluons within the p and $\bar{p}$. As shown in the figure, squarks and gluinos can be produced from quark–quark annihilation, gluon fusion, and quark–gluon interactions. Some examples of next to leading order effects are also depicted in the figure.

*See Section 4.1 for an explanation of cross section and luminosity.

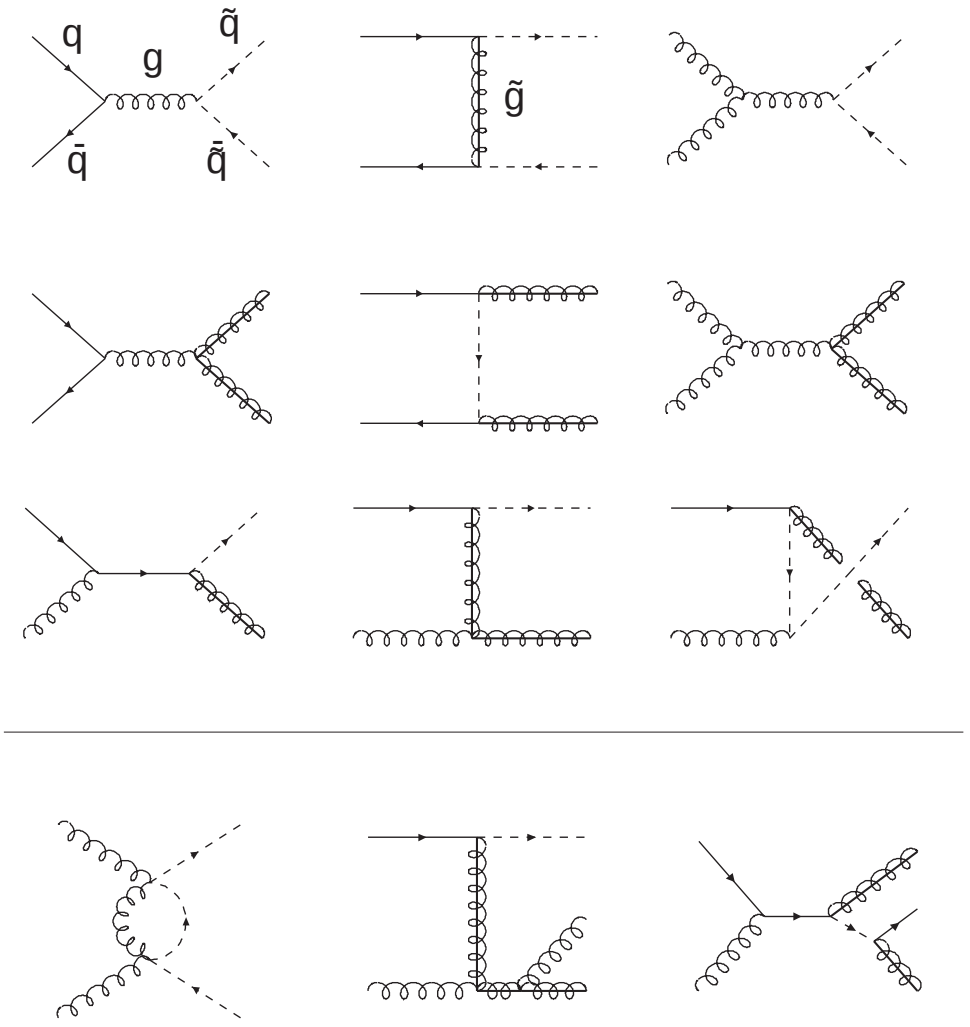

Figure 3.1: Examples of production diagrams for squarks and gluinos.[33] The first three rows are leading order diagrams involving $\tilde{q}\tilde{q}$ and $\tilde{g}\tilde{g}$ pair production and associated $\tilde{g}\tilde{q}$ production, respectively. The last row contains examples of next to leading order processes.

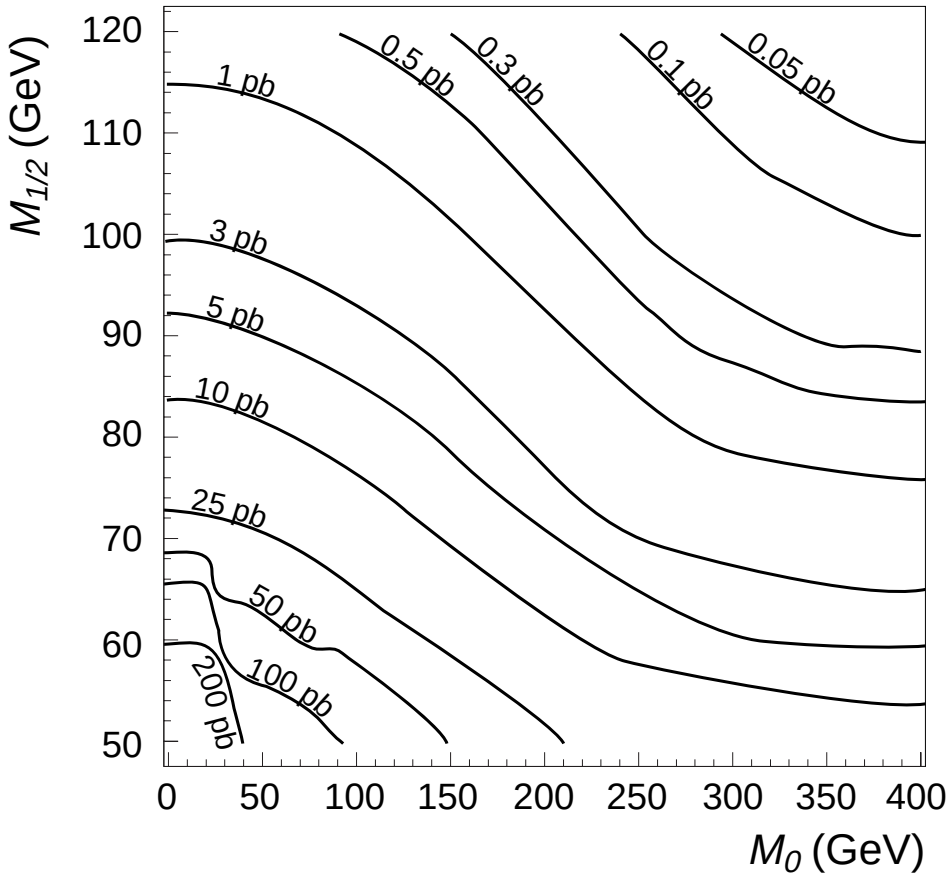

Figure 3.2: Contours of next to leading order cross sections for squark and gluino production.[33,34] Scalar tops are not included.

Next to leading order (NLO) cross sections[33] for squark and gluino production are calculated† with the `prospino` program.[34] `prospino` does not include scalar tops in its calculation (that will be available in the near future from the program's authors), therefore, this analysis will not be a search for scalar tops. This is no great loss since an analysis strategy different than the one used here is better suited for a scalar top search.[35]

To obtain a cross section from `prospino` for values of M_0 and $M_{1/2}$, the equivalent gluino and squark masses must be determined. The conversion is done with code within the `isajet` event generator.[29] The resulting squark masses are averaged (excluding the scalar tops) to calculate the degenerate squark mass that `prospino` requires. Typically,

†The MRSA′ NLO parton distribution function (pdf) is used here.

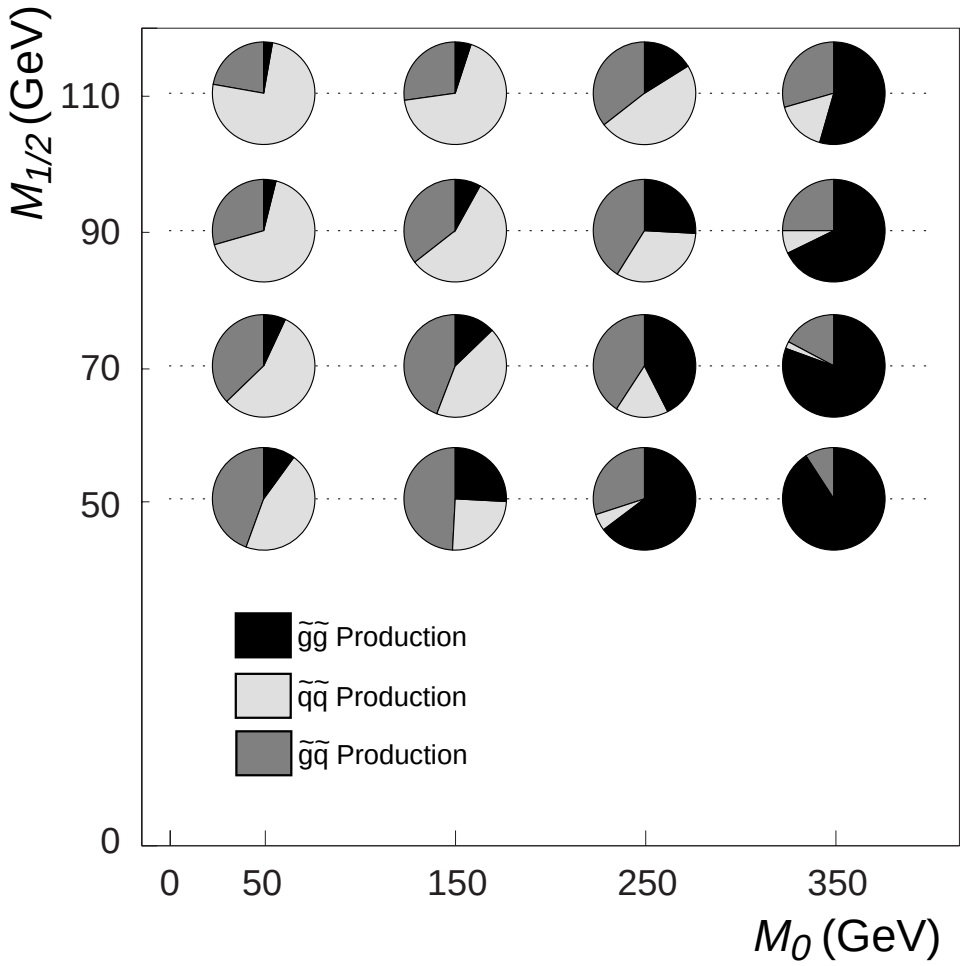

Figure 3.3: Fractions of the type of squark and gluino events produced shown on the M_0 – $M_{1/2}$ plane.

the NLO cross sections are anywhere from equal to double the leading order cross sections returned by `isajet`. Figure 3.2 shows contours of the NLO cross sections on the M_0 – $M_{1/2}$ plane.

Figure 3.3 shows the relative production of $\tilde{g}\tilde{g}$, $\tilde{q}\tilde{q}$, and $\tilde{g}\tilde{q}$ events on the M_0 – $M_{1/2}$ plane. This figure along with Figure 2.8 on page 26 explains the shapes of the cross section contours in Figure 3.2. For example, in the region of large M_0 and small $M_{1/2}$ (say $M_0 = 350$ GeV, $M_{1/2} = 50$ GeV), the squarks are much heavier than the gluinos, so $\tilde{g}\tilde{g}$ events dominate the production. The gluino mass is not very dependent on M_0, so the cross section contours form asymptotes close to lines of $M_{1/2}$ in the large M_0 region.

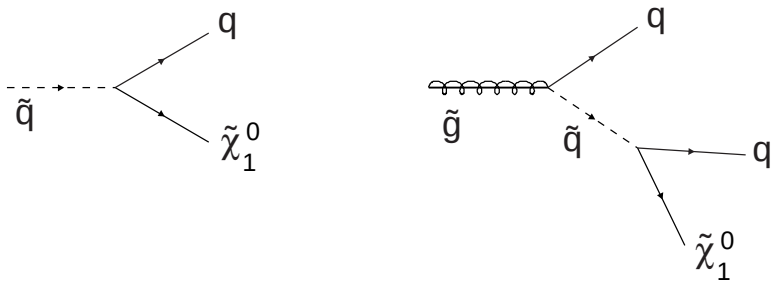

Figure 3.4: Examples of direct decays of squarks and gluinos. Here, squarks decay directly into a jet and an LSP. Gluinos decay via a squark (virtual if $M_{\tilde{q}} > M_{\tilde{g}}$), producing two jets and the LSP. If squarks are heavier than gluinos, the squark may decay first to a jet and a gluino; the latter decaying as shown.

3.2 Squark and Gluino Direct and Cascade Decays

R – Parity conservation also dictates that each squark and/or gluino produced must ultimately decay to an LSP. Squarks and gluinos may undergo direct and cascade decays.

Examples of direct decays are shown in Figure 3.4, where squarks and gluinos decay to jets and the LSP without going through intermediate gauginos (the quarks are always observed in a detector as collimated jets of hadrons; see Section 2.1.2). Since the squarks and gluinos sought in this analysis are quite heavy (> 100 GeV/c^2), the jets and the LSP will typically have high energies.

Weakly interacting LSPs are not directly observed in events, but their existence and energy can be inferred. In $p\bar{p}$ collisions at the Tevatron, the quarks and gluons within the proton and antiproton interact. The longitudinal momentum (along the beam direction) of these partons is some unknown fraction of the beam momentum, but at collision their momenta transverse to the beam are constrained to be very small. Since longitudinal momenta of the partons is unknown, total momentum conservation cannot be used. However, since the initial transverse momentum of the collision is small, one can demand transverse momentum conservation; the vector sum of the transverse momenta, p_T, and the vector sum of transverse energy, E_T, in the event must be zero. Any imbalance is interpreted as evidence of a weakly interacting particle, such as a neutrino or an LSP, with transverse energy equal to the missing transverse energy, $\not\!\!E_T$. Since direct decays

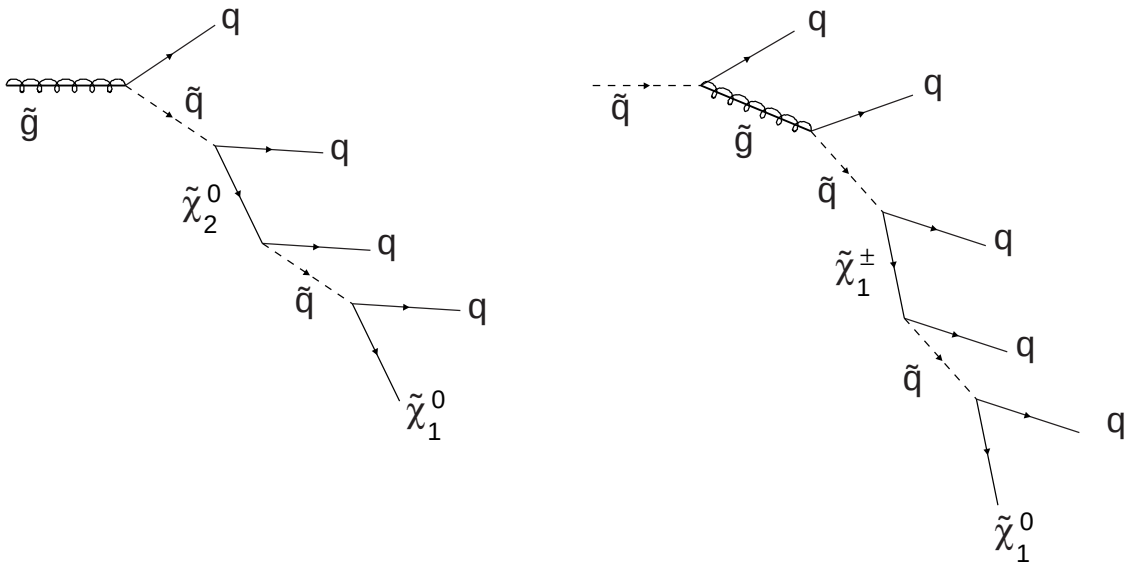

Figure 3.5: Examples of cascade decays of squarks and gluinos.

of squarks and gluinos produce high energy LSPs, one expects such events to have large $\not\!\!E_T$.

Conservation of R – parity requires pair squark and gluino production, so if both particles decay directly one expects some very high E_T jets along with $\not\!\!E_T$ due to the two LSPs. $\not\!\!E_T$ is really a vector sum of the LSP energies, and may be quite substantial when the LSPs travel close to the same direction. Since all R – parity conserving SUSY processes ultimately decay to LSPs, large $\not\!\!E_T$ is an excellent signature for SUSY events. Some distributions of $\not\!\!E_T$ and jet energies will be shown later.

Examples of cascade decays are shown in Figure 3.5. In this decay scheme, the squarks and gluinos decay through virtual or real charginos and neutralinos eventually down to the LSP. Many more jets are produced compared to direct decays, but their transverse energies as well as the $\not\!\!E_T$ will be softer. Note that the charginos and neutralinos may decay through sleptons and sneutrinos instead of squarks as shown in the figure. In those cases, leptons will be produced instead of jets. This search for squarks and gluinos is only concerned with the hadronic decays. Searches with the leptonic decays are the subject of other analyses[36] not covered here.

$M_0 = 75$ GeV, $M_{1/2} = 100$ GeV			$M_0 = 300$ GeV, $M_{1/2} = 50$ GeV		
$\tilde{q}_L$	$\rightarrow$ Direct	(5%)	$\tilde{g}$	$\rightarrow$ Direct	(17%)
$\tilde{q}_L$	$\rightarrow$ Cascade	(95%)	$\tilde{g}$	$\rightarrow$ Cascade	(83%)
$\tilde{q}_R$	$\rightarrow$ Direct	(100%)	$\tilde{\chi}_1^{\pm}$	$\rightarrow \ell\nu\tilde{\chi}_1^0$	(32%)
$\tilde{\chi}_1^{\pm}$	$\rightarrow \ell\nu\tilde{\chi}_1^0$	(100%)	$\tilde{\chi}_1^{\pm}$	$\rightarrow q\bar{q}'\tilde{\chi}_1^0$	(68%)
$\tilde{\chi}_2^0$	$\rightarrow \ell^+\ell^-\tilde{\chi}_1^0$	(2%)	$\tilde{\chi}_2^0$	$\rightarrow \ell^+\ell^-\tilde{\chi}_1^0$	(36%)
$\tilde{\chi}_2^0$	$\rightarrow \nu\nu\tilde{\chi}_1^0$	(98%)	$\tilde{\chi}_2^0$	$\rightarrow q\bar{q}\tilde{\chi}_1^0$	(64%)

Table 3.1: Branching fractions for two example mSUGRA points. For small M_0 and large $M_{1/2}$ ($M_0 = 75$ GeV, $M_{1/2} = 100$ GeV) production of squarks dominate. For the other point at large M_0 and small $M_{1/2}$ ($M_0 = 300$ GeV, $M_{1/2} = 50$ GeV), the production of sparticles is dominated by $\tilde{g}\tilde{g}$ pairs.

3.3 The Signal of Squarks and Gluinos

The signal for this squark and gluino search is events with three or more jets, large missing transverse energy, and no leptons. Rejecting leptons makes this analysis orthogonal to leptonic searches and so combining results will be easier. The characteristics of the signal varies substantially over the M_0 – $M_{1/2}$ plane.

The nature of squark and gluino decays depends heavily on the model parameters. For example, changing $\tan\beta$ and μ alters the gaugino and higgsino content of the charginos and neutralinos, changing their branching fractions and how right handed SUSY scalars couple to them. As one surveys the M_0 – $M_{1/2}$ plane, the masses of the sparticles change, opening and closing decay channels and changing branching fractions in a complicated way.

Table 3.1 shows the branching fractions determined by `isajet`[29] for two points in the M_0 – $M_{1/2}$ plane (as usual, $\tan\beta = 2$, $A_0 = 0$, and $\mu < 0$). The point on the left in the table is for small M_0 and large $M_{1/2}$ ($M_0 = 75$ GeV, $M_{1/2} = 100$ GeV). According to Figures 2.8 and 3.3, squarks dominate the production, since the gluinos are heavier than the squarks. The left handed squarks almost always undergo cascade decay, and the charginos and neutralinos always decay to leptons. In fact, because the sneutrino is lighter than the second lightest neutralino, the $\tilde{\chi}_2^0$ always decays to neutrinos, an invisible decay mode. The leptonic signature nearly disappears for this point. Fortunately, the

right handed squarks always decay directly to jets and the LSP, which will yield a very strong signature for this analysis.

For the other point in Table 3.1 at large M_0 and small $M_{1/2}$ ($M_0 = 300$ GeV, $M_{1/2} = 50$ GeV), the squarks are very heavy and so gluino pair production dominates. The majority of gluinos cascade decay through the $\tilde{\chi}_1^{\pm}$ or the $\tilde{\chi}_2^0$, which in turn decay to jets and leptons with branching fractions similar to the SM W and Z, respectively. For the hadronic decays, more jets will be produced compared to the other point, but their E_T and the $\not\!\!E_T$ will be softer.

A comparison of some distributions of the signal are shown on the M_0 – $M_{1/2}$ plane in Figures 3.6 through 3.9. The event quantities displayed are discussed in more detail in Chapter 6. One sees that for small M_0 and large $M_{1/2}$, the direct decays of the right handed squarks produce events that may have very large $\not\!\!E_T$ and highly energetic leading jets (the jet with the most E_T in the event). From Figure 3.7, typically two or three jets with $E_T > 25$ GeV are produced. Events produced in the region of large M_0 and small $M_{1/2}$, where gluinos dominate the production and cascade decay, have softer $\not\!\!E_T$ and jet E_T spectra, but more jets are produced. The quantity H_T is the scalar sum of jet E_T in the event but not including the leading jet. As seen in Figure 3.9, the H_T distributions from the upper left corner to the lower right corner remain quite constant, since for small M_0 and large $M_{1/2}$ a small number of very energetic jets are produced while for large M_0 and small $M_{1/2}$ there are many jets produced but with lower E_T.

Of course one has no idea which point in mSUGRA space is the one that nature has picked, assuming Supersymmetry and mSUGRA are correct at all. In performing an analysis, one applies requirements to the data to pick out as many potential SUSY candidate events as possible while keeping the backgrounds small. Because the signal varies substantially over the M_0 – $M_{1/2}$ plane, more than one set of requirements will be needed.

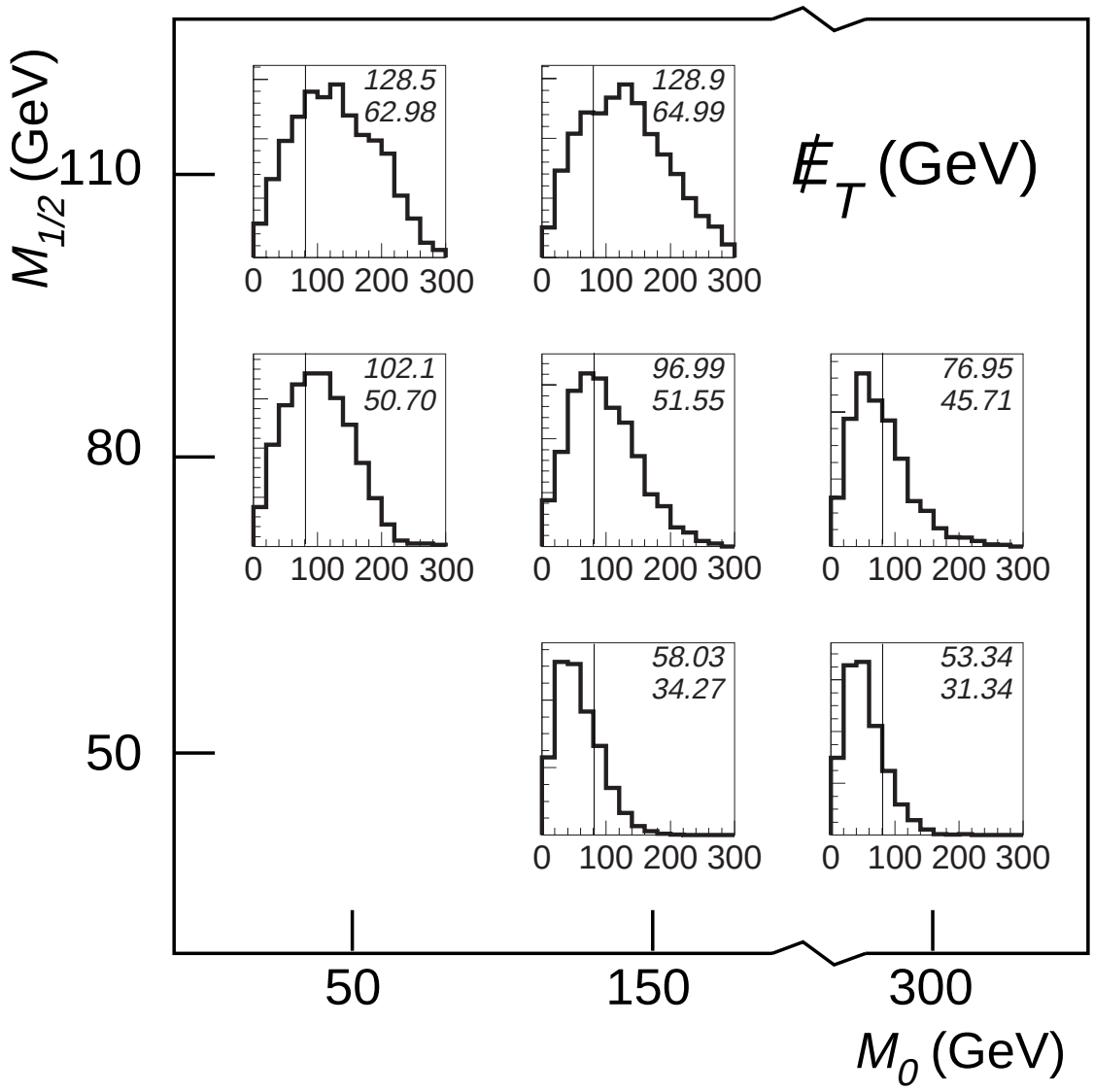

Figure 3.6: $\not\!\!E_T$ of the signal on the M_0 – $M_{1/2}$ plane. The vertical line in each plot is at $\not\!\!E_T = 75$ GeV. In each histogram, the upper (lower) number is the mean (rms) of the distribution.

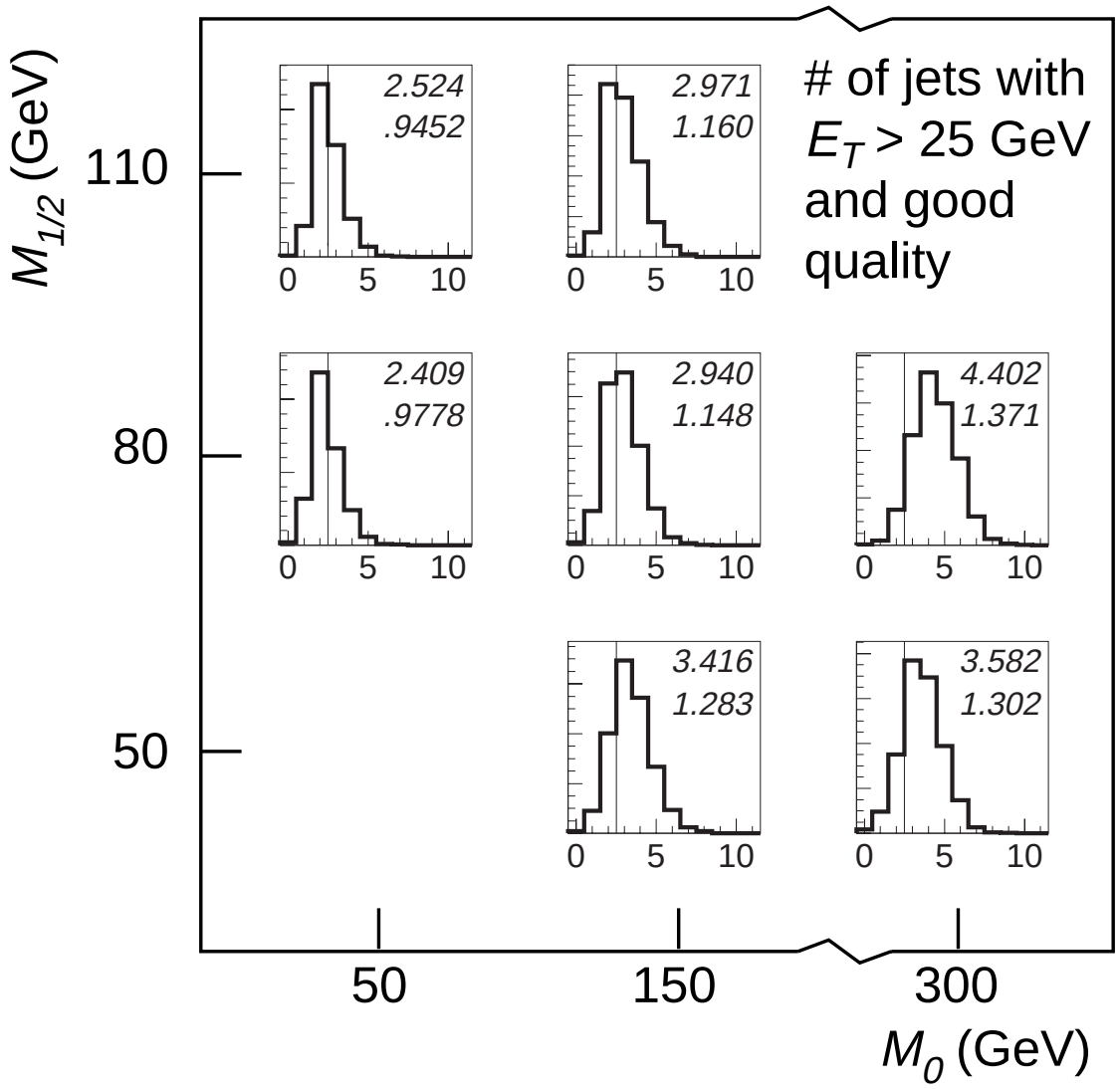

Figure 3.7: Number of jets with $E_T > 25$ GeV for the signal on the M_0 – $M_{1/2}$ plane. Events beyond the vertical lines have three or more such jets. In each histogram, the upper (lower) number is the mean (rms) of the distribution.

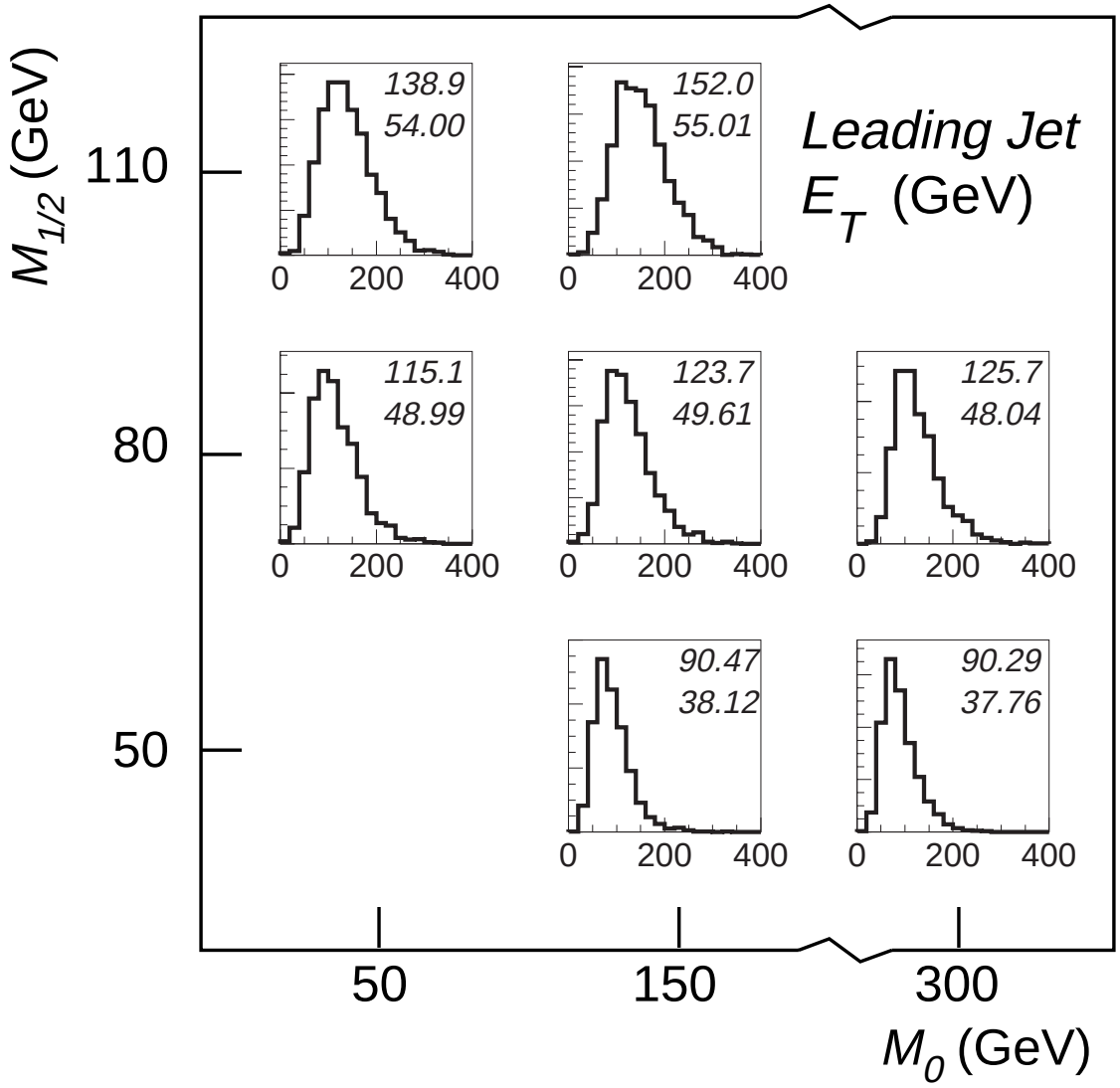

Figure 3.8: Leading jet E_T for the signal on the M_0 – $M_{1/2}$ plane. In each histogram, the upper (lower) number is the mean (rms) of the distribution.

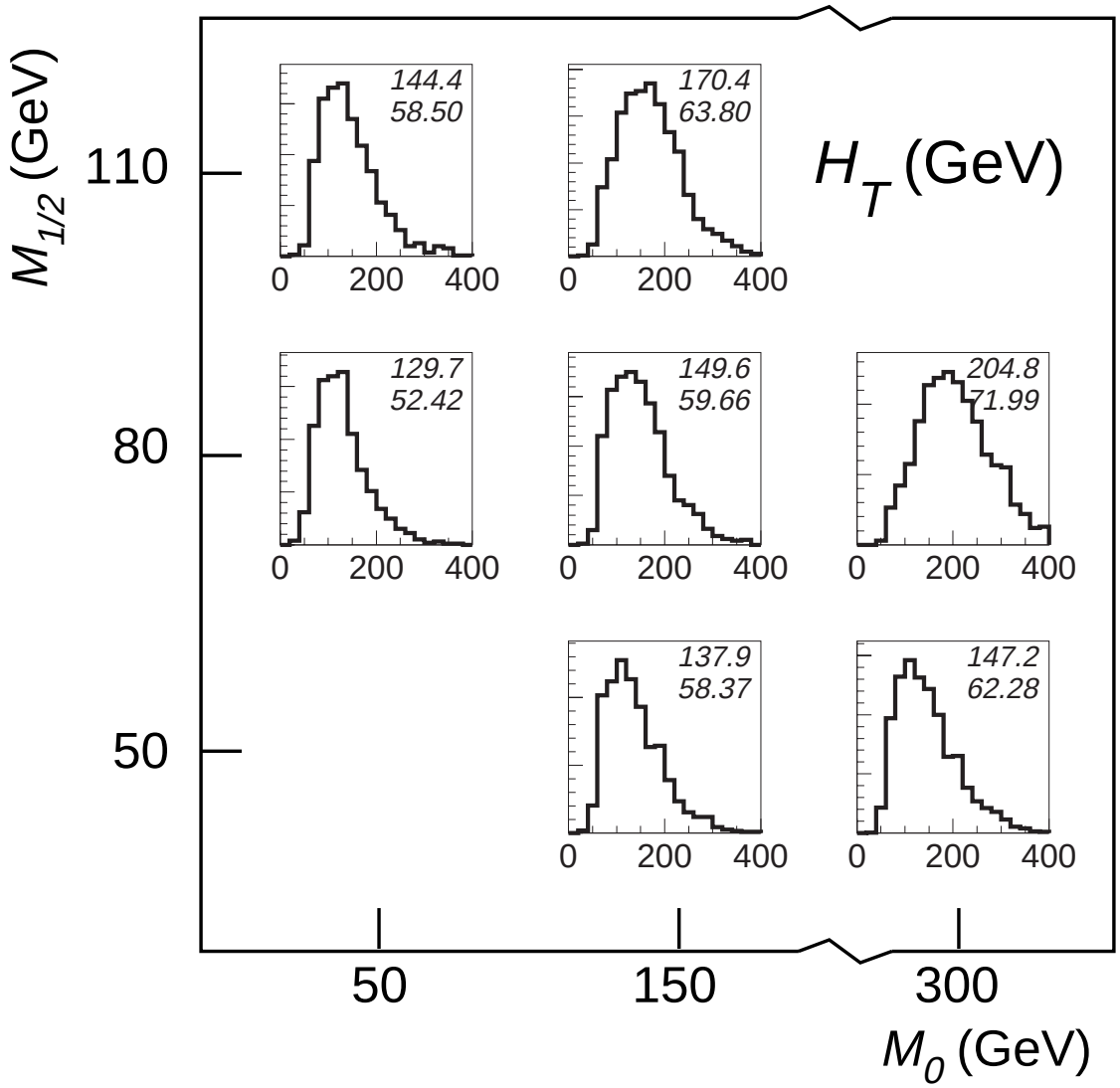

Figure 3.9: H_T of the signal on the M_0 – $M_{1/2}$ plane. H_T is defined to be the scalar sum of the E_T of jets with $E_T > 25$ GeV, not including the leading jet. In each histogram, the upper (lower) number is the mean (rms) of the distribution.

3.4 Backgrounds

While hadronic decays of squarks and gluinos have the largest branching fractions, there are a large number of processes from the SM and detector effects that produce events mimicking the signal. The background sources with many jets and large $\not\!\!E_T$ fall under two categories: those with $\not\!\!E_T$ due to physics processes where a neutrino is in the final state and those where detector effects are solely responsible for the $\not\!\!E_T$ in the event.

Backgrounds due to physics sources of $\not\!\!E_T$ include $W \to \ell\nu$ + jets, $Z \to \nu\nu$ + jets, and $t\bar{t} \to$ leptons + jets. Each of these examples involve at least one neutrino in the final state. The electrons and muons must be lost or misidentified for such events to be collected by this analysis. Such detector effects may sometimes act to enhance the $\not\!\!E_T$. The invisible decays of the Z with jets and events with the Z and W involving hadronic tau decays also mimic the desired signal.

There are also many types of backgrounds that arise from pure instrumental effects. Balanced QCD multijet and $t\bar{t} \to$ all jets events with mismeasured jets may acquire large $\not\!\!E_T$. Energy in the calorimeter may be very unbalanced in events with main ring activity, large number of interactions pasting the inner calorimeter, and negative energy (due to preamps saturated by the previous collision). Balanced jet events where the primary vertex is misplaced far from the hard scattering position may have $\not\!\!E_T$ grossly mismeasured. Finally, balanced Z decays where a lepton is lost or mismeasured may also be a source of background events. The requirements on events for this analysis are designed to retain as much of the signal as possible while reducing the background from these sources. All of the background sources will be discussed in subsequent chapters.

3.5 Previous limits on Squarks and Gluinos

Squarks and gluinos have been the subject of searches for quite some time. Figure 3.10 displays limits[37–44] on the masses of squarks and gluinos within a GUT inspired MSSM framework from DØ, CDF (the other detector at the Tevatron), and other experiments. Note that the masses of the sleptons were set large enough so none are involved in

production and decay. The DØ and CDF jets and $\not\!\!E_T$ limits are based on data collected during the 1992–1993 Tevatron run. The CDF dielectron limit uses NLO cross sections, while the CDF jets and $\not\!\!E_T$ search and the DØ search use leading order cross sections from `isajet`. The boot shape of the jets and $\not\!\!E_T$ limits is due to the fact that the LSP mass increases with the gluino mass. At the turn around point, the LSP is so heavy that little $\not\!\!E_T$ is produced when the squarks decay (since the gluinos are so heavy there, only squarks get produced). DØ's calorimeter has better $\not\!\!E_T$ resolution than CDF, which allows the DØ limit to extend farther. The straight line limits from UA1/UA2 and Delphi at CERN and Mark II at SLAC assume only direct decays. The diagonal dashed line on the bottom of the plot indicates where the squarks are lighter than the $\tilde{\chi}_1^0$, and thus they become the LSP. As mentioned previously, models with a charged LSP can be ruled out immediately.

The DØ limit is a combination of two separate jets and $\not\!\!E_T$ analyses. One required three jets and large $\not\!\!E_T$[37,45] while the other required four jets with a lower $\not\!\!E_T$ threshold.[46] The analysis described here is an extension of the three jets analysis.

The mass relations of the mSUGRA models allow indirect limits to be placed from CERN LEP results. For example, in Figure 2.9 on page 27 the LEP 1 limit on the lightest chargino[47] is shown. Experiments from LEP 1 have also resulted in limits of $M_{\tilde{\chi}_1^0} > 20$ GeV/c^2 for the $\tilde{\chi}_1^0$ [48] and $M_{\tilde{e}} > 45$ GeV/c^2 for the selectron.[47] These limits are model independent, since they come from analyses involving visible Z decays and the Z width instead of direct production of the sought particle. Newer LEP 2 limits on the lightest chargino mass are highly model dependent. The latest searches from OPAL[49] at $\sqrt{s} = 161$ GeV exclude charginos with mass less than 62 GeV/c^2 and second lightest neutralinos with mass less than 45 GeV/c^2. These limits are only valid within the mSUGRA framework with $\tan\beta = 1.5$ and M_0 as small as other limits allow. The LSP must also be at least 10 GeV/c^2 lighter than the $\tilde{\chi}_2^0$ and the $\tilde{\chi}_1^\pm$. For M_0 at 1 TeV, OPAL excludes up to a 78.5 GeV/c^2 $\tilde{\chi}_1^\pm$ and up to 51.9 GeV/c^2 for the $\tilde{\chi}_2^0$.

The first experimental limits in the $M_0 - M_{1/2}$ plane are from the dielectron search for squarks and gluinos at DØ.[36] That analysis required at least two electrons, two jets, and

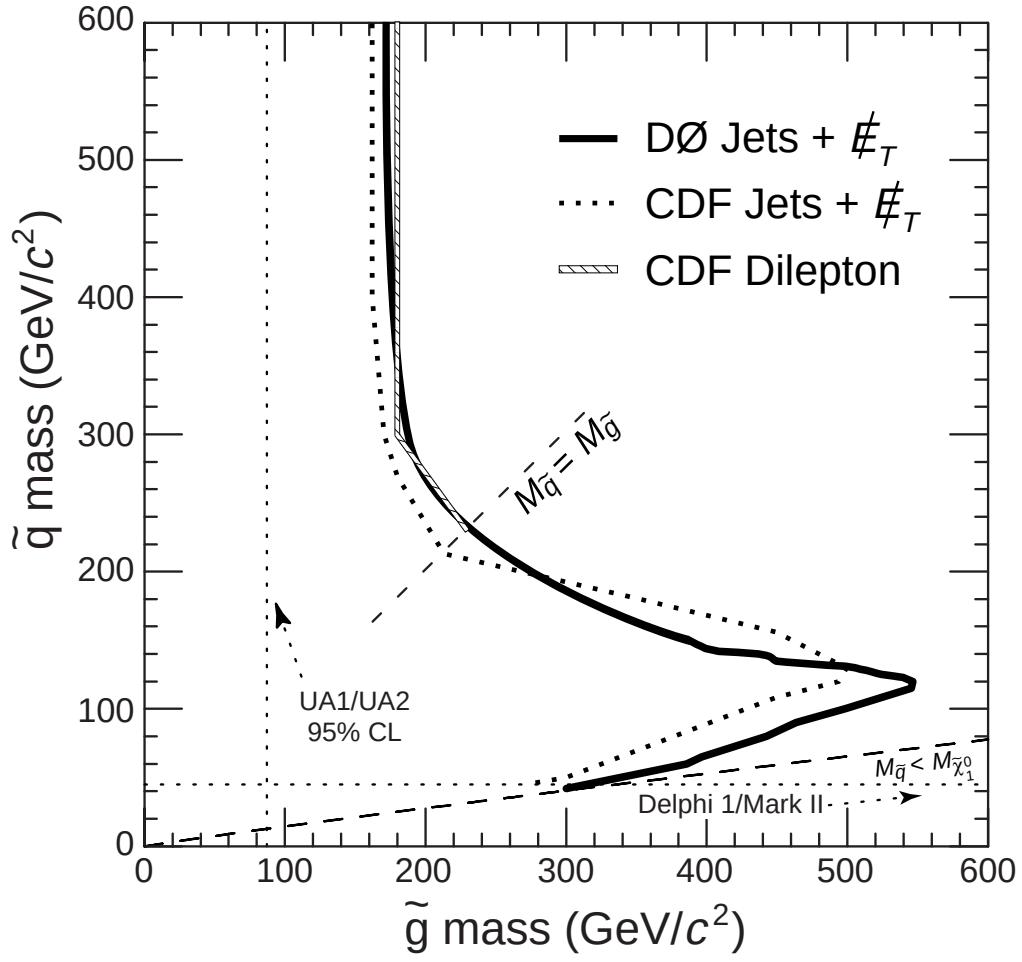

Figure 3.10: Previous MSSM squark and gluino limits. Masses within the contours are excluded. The heavy solid line is the previous preliminary DØ jets + $\not\!\!E_T$ limit[37,38] based on 7.2 pb^{-1} of data from the 1992 – 1993 Tevatron run with MSSM parameters $\tan\beta = 2$ and $\mu = -250$ GeV. The hashed line is the current CDF limit[40] from a dilepton search based on 81 pb^{-1} of data taken during the 1993–1995 run and using supergravity parameters $\tan\beta = 4$ and $\mu < 0$. The heavy dotted line is the preliminary CDF limit[39] from their jets + $\not\!\!E_T$ search based on 19 pb^{-1} of data from the 1992–1993 run with MSSM parameters $\tan\beta = 4$ and $\mu = -400$ GeV. The CDF dilepton analysis uses NLO cross sections; the others all use LO cross sections. The diagonal dashed line marked $M_{\tilde{q}} = M_{\tilde{g}}$ is the line where squarks and gluinos have equal mass. The other limits indicated on the plot are discussed in the text.

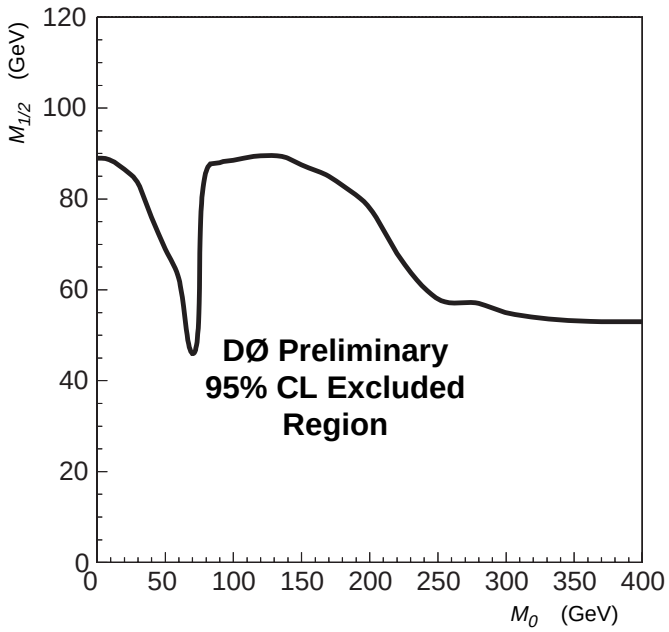

Figure 3.11: Exclusion contour from the DØ dielectron squark and gluino search. Data corresponding to 92.9 pb^{-1} were analyzed.

$\not\!\!E_T > 25$ GeV. Data corresponding to 92.9 pb^{-1} were analyzed. No events were observed over those predicted by the SM. The resulting limit contour is shown in Figure 3.11. The large dip in the limit is in the region where the $\tilde{\chi}_2^0$ decays to only sneutrinos and neutrinos, practically eliminating the lepton signature.

3.6 Outcomes of this Search

This search for squarks and gluinos with jets and $\not\!\!E_T$ will be a counting experiment. A lack of an excess of events in the collider data over what is predicted by the SM would indicate no physics beyond the Standard Model within the sensitivity of the analysis. No experiment has observed any excess so far, and this analysis will be no different. Therefore, the current limits on squark and gluino masses will be extended. Certainly, observing an excess consistent with production of squarks and gluinos would be a landmark event in particle physics. Unfortunately, that day has not arrived yet.

Although there is no experimental evidence for Supersymmetry, it has survived for a long time because experimental constraints can be easily avoided by tweaking the many

parameters of the models. It will be difficult for experiments to totally exclude all of the parameter space for all the different SUSY models. There is a point, however, where theorists start to get "worried" if mass limits are pushed up too high. If the mass splittings between the sparticles and their partner SM particles are too great, then SUSY parameters must be increasingly fine tuned for the weak scale to be predicted at the right place (the quadratic divergences discussed in Section 2.2.1 do not cancel enough). The degree of fine tuning required is a measurement of *naturalness* of the theory and can be used to place somewhat vague limits on sparticle masses. Of course, experimental limits are the most important for proving or disproving a theory, but naturalness limits can serve to give one a stopping point in performing searches when the theory gets into trouble. Indeed, common sense says that if no sparticles are found with masses below several TeV, then SUSY is probably dead. One measurement of naturalness[50] indicates that the most natural masses for the squarks and gluinos is 250 GeV/c^2. If squarks and gluinos are not discovered with mass below ~700 GeV/c^2, then, at some level, SUSY is unlikely to be a true theory.

3.7 Summary

The Tevatron particle collider at Fermilab collides protons and anti-protons at higher energies than any other collider in the world. Therefore, it is the place where previously unknown heavy particles may be produced in the collisions. The analysis described here takes advantage of the high energy Tevatron in a search for two particles predicted by SUSY called squarks and gluinos. If the unstable squarks and gluinos are produced in a collision, they would decay most often to quarks (the constituent particles within protons and neutrons) and the theoretically predicted lightest SUSY particle (the LSP). The quarks are observed in a detector as collimated sprays of particles called jets. The LSP, if it exists at all, rarely interacts with matter and so its existence and energy must be inferred by looking for energy imbalances (missing energy) in collision events.

In an effort to pick out a squark and gluino signal among all of the other processes that can occur in proton-antiproton collisions, events with many jets and large energy

imbalances are sought. Ordinary processes from the SM can mimic such events, as well as mismeasurements and glitches in the detector, therefore events are required to have other characteristics so that most events from backgrounds can be rejected while accepting as many squark and gluino candidate events as possible. Simulations and studies of collisions allow one to predict how many background events one would observe passing the analysis requirements. If the number of events seen in the actual data from the proton-antiproton collisions is significantly more than the prediction, then perhaps a new discovery is at hand. So far, no significant excess of events consistent with any theory beyond the SM has ever been observed.

If an excess of events is discovered, then perhaps squarks and gluinos do indeed exist. This would be a huge discovery for particle physics. In the event of no such significant excess, then constraints can be placed on the SUSY theories. For such a case, the results from a "null" analysis are generally mass limits on the particles sought. In other words, one can say that squarks and gluinos must be heavier than a lower limit, or else they would have been discovered in the course of the analysis. All previous searches for SUSY particles have resulted in such mass limits.

Chapter 4

Apparatus

High Energy Physics has reached a state where experiments can only be executed with very large and expensive equipment. This analysis was performed with data taken by the DØ detector, located on the four mile circumference Tevatron proton-antiproton collider at the Fermi National Accelerator Laboratory (Fermilab), a site thirty miles west of Chicago. DØ is a huge detector, weighing 5,500 tons and standing over four stories tall. The accelerator complex and the detector have been described in great detail elsewhere[51,52] and are briefly covered in this chapter after introducing the concept of cross section and luminosity.

4.1 Cross Section and Luminosity

Experimental results are most often reported in a quantity called a *cross section* (σ). The cross section is the interaction probability per unit flux of incident particles and has units of area. The idea is that a larger probability for an interaction to occur is thought of as a larger target in cross sectional area for a beam of incident particles to strike. Cross sections can be presented in units of cm^2, but a far more convenient unit is the barn (from "hitting the broad side of a barn"); 1 b = 10^{-24} cm^2. For example, the cross section for a proton and an antiproton to interact when collided at a center of mass energy of 1.8 TeV is ~48 milli-barns (mb). Theoretical probabilities for squark and gluino production from proton-antiproton collisions are on order of a few to tens of pico-barns (pb).

For colliders, the flux of the beam is given by the instantaneous luminosity ($\mathcal{L}$), such that the event rate (R) for a certain interaction is given by,

$$R = \sigma\mathcal{L} \tag{4.1}$$

Since R is events per second, the units on $\mathcal{L}$ are $\mathrm{cm}^{-2}\,\mathrm{s}^{-1}$. For the 1993–1995 run of the Tevatron, typical instantaneous luminosities ranged from 5×10^{30} $\mathrm{cm}^{-2}\,\mathrm{s}^{-1}$ to about 25×10^{30} $\mathrm{cm}^{-2}\,\mathrm{s}^{-1}$. The total number of events an experiment has collected is given in terms of the total integrated (over time) luminosity,

$$N = \sigma \int \mathcal{L}\,dt \tag{4.2}$$

For example, the total integrated luminosity collected by the `missing_et` trigger at DØ for the 1993–1995 collider run is about 79 pb^{-1}. Thus, for any interaction where the cross section is known or theoretically predicted, Equations (4.1) and (4.2) can be used to determine the rate or number of events one would expect to observe, but one must also take into account inefficiencies of the detector and analyses. For example, 79 pb^{-1} of data correspond to $\sim 4 \times 10^{12}$ $p\bar{p}$ interactions. Information about each and every $p\bar{p}$ event is not needed since most events are boring (a good thing since 10^{12} events correspond to about 10,000 Terabytes of information in the most compressed data format used by DØ). The rare processes are the interesting ones. For example, top quark pair production ($p\bar{p} \to t\bar{t}$) occurs with a cross section of 5 pb, amounting to only 400 events, though the actual number of top quark events seen in the data is much fewer due to inefficiencies. A complex triggering system is used to save only special events from processes that the collaboration wishes to study (see Section 4.3.5).

4.2 Fermilab Accelerator Complex

It is clear that if squarks and gluinos exist at all, they are not part of our natural surroundings and can only be produced by colliding particles together at extremely high energies. At Fermilab, protons and antiprotons are accelerated to 0.9 TeV and collide head on at a center of mass energy of 1.8 TeV at two locations on the Tevatron collider. A diagram of the entire accelerator complex is shown in Figure 4.1.

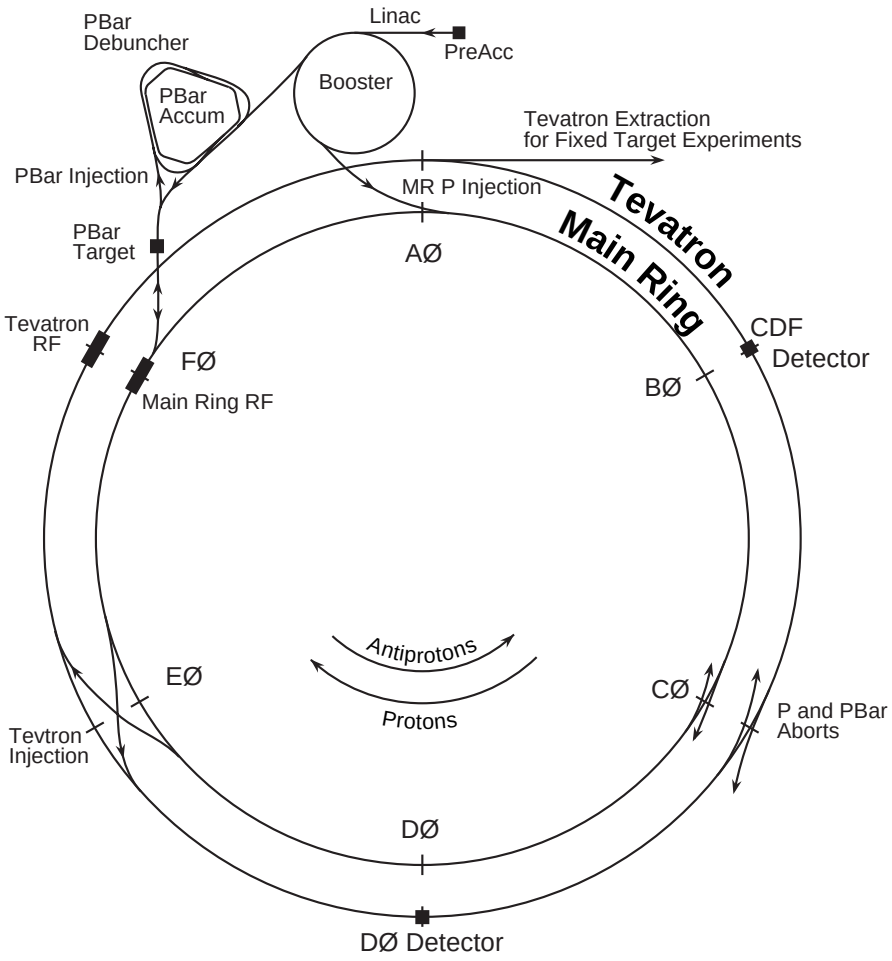

Figure 4.1: The Fermilab accelerator complex. Note that the Tevatron and the Main Ring accelerators have the same radius but are separated here for clarity. The figure is not drawn to scale.

Because accelerators are efficient only over a range of energies, five machines are required to take protons from a bottle of hydrogen gas up to an energy of 0.9 TeV. The first accelerator in the chain is the Cockroft–Walton electrostatic generator, marked preaccelerator in Figure 4.1 and is probably the device at the lab that would fit in most on an old Star Trek set. Within the dome of the Cockroft Walton is the negative hydrogen ion source, where electrons are added to ordinary hydrogen gas to make H^- ions. The ions, whose protons may eventually make their way to the Tevatron, are forced out of the dome by an electric field that accelerates them to 18 keV. The Cockroft-Walton itself is made up of large capacitors that are discharged in series, accelerating the H^- ions to 750 keV.

The ions are then passed to the linear accelerator (Linac). The Linac is 500 ft long and consists of nine resonant cavities constructed from copper cladded steel tanks. Within each tank are 42 drift tubes which the ions pass through. Electromagnetic waves at radio-frequencies (RF) are set up in the cavities. The ions "ride the RF wave" down the cavities, accelerating except when passing through the drift tubes where they coast, so they are not affected by the decelerating part of the wave. They exit the Linac at 200 MeV.

The H^- ions are transferred next to the Booster accelerator. The Booster is a circular synchrotron with a diameter of 151 m. The first phase of the Booster operation involves stripping the electrons from the ions, leaving only the protons. Acceleration begins once the booster is filled with 2.5×10^{12} protons, split amongst 83 separated groups or *bunches*.

In contrast to a linear accelerator where particles are accelerated all the way down its length, a synchrotron accelerates particles by giving them a kick at one station on the ring (the RF station), sending them coasting around the circle with slightly more energy than before. The next time around, they get another kick when they pass by the RF station to accelerate further. Magnetic fields are needed to keep the beam of particles traveling in a circle and must increase as the energy of the beam increases.

When particles are first injected into a synchrotron, they are traveling at less than relativistic velocities (slow compared to the speed of light c). The momenta of particles

in a bunch will be spread about some average value. Particles traveling faster than the average will be at the head of the bunch, while those going slow will be at the tail. To keep the particles in the bunches, the accelerating fields in the RF cavities are set up so that particles arriving at the RF station early (too fast) receive less of a kick compared to particles at the correct momentum. Particles arriving late (too slow) get a bigger kick with respect to the rest of the bunch. This situation reverses when the particles reach relativistic velocities. At that point, all particles are essentially going the same speed (close to c), but particles with more than the average momentum are bent slightly less by the magnets. They follow a slightly longer path around the ring and end up trailing the bunch. Particles with less than the average momentum are bent more and follow a shorter path around the ring, thus leading the rest of the bunch. The fields set up by the RF cavities must be altered to have the opposite effect as before to keep the bunches from blowing up. Many particles are lost in the transition.

The booster accelerates the 200 MeV protons to 8 GeV in about 33 ms. The beam cannot be accelerated beyond that energy, because the magnets cannot generate a field large enough to keep the beam in the machine. To reach higher energies, another accelerator is needed with either stronger magnets or a larger circumference (so the curve of the circle is more gentle). The next machine in the chain, the Main Ring, uses the latter approach.

The Main Ring (MR) was the final accelerator in the chain until the Tevatron was constructed in 1983 in the same tunnel just two feet below the MR. The MR is a 400 GeV proton synchrotron with a radius of $\sim$1 km. The ring itself rises at the BØ station to completely bypass the CDF detector. Unfortunately, the MR is elevated only 89.2 in above the Tevatron at DØ and passes through the upper part of the DØ calorimeter and muon system.

The MR serves a dual purpose for the complex, since it is used as an injector for the Tevatron and for accelerating protons needed to create antiprotons. Anti-matter, though plentiful in science fiction TV shows, does not exist naturally. The fact that anti-matter must have been around in the early universe but has since disappeared is a great mys-

tery (perhaps explained by CP violation). Fermilab can make antiprotons by extracting 120 GeV protons accelerated by the MR to collide with a stationary Nickel target. The cross section for creating antiprotons in the collisions is small; only 10 antiprotons are produced for every million protons striking the target. About 10^{11} antiprotons are necessary in order to do physics. Thus, the antiprotons that are produced must be stored until enough are collected.

Beyond the target and a lithium lens, antiprotons created with energy near 8 GeV are directed to the Debuncher ring (actually somewhat triangular shaped). Once the antiprotons are in stable orbits, they are transferred to the Accumulator ring, which is just slightly smaller than the Debuncher and shares the same tunnel. As more antiprotons are produced by protons from the MR, they go through the Debuncher and are added to those already in the Accumulator. These antiprotons, called the *stack*, are stored and continue to circle in the Accumulator until needed for collisions with protons in the Tevatron. It can take a little more than 24 hours to collect a stack of antiprotons large enough for physics purposes when starting from scratch (when HEP operations are just beginning or when a power glitch in the Accumulator causes all of the antiprotons collected so far to be lost). While protons and antiprotons are colliding in the Tevatron, the MR is used to make more antiprotons and increase the stack. The bunches of particles in the Tevatron usually last long enough so that the stack can be fully replenished before a fresh batch of antiprotons is needed again.

Antiprotons are convenient since they are just like protons but have the opposite charge, so they will accelerate in the same Main Ring and Tevatron accelerators but will travel in the opposite direction of the protons. In the MR, the beams are diffuse enough so that protons and antiprotons do not inadvertently collide. When colliding beams are required in the Tevatron, the 8 GeV antiprotons in the Accumulator are injected into the MR along with a fresh batch of protons from the booster. They are then accelerated to 120 GeV and are injected into the Tevatron, the machine capable of the highest energies.

To reach energies of 900 GeV (0.9 TeV), extremely large magnetic fields are necessary to keep the particles confined to the circle of the ring. The Tevatron uses magnets with

superconducting coils that can withstand the huge currents with negligible resistance. To keep magnets superconducting, the coils are immersed in liquid helium at 4.3 degrees Kelvin. Fermilab has the largest liquid helium facility in the world (but soon to be surpassed by the LHC at CERN).

Once particles are injected from the Main Ring into the Tevatron, they are coalesced into 6 separate bunches of protons and antiprotons with about 10^{11} particles in each and equally spaced around the ring. These bunches of particles are accelerated from 120 GeV to 0.9 TeV. Once this energy is reached, the Tevatron will remain at this *flat top* for quite some time while the bunches of protons collide with the bunches of antiprotons. The procedure for filling the Tevatron and ramping to flat top is called the *shot*.

Once the protons and antiprotons reach 0.9 GeV, stray particles on the edge of the beam orbits are scraped away by means of mechanical shutters and collisions begin. The bunches are only allowed to collide at two collision points: one at the center of the CDF detector at BØ and the other at the center of the DØ detector. There are special low-beta quadrupole magnets just before and after the collision points that squeeze the beams to a very small size before colliding to maximize the luminosity. With six bunches, the beams cross every 3.5 μs.

The beams in the Tevatron at flat top are called the *store*. The store can be lost abruptly when magnet power supplies fail or when the coil of a magnet suddenly goes nonsuperconducting and *quenches*. If all goes well, however, the beams will collide for many hours; hopefully long enough for the antiproton stack to be refilled. As time passes, many of the particles in the bunches are lost and the instantaneous luminosity decreases. This reduction occurs as protons and antiprotons collide with each other, collide with air in the beam pipe (beam-gas events; even though the beam pipe is at very high vacuum), or particles on the outer edges of the beam strike the beam pipe itself. When the luminosity falls to a point where the event rates for interesting physics is too small, the Tevatron is emptied of particles by aborting the beam, and a new shot begins by injecting fresh bunches of protons and antiprotons from the Main Ring. When the Tevatron was running well, stores would typically start at about $\mathcal{L} = 25 \times 10^{30}\,\mathrm{cm}^{-2}\,\mathrm{s}^{-1}$ and would be dumped

when the instantaneous luminosity dropped to about 8×10^{30} cm^{-2} s^{-1}. Beam could collide for nearly a full day before the luminosity dropped too low to continue and the store aborted.

The high energy particle collisions are needed to produce the rare interactions, such as production of top quarks and, perhaps, squarks and gluinos. One needs a detector to examine the particles released in the collision in order to learn more about the interactions that occur.

4.3 The DØ Detector

A detector's job is to measure properties of the particles emanating from the proton-antiproton collisions. Because the collisions occur at such high energy, particles heavier than protons and antiprotons can be produced, such as top quarks that have nearly 200 times the mass of a proton. Such heavy particles decay so quickly that before they even leave the beam pipe, they have already disintegrated into their daughter particles. Using different sub-detectors that measure the direction, energy, and momentum of the daughter and subsequent particles, one may be able to reconstruct the original parents.

The DØ detector resides at the DØ station on the Tevatron ring as shown in Figure 4.1. The detector was built to be multipurpose, capable of high precision measurements of particle direction, energy, and momentum as well as reliable particle identification necessary for a variety of physics topics. Such analyses include the search for the top quark, measurement of the W boson mass and the W and Z production cross sections, and the exploration of QCD and b–quark physics. High sensitivity is also crucial for new physics not yet observed, like Supersymmetry.

The squark and gluino jets + $\not\!\!E_T$ analysis requires good measurements with high resolution of the energies of jets and the missing transverse energy ($\not\!\!E_T$). To obtain such measurements, the *vertex* of the event, or where the collision occurred within the detector, must be known well. Since events with electrons and muons should not be included in the analysis, electron and muon identification are important. Furthermore, $\not\!\!E_T$ is very sensitive to problems in a detector, therefore there should be low noise and

proper safeguards so particles external to the event have little effect. Details of the DØ detector have been extensively covered in the literature.[52] Given here is a brief description of the detector with some discussion as to how the squark and gluino analysis is affected by the design. The principles of particle detection are covered in Appendix A.

4.3.1 Overview

An isometric cut-away drawing of the DØ detector is shown in Figure 4.2. The detector consists of three main parts: the central detector, the calorimeters, and the muon system.

In order to discuss where parts of the detector are located and describe the direction of particles, a consistent coordinate system is required. The right handed DØ coordinate system has the positive z-axis along the proton direction (towards site South), the y-axis pointing straight up, and the x-axis pointing towards site East. $x, y, z = 0$ is at the center of the detector. θ indicates the polar angle with respect to the z axis ($\theta = 0$ is along the proton beam direction), and ϕ is the azimuthal angle in the $x-y$ plane. As seen from the figure, the calorimeter and central tracking chambers are nearly symmetric in ϕ except for the presence of the Main Ring accelerator beam pipe passing through the top of the calorimeter and the upper part of the muon system.

For physics at a hadron collider, θ is not a convenient measurement of polar angle. Since the collision energy is so large, one actually collides a parton of the proton with a parton from the antiproton. Since each of these partons carries a different fraction of the proton or antiproton momentum, the colliding system will be boosted in the lab frame along the $\pm z$ direction. If the beams are aimed correctly, there should be no significant transverse momentum of the incident partons. The longitudinal boost affects the polar angle in a complicated way. A more relativistically invariant quantity for representing the angle is the *rapidity* (y) defined as,

$$y \equiv \frac{1}{2} \ln \frac{E + p_z}{E - p_z} = \frac{1}{2} \ln \frac{1 + \beta \cos\theta}{1 - \beta \cos\theta} \tag{4.3}$$

where E, p_z, and β, are the particle's energy, z component of momentum, and v/c respectively. A boost in z only adds an additive constant to the rapidity. In the calorimeter,

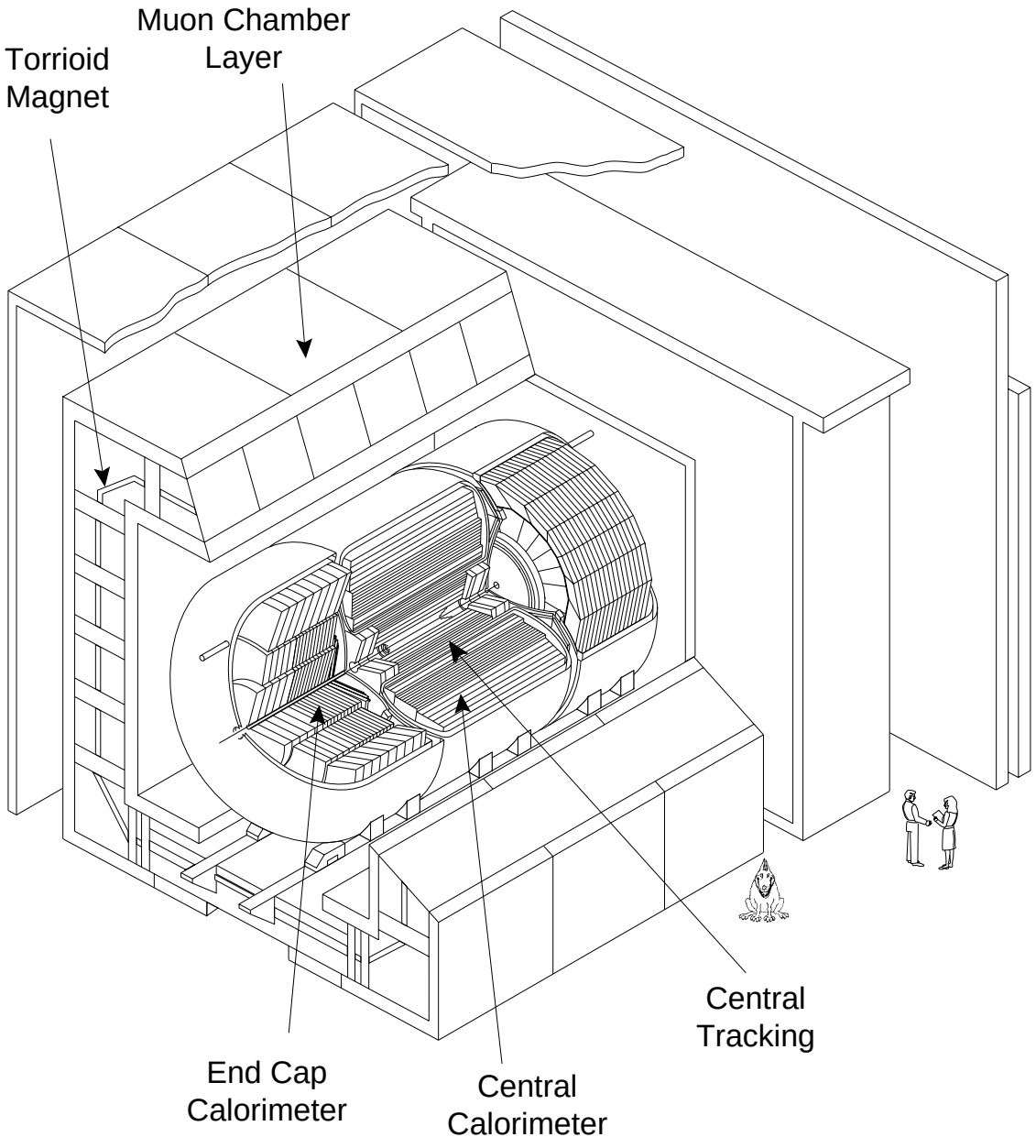

Figure 4.2: A cut-a-way view of the DØ detector.

one usually does not know the true velocity of a particle since that involves knowing its mass and thus its identity. Therefore, an approximation to the rapidity called the *pseudorapidity* (η) is used instead. η is the rapidity in the limit of a massless particle ($\beta = 1$) and is given by,

$$\eta = y|_{m\to 0} = -\ln\tan\frac{\theta}{2} \tag{4.4}$$

and the inverse,

$$\cos\theta = \tanh\eta \tag{4.5}$$

So long as the particle's mass is small compared to its transverse momentum, η will be a good approximation for y. Note that $\eta = 0$ corresponds to $\theta = 90°$, and very large positive η corresponds to the direction of the incident proton beam. The other directional quantities that the detector will measure are the transverse momentum and energy (p_T and E_T) defined to be $p_T = p\sin\theta$ and similar for E_T, the azimuthal angle ϕ, and the event missing transverse energy $\not\!\!E_T$.

4.3.2 Central Detector

The Central Detector (CD) consists of four subsystems: three tracking chambers and a transition radiation detector (TRD). The tracking chambers measure the direction of particles. Such information is necessary to determine the event vertex and aid in particle identification. Furthermore, they can also measure the dE/dx of a particle passing through which helps distinguish isolated electrons from overlapping e^+e^- pairs produced by photon conversion.

The Tevatron beam pipe within the detector is a very thin cylinder of beryllium with outer radius of ~3.7 cm. The pipe is necessary to maintain the vacuum, and beryllium was chosen to minimize multiple scattering. Forming a concentric cylinder around the beam pipe is the vertex detector (VTX). The next subsystem is the transition radiation detector (TRD) that helps to discern electrons from isolated pions. The last concentric layer of the CD is the central drift chamber (CDC). Capping the ends of the cylinder formed by these three detectors are the Forward Drift Chambers (FDC). The entire CD

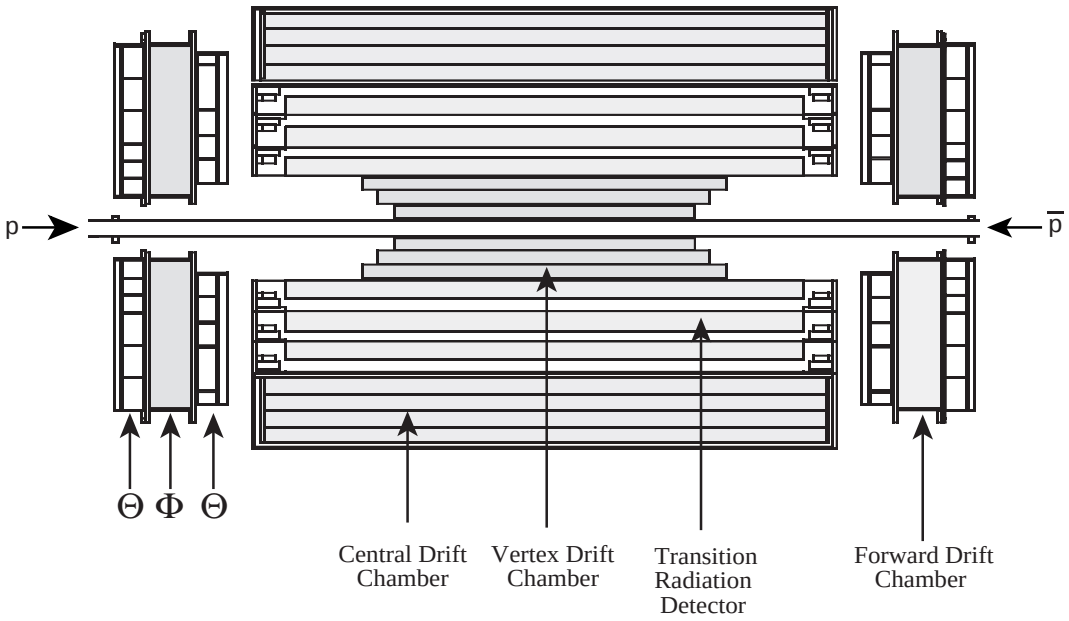

Figure 4.3: $r-z$ view of the central detectors. The interaction region, where the protons and antiprotons collide, is centered about the middle of the figure.

extends out to a radius of 78 cm from the beam pipe and to $z = \pm 135$ cm longitudinally. Figure 4.3 is a side view of the CD arrangement. The CDC and FDC detectors are important for the squark and gluino analysis for tracking and vertex finding. The VTX chamber and the TRD are not used by this analysis.

DØ has an unusual tracking system in that the tracking detectors are not immersed in a magnetic field, meaning that they cannot perform momentum measurements. A tracking magnet was not a part of the design to keep the detector compact and less expensive, though a magnet will be installed for the upgrade of the detector. The lack of a magnetic field means that the charge of tracks cannot be determined, so electrons cannot be distinguished from positrons.

Brief descriptions of the CD subsystems are now provided. Appendix B gives some details on the principles of drift chambers and how they pertain to the DØ tracking detectors.

4.3.2.1 Vertex Drift Chamber[52–54]

The VTX chamber resides just outside of the beam pipe with an inner radius of 3.7 cm and an outer radius of 16.2 cm. It consists of 3 concentric layers in the radial direction. The inner layer is 97 cm long and has 16 drift cells in azimuth. The two outer layers are 10 cm longer compared to their next inner layer and have 32 cells each. To measure the $r - \phi$ coordinate of a hit, each cell contains eight sense wires that are offset ± 100 μm with respect to each other to eliminate the left-right ambiguities. The layers themselves are also rotated with respect to each other to further aid pattern recognition. This arrangement is shown in Figure 4.4.

The z component of a hit is measured using charge division (see Appendix B). Unfortunately, this technique does not work well if occupancies (number of particles passing through each cell) are high, as is the case at the Tevatron. The z position resolution is only about 1.5 cm. Due to this poor resolution, the VTX chamber is not used by this analysis. The VTX chamber does have good $r - \phi$ position resolution ($\sim$60 mm) and also has 90% efficiency for separating two hits 0.63 mm apart. Thus, some other analyses

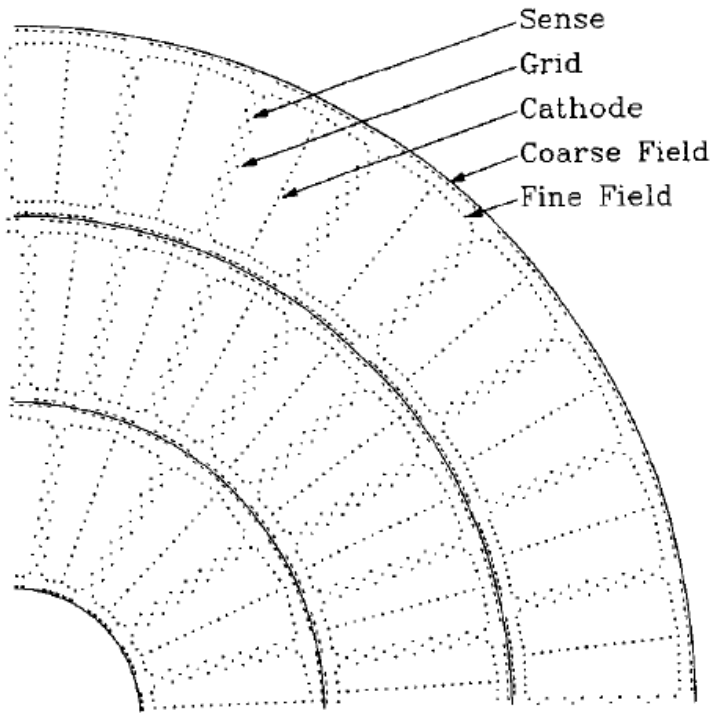

Figure 4.4: End view of one quadrant of the VTX chamber

requiring good electron identification make use of the VTX. Table 4.1 gives some VTX chamber properties.

4.3.2.2 Central Drift Chamber[52, 53, 55]

The central drift chamber (CDC) comes after the transition radiation detector (TRD) and before the electromagnetic calorimeter with inner radius at 49.5 cm and outer radius at 74.5 cm. It extends ±92 cm in z out to $|\eta| \sim 1.2$. It consists of four concentric rings of 32 azimuthal drift cells each. Each cell contains seven sense wires that are staggered by ±200 mm. In addition, the rings themselves are situated so cells are offset by one-half cell width. The construction of the CDC is unique in that none of the 32 free standing modules alone form a complete drift cell, as evident in Figure 4.5.

To measure the z position of the avalanche, delay lines are embedded in the inner and outer shelves (at the top and bottom of each cell). A higher voltage is applied to the adjacent sense wires so that a large signal will be induced. The delay lines are carbon fiber rods wrapped with a winding of magnet wire.[55] Signals propagate at 2.35 mm/ns,

Fiducial dimensions	$R_{inner} = 3.7$ cm, $R_{outer} = 16.2$ cm, 3 layers L_{layer}: $L_0 = 97$ cm, $L_1 = 107$ cm, $L_2 = 117$ cm
Sectors	16 azimuthal sectors in layer 0, 32 sectors in layers 1 and 2
Sense Wires	8 per sector, 640 total 4.57 mm radial separation ± 100 μm stagger in $r - \phi$ +2.5 kV
Wire Properties	Sense: 25 μm NiCoTin, 80g tension, 1.8 $k\Omega/m$ Field/Grid: 152 μm Au plated Al, 360g
Gas	95% CO_2, 5% Ethane, 0.5% H_2O
Drift Properties	Max. Drift Distance 1.6 cm <Drift field> 1 kV/cm $< v_{\rm drift} >$ 7.3 μm/ns
Gas Gain	4×10^4
Channels	2×640 (sense wires read out on both ends)
Resolutions	$r - \phi$ $\sim$50 μm z $\sim$1.5 cm two hit 90% eff. at 0.63 mm separation

Table 4.1: Properties of the Vertex Drift Chamber.[52–54]

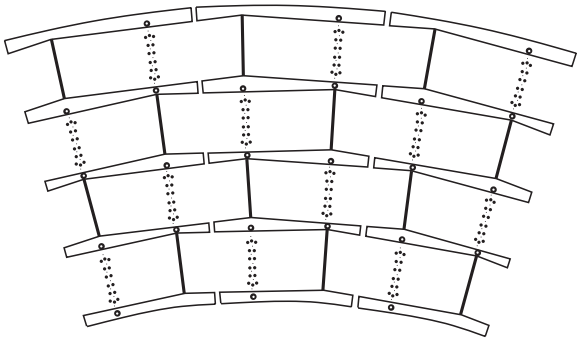

Figure 4.5: End view of part of the CDC.

Fiducial dimensions	R_{inner} = 49.5 cm, R_{outer} = 74.5 cm, 4 layers Length = 184 cm
Cells	32 in azimuth
Sense Wires	7 per cell, 896 total 6 mm radial separation $\pm$200 μm stagger in $r-\phi$ Outer two cell wires at 1.58 kV Inner five cell wires at 1.45 kV
Delay lines	2 per cell, 256 total v_{signal} = 2.35 mm/ns
Wire Properties	Sense: 30 μm Au plated W, 110g tension Field: 125 μm Au plated CuBe, 670g Delay: magnet wire around carbon fiber epoxy core
Gas	92.5% Ar, 4% CH_4, 3% CO_2, 0.5% H_2O
Drift Properties	Max. Drift Distance 7 cm <Drift field> 620 V/cm $< v_{\rm drift} >$ 34 μm/ns
Gas Gain	6×10^4 for outer two cell wires 2×10^4 for inner five cell wires
Channels	2 $\times$ 896 (sense read out at one end) + 2 $\times$ 256 (delay)
Resolutions	$r-\phi$ 150 – 250 μm z $\sim$2 mm two hit 90% eff. at 2 mm separation

Table 4.2: Properties of the Central Drift Chamber.[52, 53, 55]

and the resulting z position resolution is 2 mm. The CDC has $r-\phi$ resolution between 150 and 250 μm, which is poorer than the VTX since the CDC is so much larger. The CDC can resolve two hits with 90% efficiency at a separation of about 2 mm.

The CDC is crucial for the jets and $\not\!\!E_T$ analysis since it measures the vertex position of the event from which the measurements of the jets and the $\not\!\!E_T$ depend upon. Because DØ has no central magnetic field, the CDC does not measure the momentum of the found tracks, and as a result the vertex can be misplaced as discussed in Section 5.8. Some details of the CDC are displayed in Table 4.2.

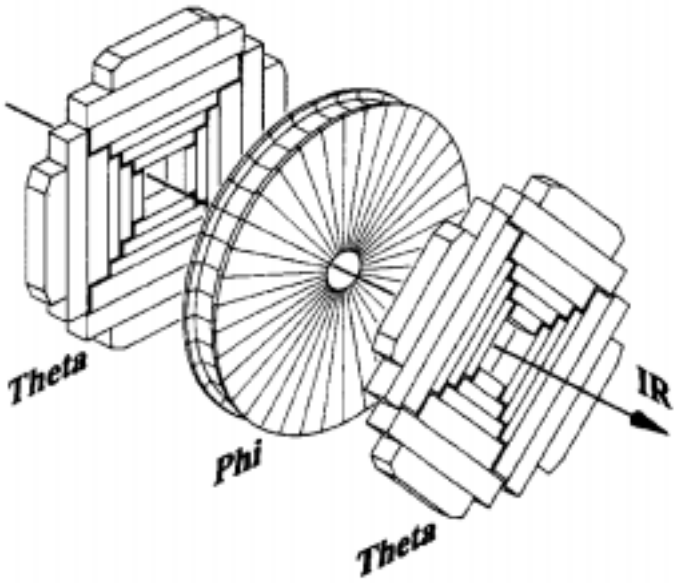

Figure 4.6: Exploded view of one of the two FDC packages. The sense wires run parallel to the rectangles in the Θ modules.

4.3.2.3 Forward Drift Chambers[52, 53, 55, 56]

As seen in Figure 4.3, the central detectors are capped by the two forward drift chambers (FDC), covering the forward regions of the detector. Particles traveling at θ as small as 5° can be measured by the FDC. Each FDC device consists of a Φ module sandwiched in between two Θ modules, as shown in Figure 4.6. The Φ chamber has its sense wires directed radially from the beam to measure the ϕ coordinate. It is one chamber containing 36 sectors over the full 2π azimuth. Each sector has sixteen anode wires spaced 8 mm apart along the z direction staggered transversely by ± 200 μm.

Each Θ chamber consists of four separate quadrants with six rectangular cells each. Each cell contains eight anode wires strung transverse to the direction of the beam, as shown in Figure 4.6. Like the Φ chambers, the sense wires are spaced 8 mm apart in z and are staggered. The sense wires in the three inner cells are situated near the edge of the cell, so there is only one drift direction. These chambers also contain delay lines identical in construction to those in the CDC to measure the orthogonal coordinate. The two Θ chambers are rotated 45° with respect to each other.

	Φ **Chamber**	Θ **Chambers**
Fiducial dimensions	$11 < R < 61.3$ cm $113 < \|z\| < 127$ cm	$11 < R < 62$ cm $104.8 < \|z\| < 111.2$ cm and $128.8 < \|z\| < 135.2$ cm
Cells	36 in azimuth	4 quadrants with 6 cells each
Sense Wires	8 per cell, 288 total 8 mm z separation ± 200 μm stagger in $r-\phi$ 1.55 kV	8 per cell, 384 total (2 chambers) 8 mm z separation ± 200 μm stagger in $r-\phi$ 1.66 kV
Delay lines	none	1 per cell, 48 total $v_{signal} = 2.35$ mm/ns
Wire Properties	Sense: 30 μm Au plated W, $50-100$ g tension Field: 163 μm Au plated Al, $100-150$g tension Delay (Θ only): magnet wire/carbon fiber core	
Gas	92.5% Ar, 4% CH_4, 3% CO_2, 0.5% H_2O	
Drift Properties	Max. Drift Distance 5.3 cm <Drift field> 1 kV/cm $< v_{\rm drift} >$ 37 μm/ns (Φ), 40 μm/ns (Θ)	
Gas Gain	3.6×10^4	2.3×10^4 for inner cell wires 5.3×10^4 for outer cell wires
Channels	288 for sense wires	384 for sense wires + 2×48 for delay lines
Resolutions	$r-\phi$ $\sim$200 μm z $\sim$2 mm two hit 90% eff. at 2 mm separation	

Table 4.3: Properties of the Forward Drift Chamber.[52,53,55]

The gas used in the FDC is the same as that used in the CDC, and so it shares many of the CDC characteristics. Some properties of the FDC are given in Table 4.3.

4.3.2.4 Transition Radiation Detector[52,57]

The TRD is a device located in between the VTX chamber and the CDC ($17.5 < R < 49$ cm). Its purpose is to provide independent electron identification, specifically to help separate electrons from charged pions since they can produce similar signatures in the calorimeter. This analysis only requires loose electron identification for the veto, so TRD information is not used.

4.3.2.5 CD Read Out[52, 58]

The read out electronics for all of the components of the central detector are nearly the same. Signals from preamplifiers located on the chambers are routed to shaper circuits on the detector platform below the calorimeter. From there, they are routed to the movable counting house (MCH) outside of the collision hall. There they are digitized by 8-bit flash analog to digital converters (FADCs) operating at 106 MHz. The full read out of the CD consists of 6080 channels.

The CD is not used for the first stage of the trigger, and so data from the system is read at a rate of about 200 events per second (200 Hz), which is the level 2 trigger input rate (see Section 4.3.5). At that rate with 256 FADC samples necessary to cover full drift times, a data transfer rate of over 300 Mbytes/sec is needed. Since the data cables transferring the digitized information from the FADCs to the level 2 computers can handle up to 40 Mbytes/sec, data compression is required. Zero suppression is thus applied as part of the digitization process, so regions of the signal not in between the leading and trailing edges of a pulse are discarded reducing significantly the amount of data.

Even with zero suppression, the FADC information makes up more than half of the size of a DØ event, contributing to the time it takes to write an event to tape. Near the end of the 1993–1995 run, an algorithm to find hits in the VTX and CDC detectors was run in the level 2 nodes instead in the reconstruction program off-line, reducing the amount of data to be written out and increasing the data taking rate from ∼5 Hz to ∼20 Hz. Of course, hit finding cannot be redone on that data, since the raw FADC information was discarded.

4.3.3 Calorimetry

Calorimeters are devices that measure the energy of particles. They play an extremely important role in every DØ physics analysis, especially since the tracking chambers are not capable of determining momenta. The total energy of all visible particles except for muons are measured by the calorimetry system. It was designed so that even the total

energy of weakly interacting particles (neutrinos and perhaps LSPs) can be accurately inferred. The properties of the calorimeters were chosen to aid in identifying electrons, photons, jets and muons. Without the excellent performance of the DØ calorimetry, a search for squarks and gluinos with the jets + $\not\!\!E_T$ signature would be impossible. The principles behind calorimeters and how they pertain to DØ calorimetry are covered in Appendix C.

4.3.3.1 DØ Calorimeters[52,59–63]

The DØ calorimeters are sampling, compensating, 4π hermetic (few uninstrumented holes and cracks), finely segmented devices for measuring energies of particles. Liquid Argon (at 78 Kelvin or -319° F) was chosen for the ionization medium, and so the calorimeters are contained in three separate cylindrical cryostats: one holding the central calorimeter (CC) and two mirror image vessels containing the end cap (EC) calorimeters capping both ends of the CC. The cryostats extend to a radius of 2.6 m from the beam line. The CC cryostat is 3.1 m in length and the EC vessels are 2.6 m long. The calorimeters are divided further into electromagnetic and hadronic sections. Each calorimeter in constructed from separate modules consisting of read out cells.

The basic calorimeter cell structure is the same regardless of its position in the calorimeter and the type of calorimetry (electromagnetic or hadronic). This structure is shown in Figure 4.7. The liquid argon gap between a grounded absorber plate and a signal read out board is 2.3 mm thick. Ionization occurs in this gap and charge drifts to the signal board within 450 ns. The signal boards for most of the calorimeter consist of two laminated sheets of 0.5 mm thick G10. The outer surfaces of each sheet are coated with a high resistivity epoxy and are held at high voltage (approximately 2.5 kV) to act as the "anode". One inner G10 surface is left bare while the other retains its original copper cladding but milled into the desired read out pad shape and size. The pad shapes are typically square and sized to match the transverse dimensions of electromagnetic (EM) and hadronic showers (side lengths of $\sim$1 – 2 cm for the EM calorimeters and $\sim$10 cm for hadronic). Signals from several pads at the same η and ϕ are ganged in depth to form

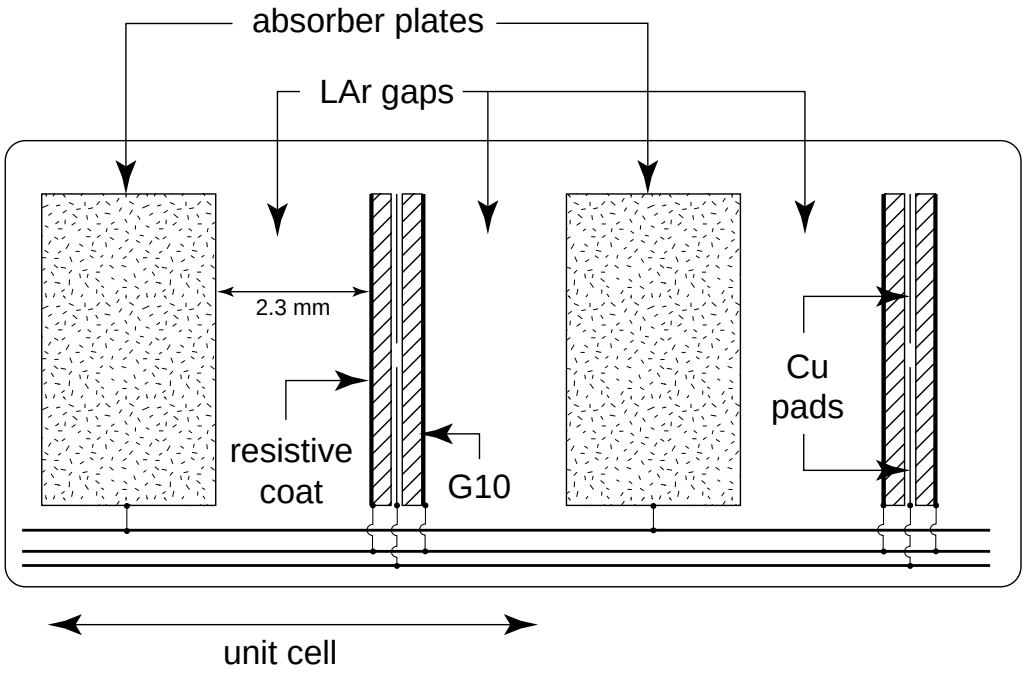

Figure 4.7: A calorimeter cell. The cell is immersed in liquid argon, the ionization medium.

a read out layer. The endcap electromagnetic calorimeter (ECEM) and the two smallest angle EC modules use multilayer circuit boards instead of the G10 sandwich.

Figure 4.8 shows the structure of the read out layers. A map of the detector indicating the placement of different calorimeter sections is displayed in Figure 4.9. From Figure 4.8, one sees that the calorimeter modules form towers emanating from the nominal interaction point and following rays of pseudorapidity (η). The alternating light and dark patterns set off one tower from the next to guide the eye. The arrangement is called pseudoprojective: though the centers of the modules follow lines of constant pseudorapidity, the module boundaries are aligned perpendicular to the absorber plates. All towers except those extremely forward are 0.1×0.1 in $\eta \times \phi$.

The calorimeter is divided into electromagnetic and several hadronic sections. Specifics of the calorimeters in the CC and EC cryostats are shown in Table 4.4 and Table 4.5, respectively. The EM calorimeters primarily measure the energies of electrons and photons and are made of four read out layers, each containing from two to ten unit cells. The EM layers of the CC (CCEM) use 3 mm thick depleted uranium ^{238}U absorber plates,

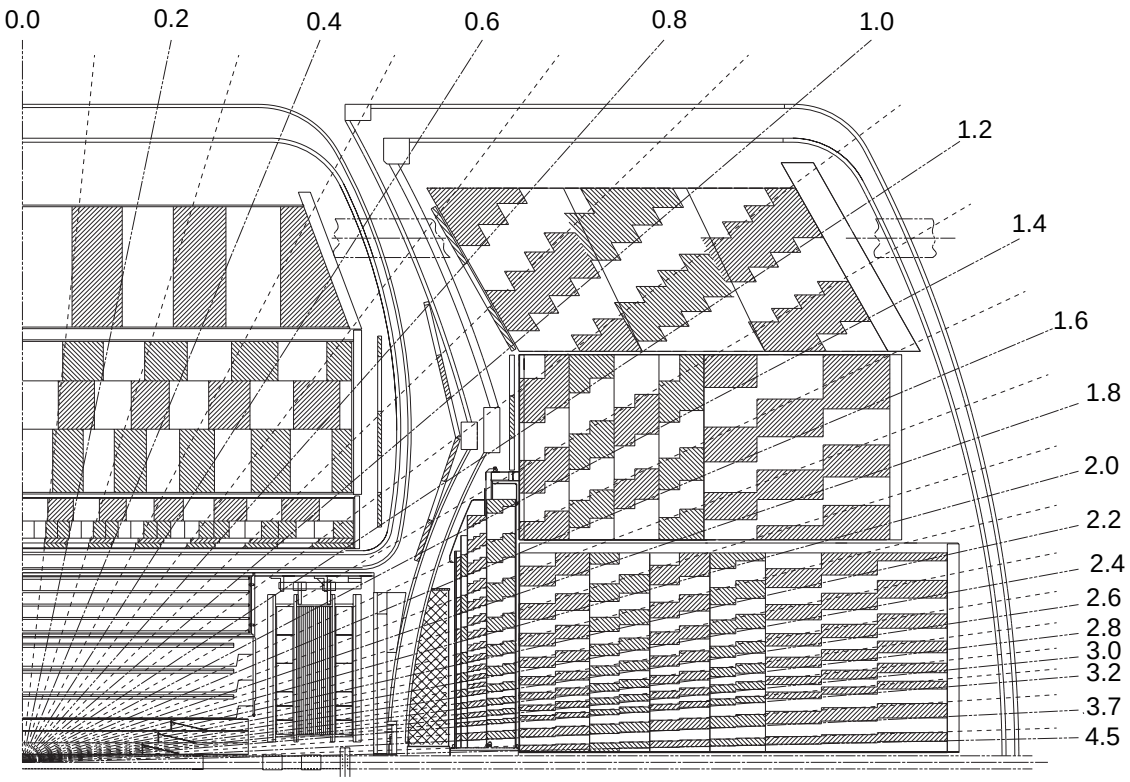

Figure 4.8: Calorimeter tower structure. A one quarter view of the detector is shown. The numbers indicate pseudorapidity (η).

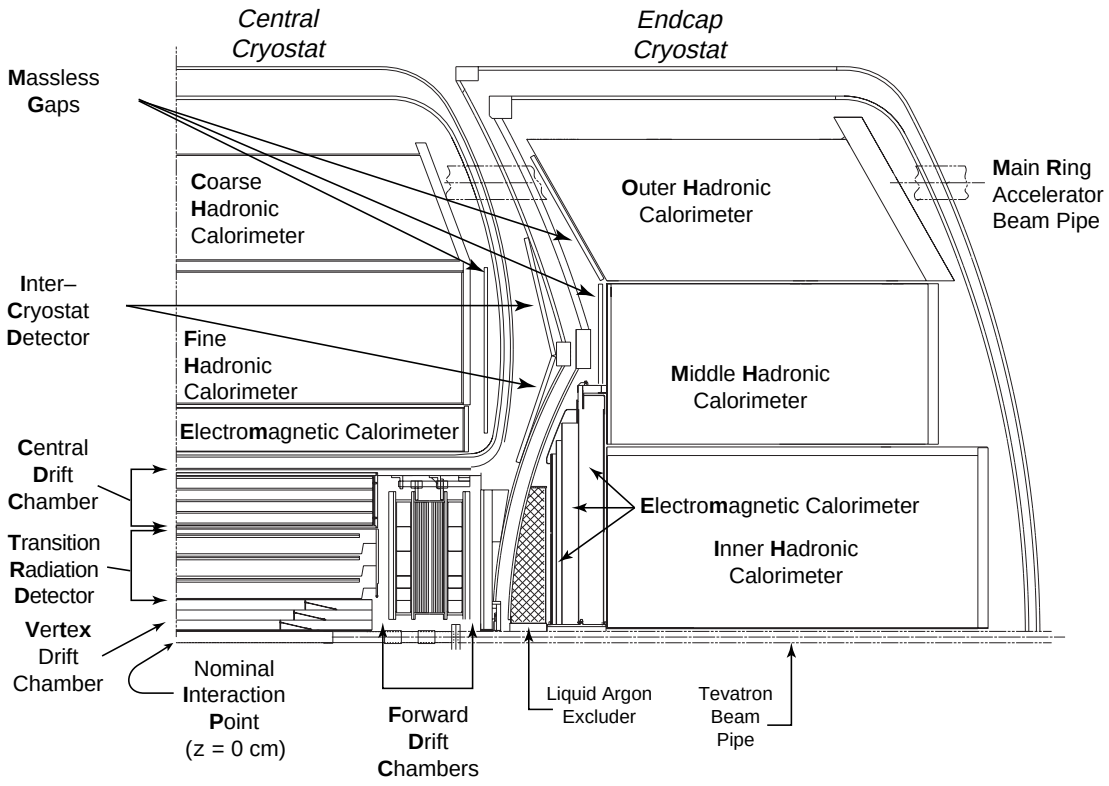

Figure 4.9: Map of the calorimeters and central detector. A one quarter view showing half of the CC and one EC cryostat is displayed. All of the parts displayed except for the MR accelerator beam pipe are symmetric in azimuthal angle, ϕ, about the Tevatron beam pipe.

Calorimeter	**CCEM**	**CCFH**	**CCCH**
# Modules	32	16	16
Absorber Plates[a]	3 mm U	6 mm UNb	46.5 mm Cu
# Read Out Layers	4	3	1
# Cells / Read Out Layer	2, 2, 7, 10	20, 16, 14	9
Layer Thicknesses	2.0, 2.0, 6.8, 9.8 X_0	1.3, 1.0, 1.9 λ	3.2 λ
Total X_0 Thickness[b]	20.5	96.0	32.9
Total λ Thickness	0.76	3.2	3.2
Sampling Fraction	11.79%	6.79%	1.45%
# Channels	10,368	3,000	1,224
η Coverage	≤ 1.2	≤ 1.0	≤ 0.6

[a] U = depleted uranium ^{238}U (tank armor), UNb = depleted uranium + 1.7% niobium alloy.

[b] All thicknesses measured at $\eta = 0$.

Table 4.4: Central cryostat (CC) calorimeters[52, 55, 59, 62]

while 4 mm plates are used in the EC (ECEM). The third longitudinal read out layer (EM3) is at the depth where an EM shower will, on average, reach its maximum (most number of particles). Therefore, the transverse segmentation of that layer is very fine, 0.05×0.05 in $\eta \times \phi$, in order to measure the shower properties most precisely. Since EM showers develop quickly with the uranium absorbers, the EM calorimeters are the thinnest, corresponding to 20.5 X_0 or 0.76 λ.

In the CC, the EM calorimeter is made up of thirty-two ϕ modules arranged in a cylinder around the beam pipe. The CCEM is 260 cm in length, and each module is $\sim$12 cm in depth and weighs 0.6 metric tons. The ECEM is comprised of one disk shaped module in order to avoid uninstrumented inter-module cracks. The inner radius is at $R =$ 5.7 cm, and the outer radius ranges from 84 to 104 cm depending on depth. Each ECEM module weighs 5 metric tons (there are two of them, one for each end cap cryostat). The cross hatched region in front of the ECEM calorimeter shown in Figure 4.9 is a lattice of hardened Rohacell foam called the liquid argon excluder, displacing LAr with the much less dense Rohacell. Without it, the LAr in front of the first ECEM layer would be too thick and electromagnetic showers would develop prematurely.[64] Although the first ECEM layer is very thin, 0.3 X_0, there is enough material in the excluder and the cryostat walls to bring the total absorber thickness up to the desired 2.0 X_0 for that layer.

The hadronic calorimeter sections measure energies from showers of hadronic particles making up jets. The very fine transverse segmentation is used to accurately measure the position of jets and to probe their shapes. The CC has two hadronic calorimeters: the fine hadronic (FH) and coarse hadronic (CH). The FH is segmented into three longitudinal read out layers, each comprising of from 14 to 20 unit cells with 6 mm thick absorbers made from depleted uranium plus 1.7% Niobium alloy. The bulk of a hadronic shower is contained within the 3.2 λ thick FH. Behind the FH is the coarse hadronic section made up of one read out layer of nine cells with 46.5 mm thick copper absorber plates. The CH is also 3.2 λ thick and is meant to catch shower tails extending beyond the FH. The FH and CH are each made up 16 separate ϕ modules. Note that rings of CC modules are rotated with respect to each other so that a projective ray only crosses one inter module

crack. The entire CC is 305 metric tons in weight, not including 26 metric tons due to the LAr. Its total thickness of 7.2 λ at $\eta = 0$ is sufficient to reduce punchthrough, or showers leaking out the back of the CH modules and into the muon system.

The EC contains three hadronic sections pictured in Figure 4.9. From Figure 4.8, one sees that the inner hadronic (ECIH) and middle hadronic (ECMH) sections are comprised of four finely segmented layers and one large coarse layer, very similar to the FH and CH calorimeters in the central cryostat. Thicknesses and other details are shown in Table 4.5. The outer hadronic section (ECOH) consists of 46.5 mm thick stainless steel absorbers to catch the tail of hadronic showers and reduce punchthrough. Each EC cryostat weighs 238 metric tons.

Particles traversing the region of $0.8 \leq |\eta| \leq 1.4$ encounter a large amount of uninstrumented material, such as cryostat walls, endplates, and other hardware. In order to correct for energy deposited in this material and to improve the energy resolution of the calorimeter as a whole, scintillator counter arrays called intercryostat detectors (ICD) are mounted on the front surface of each EC, as shown in Figure 4.9. Each ICD consists of rings of 384 scintillator tiles sized to match the transverse segmentation of the calorimeter. In addition, inside each cryostat in between the first or last calorimeter module and the cryostat wall are the massless gaps (MG), also shown in Figure 4.9. A massless gap is a ring of calorimeter signal boards without absorbers, sampling the shower energy before its particles leave the cryostat or just as they enter. Note that in between $1.1 \leq |\eta| \leq 1.4$ there is little EM coverage, thus reducing the acceptance for electrons and photons.

Figures 4.8 and 4.9 also indicate the passage of the Main Ring (MR) accelerator through the upper ECOH and CCCH layers. During colliding beam in the Tevatron, the MR is still accelerating protons for antiproton production, as discussed in Section 4.2. Losses from the MR make distinctive energy deposits in those layers of the calorimeter. Such "Main Ring events" can be avoided by inhibiting data taking for certain sensitive triggers (such as those requiring missing energy) when beam in the MR passes through DØ and when MR losses are high during proton injection and transition (see Section 4.3.5.1).

Calorimeter	**ECEM**	**ECIH**		**ECMH**		**ECOH**
		FH	CH	FH	CH	
# Modules	1	1		16		16
# Read Out Layers	4	4	1	4	1	1
Absorber Plates[a]	4 mm U	6 mm UNb	46.5 mm S	6 mm UNb	46.5 mm S	46.5 mm S
LAr Gap Width	2.3 mm	2.1 mm	2.1 mm	2.2 mm	2.2 mm	2.2 mm
Cells / r.o. layer	2, 2, 6, 8	16 each	14	15 each	12	8
Layer Thicknesses	0.3, 2.6, 7.9, 9.3 X_0	1.2 λ each	3.6 λ	1.0 λ each	4.1 λ	7.0 λ
Total X_0	20.5	121.8	32.8	115.5	37.9	65.1
Total λ	0.95	4.9	3.6	4.0	4.1	7.0
Sampling Fraction	11.9%	5.7%	1.5%	6.7%	1.6%	1.6%
# Channels	7488	4288	928	1432	384+64+896[b]	
$\|\eta\|$ Coverage[c]	1.4 – 4.0	1.6 – 4.5	2.0 – 4.5	1.0 – 1.7	1.3 – 1.9	0.7 – 1.4

[a] U = depleted uranium ^{238}U, UNb = depleted uranium + 1.7% niobium alloy, S = Stainless Steel.

[b] ECMH(CH) and ECOH cells are summed together at $|\eta| = 1.4$.

[c] Tower size increases beyond 0.1×0.1 at $|\eta| > 3.2$ up to 0.4×0.4 at $|\eta| \sim 4$.

Table 4.5: End cap cryostat (EC) calorimeters[52,55,61–63]

4.3.3.2 Calorimetry Read Out[52]

Signals induced on the read out pads within the 450 ns drift time are brought outside of the cryostats by means of four feedthrough ports and are routed to charge sensitive preamplifiers mounted outside of the CC and ECs. From there, signals are sent to base line subtractor (BLS) cards located on a platform below the detector for shaping and sampling. One purpose of the BLS modules is to form the level one calorimeter trigger information by picking off the leading edge of signals from all FH and EM modules and summing them into trigger towers of size 0.2×0.2 in $\eta \times \phi$. The resulting signal is passed to the level 1 trigger framework described in Section 4.3.5.1.

For the main readout, the BLS cards also take the original calorimeter read out signals and samples them just before a beam crossing, when the calorimeter is supposed to be quiet, and again 2.2 μs later (signal shaping circuits slow the signals so that all reach their peak near 2.2 μs after the beam crossing). The difference is a DC voltage proportional to the collected charge for a read out layer. Those results are passed to the ADCs in the movable counting house for digitization. The ADC counts are then sent to the software trigger (level 2) for further processing and are saved with the event if the trigger requirements are fulfilled. If the event is not accepted by either the hardware or software triggers, the BLS cards are reset and their information is discarded.

On some occasions, a negative energy can be read out from a section of the calorimeter. This occurs when the signal level sampled before the beam crossing is higher than after the interaction takes place. Such an elevation in signal can be due to a fluctuation in the uranium noise when the first sample is taken. In addition, if losses from the MR are large and the calorimeter preamps have not reached base line levels by the next beam crossing, negative energy will be observed in the outer calorimeter layers.

4.3.3.3 Calorimeter Performance[52, 59–61, 65]

The response of the calorimeter to particles has been studied by exposing CCEM and ECMH calorimeter modules to electron and pion beams with energies ranging between

10 and 150 GeV at a test beam facility at Fermilab. Studies determine that the CCEM calorimeter modules produce signals that are linear with electron energy to within 0.5%.

The energy resolutions of the modules were also determined. Calorimeter energy resolution is usually parameterized as

$$\frac{\sigma}{E} = C + \frac{S}{\sqrt{E}} + \frac{N}{E} \tag{4.6}$$

where C, S, and N are constants representing calibration errors, sampling fluctuation errors, and errors from noise, respectively. The noise term is usually only important at low energies, and the sampling term has the $1/\sqrt{E}$ dependence discussed in Appendix C. Ignoring the noise term, the EM calorimeter resolution measured with an ECEM module in the electron test beam was determined to be

$$\frac{\sigma(E_{EM})}{E_{EM}} = 0.3\% \oplus \frac{16\%}{\sqrt{E_{EM}}} \tag{4.7}$$

and the hadronic resolution measured with an ECMH module in a pion beam is

$$\frac{\sigma(E_{had})}{E_{had}} = 3.2\% \oplus \frac{50\%}{\sqrt{E_{had}}} \tag{4.8}$$

Note that $\oplus$ indicates addition in quadrature.

The compensation value of the hadronic calorimeter was also measured with the test beam. Using an EMIH module, the e/π ratio was measured to be 1.11 for 10 GeV pions and electrons and falls to 1.04 with 150 GeV pions. The equivalent e/h value is about 1.08, and so the DØ calorimeter is nearly compensating.

4.3.4 DØ Muon System[52, 66]

Only loose requirements are placed on muons, therefore a brief description of the muon system is given here.

Because muons are rather massive electromagnetic particles, they do not usually undergo bremsstrahlung nor do they interact with nuclei. Thus no showers are formed, and they leave energy in the calorimeter consistent with a minimum ionizing particle. Since the calorimeter cannot measure the energy of muons, their momenta are measured by bending the directions of muons in magnets. Beyond the calorimeter is the region where

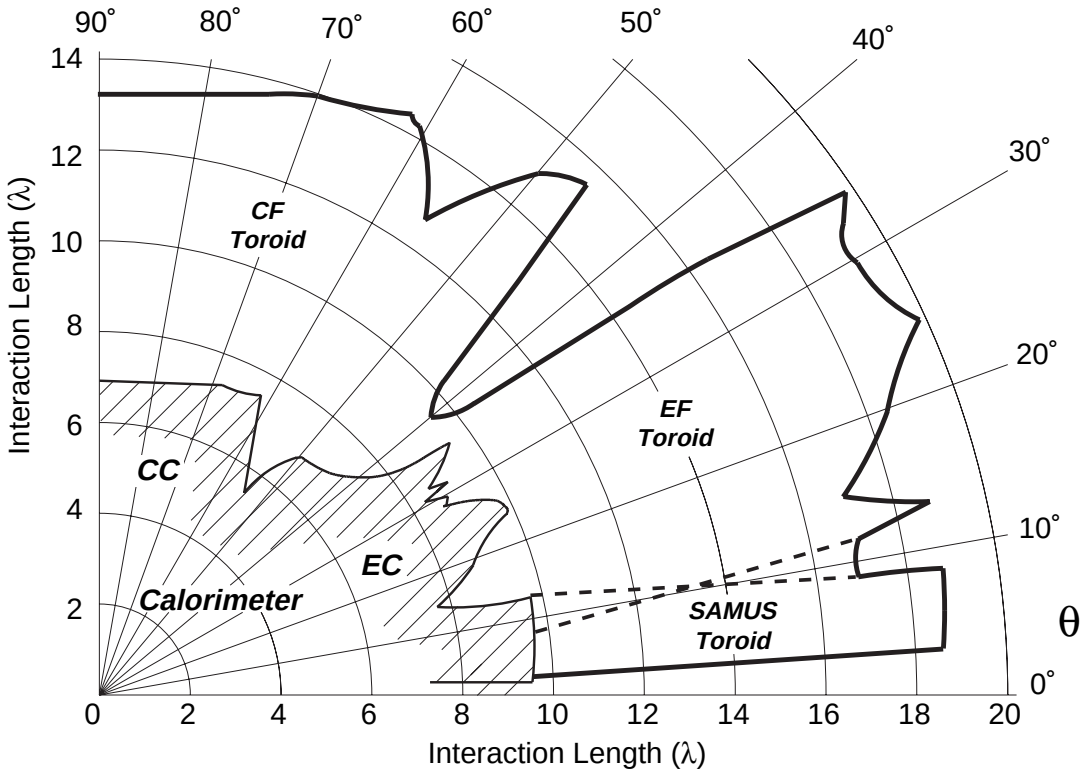

Figure 4.10: Thicknesses of the calorimeters and muon toroids. Shown are the number of interaction lengths of material a particle would encounter vs. polar angle if it were able to exit the detector.

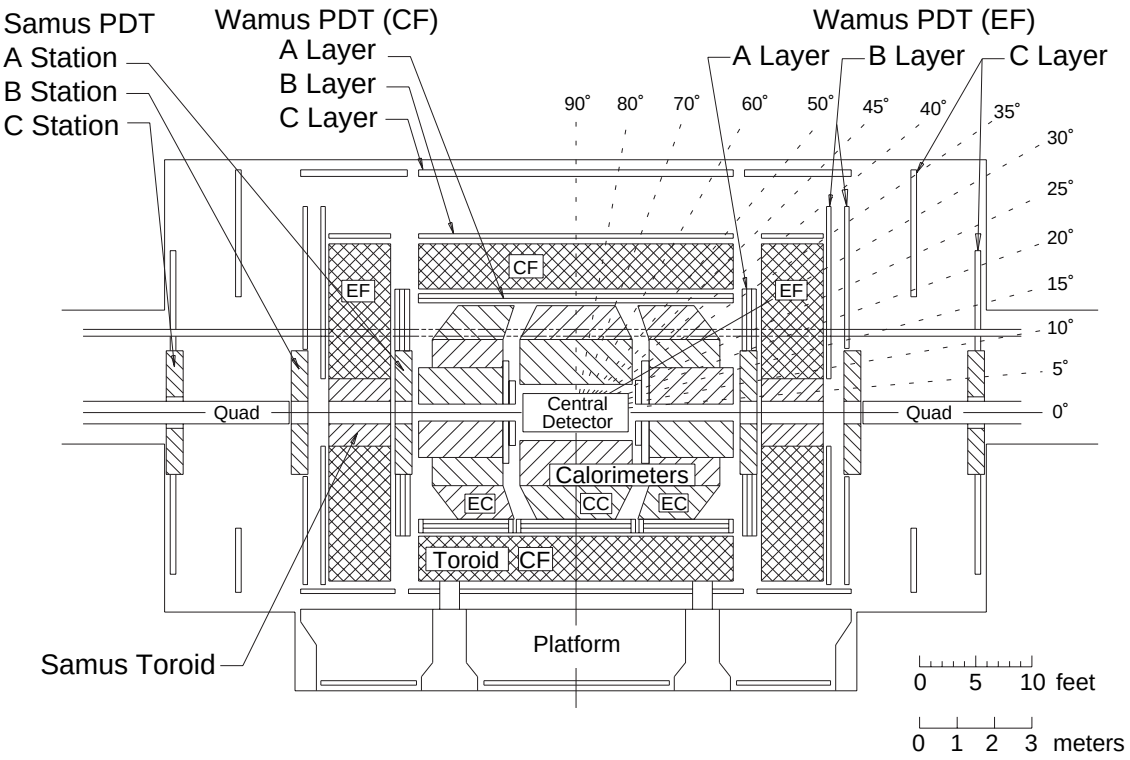

Figure 4.11: DØ muon system. A full side view of the detector is shown.

muons are identified by a system of toroid magnets and drift tubes. One hopes that particles reaching the muon system are indeed all muons. Because the calorimeter is so thick that is usually the case, and the magnets themselves also serve to stop and filter out particles other than muons. A profile of the thickness of various regions of the detector is displayed in Figure 4.10

Figure 4.11 shows a side view of the DØ detector with the muon system. The system is split into two parts: the Wide Angle Muon System (WAMUS) for measuring muons at $\theta > 10^{\circ}$ or $|\eta| < 2.5$, and the Small Angle Muon System (SAMUS) that measures muons close to the beam pipe in the region $2.5 < |\eta| < 3.6$.

The WAMUS system consists of large iron toroid magnets to bend the direction of muons. There are three WAMUS toroid magnets: muons within $|\eta| < 1$ encounter the central toroid (CF), and two end toroid magnets (EFs) cover $1 < |\eta| \leq 2.5$. The CF magnet surrounds the calorimeter and is about 1 m thick with its inner surface 318 cm from the beam pipe. Currents of 1900 A generate a 1.9 T magnetic field in the iron.

The CF weighs 2000 metric tons. The two EF toroids cap the CF, completely enclosing the calorimeter. Each EF magnet is located at $447 < |z| < 600$ cm with the outer edge 427 cm from the beam pipe. The SAMUS magnets are placed within a 183 cm square hole centered about the Tevatron beam pipe in the WAMUS end toroids. Like the calorimeter, the Main Ring accelerator beam pipe passes through the upper part of each EF toroid. Again, 2000 A currents generate a 2 T magnetic field in the iron. Each EF weights 800 metric tons.

The magnetic fields set up in the toroids run in the $\hat{\phi}$ direction, so the path of a muon is bent in the $r - z$ plane as it passes through the iron. Muons with more momentum bend less than slower muons, so the muon momentum can be determined by measuring the bend angle. For the WAMUS system, three stations of proportional drift tubes (PDTs), one before the magnets (the A layer) and two beyond (B and C layers), are used to measure the muon direction before and after bending. Details of the WAMUS drift tubes are shown in Table 4.6. The position of the muon track must be measured well to achieve good momentum resolution. Position resolution is about ± 0.3 mm and yields a momentum resolution of,

$$\left(\frac{\sigma(1/p)}{1/p}\right)^2 \approx (0.18)^2 + \left(\frac{0.01p}{\text{GeV}}\right)^2 \tag{4.9}$$

where p is the muon momentum. The constant term (18%) is due to multiple scattering in the calorimeter and iron, and the linear term comes from the position resolution of the PDTs.

Because occupancies are much greater in the forward regions, the SAMUS PDTs are much smaller than those used for WAMUS. The two SAMUS magnet toroids are embedded in the WAMUS EF magnets just around the beam pipe (outer edge at 170 cm from the beam). 1000 A of current generates the 2 T magnetic field. Details of the SAMUS PDTs are displayed in Table 4.6

4.3.5 Triggering and Data Acquisition[52]

At the Tevatron, the beams of protons and antiprotons cross every 3.5 μs for a potential interaction rate of 286 kHz (286,000 $p\bar{p}$ collision events per second), but interesting physics

	WAMUS	SAMUS
Organization	164 total chambers in A, B, and C stations. 3 or 4 cells per chamber in depth, 14–24 cells in width.	3 doublets of tubes in x, y, and u (45°). 864 tubes for A and B stations, 926 tubes in C station.
Sense Wire Properties	50 μm Au plated W, 300g tension, 4.6 kV	50 μm Au plated W, 208g tension, 4.0 kV
Cathode Properties	Glasteel coated copper strips, 2 per cell, 2.3 kV	No Cathode
Gas	90% Ar, 5% CF_4, 5% CO_2	90% CF_4, 10% CH_4
Drift Properties	Max drift dist 5 cm $\langle v_{drift} \rangle$ 6.5 cm/μs	Max drift time 150 ns $\langle v_{drift} \rangle$ 9.7 cm/μs
Total sense wires	11,386	5,308
Resolutions	Bend view 0.53 mm Non-bend view 0.3 mm	0.35 mm 0.35 mm

Table 4.6: Muon system properties.

does not occur at every beam crossing. In fact, the processes DØ physicists are looking for occur very rarely. The trigger system is designed to quickly examine an event to see if it contains physics deemed important enough for the event information to be written to tape. This task is accomplished by the Level 1 hardware trigger system and the Level 2 software filter system. The data acquisition system handles assembling the digitized signals from the flash ADCs and ADCs into an event and transporting it to the various trigger nodes and eventually to tape if it is accepted. The DAQ system can write out events to tape at ~5 Hz, so the entire trigger system must reduce the input rate of 286 kHz by a factor of 57,000!

4.3.5.1 Hardware Trigger Framework (Level 1)[52, 63, 67, 68]

The hardware trigger is made up of the Level 1 and Level 1.5 frameworks and their inputs. The Level 1 framework is the master in charge of producing the result of the hardware trigger and is the first step in the decision to accept an event.

The Level 1 framework takes inputs from the calorimeter, muon, main ring veto, and Level 0 trigger components (each discussed below) to form up to 256 trigger terms. A term is a yes/no answer to a particular requirement on the event. For instance, "Was there a hard scattering collision?", "Are there 2 calorimeter towers with $E_T > 3$ GeV?", "Is the $\not\!\!E_T > 40$ GeV?", "Was the Main Ring active during the Tevatron beam crossing?", and so on. The framework is very flexible in that the thresholds for most of the requirements are downloaded by a control computer and can be changed.

The trigger terms are grouped into AND/OR networks to form 32 specific triggers (usually just called triggers). The requirements of at least one of these triggers must be fulfilled in order for the event to be read out and passed to Level 2 for further analysis. For example, the trigger for the jets + $\not\!\!E_T$ analysis required the terms for calorimeter $\not\!\!E_T > 40$ GeV and at least one calorimeter trigger tower with $E_T > 5$ GeV to be true. There are a wide variety of triggers at DØ, representing the physics that the collaboration wants to examine. The requirements of the specific triggers are also downloaded and can be altered, as they were many times over the run. Triggers can also be prescaled; that is triggers that fire at too high a rate are instructed to only accept one out of every n events (e.g. a prescale factor of 5 means to accept only one of every five events that fire that trigger). The prescale factors change as the instantaneous luminosity of the collisions changes, since at high instantaneous luminosity, the rates are much higher and thus more triggers must be prescaled and at a larger factor. As the luminosity drops over the course of a store, the prescale factors drop as well, and some triggers will not be prescaled at all. A few triggers designed for new particle searches, including the trigger used for this analysis, were never prescaled.

The Level 1 and Level 1.5 frameworks are specialized hardware designed to examine parts of the detector very quickly, but coarsely. If no specific trigger is satisfied, the event is discarded and the detector is allowed to accept a new event. The Level 1 framework can usually make its decision within the 3.5 μs beam crossing time, so it is deadtimeless. The detector is "dead", that is unable to examine new events if the trigger system is still considering the current event or the event is being read out. Some triggers require

a Level 1.5 confirmation, discussed below, that can extend the Level 1 decision time to between 5 μs and 100s of microseconds. Since new events will be ignored while Level 1.5 is working, those triggers are designed to fire rarely to keep the deadtime low. If the one or more triggers are satisfied, the FADCs and ADCs start digitizing the central tracking, calorimeter, and muon system signals and the results are passed to the Level 2 processing farm for further examination. Level 1 reduces the input event rate of ~300 kHz down to 200 – 300 Hz. The four main components of the Level 1 trigger framework are now briefly described.

Level 0 Trigger[52, 55, 69]

Level 0 determines if there was an interaction during the most recent beam crossing and gives an estimate on the z position of the collision vertex (the position along the beamline where the proton–antiproton collision occurred). Its hardware consists of scintillator hodoscopes mounted on the inside faces of both EC calorimeter cryostats at $|z| = 140$ cm. The hodoscopes cover a partial range in ϕ between $1.9 < |\eta| < 4.3$ and have full azimuthal coverage between $2.3 < |\eta| < 3.9$. When a hard scattering interaction occurs in the detector, jets of particles from the quarks of the proton and antiproton not participating in the collision (spectator quarks) travel close to down the beam pipe. The Level 0 counters detect these jets and fulfills a Level 1 trigger term ("There was an interaction"). By measuring the time difference in the arrival of the jets at the counters on either side of the detector, an estimate of the z vertex can be calculated. Two values are reported: a vertex available within 800 ns after the beam crossing with a z resolution of 15 cm (FastZ), and a more refined value available 2.6 μs after crossing with a resolution $\sigma_z = \pm 3$ cm (SlowZ). The FastZ number is used by the calorimeter and muon hardware triggers to calculate E_T and p_T values. SlowZ is passed to the Level 2 processing farm if the event is accepted by Level 1. If a soft collision occurs along with the hard scattering, the vertex can be unreliable and the Level 0 trigger sets a multiple interaction flag that is recorded with the event. The Level 0 system has a timing resolution of 226 ps and is $\geq$91% efficient for detecting non-diffractive inelastic collisions.

Calorimeter Trigger[63, 68, 70]

The calorimeter trigger uses the 1280 0.2×0.2 in $\eta \times \phi$ trigger towers read out directly from the BLS cards. Signals representing the total energy in a tower (FH + EM; CH is not used by the trigger) and the energy in just the combined EM layers are digitized by flash ADCs, which are less precise but faster than the main calorimeter ADCs. The number of towers with total E_T and EM exceeding certain thresholds are determined and passed to the Level 1 framework for constructing trigger terms. Global calorimeter quantities are calculated as well, such as a coarse measurement of the $\not\!\!E_T$ (negative of the vector sum of all but the most forward towers) and total scalar E_T (scalar sum of over all towers).

Certain electron triggers (e.g. one might require at least one electromagnetic tower with $E_T > 7$ GeV) will ask for a Level 1.5 confirmation if their requirements are met. The calorimeter Level 1.5 system consists of 12 digital signal processors (DSPs) that examine the 1280 towers to apply an isolation requirement. While the Level 1 calorimeter trigger can only count towers exceeding thresholds, Level 1.5 is able to compare energies in towers near a high energy EM tower. If an EM tower is isolated, that is there is little energy in towers nearby, then Level 1.5 is passed and the specific Level 1 trigger passes as well. The calorimeter Level 1.5 DSPs may take up to 250 μs to reach a decision, thus introducing some deadtime but providing a rejection factor of 5 with greater than 95% efficiency for electron confirmation (a real electron will be accepted by the trigger 95% of the time). Level 1.5 is helpful since the rejected events do not have to be digitized and sent to Level 2 only to be rejected there after introducing much more deadtime.

Muon Trigger[55, 71]

The muon hardware trigger receives a bit corresponding to each muon chamber tube indicating whether or not it was hit. By looking for patterns of hit tubes in different regions of the detector, the muon trigger can count tracks (contiguous muon hits leading back to the interaction vertex) representing possible muons. The Level 1 muon system only looks quickly for patterns and cannot measure muon p_T. Some specific muon triggers

require a Level 1.5 confirmation where the hit patterns are examined more closely with specialized hardware for a rough p_T determination so that p_T requirements can be made. Depending on the number of hits in the muon system, the decision made by Level 1.5 can take up to 5 μs for WAMUS regions and can exceed 100 μs for SAMUS.

Main Ring Veto[72,73]

Protons traveling in the Main Ring accelerator can be lost in the regions where the MR passes through the DØ detector. Such losses make hits in the muon chambers and deposit energy in the calorimeter, especially in the CH layer where the MR passes through. Since MR losses will add energy to calorimeter trigger towers and will confuse the muon triggers with the additional hits, two schemes have been devised to veto on triggers that occur when the Main Ring is active and producing losses. The first method uses timing signals from the accelerator system to set two MR veto trigger terms. The `MRBS_LOSS` term is set if the MR is in injection or transition when losses are particularly high (see Section 4.2). Those conditions occur between 100 ms and 500 ms in the 2.4 s MR cycle. So for 400 ms of every MR cycle, triggers checking `MRBS_LOSS` are inhibited amounting to a 17% loss in integrated luminosity seen by those triggers. Furthermore, even after transition there may be losses occurring when bunches of protons are coasting through DØ. The `MICRO_BLANK` term is set if there is a MR bunch passing through the detector in coincidence with a Tevatron crossing. Triggers inhibited by `MICRO_BLANK` lose 9% of the total integrated luminosity. All muon, nearly all jet, some electron triggers, and the `missing_et` trigger are inhibited if either `MRBS_LOSS` or `MICRO_BLANK` terms are set.

Since electrons are well defined objects and are measured in regions of the detector far from the Main Ring pass through, an active vetoing system was developed in order to keep the lost luminosity down to a minimum. Instead of using timing signals from the accelerator, scintillator counters were mounted near the Main Ring beam pipe to measure the losses directly. Only when the rate in the counters exceeds a threshold are the so called `MAX_LIVE` triggers inhibited. Certain triggers are also inhibited for an additional 100 μs after the counter rate drops below threshold to allow the calorimeter signals to

return to base line levels. The advantage of the active veto scheme is that the trigger deadtime is directly linked to the losses in the Main Ring. If the Main Ring is running cleanly, then the live time can be increased dramatically for those triggers. Since $\not\!\!E_T$ is very sensitive to any spurious energy in the detector, the active veto is not used.

4.3.5.2 Software Filter (Level 2)[52, 63, 74, 75]

If Level 1 accepts an event, then all of the FADCs for the central detector and ADCs for the calorimeter and muon systems begin digitizing the detector signals. Analog signals from the detector are read into 80 VME front end crates and processed by the FADCs or ADCs. The central tracking output is also zero suppressed (see Section 4.3.2.5). To reduce deadtime, output from the digitizers are doubled buffered, so an event can be digitized while others are waiting to be passed to Level 2. If all of the buffers are full, the detector is inhibited from taking a new event until buffers are free.

Each crate contains a VME buffer/driver board (VBD) attached to one of eight data highways that connect VBDs to the Level 2 system. A VAX computer called the sequencer circulates a token to each VBD in turn on the data highway. If the VBD has data to be read out, it grabs to token, transmits the data for its part of the current event on the highway, and then returns the token to the network. Embedded in the token is a numerical tag for the current event, so a VBD knows which of its buffers to read. The token ring network is very efficient since the system can read out completed digitizers while slower ones are still processing. The data are passed from the VBDs to the Level 2 nodes on 32 bit wide 40 Mbyte/s highways. There are eight separate data highways that particular VBDs connect to: one for each central tracking detector, two for the calorimeter, one for the muon system, and one for trigger information. All of the data highways are connected to each Level 2 processor, yielding an effective bandwidth of 320 Mbytes/s.

The final step in the decision to accept an event occurs in the Level 2 farm of fifty VaxStation 4000/60 and 4000/90 computers. Each computer processes an event and decides if it passes certain filter requirements and should be written to tape. Level 2

reduces the input rate of ∼200 Hz down to the rate that can be written to tape – about five events per second.

As mentioned above, the data highway cables are all connected to each Level 2 computer. When an event is being readout from the VBDs, a supervisor computer decides which Level 2 node is available and directs the data there. The Level 2 nodes are connected to the data highways through multiport memory boards (MPMs), which are directly addressed by the Vaxes, eliminating the need for copying data into the computer itself. Data coming over the cables are assembled in the MPMs and eventually form a complete event once all of the front end VBDs have transmitted their information. The Level 2 node then converts data into Zebra[76] format (the memory format used for DØ data) and begins processing.

The Level 2 node does rudimentary reconstruction of physics objects in the event based on the entire detailed readout of the detector. For example, where Level 1 only had access to calorimeter trigger towers, Level 2 can examine all of the calorimeter readout layers in the fine 0.1×0.1 towers. Level 2 is capable of performing high level algorithms on the event, such as tracking, electron identification, jet cone algorithms and muon finding. The filters that are run by the Level 2 node depend on which Level 1 triggers passed. For example, if a Level 1 jet trigger passes, Level 2 will attempt to further examine the calorimeter by finding jets with a $R = 0.7$ cone algorithm so that requirements on the jets themselves, such as E_T, can be made. If the event passes none of the attempted filters, it is discarded and the Level 2 node becomes free. It can take a Level 2 computer anywhere from 200 ms to 5 s (for some muon filters) to make its decision. If all of the Level 2 nodes are busy processing events, the detector is inhibited from taking new events.

4.3.5.3 Recording of Events[63, 74]

If Level 2 accepts an event, then it is has been selected to be written to tape and used for physics analyses by the collaboration. Each Level 2 node has its own VBD card where the event is copied and awaits transfer. Another sequencer computer circulates a token to each Level 2 node VBD. If a VBD has data, it holds the token and transmits the

event over a data highway, similar to those used to read out events from the detector, to the sequencer computer's multiport memory. The sequencer then copies the event to preallocated memory in the host VAX and signals the host that the event is there.

The host VAX is responsible for the final handling of events. When the host is ready to accept the next event, it tells the sequencer where in memory it should be written, and the sequencer allows the token to be circulated amongst the VBDs. The host VAX logs the event and copies it to a disk buffer. The event is also copied to other memory locations so programs monitoring the quality of the data can do some rudimentary analysis. A tape server copies the events from the disk buffer onto 8 mm tapes that are transported by hand to the Feynman Computing Center at Fermilab for processing and storage.

4.4 Summary

The Tevatron proton–antiproton collider and the DØ detector at Fermilab are the machines used for this search. Squarks and gluinos can only be produced in high energy particle collisions, since they clearly are not present in the every day world assuming they exist at all. The Tevatron may possibly be producing these particles in proton–antiproton collisions.

The collider is only half of the required apparatus. Once a proton-antiproton collision takes place, there must be a device that looks to see what happened. Therefore, collisions are made to occur in the middle of detectors that measure characteristics of the particles emanating from the collision point. There are two detectors for collider physics on the Tevatron, DØ and CDF. The DØ detector is used for this analysis. If squarks and gluinos are being produced, they would not be observed directly. Heavy particles decay almost immediately into lighter daughter particles. The particles that end up entering the detector are leptons and jets of hadrons. By examining their properties, the existence and properties of their heavy parents may be inferred.

As described in the section, DØ is made up of three main subsystems. The trackers (central detector) accurately measure the directions of particles, the calorimeter measures the energy and direction of electrons, photons, and jets, and the muon system measures

the momentum of muons. The calorimeter makes the DØ detector especially well suited for this squark and gluino jets and missing transverse energy search. Since the calorimeter has few holes, energy imbalances are measured very accurately. Such measurements are crucial for this analysis.

Chapter 5

Event Reconstruction and Particle Identification

The data direct from the detector consist of digitized ADC traces for the tracking chambers, raw ADC counts for the calorimeter, and hit information from the muon system. The DØ reconstruction program and other software convert these raw detector signals into information about the physics objects in the event: the electrons, photons, muons, jets, and the $\not\!\!E_T$. This chapter describes the identification and reconstruction algorithms that pertain to the squark and gluino jets and $\not\!\!E_T$ analysis.

5.1 The Reconstruction Program[77,78]

The reconstruction program (`RECO`) converts the raw digitized detector signals into measurements that can be used more easily. The `RECO` program performs particle ID with very loose requirements, but provides much detail on the candidate objects. One can then place further requirements to refine the definitions of electrons, photons, muons, and jets. Details of particle ID and reconstruction are given in subsequent sections.

Running `RECO` is a major endeavor. `RECO` is run offline, that is not in real time with data taking. With the huge amount of data DØ collects, it is still important that the processing rate for `RECO` be close to the data taking rate, or else reconstruction would get hopelessly behind. To speed the process along, DØ employs a farm of about one hundred high speed (at the time) Silicon Graphics and IBM workstations all running `RECO` in parallel. The farm can process a few events per second, nearly as fast as the detector output rate.

5.2 Tracking and Vertex Reconstruction

One of the first steps in RECO is to process the flash ADC output from the tracking chambers. The central detector and muon FADC signals are analyzed, and the points where particles ionized in the drift cells are located. A pattern recognition algorithm searches for contiguous lines of these hits to build tracks. A track reconstructs the path of a particle within the tracking volume and indicates the direction the particle took through the detector. The amount of ionization can also be determined from the raw data to calculate the dE/dx for each track.

The vertex is the position within the detector where the proton–antiproton collision occurred and is the location from where the particles in the event emanate. Quantities involving the polar angle (θ) of a particle's direction, such as η, E_T, and, p_T, all depend on the vertex position, so it is a very important measurement.

The beam size is constrained to be approximately 40 μm $\times$ 40 μm in the $x-y$ plane (well within the beam pipe). The $x-y$ vertex position changes little from store to store except when some accelerator maintenance or realignment was performed during a shutdown. The average $x-y$ vertex position for a store is determined online and is used by RECO.

Because the proton and antiproton bunches in the Tevatron are quite long (the 1σ distance is 30 cm), the z position of the vertex must be measured event by event. RECO determines the vertex z position from tracks in the CDC and the FDC detectors in several steps.

1. CDC tracks in the event are extrapolated back to the beam pipe to determine where they cross the z axis. The z positions of the intersections are recorded in a histogram. If the CDC has no tracks, then tracks from the FDC are used.

2. A clustering algorithm is applied to the histogram to find groups of tracks that emanate from the same point in z. A cluster must have at least three tracks, unless only one cluster is found. A Gaussian is then fit to each cluster and the means are recorded as the event vertices.

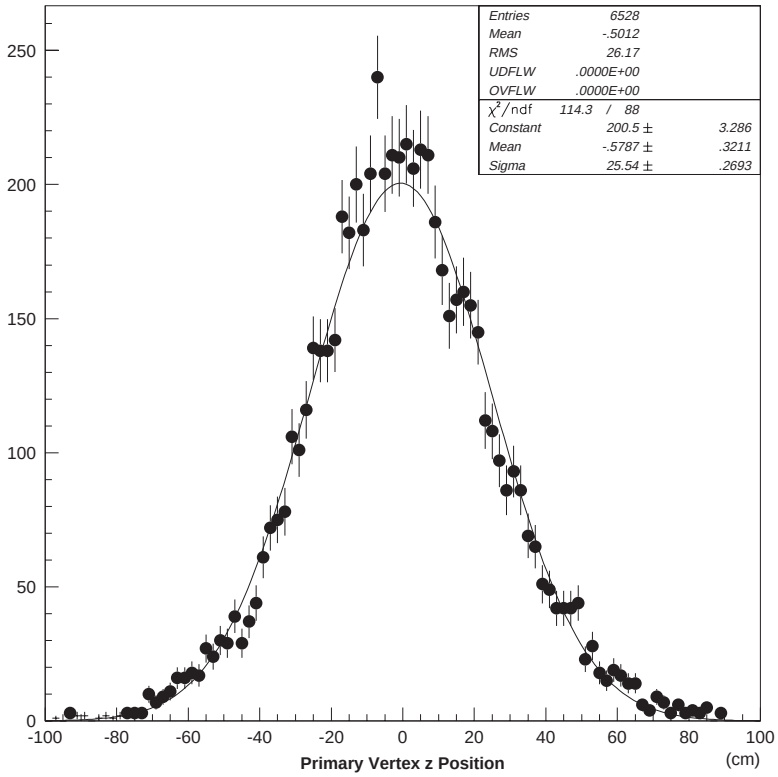

Figure 5.1: Primary vertex z distribution for $Z \to ee$ events. The fit is to a Gaussian.

3. If more than one vertex is found, then the vertex with the most tracks emanating from it is the primary vertex.

The primary vertex is used to calculate physics θ and η that go into E_T, p_T, and the $\not\!\!E_T$ measurements. The vertex z resolution can be as good as 6 mm if many tracks are involved. If a single CDC track determines the vertex, the resolution worsens to $2 - 3$ cm. The resolution is $\sim$10 cm if `RECO` must resort to FDC tracks. Multiple vertices are separated if they are at least 8 cm apart. The presence of multiple vertices indicates possible multiple interactions which may cause `RECO` to choose the wrong vertex as discussed in Section 5.8. An example vertex distribution from $Z \to ee$ events is shown in Figure 5.1.

5.3 Jet Identification

Light quarks and gluons released in an event will hadronize, producing collimated jets of particles. The electromagnetic and hadronic calorimeters are used to reconstruct the jets, which point along the direction of the original quarks and gluons. The number of jets found in an event and their size and shape are influenced by the algorithm chosen to identify them.

This analysis uses the cone algorithm[79, 80] to identify jets. Since the particles making up a jet are collimated in the detector, jets are found by drawing a cone in $\eta \times \phi$ space around energy deposits in the calorimeter. The total energy absorbed by the calorimeter within a cone is, to first order, the energy of the jet. The DØ calorimeter is well suited to the cone algorithm with its pseudoprojective tower structure seen in Figure 4.8.

Before the cone algorithm is run, the E_T in each calorimeter tower must be determined. A projective tower consists of all the cells in the calorimeter than lie along the same detector η and ϕ (detector angles are always measured from a vertex at $z = 0$, while physics angles are measured from the event vertex). Note that here a cell refers to a read out layer, not the individual unit cells. Each calorimeter cell has an energy vector defined as,

$$\vec{E}_i = \hat{n} E_i \tag{5.1}$$

where E_i is the measured energy deposited in cell i and $\hat{n}$ is a unit vector directed from the event vertex towards the cell center. The energy vector of the k^{th} tower, $\vec{E}_k^{\text{tower}}$, is the vector sum of the energy of its cells. The transverse energy of a tower is given by,

$$E_T^{\text{tower}} = E^{\text{tower}} \frac{\sqrt{(E_x^{\text{tower}})^2 + (E_y^{\text{tower}})^2}}{\sqrt{(E_x^{\text{tower}})^2 + (E_y^{\text{tower}})^2 + (E_z^{\text{tower}})^2}} \tag{5.2}$$

where E^{tower} is the scalar sum of the cell energies for that tower and E_j^{tower} $(j = x, y, z)$ is the specified component of $\vec{E}^{\text{tower}}$.

A cone in $\eta \times \phi$ space has a fixed radius of $R = \sqrt{\Delta\eta^2 + \Delta\phi^2}$. A radius of $R = 0.5$ is used for this analysis. The cone finding algorithm has three steps: preclustering,

clustering, and splitting/merging. `RECO` is nearly 100% efficient for identifying 0.5 cone jets with $E_T > 25$ GeV.[81]

5.3.1 Preclustering

Preclustering generates a list of starting positions for the cone clustering algorithm. Calorimeter towers with $E_T > 1$ GeV are sorted by E_T to make a seed list. A precluster is formed by taking the largest seed tower in the list and examining adjacent towers around it ($\pm$ 1 cell in η and $\pm$ 1 cell in ϕ). Any adjacent towers in the seed list ($E_T > 1$ GeV and not already assigned to another precluster) are added to that precluster and removed from the seed list. Then, towers adjacent to those newly added towers are checked and added to the precluster in the same manner. This process continues until towers a distance of $R = 0.4$ from the precluster start tower are checked and added if necessary. At that point, the precluster is complete and its center position is calculated by averaging over the E_T weighted η, ϕ centers of its towers. The total precluster E_T is also determined. The next precluster is then started with the largest E_T tower remaining in the seed list. Preclustering stops once the seed list is exhausted.

5.3.2 Clustering

The E_T sorted preclusters provide the starting point for the jet clustering algorithm. Clustering is performed by associating *all* towers within a cone of radius R ($R = 0.5$ for this analysis) centered about the direction of a precluster. The E_T weighted η, ϕ axis of this new jet is calculated and clustering is repeated about the new axis. This process continues until the jet axis stabilizes or fifty iterations have been performed. The latter condition allows escape from a bistable solution. The total E_T of the jet is determined as well as its η, ϕ axis. If the jet has $E_T < 8$ GeV, the reconstruction threshold, it is discarded. The cone algorithm repeats for each precluster. If a precluster is within $R < 0.5$ of any previously found jet, that precluster is skipped.

5.3.3 Splitting and Merging

There is nothing in the clustering algorithm to prevent jets from sharing towers. Splitting and merging is a mechanism to either split jets that have towers in common or merge the jets into one large jet. The jets are checked in the order they were found. Starting with the second jet (by definition, the first jet does not share any towers with a previously found jet), the jets are checked if they share any towers with a jet previous in the jet list. If shared towers are found between two jets and the jet axes are less than 0.01 apart in $\eta \times \phi$ space, the newer jet is dropped since it is just a rediscovery of a previous jet. If that is not the case, then the split/merge fraction is calculated,

$$f_{SM} = \frac{E_T^{\text{shared}}}{E_T^{\text{min}}} \tag{5.3}$$

where E_T^{shared} is the total E_T of the shared towers and E_T^{min} is the lesser E_T of the two jets. If $f_{SM} \leq 0.5$, then the common energy is split amongst the two jets giving each common *cell* to the jet that is closer to it. If $f_{SM} > 0.5$, then the two jets are merged into one jet. Note that merged jets may be larger than the specified cone size.

5.3.4 Kinematic Quantities

The final kinematic quantities for a jet are,

$$E_i = \sum_{\text{cells } k} E_i^k, \quad (i = x, y, z), \tag{5.4}$$

$$E_T = \sum E_T^k, \tag{5.5}$$

$$E = \sum E^k, \tag{5.6}$$

$$\phi = \tan^{-1}(E_y/E_x), \tag{5.7}$$

$$\theta = \cos^{-1}\left(E_z/\sqrt{E_x^2 + E_y^2 + E_z^2}\right), \tag{5.8}$$

$$\eta = -\ln\tan(\theta/2) \tag{5.9}$$

where E_i indicates the i^{th} component $(i = x, y, z)$.

Two other important quantities are also determined. The EM fraction is the fraction of the jet's energy that comes from cells in the electromagnetic layers of the calorimeter.

A large EM fraction ($> 90\%$) indicates that the jet could really be an electron or a photon. Since hadronic showers are made up of electromagnetic particles as well, hadronic jets should have some EM fraction (5% at the very least). A jet with close to zero EM fraction is probably in reality noise in the hadronic calorimeter. Similar to EM fraction, CH fraction is the fraction of the jet's energy from coarse hadronic calorimeter cells. Jets with large CH fraction ($> 40\%$) are due to noise in the CH or losses from the Main Ring.

Details of jet resolutions can be found in Reference 82. For 100 GeV jets in the very central region ($|\eta| < 0.5$), the resolution is $\sim$7%. The resolution changes only slightly for other calorimeter regions except for jets in the intercryostat region (measured with the ICD and the massless gaps). There, the resolution for 100 GeV jets worsens to nearly 10%.

5.4 Missing Transverse Energy Reconstruction

As mentioned previously, the presence of neutrinos and LSPs, if the latter exist, can be inferred by measuring the missing transverse energy ($\not\!\!E_T$) of the event. Remember that since the actual collision involves a parton from the proton and a parton from the antiproton, the longitudinal or z component of momentum of the colliding particles is not known and one cannot use conservation of p_z. The p_x and p_y components of the initial partons, however, are constrained to be negligible, and so conservation of transverse momentum and energy can be used to calculate the imbalance in E_T. This imbalance is the $\not\!\!E_T$.

Calorimeter $\not\!\!E_T$ is based on energy deposits in all cells of the calorimeter, including energy in the ICD and massless gaps. From the cell energy vector of Equation (5.1), the $\vec{\not\!\!E}_T$ is defined to be,

$$\not\!\!E_x = -\sum_{\text{cells } k} E_x^k, \quad \not\!\!E_y = -\sum_{\text{cells } k} E_y^k, \quad \vec{\not\!\!E}_T = \hat{x}\not\!\!E_x + \hat{y}\not\!\!E_y \tag{5.10}$$

where the sums are over all cells in the calorimeter and $\not\!\!E_x$ and $\not\!\!E_y$ are the x and y components of $\vec{\not\!\!E}_T$, respectively. The azimuthal direction of the $\not\!\!E_T$ vector is then,

$$\phi_{\not\!\!E_T} = \tan^{-1}(\not\!\!E_y/\not\!\!E_x) \tag{5.11}$$

Obviously, the z component of $\vec{\not\!\!E}_T$ is meaningless.

The muon corrected $\not\!\!E_T$ vector takes into account p_T of muons (calorimeter $\not\!\!E_T$ minus $\vec{p}_T$ of muons). This analysis uses the calorimeter $\not\!\!E_T$ only.

The $\not\!\!E_T$ resolution has been studied elsewhere[83,84] and is parameterized with the total calorimeter scalar E_T (S_T). S_T is the scalar sum of cell E_T over the entire calorimeter. The $\not\!\!E_T$ resolution is given by,

$$\sigma(\not\!\!E_T) = 1.08 \text{ GeV} + 0.019\, S_T \tag{5.12}$$

A signal scalar E_T spectrum is shown in the top histogram of Figure 6.1. For a typical value of $S_T = 500$ GeV, the $\not\!\!E_T$ resolution is $\sim$10 GeV.

5.5 Electron, Photon, and Muon Reconstruction

Reconstruction of electrons and photons is quite complicated. They are identified by small isolated clusters of energy in the electromagnetic layers of the calorimeter. Such clusters with an associated track in the tracking chambers are probably electrons. Since photons are neutral, they do not ionize the gas in the tracking chambers and so no tracks will be associated with their clusters. Reference 85 has a concise description of the latest DØ electron ID algorithm. To veto electrons, this analysis only uses the EM fraction to determine if a jet is actually an electron.

Muon reconstruction is similar to the tracking algorithm for the CDC and FDC. A global fit is performed as the last step using the muon system tracks, the primary vertex, the MIP (minimum ionizing particle) trace in the calorimeter, and a track from the CDC or FDC if present. The muon p_T is determined from the bend of the track due to the muon passing through one of the toroid magnets.[86] Various information about the track discussed in Section 6.1.5 are used to determine the quality of the muon.

The fine segmentation of the calorimeter allows one to use the muon MIP trace for tracking and muon confirmation. The MTC[87] software package (muon tracking in the calorimeter) performs the tracking and is described in Section 6.1.5.

5.6 Corrections

Various corrections must be applied to the physics objects. Only those concerning jets and $\not\!\!E_T$ are described here.

5.6.1 Jet Corrections

Jet corrections are described in much detail elsewhere.[85,88] The main corrections that are made are as follows,

Underlying event: The remnants of the proton and antiproton that are not involved with the hard scattering may deposit some energy in the detector. There is also noise in the calorimeter due to the radioactive uranium plates and the electronics.

Low energy particles: Many low energy particles are produced in hadronic showers. Since the calorimeter response is nonlinear at low energies, a correction is necessary.

Out of cone: The cone used by the jet algorithm may not be large enough to enclose for all of the energy of a jet. A correction is made for the energy leaking outside of the cone.

Some details on how these corrections are applied are given below.

5.6.2 Electromagnetic Energy Scale

A sampling calorimeter measures only a small fraction of the energy it absorbs. Data from a testbeam, where the response of calorimeter modules from electrons and pions of known energies is measured, are used for basic calibration and determination of the sampling weights. Testbeam data, however, cannot give the final corrections. Further refinements are made with *in situ* measurements.

One would like to determine the energy of the original parton that produced the jet. The calorimeter measures the energy "flow" of the jet, which is related to the energies of the constituent particles in the jet, and, in some way, is related to the energy of the original parton. The energy scale determines the correction factor that gives, on average, the energy of the jet at the particle level when applied to the measured jet energy. The particle level energy should be close to the energy at the parton level, but the details depend on the model of parton fragmentation. The corrections described here do not attempt to go back to the parton level, which is fine for the purposes of this analysis.

The energy scale of the EM calorimeter is determined from very pure samples of $Z \to ee$, $J/\psi \to ee$, $J/\psi \to \gamma\gamma$, and $\pi^0 \to \gamma\gamma$ events. Since the masses of the Z, J/ψ, and π^0 have been measured accurately elsewhere, the EM energy scale is just the correction factor to take their masses measured by the calorimeter to the correct values.

5.6.3 Hadronic Energy Scale

Determination of the hadronic energy scale is much more complicated, since it is impossible to obtain large pure samples of events equivalent to those used in determining the EM energy scale (such as $W \to qq$). Instead, hadronic jets are balanced against EM objects or other jets in a procedure described here.

The basic form of the hadronic jet energy scale correction is,

$$E^{\text{jet}}_{true} = \frac{E^{\text{jet}}_{measured} - O}{R(1-S)} \tag{5.13}$$

where E^{jet}_{true} is the "true" energy of the jet at the particle level, O is the offset correction, S is the showering correction, and R is the hadronic calorimeter response. The offset correction is the corrections from underlying event, uranium noise, electronic noise, and the effects of multiple interactions. Showering effects are the out of cone corrections and are determined from Monte Carlo events overlayed with test beam data.

The response involves the correction due to low energy particles and energy from particles lost in intermodule cracks and other dead (uninstrumented) material. The response is measured from data using the Missing E_T Projection Fraction (MPF) method.[85, 88]

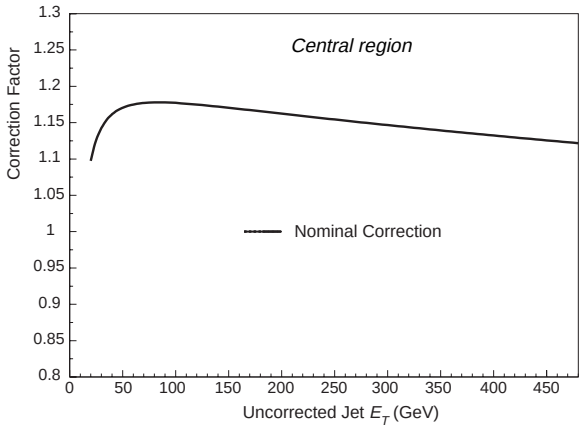

Figure 5.2: Jet corrections for the central region

The basic idea is that the hadronic energy scale is determined by balancing jets against a highly electromagnetic object (a high quality photon or electron). For unbiased results, the EM object is used to trigger the event. Since the EM energy scale is well known and the EM calorimeter resolution is very good, EM objects are measured precisely. Any $\not\!\!E_T$ in the event is then due to mismeasurement of the hadronic jets, since no neutrinos are expected. The hadronic energy scale is computed by projecting the $\not\!\!E_T$ vector along photon direction. There are few photon events with high E_T jets, and so dijet data is used to extend the response measurement. Since quality cuts are applied to the trigger jet, the $\not\!\!E_T$ may be biased. What matters, however, is the relative response with respect to some observable in the event, and so the effects of the bias can be normalized away.

The jet corrections are determined as a function of jet E_T, η, and EM fraction. Figure 5.2 shows the correction factor from Equation (5.13) as a function of uncorrected jet E_T for jets in the central region of the detector ($\eta < 1.1$).

5.6.4 $\not\!\!E_T$ Correction

Since the jet corrections change the E_T of the jets in the event, the $\not\!\!E_T$ should change as well. The only corrections that are applied to the $\not\!\!E_T$ vector are those from the electromagnetic and hadronic response (the energy scale corrections). Thus, the $\not\!\!E_x$ and $\not\!\!E_y$ components of $\not\!\!E_T$ are adjusted to reflect the response corrections to each jet in the event.

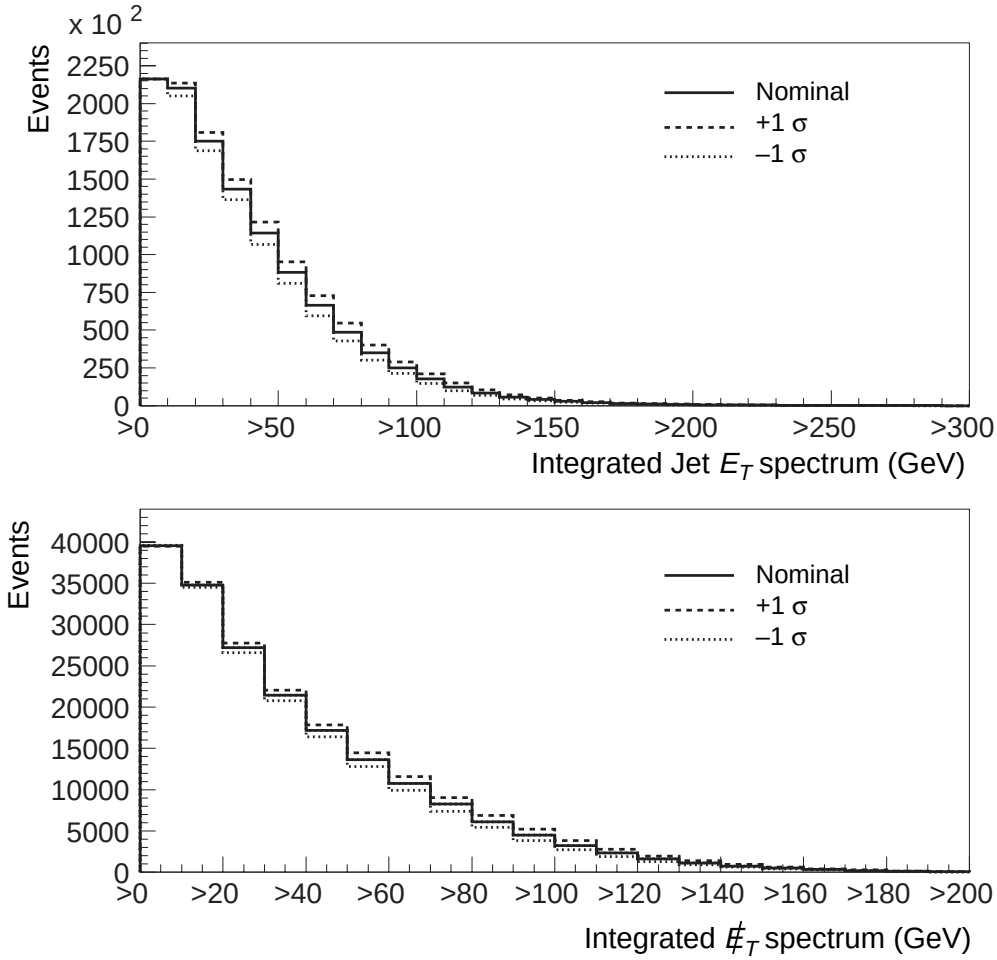

Figure 5.3: Energy scale errors. These histograms are integrated jet E_T and $\not\!\!E_T$ spectra from $t\bar{t}$ Monte Carlo (e.g. > 50 GeV indicates the number of events in the MC sample with jet E_T or $\not\!\!E_T > 50$ GeV). The nominal value is the corrected jet E_T or $\not\!\!E_T$. $\pm 1\sigma$ is the energy scale error described in the text.

The other corrections are not made to $\not\!\!E_T$ for various reasons. The offset correction, O, is assumed to be ϕ independent. Since $\not\!\!E_T$ is calculated by summing over the all cells in the calorimeter, the effects of O cancel. Similarly, the out of cone corrections, S, reflect energy lost by the algorithm. $\not\!\!E_T$ is independent of the jet algorithm, and so S does not apply as well.

5.6.5 Correction Errors

The error on a jet's E_T due to the energy scale corrections is determined by the following formulae,[89]

$$E_{T_{+1\sigma}} = 4\% \cdot E_T + 1 \text{ GeV} \tag{5.14}$$

$$E_{T_{-1\sigma}} = -4\% \cdot E_T - 1 \text{ GeV} \tag{5.15}$$

where E_T is the corrected transverse energy of the jet. The error on the $\not\!\!E_T$ is the cumulative effect of applying the energy scale error to each jet and then adjusting the $\not\!\!E_T$ accordingly. Figure 5.3 shows integrated jet E_T and $\not\!\!E_T$ spectra from $t\bar{t}$ Monte Carlo, indicating the size of the energy scale errors.

5.7 Anomalous Energy Deposits

Anomalous energy deposits, or hot cells, are isolated calorimeter cells measuring a large amount of energy. Since electrons, photons, and jets typically span many cells, these hot cells are probably caused by intermittent shorts or sparks in calorimeter modules due to contaminants in the liquid argon or contaminants inside the modules themselves. A hot cell can generate $\not\!\!E_T$ and spurious jets. Since events with hot cells will quickly drive up trigger rates and swamp high $\not\!\!E_T$ data samples, a "hot cell killer" run at level 2 for some triggers and in the reconstruction program removes isolated high energy cells from events.

The hot cell killer, called `aida`,[77] removes hot cells by looking for large energy deposits that are isolated *longitudinally*. For a cell to be removed, it must meet the following criteria,

- The suspect cell must have $E_T > 10$ GeV.
- $E_{T_{\text{neighboring cell}}} < 0.05 E_{T_{\text{suspect cell}}}$ is true for each cell neighboring the suspect cell in depth.

`aida` does not examine transverse neighbor cells. The hot cell killer in Level 2 can only remove one hot cell from the $\not\!\!E_T$ and total scalar E_T calculations and was only run on

events taken by the `missing_et` and `scalar_et` triggers. `aida` in `RECO` will remove as many hot cells as it finds. Those removed cells will not be included in $\not\!\!E_T$ and scalar E_T calculations and will not make up any jets.

The hot cell killer keeps spurious events with large $\not\!\!E_T$ due only to a hot cell from swamping the high $\not\!\!E_T$ data sample. Unfortunately, `aida` can sometimes inadvertently remove good cells that are within jets. The effects of such mistakes are discussed in Section 6.1.3.

5.8 Multiple Interactions

Multiple interactions are events with one or more soft $p\bar{p}$ collisions that occur in the same beam crossing as the hard scattering. A soft interaction is an uninteresting event that may produce many particles from the remnants of the proton and antiproton, but very few at high E_T. Samples of these events can be collected with a *minbias* trigger that requires only hits in the level 0 hodoscopes, and so these soft interactions are generally called minbias events. Minbias events alone are not interesting, except for special purposes, so the detector will not trigger on them. But sometimes the detector triggers on a hard scattering event (an interesting event with high E_T particles) with one or more soft interactions in coincidence.

The multiple interaction rate changes with the instantaneous luminosity. The average number of minbias interactions in addition to the hard scattering, assuming the hard scattering triggers the detector, is given by,

$$\mu = \mathcal{L}\,\sigma_{p\bar{p}}\,\tau \tag{5.16}$$

where $\mathcal{L}$ is the instantaneous luminosity, $\sigma_{p\bar{p}}$ is the visible $p\bar{p}$ cross section, and τ is the crossing time. For DØ, $\sigma_{p\bar{p}}^{\rm vis}$ =44.5 mb and τ = 1/(286 kHz). For example, the average number of minbias interactions in addition with the hard scattering at the average instantaneous luminosity for the 1993-1995 Tevatron run ($\sim 8 \times 10^{30}$ cm^{-2} s^{-1}) is 1.25.

The probability for multiple interactions to occur with the hard scattering trigger is given by the Poisson probability. For example, at the average instantaneous luminosity,

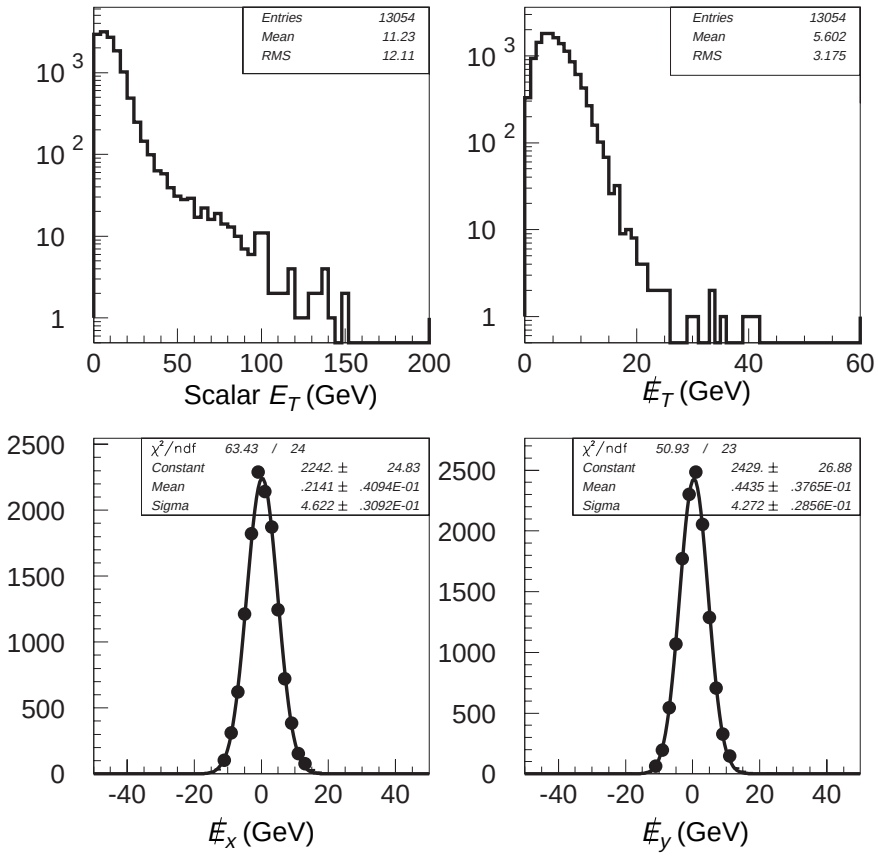

Figure 5.4: $\not\!\!E_T$ and total scalar E_T for minbias events. These events were collected at very low luminosity, so there is most likely only one soft interaction per event. The lower two plots show the x and y components of $\not\!\!E_T$. The fits (solid lines) are to Gaussians. The $\not\!\!E_T$ spectrum in the upper right hand plot

there is a 71% chance that a hard scattering event will be overlayed with one or more multiple interactions. The additional transverse energy added by a minbias event is typically very small and only very rarely produces new jets in events. Figure 5.4 shows the $\not\!\!E_T$ spectrum for minbias events collected at very low instantaneous luminosity.

One may worry that Monte Carlo (MC) may underestimate backgrounds, since MC only produces the hard scattering interaction and additional energy from the minbias events will not be included in the $\not\!\!E_T$. This effect was checked by taking a MC $t\bar{t}$ sample and randomly adding the $\not\!\!E_T$ due to several minbias interactions. There was no significant difference between the resulting $\not\!\!E_T$ spectrum and the $\not\!\!E_T$ spectrum with no minbias

events added. The $t\bar{t}$ $\not\!\!E_T$ spectrum is steeply falling, but not enough to be affected by extra energy from multiple interactions.

Although minbias interactions do not add much extra energy to an event, their extra particles make additional tracks in the tracking detectors. Rarely, a minbias event will make more tracks than the hard scattering interaction, causing the minbias vertex to be chosen as the primary. If the minbias vertex is far from the hard scattering, the E_T of the jets and the $\not\!\!E_T$ may be grossly mismeasured. The effects of such mistakes are discussed in Section 6.1.10. Misvertexing would occur much more rarely if DØ had magnetic tracking, since only the high p_T tracks would be used in the vertex determination.

Chapter 6

Analysis

With any triggering system, one runs the risk of discarding potentially interesting physics events. The trigger and filter requirements are thus made as loose as the bandwidth allows, and so data samples that (perhaps) contain signal events may be heavily contaminated with uninteresting background events. Further event selection criteria or *cuts* are placed on the data to select the events that could be signal.

It is difficult to design a set of criteria that will select every signal event and reject every background event, especially since one usually does not know on an event by event level which events could be signal and which are background. The signal efficiency is the fraction of signal events the cuts accept. Similarly, the background rejection rate is the fraction of background events not accepted by the cuts. The idea is to design a set of requirements that keeps the most signal (high signal efficiency) while reducing the background contamination as much as possible (large background rejection). In some sense, this part is the art of the analysis.

Monte Carlo (MC) simulations are used to determine the characteristics of the signal, and MC and collider data are used to examine the backgrounds. The cuts exploit well understood differences between the signal and backgrounds. In this chapter, Section 6.1 details the cuts that are applied to the data and the differences between signal and background events that justify them. The backgrounds to this analysis were introduced in Section 3.4 and are covered in more detail in Section 6.3.

Section 6.2 discusses the effects of the cuts on the collider data passing the analysis filter. The events that pass are the *candidates*. Since this candidate sample is still contaminated with background events, the background contribution to the data is estimated using MC and collider data. That procedure is described in Section 6.3. If the background estimate accounts for all of the data passing the analysis requirements, then the desired signal is not observed.

6.1 Event Selection Criteria

The criteria used to select the squark and gluino candidate events and reduce background contamination are described in this section. One must be careful not to examine in detail the collider data passing the analysis trigger and filter until after the analysis requirements are decided upon. Setting the event selection criteria based on the candidate data will result in picking out data fluctuations, rendering incorrect results from the analysis. Keeping that in mind, a summary of the event requirements is shown below. Subsequent sections describe them in detail.

Total Scalar Transverse Energy (Clean up) Removes events with main ring activity, beam halo activity, negative energy, electronics failures, and cosmic rays.

Vertex Position (Clean up) Assures a well centered event.

Removed Cells from Jets (Clean up) Events are rejected if a jet had a cell removed by the hot cell killer.

Bad Jets (Clean up) Remove events with jets that fail good quality requirements. Also removes events with electrons.

Jet – Missing Energy Correlations Reduces mismeasured QCD multijet background.

Muon Veto Defines signal and reduces background with muons.

Missing Transverse Energy Defines signal and reduces all backgrounds.

Three Good Jets Defines signal and reduces all backgrounds.

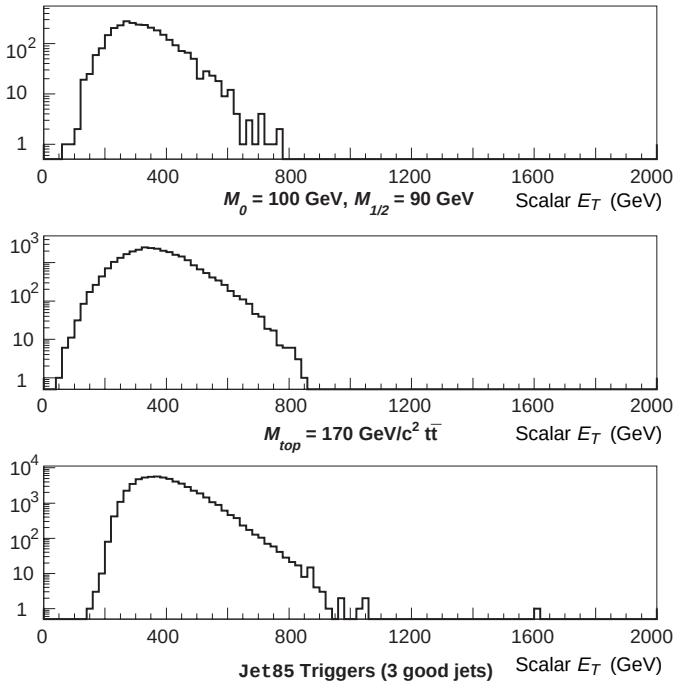

Figure 6.1: Total calorimeter scalar E_T. The top plot is a signal MC sample. The middle histogram is from $t\bar{t}$ MC. The bottom plot is collider data QCD multijet events with at least three good jets. Events where the hot cell killer removed a cell from a jet are rejected.

Leading Jet $\mathbf{E_T}$ Allows use of `jet85` multijet background model.

$\mathbf{H_T}$ Removes vector boson backgrounds.

Confirmation of Primary Vertex (Clean up) Removes events that are misvertexed.

6.1.1 Total Calorimeter Scalar Transverse Energy

In order to eliminate events due to high energy cosmic rays showering in the calorimeter and calorimeter electronics failures (e.g. bad BLS cards), events are required to have less than 1.8 TeV of scalar transverse energy deposited in the calorimeter. Total calorimeter scalar E_T was introduced in Section 5.4.

The top two plots of Figure 6.1 are histograms of total scalar E_T for a signal sample and a $t\bar{t}$ Monte Carlo sample. The bottom plot is scalar E_T for data QCD multijet events

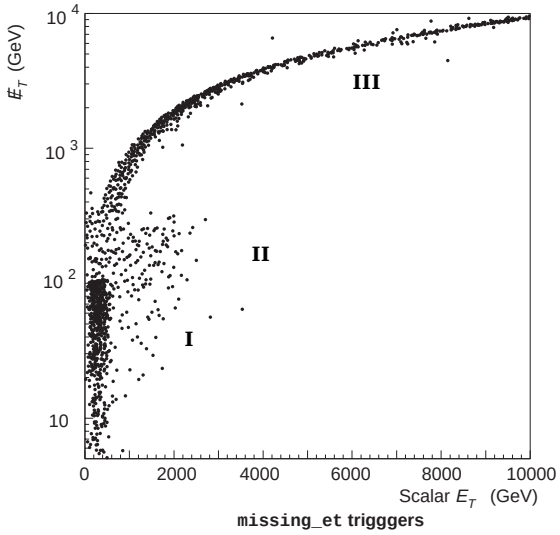

Figure 6.2: $\not\!\!E_T$ vs. total scalar E_T for collider data passing the `missing_et` filter. The regions denoted by roman numerals are described in the text.

collected by the `jet85` filter where at least three good jets are also required (events where `aida` removed a cell from within a jet are rejected; see Section 6.1.3). Events passing the `jet85` filter, which requires at least one jet at Level 2 with $E_T > 85$ GeV and no $\not\!\!E_T$ requirement (see Section 6.1.9 for further details), are used to examine the characteristics of mismeasured QCD multijet events. Not seen on the bottom histogram are 10 overflow events with one event at scalar E_T of 2.5 TeV and the rest over 80 TeV. Note that this total scalar E_T condition is used instead of a *total energy* requirement. Requiring total $E < 1.8$ TeV may inadvertently remove events with multiple interactions.

To see what this requirement rejects, a plot of $\not\!\!E_T$ vs. scalar E_T for events passing the `missing_et` analysis filter (requiring only Level 2 $\not\!\!E_T > 40$ GeV; see Section 6.2.1 for details) is displayed in Figure 6.2. Several events in the three distinct regions of the plot denoted by roman numerals were scanned in order to determine the type of backgrounds that are present. Note that the plot is misleading; 99% of events lie in the "good" region with $\not\!\!E_T < 300$ GeV and scalar $E_T < 800$ GeV.

Region I contains events used by this analysis. Anomalous events with small $\not\!\!E_T$ and very large scalar E_T seem to be due to beam halo where one end of the detector has large energy deposits and many hits in muon and central tracking chambers. Events in region

II have $\not\!\!E_T$ much larger than expected for a good event. A scan of events there found several clear cosmic ray events (where a muon showered in the calorimeter), a beam halo event, and an event with large energy deposits from the main ring. In region III, events have huge $\not\!\!E_T$ and scalar E_T and appear to be caused by enormous main ring losses.

Events are also required to have scalar $E_T > 0$ GeV. This requirement eliminates events with large amounts of negative energy in the calorimeter. Negative energy arises when a previous event saturated some calorimeter preamps, and the current event was taken before those preamps returned to baseline levels. The `missing_et` filter will not fire on negative energy (see Section 6.2.1), but may still collect such an event if it is accompanied by large amounts of noise due to the unsettled preamps. The scalar E_T requirements are not applied to the Monte Carlo samples and are assumed to be 100% efficient.

6.1.2 Vertex Position

To assure that events are well centered in the detector, the z position of the primary vertex is required to be within ± 60 cm of the center of the detector. A sample vertex position distribution is shown for $Z \to ee$ events in Figure 5.1 on page 91. For MC samples, this requirement is applied to the simulated vertex position and is 98% efficient.

6.1.3 Removed Cells from Jets

Anomalous isolated high energy calorimeter cells (hot cells) and the hot cell killer routine, `aida`, were described in Section 5.7. Generally, when a hot cell is removed from an event the $\not\!\!E_T$ will decrease, since most events are balanced QCD multijet events and will no longer have the anomalous cell to drive up the $\not\!\!E_T$. Rarely, it has been observed that a jet will have a longitudinal shower profile such that a cell within a jet cone will meet the removal criteria, although the cell's energy is probably not anomalous. Since `aida` only looks in the longitudinal direction to determine if a cell is anomalously larger than its neighbors, such cells within jets will be removed, possibly *raising* the $\not\!\!E_T$ of the event.

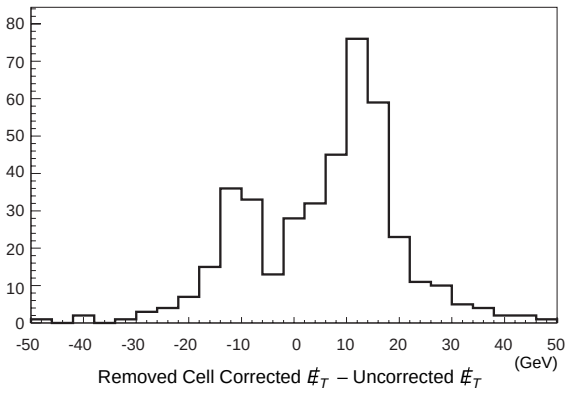

Figure 6.3: Removed cell corrected $\not\!\!E_T$ − uncorrected $\not\!\!E_T$ for mSUGRA MC. Note the larger peak when the difference is positive. In that region, the $\not\!\!E_T$ increases when the removed cell is added back into the event. The distribution shown is from an `isajet` mSUGRA sample with $M_0 = 150$ GeV and $M_{1/2} = 80$ GeV. Distributions for other values of M_0 and $M_{1/2}$ are similar.

Even though it is rare for the hot cell killer to remove a cell from a good jet, the mistake has a significant effect on the determination of the QCD multijet background. Applying a $\not\!\!E_T$ requirement also tends to select such balanced events with a good cell removed and thus enhances the contamination. Therefore, some procedure must be used to handle these events.

Top quark analyses[90] "recover" the removed cells by adding them back into the jet and correcting the $\not\!\!E_T$ accordingly. When they perform a $\not\!\!E_T$ requirement, they use the minimum of the hot cell corrected and uncorrected $\not\!\!E_T$. That procedure works to recover events if the expected signal is balanced (or close to balanced) events. For squarks and gluinos, the signal is very unbalanced ($\not\!\!E_T$ of at least 75 GeV is required). An event of this type will typically have most of the jets on one side of the calorimeter (in ϕ) with the $\not\!\!E_T$ vector pointing on the other side. If a jet is reduced by a removal of a cell, the $\not\!\!E_T$ will decrease (opposite to that of a balanced event). When the cell is added back in, the corrected $\not\!\!E_T$ will increase back to the true value. Using the procedure of cutting on the minimum of the hot cell corrected and uncorrected $\not\!\!E_T$ will often result in use of the wrong $\not\!\!E_T$ value, as shown in Figure 6.3.

One may consider correcting the event if a hot cell is found within a jet and always use the hot cell corrected $\not\!\!E_T$ for testing the $\not\!\!E_T$ requirement. But the hot cell killer sometimes

does do its job correctly. Always using the hot cell corrected $\not\!\!E_T$ would possibly introduce events with real hot cells; a background that is hard to model.

Since this analysis is extremely sensitive to the $\not\!\!E_T$ tail of QCD multijet events, events with hot cells in jets are rejected altogether. The following criteria must be met to reject such events:

- A cell that was removed by `aida` must be within $DR = 0.5$ (in $\eta \times \phi$ space) of the axis of a jet.
- That jet must have $E_T > 15$ GeV and $|\eta| < 3.5$.

Efficiency of Removed Cells from Jets Requirement

A squark and gluino event will be rejected if a jet has a cell removed by `aida`, so an efficiency must be calculated. In fact, unless the event is corrected by putting the removed cell back into the jet, this efficiency is always present since removing a cell from a jet in a very unbalanced event acts to lower the $\not\!\!E_T$ that goes into the event information, possibly causing the event to fail a large $\not\!\!E_T$ requirement. To obtain a measurement of the efficiency from the data, one would like to start with a sample of clean events that are not enhanced in hot cells. QCD jet triggers are unsuitable since they will fire on a hot cell. In order to get an unbiased jet sample, the `ele_1_mon` filter, which requires a cluster in the electromagnetic calorimeter passing some electron shape criteria, is used. An electron passing the Top group tight criteria is then required. About 6000 events pass and there are approximately 4000 total jets (not overlapping with the electron) in the sample. Since it is unlikely that a hot cell could masquerade as a good quality electron that triggered the taking of the event, this sample should be as clean as possible. Out of the nearly 4000 jets, twelve are flagged as having a hot cell within a jet that would cause the event to be removed by the hot cell in jet criteria. This information is displayed in Figure 6.4.

The filled points of Figure 6.5 show the cell removal rate derived from Figure 6.4. Since the statistics for the last few bins are very low, the last point at ~82 GeV is the sum of bins from Figure 6.4 over 60 GeV. Its E_T position is the weighted mean of the E_T

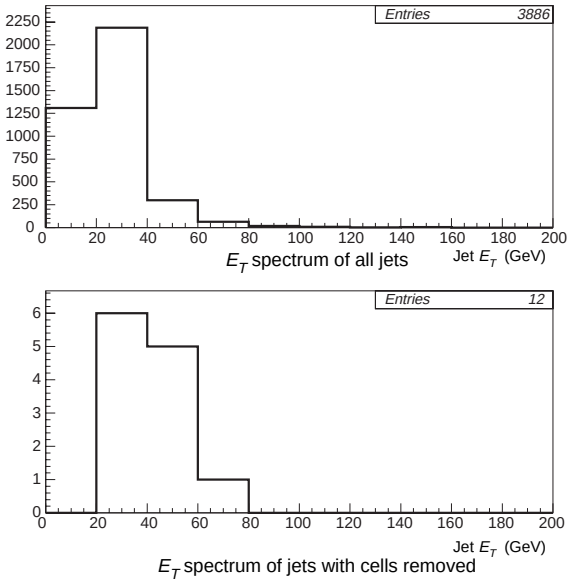

Figure 6.4: Jet E_T spectra for events with a good electron taken by `ele_1_mon`. The lower plot is the E_T spectra for jets that had a cell removed by `aida`. The jet E_Ts do *not* include the E_T of the removed cell.

of the entries. The solid line is a straight line fit to those points with slope and intercept shown in the solid lined box. To simulate the effects of `aida` removing cells from jets, each MC event (signal and background) is rejected with a probability determined by applying to each jet in the event the removed cell within jets frequency derived from the fit. With this procedure, about 5% of squark and gluino events are rejected.

Effect of Removed Cells from Jets on the Monte Carlo

One may ask why a Monte Carlo sample cannot be used to determine the hot cell within jets rate, since MC events without noise do not have real hot cells. The answer is that the detailed cell-by-cell structure of jets is not expected to be modeled correctly by showerlibrary Monte Carlo*, and thus the rate at which cells are removed by `aida` in Monte Carlo does not match the data. The discrepancy can be seen in Figure 6.5. The open circles are the fraction of jets that have a cell removed by `aida` in an `isajet` $t\bar{t}$

*In order to speed up the detector simulation program, a showerlibrary is used. Tens of thousands of calorimeter showers were simulated and placed in a library. When a particle is tracked into the simulated calorimeter for showerlibrary MC, the appropriate shower is pulled from the library and added to the event. The showerlibrary speeds up the detector simulation by more than a factor of 20.

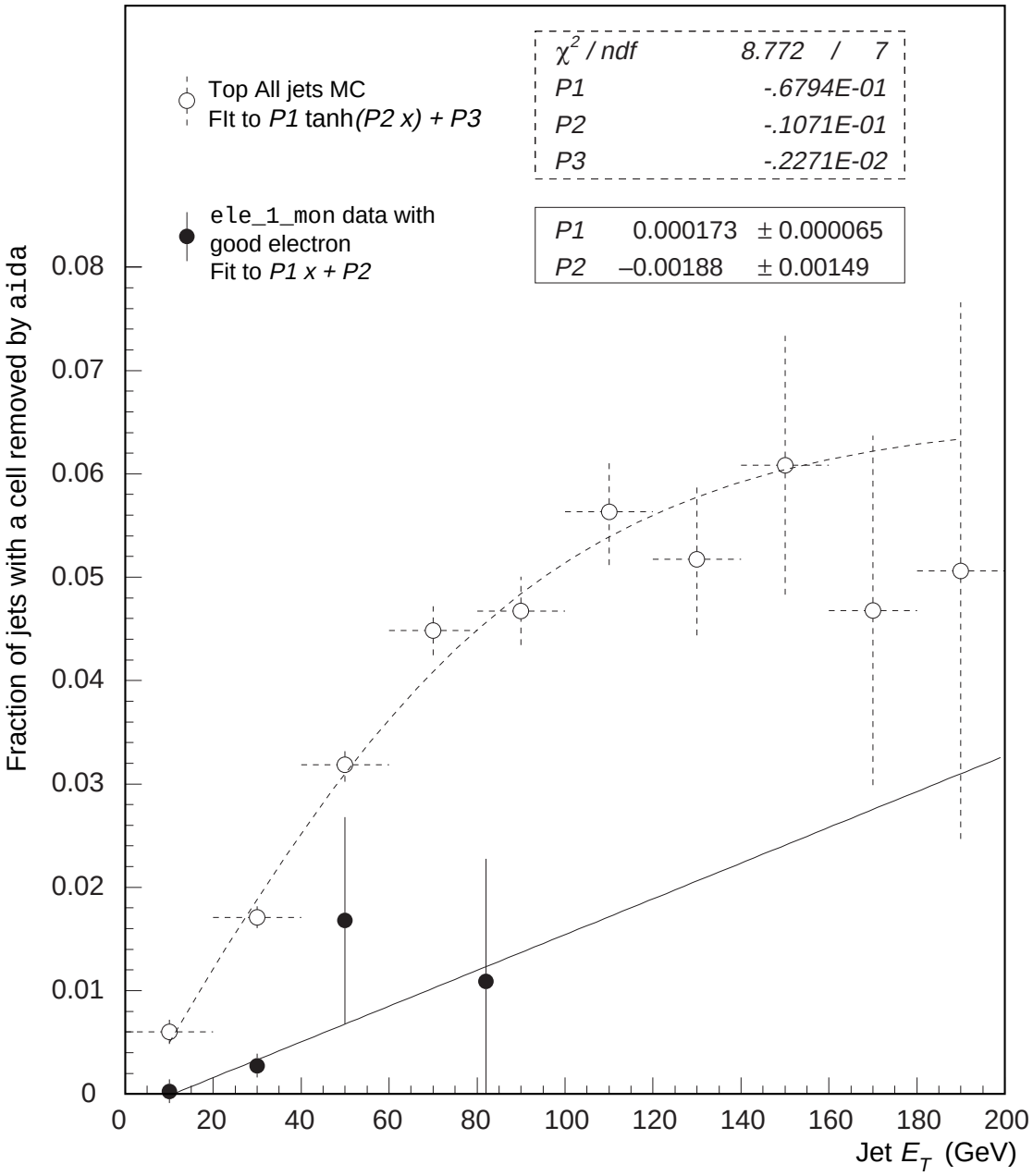

Figure 6.5: Hot cell in jets rate for data and Monte Carlo. Jet E_T does not include the hot cell E_T.

($M_t = 170$ GeV/c^2) sample where the top quarks always decay to jets. Such an all jets sample will have low intrinsic $\not\!\!E_T$. The Monte Carlo grossly overestimates the number of hot cells within jets. One is not even sure if the shape of the MC distribution is correct, since it is not suggested by the data.

Since `aida` is run on MC samples, there will be cells removed from jets. Clearly, any hot cell found in a Monte Carlo event with no noise added is a mistake by `aida`. Therefore, for all Monte Carlo samples cells removed from jets are added back into the event. Jet quantities and the $\not\!\!E_T$ are corrected accordingly.

One may worry that an entire jet can disappear when a cell containing most of its energy is removed and the remains of the jet has E_T below the reconstruction threshold of 8 GeV. An isolated hot cell in a Monte Carlo event would indicate an occurrence of this effect. Fewer than 1% of squark and gluino events passing the analysis requirements have such an isolated hot cell. Such events are deemed defective and are ignored (not counted in event tallies).

6.1.4 Jet–Missing Energy Correlations (Angular Cuts)

One instrumental background to the squark and gluino signature comes from QCD multijet events, where one or more jets are poorly measured creating missing transverse energy. This background can be reduced by examining the correlation between the directions of the jets and the $\not\!\!E_T$ vector. For example, if in a balanced event a jet's energy is mismeasured such that the jet becomes the leading jet, it will generate $\not\!\!E_T$ opposite to its direction (in ϕ). If a jet's energy is mismeasured low, it will tend to lie along the direction of the $\not\!\!E_T$. Figure 6.6 is a plot of $\phi_{\text{2nd jet}} - \phi_{\not\!\!E_T}$ vs. $\phi_{\text{Leading jet}} - \phi_{\not\!\!E_T}$ for QCD multijet events taken by the `jet85` filter, $t\bar{t}$ Monte Carlo events ($M_{\text{t}} = 170$ GeV/c^2), and two mSUGRA signal Monte Carlo samples. Events displayed were required to have at least three good jets with $E_T > 25$ GeV, no other bad jets with $E_T > 15$ GeV (see Section 6.1.7 for the good jet requirements), $\not\!\!E_T > 25$ GeV, and no removed cells from jets. Note the clumping of events in the corners of the QCD multijet plot due to poorly measured jets.

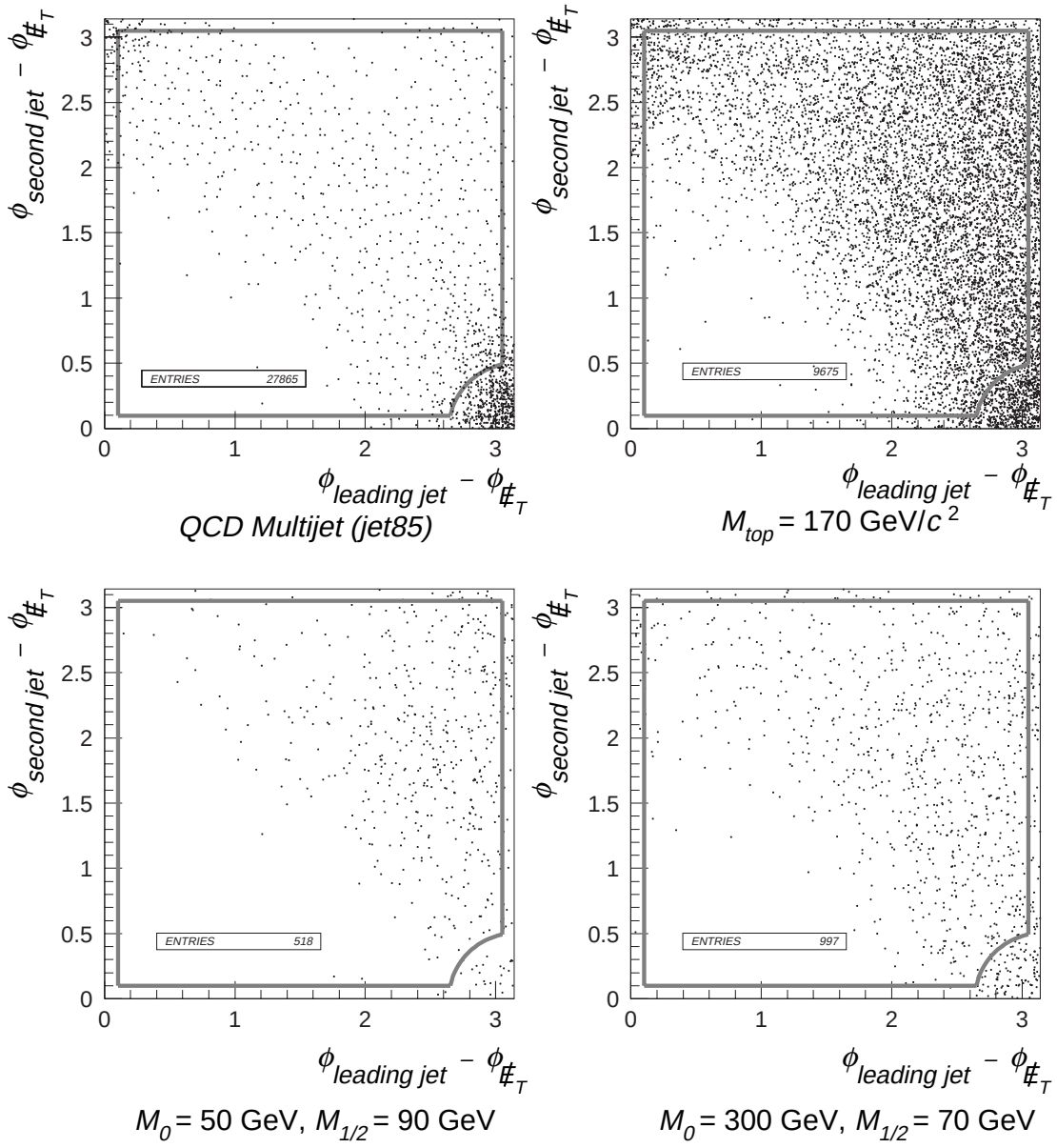

Figure 6.6: Jet – $\not\!\!E_T$ correlations. The angle differences are in radians. The solid line indicates the placement of the angular cuts described in the text. All samples were required to have three good jets, no bad jets, no removed cells from jets, and $\not\!\!E_T >$ 25 GeV.

Prezap	Postzap	
CF μ	CF μ	EF μ
$\lvert\eta\rvert < 1$	$\lvert\eta\rvert < 1$	$1 < \lvert\eta\rvert < 2.5$
`ifw4` ≤ 1	`ifw4` ≤ 1	`ifw4` $= 0$
$p_T > 15$ GeV		
`Hfrac` > 0.6 and `Efrac(H1)` > 0 or `Hfrac` $= 1$		
`ifw1` $\neq 5$		
$DR(\mu, \text{nearest jet}) > 0.5$		

Table 6.1: Requirements for muon rejection. An event will be rejected if it contains a muon meeting the criteria shown here.

No pronounced clustering of events is seen in any of the signal, top quark, or vector boson background Monte Carlo samples.

To eliminate the poorly measured QCD multijet events, an event is rejected if any jet with $E_T > 25$ GeV is either along or opposite in ϕ to the $\not\!\!E_T$ vector within 0.1 radian. In order to reject events where a fluctuation of the second jet masks the correlation with the leading jet, events are required to have $\sqrt{(\delta\phi_1 - \pi)^2 - (\delta\phi_2)^2} \geq 0.5$ where $\delta\phi_i$ is the azimuthal angle between the i^{th} jet and the direction of $\not\!\!E_T$. The placement of the cuts are displayed in Figure 6.6. An event falling outside of the heavy solid line is rejected. All of these angular requirements are applied to the signal and background Monte Carlo samples, but the background from QCD multijet events passing is estimated from data (see Section 6.3.2.1). This requirement is ~75% efficient for the squark and gluino signal.

6.1.5 Isolated Muon Veto

Since only squark and gluino events with hadronic cascade decays are sought, events with isolated muons are vetoed (electrons are vetoed with the good jet requirements discussed in Section 6.1.7). An event is rejected if it has a muon meeting the criteria in Table 6.1. These requirements are the standard loose muon criteria used by the Top group[91, 92] and are explained in more detail below.

Prezap/Postzap: Only CF muons ($|\eta| < 1$) are vetoed for the Prezap era (Run # $< 89{,}000$) when forward muon chambers suffered low efficiency due to accelerated aging.[93,94]

`ifw4` muon quality word: `ifw4` starts at zero and is incremented for each failure of the WAMUS muon track to meet the following quality criteria,[55]

- Every WAMUS module along the track contributes hits.
- Nonbend view impact parameter ≤ 100 cm.
- Bend view impact parameter ≤ 80 cm.
- Nonbend view track fit has hit residual RMS ≤ 7 cm.
- Bend view track fit has hit residual RMS ≤ 1 cm.

`MTC` quantities (`Hfrac` and `Efrac`): `MTC`[87] is a package run during reconstruction that performs muon tracking in the calorimeter. It starts by forming a 5 cell $\times$ 5 cell road centered about the muon track from WAMUS projected into the calorimeter. The road extends through all electromagnetic and hadronic layers. Tracking begins at the hit cell closest to the center of the road in the last layer of the calorimeter before the muon system. Hit cells in inner layers are added to the track if they are transversely offset by no more than one cell in η or ϕ compared to a hit cell in the layer above. If a layer has no hit cells meeting the neighbor criteria, the layer is skipped.

The `Hfrac` value is the fraction of hadronic layers that have a cell contributing to the muon track out of the total number of hadronic layers the track traverses.

Along with the standard 5 $\times$ 5 road, a 3 cell $\times$ 3 cell "core" road is also constructed. `Efrac(H1)` is the fraction of energy in the outer most layer of the calorimeter within the core road out of the total energy (sum of all layers) within the core.

The special case of `Hfrac` $= 1$ is to allow vetoing of muons with a very good track (a hit in every calorimeter layer) that lies outside the 3 cell $\times$ 3 cell core cone and fails the `Efrac(H1)` requirement.

Quadrant	Multiplicative Efficiency	
	`musmear` Postzap Monte Carlo	non-`musmear` MC
CF	0.937	0.815
EF	0.400	0.337

Table 6.2: Corrections to Monte Carlo muon efficiencies.[91, 92]

`ifw1` missed layer word: `ifw1` indicates if the muon is an "A–stub" with only hits in the first layer of WAMUS (A layer) before the toroid magnet. If `ifw1` $\neq 5$, then the muon is not an A–stub.

Isolation (DR): Squarks and gluinos may decay to b–quarks, which in turn may decay to muons that will appear within the b–jet. Therefore, only events with muons isolated from hadronic activity are rejected. A muon is considered isolated if its distance to the nearest jet is $DR > 0.5$ where DR is measured in $\eta \times \phi$ space.

The muon veto is applied to all signal and background samples. For Monte Carlo, there is a correction to the efficiency. If a muon meeting the requirements in Table 6.1 is found in a Monte Carlo event, the event to be rejected at a rate[91, 92] given in Table 6.2. Overall, these requirements are ∼90% efficient for the squark and gluino signal. 52% of a MC $W \to \mu\nu + \geq 3$ jets sample is rejected.

6.1.6 Missing Transverse Energy Requirement

Missing transverse energy is one of the key event quantities used in selecting squark and gluino events and reducing backgrounds. This analysis uses calorimeter $\not\!\!E_T$ after jet corrections (see Sections 5.4 and 5.6). The $\not\!\!E_T$ thresholds are optimized for each mSUGRA point that was tested. See Section 7.2 for details of the optimization procedure. The $\not\!\!E_T$ thresholds used are $\not\!\!E_T > 75$, 90, and 100 GeV. This requirement is applied to all signal and background Monte Carlo samples. Several example spectra from Monte Carlo are shown in Figure 6.7. Note that the $Z \to \nu\nu$ sample has a generator $\not\!\!E_T > 40$ GeV

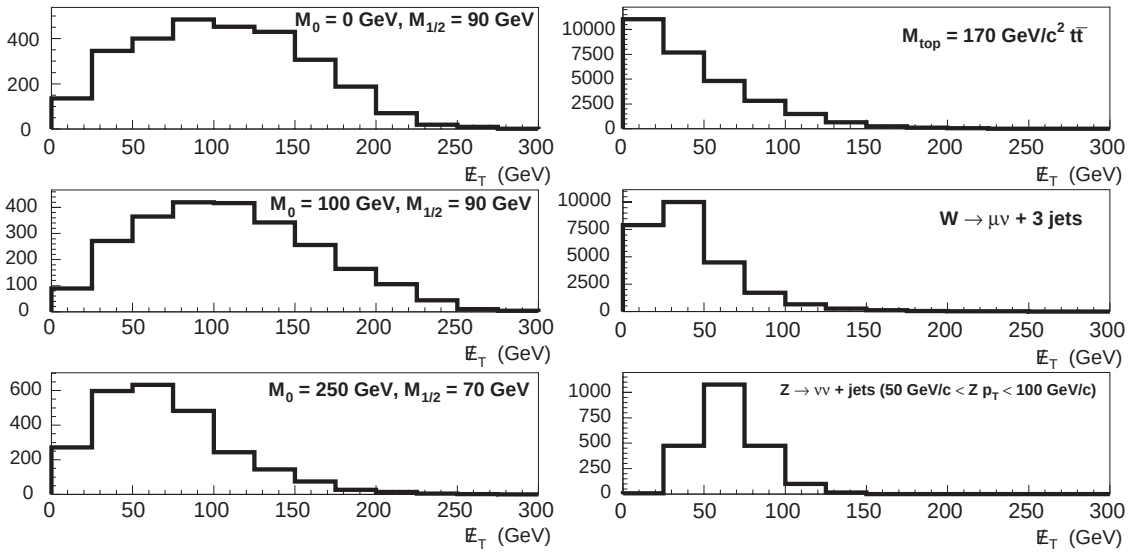

Figure 6.7: $\not\!\!E_T$ spectra. All distributions are from Monte Carlo. The upper right histogram is from a MC $t\bar{t}$ sample where the mass of the top quark is set to 170 GeV/c^2. The $Z \to \nu\nu$ sample has a generator $\not\!\!E_T > 40$ GeV requirement already applied as described in the text. The vertical axis scale reflects the number of events in the Monte Carlo sample.

requirement already applied.[†] $\not\!\!E_T$ spectra for some other signal samples were shown in Figure 3.6 on page 38.

6.1.7 Good Jet Requirements (Electron Veto)

Along with large $\not\!\!E_T$, the squark and gluino signature stipulates that such events should have a large jet multiplicity due to the cascade decays. To be as inclusive as possible while providing background rejection, the jet requirements are that an event must contain at least three good jets of corrected $E_T \geq 25$ GeV (backgrounds become unmanageable if only two jets are required). Jets of cone size 0.5 in $\eta \times \phi$ space are used for this analysis ($DR = \sqrt{(\Delta\eta)^2 + (\Delta\phi)^2}$). The 25 GeV requirement is placed beyond where the reconstruction of 0.5 cone jets is fully efficient.

A good jet must pass the clean jet requirements shown in Table 6.3, where EM fraction and CH fraction are the fraction of the jet's E_T deposited in the electromagnetic

[†]Generator $\not\!\!E_T$ is the negative vector sum over particle E_T as calculated by the event generator with no detector simulation and no resolution smearing.

$0.1 \leq$ EM Fraction	$\leq$	0.9
CH Fraction	$\leq$	0.4
$\lvert\eta\rvert$	$\leq$	3.5

Table 6.3: Good jet requirements.

and coarse hadronic layers of the calorimeter, respectively. The low end EM fraction requirement eliminates jets formed from hot cells in the hadronic calorimeter. The high EM fraction cut eliminates electrons and photons, since they deposit nearly all of their energy in the EM calorimeter. The calorimeter was built so that hadronic jets shower in the FH with the CH catching the tails. A jet showering predominately in the CH is in reality probably noise in a CH module or losses from the Main Ring accelerator, thus the purpose of the CH fraction requirement. The large η requirement assures that the jet is not extremely forward and close to the beam pipe. Figure 6.8 displays the number of good jets passing these requirements with $E_T \geq 25$ GeV for various signal and background samples. Distributions for several other mSUGRA samples were shown in Figure 3.7 on page 39.

The Monte Carlo efficiency for true good jets passing the good jet requirements matches the data (see Reference 95 for the data efficiencies). Overall, a good jet is $\sim$96% efficient.

Because of degraded jet energy resolution and lack of good EM coverage, events with the leading jet pointing to the intercryostat region ($1.1 \leq |\eta_{\text{detector}}| \leq 1.4$) are also rejected. This requirement is $\sim$88% efficient for the squark and gluino signal.

To further reduce contamination from bad jets, all jets in the event with $E_T > 15$ GeV are required to pass the good jet tests, or else the event is rejected. One effect of this cut is to eliminate events with poorly measured jets and events with $\not\!\!E_T$ due to main ring noise or many interactions that paste the inner calorimeter with energy. In this analysis, it also acts as a very efficient electron veto for electrons with $E_T > 15$ GeV. The signal is 75% to 85% efficient depending on the values of M_0 and $M_{1/2}$. The electron veto rejects 83% of a $W \to e\nu + \geq 3$ jets sample.

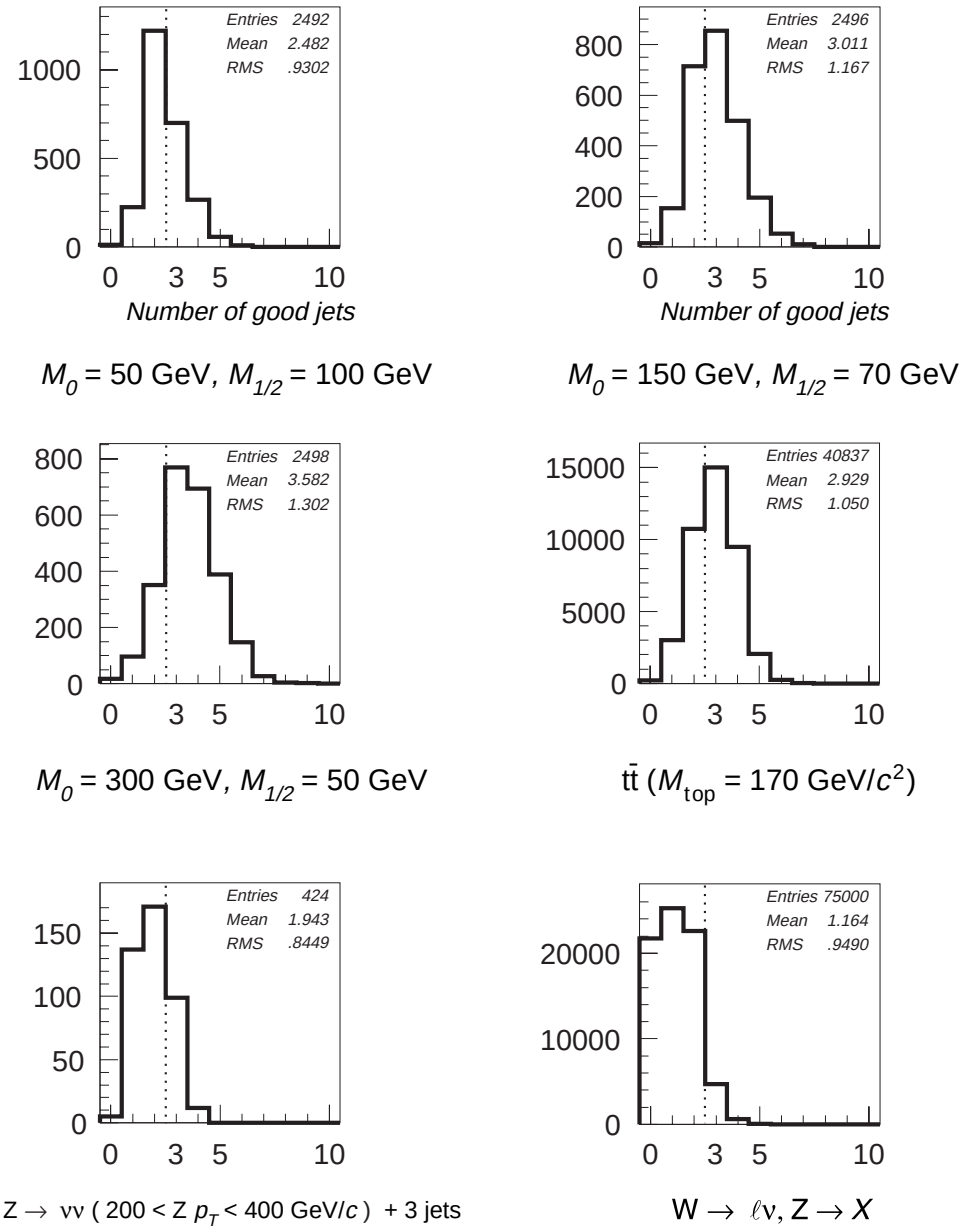

Figure 6.8: Number of good jets with $E_T > 25$ GeV. The dashed lines indicate the three jet requirement. The vertical scale reflects the number of events in the MC sample.

6.1.8 H_T Requirement

A large H_T requirement is used to reduce severely the Standard Model vector boson plus jets backgrounds. It is defined as follows,

$$H_T = \sum_{i=2}^{N} E_{T_{\text{jet } i}} \tag{6.1}$$

where the sum is over the number N of good jets with $E_T \geq 25$ GeV excluding the leading jet. The good jet requirements are the same as in Table 6.3 except that the Top group's requirement of $|\eta| \leq 2.5$ is applied (widening it to $|\eta| \leq 3.5$ makes no difference). An H_T requirement of at least 150 GeV is approximately 50% efficient for the signal for the worst case and reduces the vector boson background by nearly a factor of ten, leaving $t\bar{t}$ production as the dominant SM background. Shown in Figure 6.9 are histograms of H_T for various signal and background Monte Carlo samples. H_T distributions for several other signal samples were shown in Figure 3.9 on page 41.

Along with $\not\!\!E_T$, the H_T threshold is optimized for each signal point (see Section 7.2). H_T thresholds of $H_T >$ 100, 120, 140, 150, and 160 GeV are used.

6.1.9 Leading Jet E_T Requirement

A collider data sample of events passing the `jet85` filter (at least one Level 2 jet with $E_T > 85$ GeV) is used to determine the background from mismeasured QCD multijet events (see Section 6.3.2.1). `jet85` is the only sample suitable, since other jet triggers were heavily prescaled and have little collected luminosity or have undesirable extra requirements such as only passing events with a single interaction (such events will not have the same characteristics as candidate events passing the analysis filter). A leading jet E_T requirement of $E_T > 115$ GeV is applied in this analysis so that the QCD multijet background contributing to the data passing the `missing_et` analysis filter is described by the `jet85` model.

The $E_T > 115$ GeV threshold is set where the `jet85` filter is fully efficient as shown in Figure 6.10 (the `jet50` filter requires at least one Level 2 jet with $E_T > 50$ GeV). Leading jet E_T spectra for some mSUGRA points are shown in Figure 3.8 on page 40.

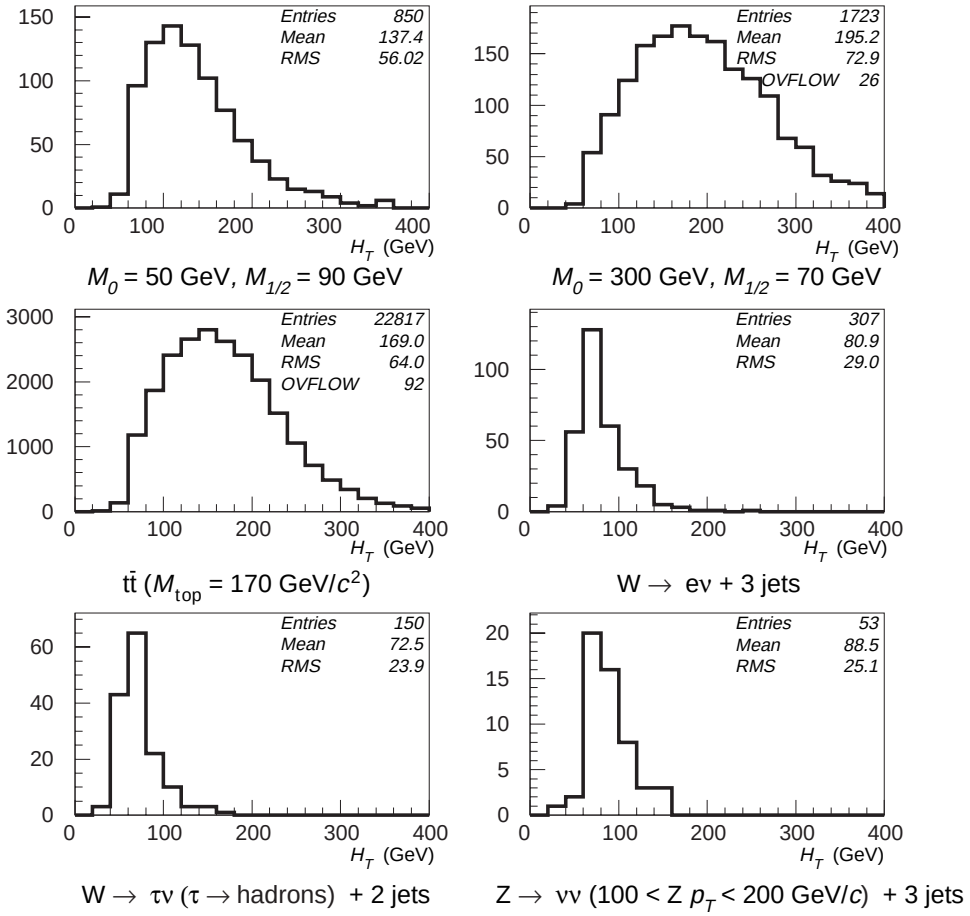

Figure 6.9: H_T spectra for signal and background Monte Carlo samples. 3 good jets are required.

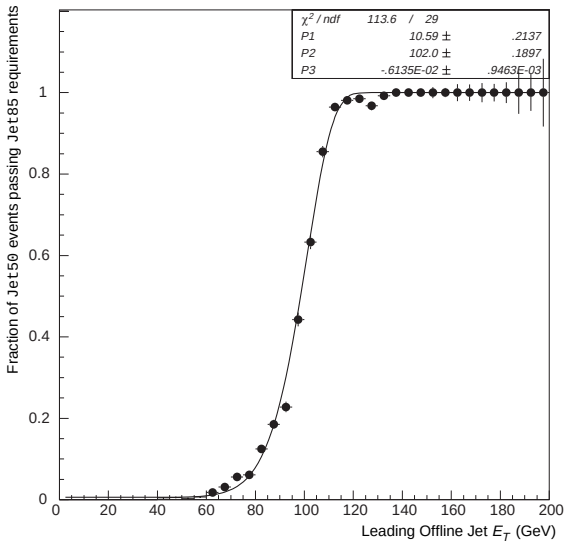

Figure 6.10: `jet85` turn on curve measured by the ratio of events taken by the `jet50` filter that pass `jet85` requirements. The parameterization is described in the text.

The turn on curve is best parameterized by the following formula:

$$\text{PassingFraction}(E_T) = 1 - e^{-\left(\frac{E_T}{P_2}\right)^{P_1} - P_3} \tag{6.2}$$

This requirement is applied to all signal and background samples. Its effect on some of those samples is shown in Figure 6.11.

6.1.10 Confirmation of the Primary Vertex

In the DØ searches for squarks and gluinos based on data from the 1992–1993 Tevatron run,[45, 46] it was discovered that some multiple interaction events contribute a large instrumental background to the squark and gluino signature. Such events are nearly always QCD multijet events with very low true $\not\!\!E_T$ but large measured $\not\!\!E_T$. The cause of the mismeasurement is misplaced vertices. As described in Section 5.8, if an additional min-bias event produces enough tracks, its interaction point will be assigned as the primary vertex from where the event is reconstructed. If the true hard scattering vertex is far enough from the misplaced primary vertex, the $\not\!\!E_T$ can be grossly mismeasured to a very high value.

These events with misplaced vertices are rare, but they are preferentially selected by this analysis due to the large $\not\!\!E_T$ requirement. The trigger and filter use `fastZ` and

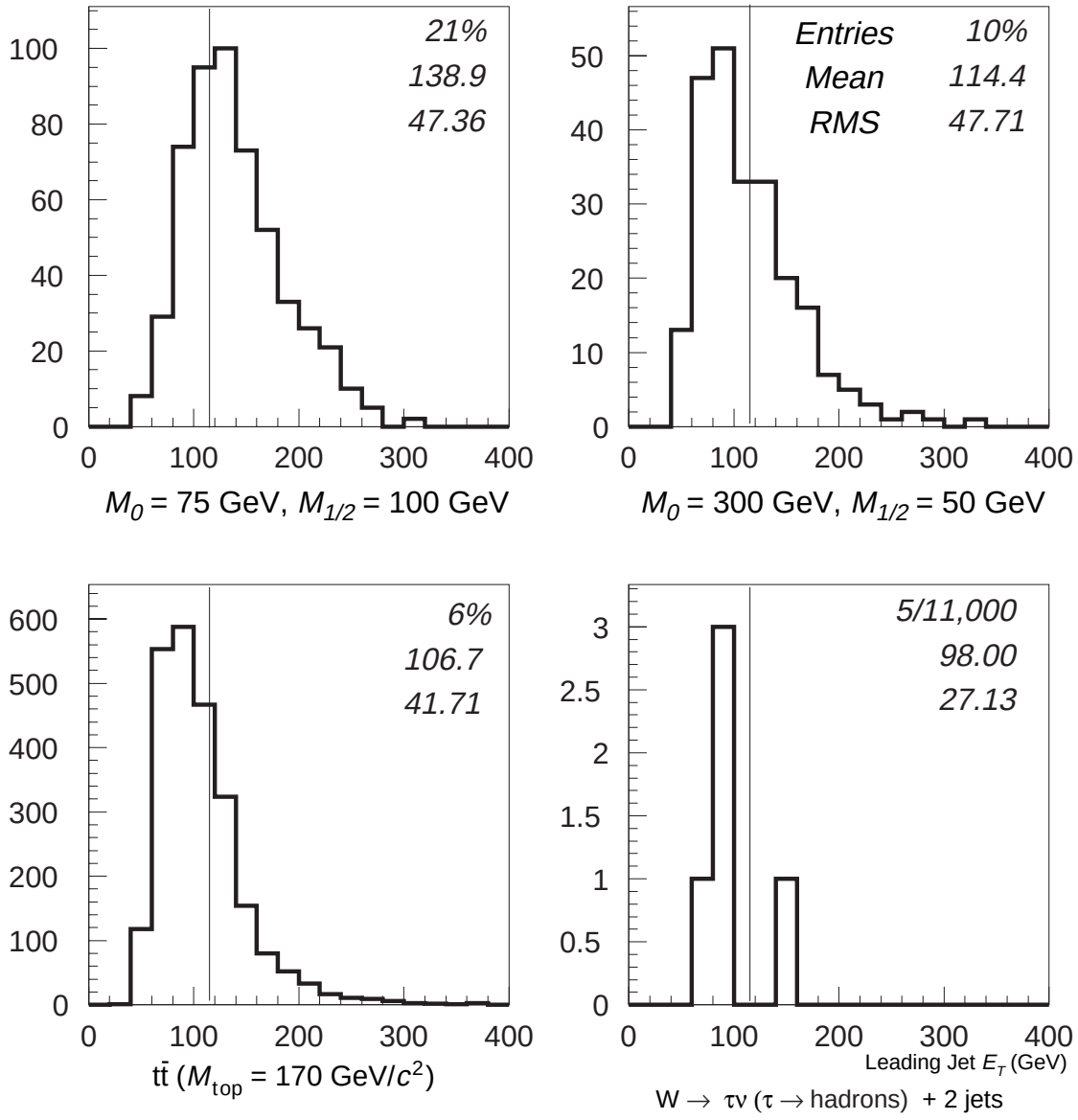

Figure 6.11: Leading Jet E_T after $\not\!\!E_T > 75$ GeV, $H_T > 100$ GeV, and 3 good jets with $E_T > 25$ GeV requirements are applied. The top number in each plot is the fraction of events surviving those requirements. The middle and bottom numbers are, respectively, the mean and RMS of the leading jet E_T distribution shown.

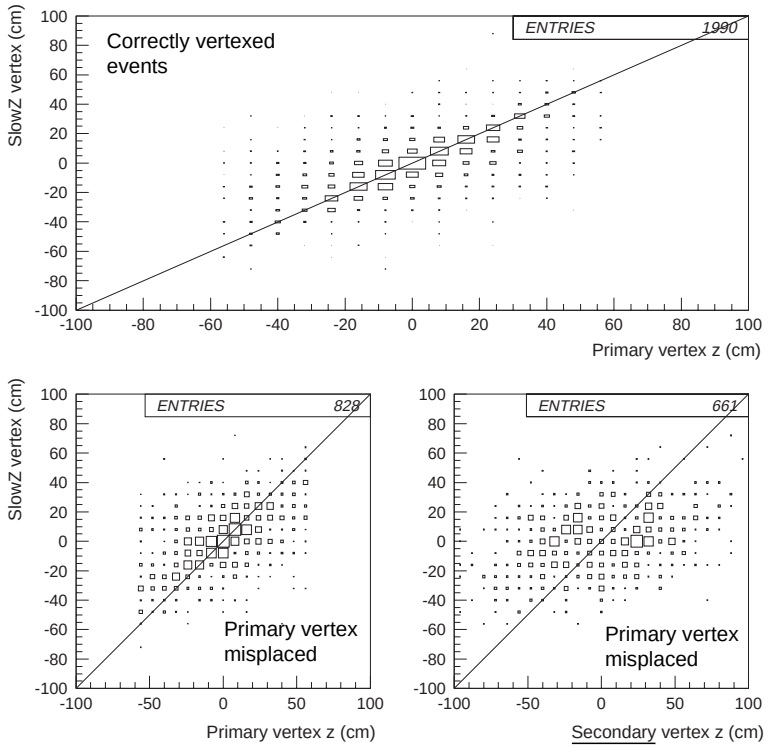

Figure 6.12: Trigger and offline vertex correlation. Data is from the `jet85` filter passing $\not\!\!E_T$ and H_T requirements. The top plot is for events passing jet pointing (described in the text). The bottom two plots are those events that fail. Note how `slowZ` and the incorrect primary vertex are still quite correlated.

`slowZ` vertices, respectively, which are generated by timing information from the level 0 hodoscopes, not the tracking system (`fastZ` and `slowZ` are described in Section 4.3.5.1). However, in events where the primary vertex is far from the true hard scattering vertex, the `fastZ`/`slowZ` vertex is still correlated with the incorrect primary vertex position as shown in Figure 6.12. Thus not only will the offline requirements accept these events, but the trigger will take them as well. Such balanced misvertexed events with large measured $\not\!\!E_T$ swamp the candidate sample.

The solution to this problem for the analyses based on the 1992–1993 Tevatron run data[37, 38, 45, 46] was to impose a single interaction requirement on the data using the multiple interaction tool (`mi_tool`).[96] Any event with `mi_tool` value over 2, indicating a probable multiple interaction, was rejected. This cut reduced the observed integrated luminosity from $\sim$13 pb^{-1} to $\sim$7 pb^{-1}, for a loss of just less than half of the data. In the

1993-1995 Tevatron run used for this analysis, the average instantaneous luminosity was much greater than in the previous run. Requiring only single interactions would result in discarding a much larger fraction of the collected luminosity (approximately 2/3).

Most multiple interaction events are not a problem; rather it is only those where the vertex has been misidentified that give rise to mismeasured large $\not\!\!E_T$ events and constitute the instrumental background. In order to eliminate such events, the leading E_T central jet is required to emanate from the *primary* vertex selected by `RECO`, and this confirms that vertex as the true interaction point of the hard scattering. This requirement is executed by using a technique for jet pointing[97] adapted and tuned for this analysis.

The procedure works in the following manner. Tracks within $DR = 0.4$ (in $\eta \times \phi$ space) of the axis of the leading E_T central jet projected into the Central Drift Chamber (CDC) are marked as associated with that jet. The origin of each of those tracks is determined by extrapolating them to the z axis (at $r = 0$). If a track extrapolates to within 10 cm of a reconstructed vertex, it is recorded as emanating from that vertex. An event will be rejected if the leading E_T central jet does not confirm the primary vertex as stipulated by the following criteria,

- The primary vertex is not confirmed if there are no tracks associated with the leading E_T central jet or none of the tracks emanate from any reconstructed vertex. In the latter case, one has no faith that the primary vertex is correct. If no tracks are found close to the jet, as in the former case, it is unclear how the primary vertex was even determined.

- The primary vertex is not confirmed if 50% or more tracks associated with the leading E_T central jet emanate from a different vertex.

- The primary vertex is not confirmed if half or more of the tracks associated with the leading E_T central jet emanate from $|z| > 60\,\mathrm{cm}$. This requirement handles the case where the true interaction point falls in the region where vertex finding is less efficient or outside of the region where vertices are reconstructed.

Because full tracking is only performed for the CDC, only central jets can be used for this jet pointing technique. Using only the leading E_T central jet is sufficient to confirm the primary vertex and retains high signal efficiency. Nearly 100% of squark and gluino events have at least one central jet. Requiring a second central jet has an efficiency of approximately 90%.

This requirement is performed last in the analysis because more event information is needed than what is available on compressed data files.

Details of Jet Pointing

In order to tune the jet pointing procedure and determine its efficiency, a QCD jet data sample is needed. The goal is to keep the probability of rejecting a correctly vertexed event small while reducing as much of the misvertexed events background as possible.

Since activity in the CDC increases as the instantaneous luminosity increases, the jet pointing method will fail good events more often in periods of high instantaneous luminosity. Therefore, a sample of events is needed at a variety of instantaneous luminosities to measure the luminosity dependent efficiency. Ideally, one would like to use a sample with a low E_T jet trigger threshold so that the cross section for production of SUSY particles will be negligible compared to the QCD cross section. Unfortunately, the filter with the lowest threshold, `jetmin`, was heavily prescaled and eliminated altogether after about 3/4 of 1993-1995 run. Other slightly higher threshold jet triggers appeared for only a short time or included a Level Zero single interaction requirement. The only jet triggers that are usable are `jet85` (one level 1 large tile over 35 GeV as well as two large tiles over 6 GeV; level 2 jet over 85 GeV) and `jetmax` (one large tile with E_T over 45 GeV and two large tiles over 10 GeV at level 1; level 2 jet over 115 GeV). Fortunately, it appears that jet spectra of the leading jet from squark and gluino events resemble the leading jet spectra from these filters, as shown in Figure 6.13. Events from these filters containing at least three good jets are used to tune and determine the efficiency of jet pointing. One still expects the SUSY cross section to be tiny compared to QCD when examining events at the low end of the $\not\!\!E_T$ spectrum.

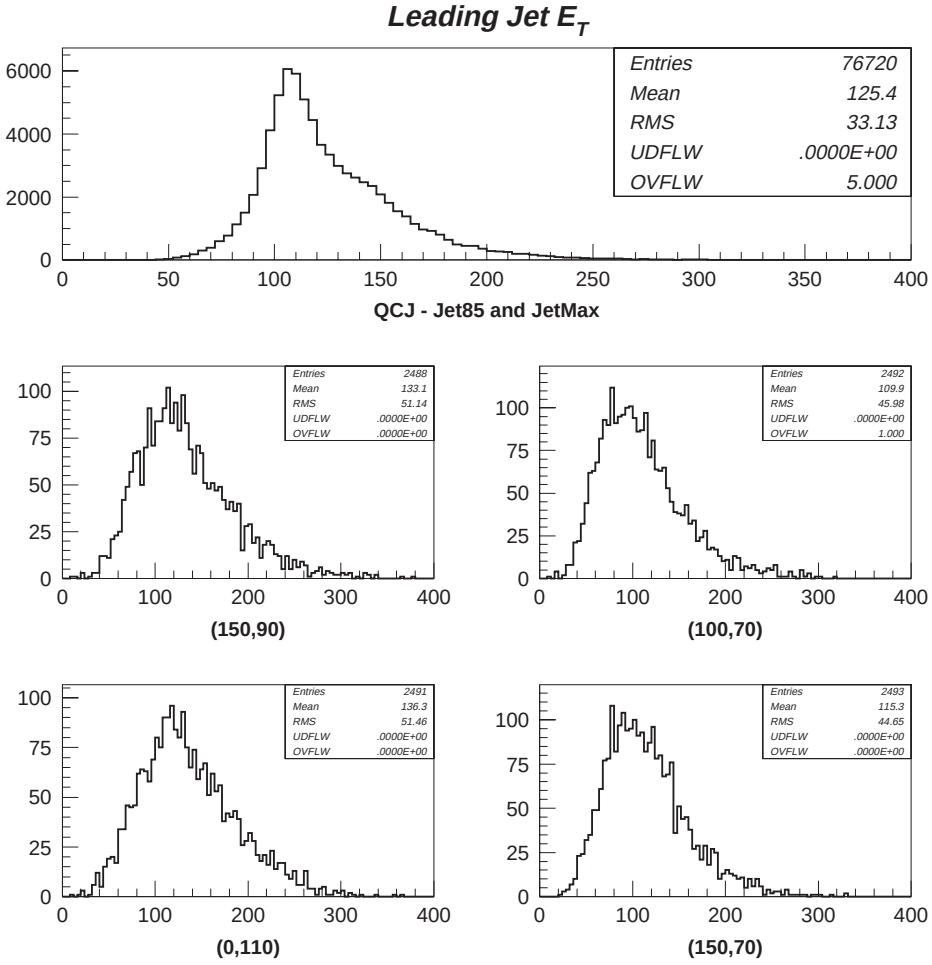

Figure 6.13: Leading jet E_T spectra. The lower four plots are from mSUGRA MC samples with $(M_0, M_{1/2})$ as denoted.

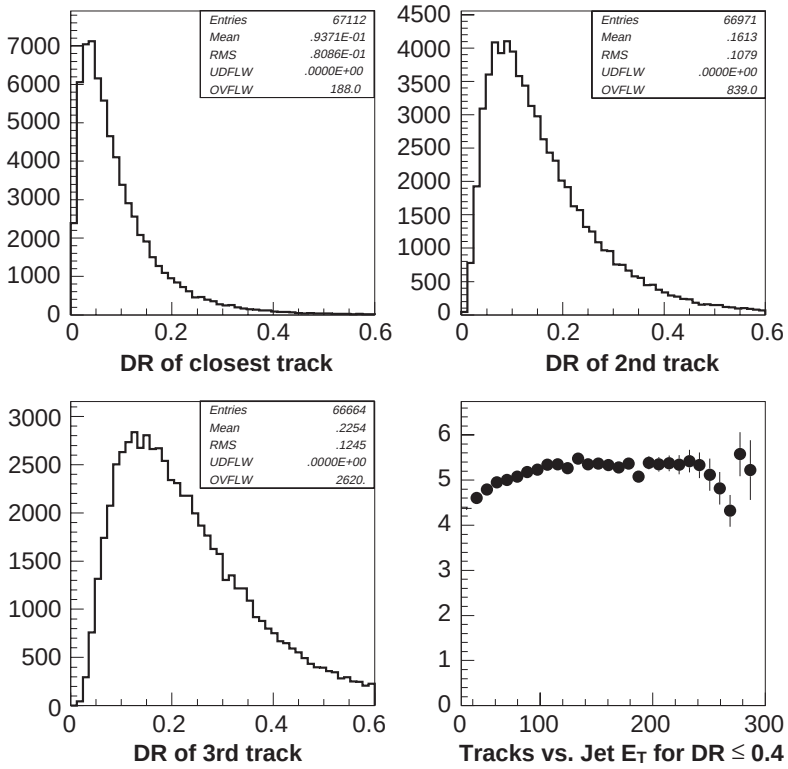

Figure 6.14: Jet – track matching. The first three plots show how close tracks come to the jet axis in $\eta \times \phi$ space. The vertical scale reflects the number of events in the data sample. The lower right plot displays the average number of tracks found in a $DR = 0.4$ cone about the jet axis vs. jet E_T in GeV.

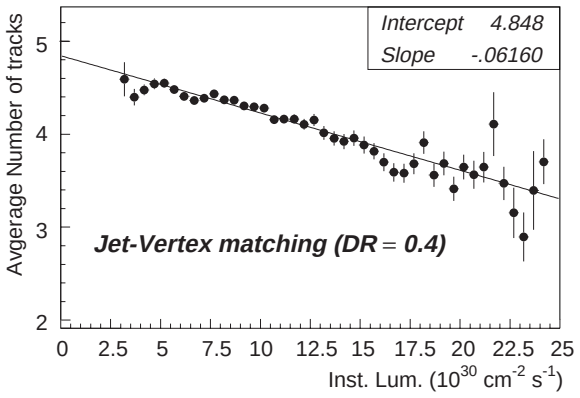

Figure 6.15: Average number of tracks in jets vs. instantaneous luminosity.

As mentioned, the jet pointing method involves drawing a cone about the jet axis extrapolated into the CDC tracking volume. Any good track found within this cone is associated with that jet. Tracks are bad if they have no $r-z$ view (tracking is done in $r-\phi$ first, then $r-z$), have only two or fewer hits, have a bad χ^2 from fitting the hits, or have an $x-y$ impact parameter indicating that the track emanates from outside of the beam pipe. Figure 6.14 shows histograms of the distance that the closest, next closest and third closest tracks come to the jet axis. The jets are only from the central region ($|\eta_{\rm detector}| < 1.1$). A cone size of $DR = 0.4$ about the jet axis, where DR is the distance in $\eta \times \phi$ space, is appropriate to associate tracks with 0.5 cone jets. Enlarging the tracking cone increases the probability that a stray track will be associated with the jet and thus will decrease the jet pointing efficiency.

The bottom right plot of Figure 6.14 shows the average number of tracks associated with a jet (found within the $DR = 0.4$ cone) vs. jet E_T. One would expect to find more tracks within higher E_T jets, since they are made up of more particles than jets of low E_T. The plot does not show that behavior and seems to indicate that the CDC and/or tracking algorithm saturates if too many particles are present. Further indication of this saturation effect can be seen in Figure 6.15, showing the average number of tracks associated with the leading E_T central jet vs. instantaneous luminosity.

Now that the size of the cone to use for associating tracks is set, the efficiency of the jet pointing requirement must be determined. Multiple interactions are not included

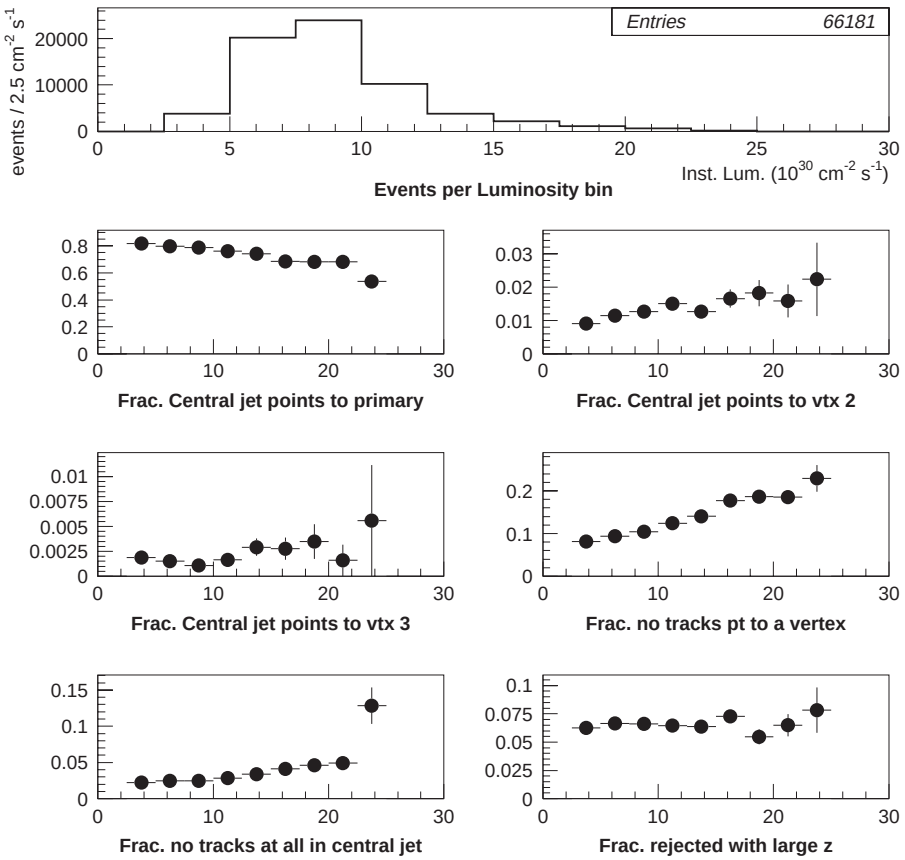

Figure 6.16: Efficiency of jet pointing. Plots are described in the text.

in the Monte Carlo samples, and the MC tracking efficiency is probably too high to accurately model high occupancy regions of the CDC, therefore the QCD multijet data (from `jet85` and `jetmax`) are used to determine the jet pointing efficiency. Events from the QCD multijet sample are required to have at least three good jets (see the good jet requirements in Section 6.1.7) and $\not\!\!E_T < 25$ GeV. The requirement of low $\not\!\!E_T$ is used to assure that the events examined are less likely to suffer from misvertexing, since the efficiency should indicate how often correctly vertexed events are mistakenly rejected by the jet pointing procedure. This efficiency is shown vs. instantaneous luminosity in the plots displayed in Figure 6.16.

The top histogram in Figure 6.16 shows the instantaneous luminosity distribution for the QCD multijet events (after the good jet and low $\not\!\!E_T$ requirements are applied). The remaining plots show the fraction of events in each luminosity bin yielding a particular

outcome of the jet pointing algorithm. The fractions for the same luminosity bin sum across the plots to one.

- Upper left plot: fraction of events where the primary vertex is confirmed, because the tracks in the central jet point to the primary vertex. Events shown here pass the jet pointing requirement, and the fractions are thus the efficiency of jet pointing vs. instantaneous luminosity. All events in the other plots fail jet pointing.
- Upper right: fraction of events where the jet had more tracks emanating from the secondary vertex than the primary.
- Middle left: fraction of events where the jet had more tracks emanating from the tertiary vertex than the primary. Only a few events have three vertices found.
- Middle right: fraction of events where none of the tracks associated with the jet point to a reconstructed vertex.
- Lower left: fraction of events where no tracks could be associated with the leading E_T central jet.
- Lower right: fraction of events where the jet had half or more of its associated tracks emanating from beyond $|z| = 60$ cm.

The jet pointing efficiency ranges from 82% for very low instantaneous luminosity to 68% for very large instantaneous luminosity (the last two bins displayed in the efficiency plots are for instantaneous luminosities where a minuscule amount of data was collected). When the luminosity profile of the data run (integrated luminosity vs. instantaneous luminosity, see Figure 6.20) is taken into account, the jet pointing method is 80% efficient overall.

Figure 6.17 shows at some level the effectiveness of the jet pointing procedure. The data come from a `jet85` QCD multijet sample passing most of the analysis cuts (except $\not\!\!E_T$ and leading jet E_T). The log plot shows three $\not\!\!E_T$ spectra, normalized to the first two bins. The open circles denote the spectrum for all events. The open triangles are for events passing the single interaction requirement of `mitool` < 2. Note that only a small

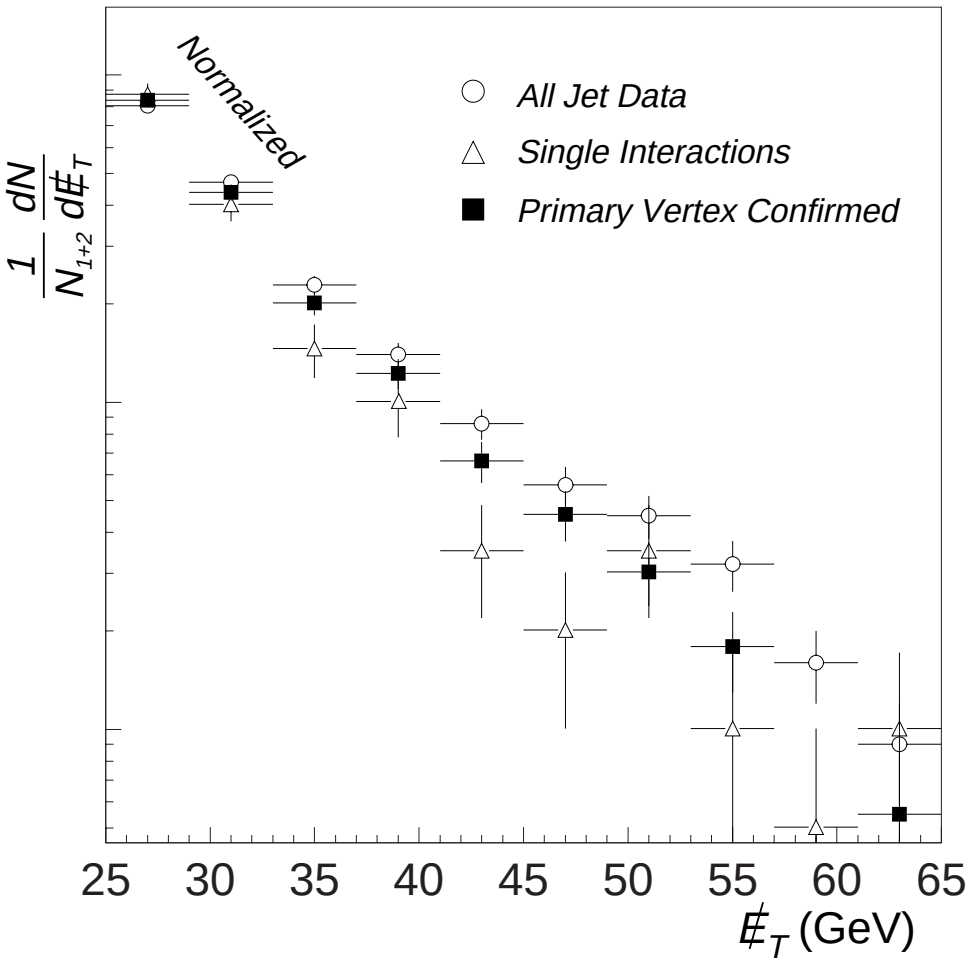

Figure 6.17: Effectiveness of jet pointing. The curves are normalized to the first two bins.

fraction of the data passes this condition, as seen by the large error bars on the single interaction points. The filled squares are the data passing the jet pointing algorithm. At low $\not\!\!E_T$, all three types of points track together. As $\not\!\!E_T$ increases, the "all data" points develop the enhanced tail due to the misplaced vertex events. The "pass jet pointing" points tend to lie well below the "all data" points for large $\not\!\!E_T$.

The expected background, that is misvertexed events that pass the jet pointing requirement, is not explicitly determined since such events will contribute to the calculated QCD multijet background (see Section 6.3.2.1). An examination of the final event sample yielded no such mistakes by the jet pointing algorithm, indicating that the background is probably quite small.

6.2 Collider Data

Now that the analysis requirements are set, the number of events passing in the collider data can be examined. The data taken for this analysis correspond to an integrated luminosity of 79.2 pb^{-1}. Data were collected by an unprescaled filter and then streamed into manageable file sets. The analysis event criteria were applied to the data and yielded 49 events from the loosest $\not\!\!E_T$ and H_T requirements ($\not\!\!E_T > 50$ GeV and $H_T > 100$ GeV).

6.2.1 Trigger and Filter

Events were collected for this analysis with the `missing_et` trigger and filter. This trigger was not prescaled at any time. The requirements of the trigger and filter are,

Level 1: L1 $\not\!\!E_T > 40$ GeV and at least one calorimeter trigger tower with $E_T > 5$ GeV and $|\eta_{\text{detector}}| < 2$

Level 2: L2 $\not\!\!E_T > 40$ GeV

Level 1 calculates $\not\!\!E_T$ from trigger towers within $|\eta_{\text{detector}}| < 1.6$, and does not include energy in the ICD and CH layers of the calorimeter. Since the CH is excluded, the `missing_et` trigger will not usually fire on events with only negative energy. Level 2

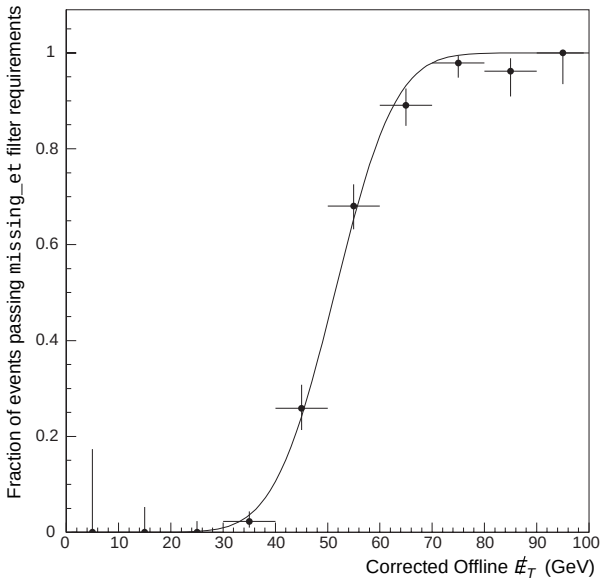

Figure 6.18: Turn on curve for the `missing_et` trigger from the "jet erasure" procedure.

uses the entire calorimeter for its calculation and may remove at most one cell flagged as hot by the hot cell killer (see Section 6.1.3). The trigger also requires `good_beam`, which means that the trigger is inhibited from taking data while the Main Ring is in injection or transition (`MRBS_LOSS`) or while Main Ring protons are passing through the DØ calorimeter (`MICRO_BLANK`).

Figure 6.18 shows the turn on curve for the `missing_et` filter. Obtaining a turn on curve for $\not\!\!E_T$ is nontrivial since there are many sources of $\not\!\!E_T$ in events, including instrumental ones. One would like to measure the turn on characteristics for events with true $\not\!\!E_T$ caused by physics processes, such as neutrinos. Two procedures are used.

One method[98] is used to generate the curve in Figure 6.18. The procedure is to take balanced multijet events collected by QCD jet triggers and replace one jet cell by cell with calorimeter noise. This "erases" the jet from the event, generating $\not\!\!E_T$ as if the jet were a neutrino. The altered events are then passed through `RECO` (version 12.20) and the trigger simulator (version 7.08). Finally, the jet corrections are applied to the remaining jets and the $\not\!\!E_T$. The trigger simulator was designed to mimic exactly the online Level 1 and Level 2 systems, giving the $\not\!\!E_T$ that Level 1 and Level 2 would have seen. Figure 6.18

displays the fraction of events passing the `missing_et` trigger and filter requirements vs. corrected calorimeter $\not\!\!E_T$.

The other method involves a sample with high p_T muons. Since muons pass through the calorimeter leaving little energy, they generate calorimeter $\not\!\!E_T$. The statistics for the muon sample are very small, but the turn on curve is consistent with what is measured by the jet erasure method.

As seen in Figure 6.18, the `missing_et` filter is fully efficient at ~75 GeV. The curve is parameterized by the function,

$$f(\not\!\!E_T) = \frac{1}{2}\left[\mathrm{erf}\left(\frac{\not\!\!E_T - x_0}{\sqrt{2}\sigma}\right) + 1\right] \tag{6.3}$$

The fit parameters are,

$$x_0 = 51.4 \pm 0.4$$

$$\sqrt{2}\sigma = 12.9 \pm 1.4$$

The χ^2 is 0.5 per degree of freedom.

The parameterization of the `missing_et` turn on curve is only used to calculate background estimates for $\not\!\!E_T < 75$ GeV which only serve as checks. Since the QCD multijet background rises dramatically in between $\not\!\!E_T = 50$ and 75 GeV, the optimized $\not\!\!E_T$ thresholds are always > 75 GeV where the trigger is fully efficient.

6.2.2 Applying Analysis Requirements to the Data

All data were reconstructed with version 12 of the DØ reconstruction program (`RECO`). The jet and $\not\!\!E_T$ corrections were applied with the `cafix` v5.0 software package.[88] Table 6.4 shows the effects of each of the analysis requirements on the data. The initial sample comes from the `run1b_np_met dødad` stream. A stream is a set of files containing events passing one or more specific filters. `dødad` streams are files of run and event pointers, allowing direct access to event files. The `run1b_np_met dødad` stream contains pointers to all events passing the `missing_et`, `scalar_et`, and `jet_1_miss` filters.

Some events from the `run1b_np_met dødad` stream meeting loose requirements are extracted to a smaller file that can be managed more easily. The initial selection require-

Analysis Requirement	*Events remaining*
Events in `run1b_np_met` stream	1,628,939
Events passing initial selection ($\not\!\!E_T > 40$ GeV, 2 jet banks)	682,399
Pass `missing_et` filter	173,724
$0 < E_T^{\rm scalar} < 1800$ GeV	171,270
$-60 \leq$ primary vertex z position ≤ 60 cm	150,828
No cells removed from jets	118,762
All jets of $E_T > 15$ GeV pass good jet requirements	79,190
Leading jet not pointing towards ICR	71,023
At least 3 jets with $E_T > 25$ GeV	9,012
Jets not correlated with $\not\!\!E_T$ vector	2,838
$\not\!\!E_T > 50$ GeV	1,218
$H_T > 100$ GeV	418
Leading jet $E_T > 115$ GeV	136
No isolated muons with $E_T > 15$ GeV	135
Leading E_T central jet confirms primary vertex	**49**

Table 6.4: Analysis requirements on the data. The initial selection criteria are described in the text.

ments are that events must have corrected $\not\!\!E_T > 40$ GeV and at least two jet banks (any quality jets with E_T over 8 GeV). Note that the `missing_et` filter requirement was not made when filling the initial selection file to make it more usable to others.

A summary of the number of events passing for different $\not\!\!E_T$ and H_T thresholds is shown in Table 6.5. Some distributions of the data passing the analysis requirements are shown in Figure 6.19. The points with $\not\!\!E_T$ threshold of 50 GeV are used only as checks and do not contribute to the final results of the analysis.

6.2.3 Luminosity

The observed luminosity is determined by running the production data base utilities over the list of data files that were examined in the analysis. The total luminosity seen by the `missing_et` trigger is 84.3 pb^{-1}. 3.4 pb^{-1} of luminosity from runs flagged as "bad" are

$\not\!\!E_T >$ (GeV)	$H_T >$ (GeV)	Candidates	$\not\!\!E_T >$ (GeV)	$H_T >$ (GeV)	Cand.
50	100	49	50	150	31
75	100	15	75	120	12
75	140	11	75	150	8
75	160	6	90	100	8
100	100	7	100	150	3

Table 6.5: Number of candidate events passing all requirements with varying $\not\!\!E_T$ and H_T thresholds.

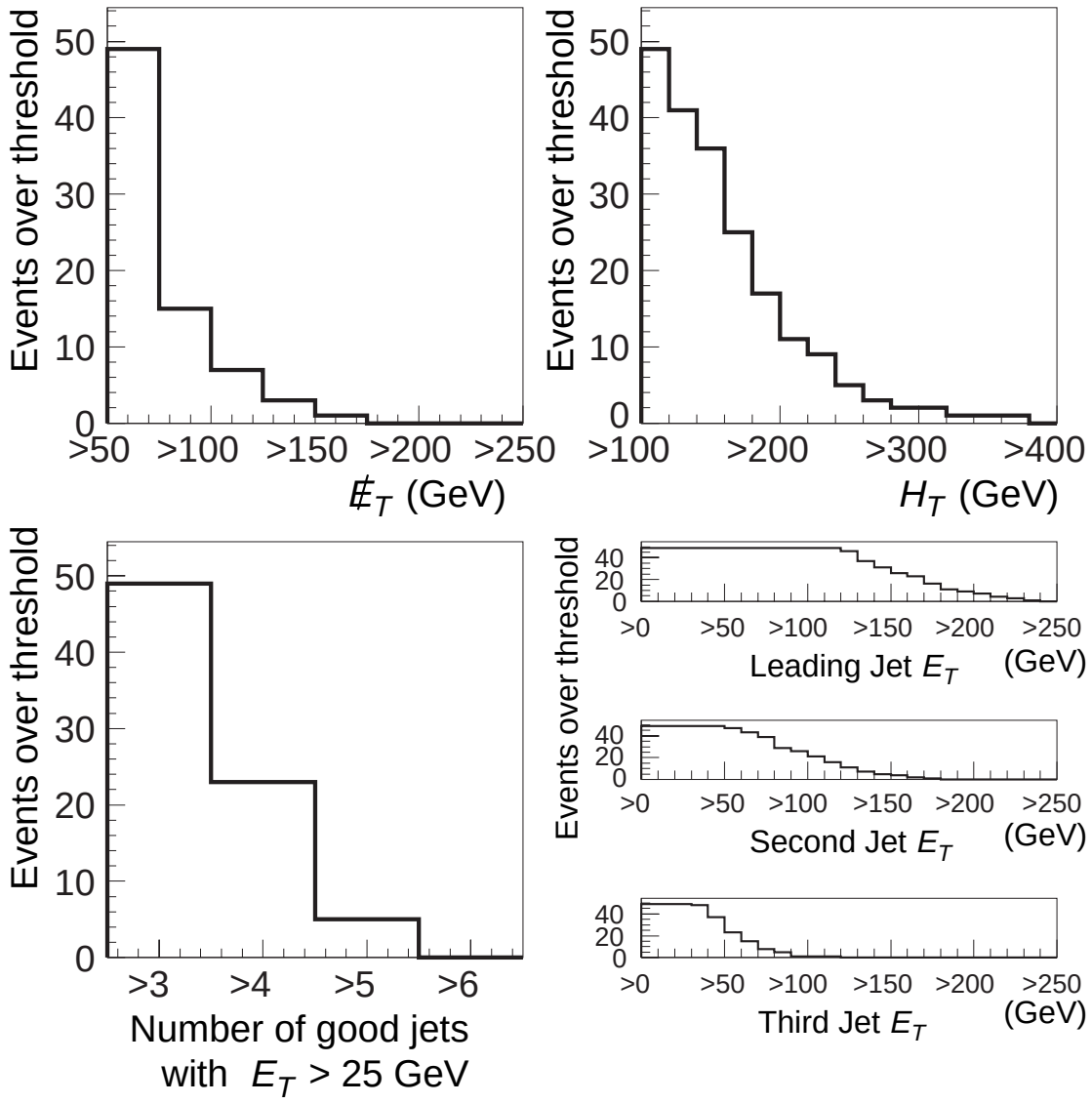

Figure 6.19: Integrated distributions of $\not\!\!E_T$, H_T, jet E_T, and the number of jets for `missing_et` data passing analysis requirements with $\not\!\!E_T > 50$ GeV and $H_T > 100$ GeV.

missing_et	jet85	jet50
79.2 ± 4.2 pb^{-1}	55.9 ± 3.0 pb^{-1}	4.7 ± 0.2 pb^{-1}

Table 6.6: Luminosity for triggers used in this analysis.

subtracted as well as 1.6 pb^{-1} from files that dødad failed to locate. 79.2 pb^{-1} remains. A summary of the luminosity information is given in Table 6.6. The systematic error on the luminosity is 5.3%.[99]

A plot of the instantaneous luminosity profile is given in Figure 6.20. The average instantaneous luminosity for the 1993–1995 run for events collected in the missing_et stream is 8.76×10^{30} cm^{-2} s^{-1}.

6.3 Background Estimation

A disadvantage of the jets and missing energy signature for squarks and gluinos is the large background. Section 6.1 describes the requirements on the analysis designed to reduce the backgrounds as much as possible while still retaining signal efficiency. There are two types of background sources: those with $\not\!\!E_T$ due to one or more neutrinos produced in the event and those with $\not\!\!E_T$ from purely instrumental effects. Many background sources are considered. A summary of the background estimates are shown in Tables 6.9 through 6.18.

6.3.1 Physics Backgrounds

The examined SM processes that have $\not\!\!E_T$ due to one or more neutrinos in the final state are:

- $t\bar{t}$ decays
- $W \to e\nu$ + jets
- $W \to \mu\nu$ + jets
- $W \to \tau\nu$ + jets, $\tau \to \ell\nu$

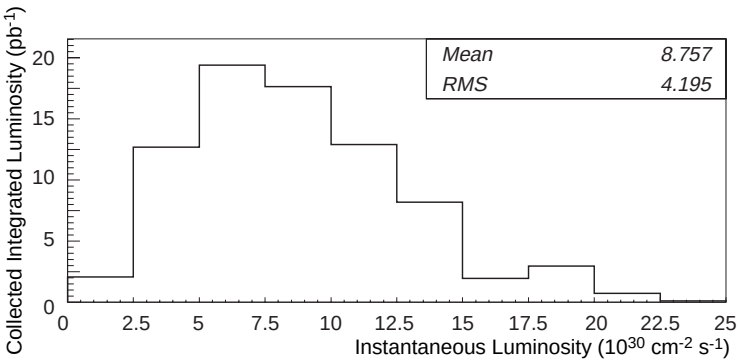

Figure 6.20: Luminosity profile for the `missing_et` trigger.

- $W \to \tau\nu$ + jets, $\tau \to$ hadrons
- $W \to \ell\nu$, $Z \to X$
- $W \to \ell\nu$, $W \to qq'$
- $Z \to \tau\tau$ + jets
- $Z \to \nu\nu$ + jets

The background summary tables indicate the background estimates for different $\not\!\!E_T$ and H_T requirements.

The analysis requirements are applied to all background Monte Carlo samples. Events where `aida` removed a cell from a jet are corrected by putting the cell back into the event and adjusting the jet quantities and $\not\!\!E_T$ accordingly. Events that have an isolated hot cell, indicating that a jet was lost to the hot cell killer, are not counted. Furthermore, the removed cell efficiency as described in Section 6.1.3 is applied to all Monte Carlo events. A summary of the background Monte Carlo information is given in Table 6.7. Each background is discussed in subsequent sections. All Monte Carlo samples produced were processed by the detector simulation program and the same `RECO` program as used on the data.[‡]

[‡] `showerlibrary geant` version 3.14 and 3.15[100,101] and `RECO` v12.

Process	σ (pb)	$\pm\delta\sigma$ (pb)	MC events generated
$t\bar{t} \to X$	5.77	1.72	39512
$W \to e\nu + \geq 3$ jets	95.67	28.70	18052
$W \to \mu\nu + \geq 3$ jets	95.67	28.70	18205
$W \to \tau\nu + \geq 3$ jets, $\tau \to \ell\nu$	34.15	10.24	6665
$W \to \tau\nu + \geq 2$ jets, $\tau \to$ hadrons	173.82	34.76	11165
pair $W \to \ell\nu$, $W \to qq'$	5.54	1.66	47579
pair $W \to \ell\nu$, $Z \to X$	0.32	0.10	48121
$Z \to \mu\mu + \geq 3$ jets	3.19	0.96	11987
$Z \to \tau\tau$, $25 < Z\,p_T < 50$	18.50	5.55	11932
$Z \to \tau\tau$, $50 < Z\,p_T < 100$	4.10	1.30	2971
$Z \to \tau\tau$, $100 < Z\,p_T < 200$	0.48	0.14	988
$Z \to \tau\tau$, $200 < Z\,p_T < 400$	0.02	0.006	982
$Z \to \nu\nu$, $25 < Z\,p_T < 50$	70.00	21.00	39929
$Z \to \nu\nu$, $50 < Z\,p_T < 100$	20.00	6.00	9976
$Z \to \nu\nu$, $100 < Z\,p_T < 200$	2.50	0.75	999
$Z \to \nu\nu$, $200 < Z\,p_T < 400$	0.08	0.02	981

Table 6.7: Background Monte Carlo Generation. Cross sections and errors are shown for all processes generated with Monte Carlo. Events with hot cells are not counted.

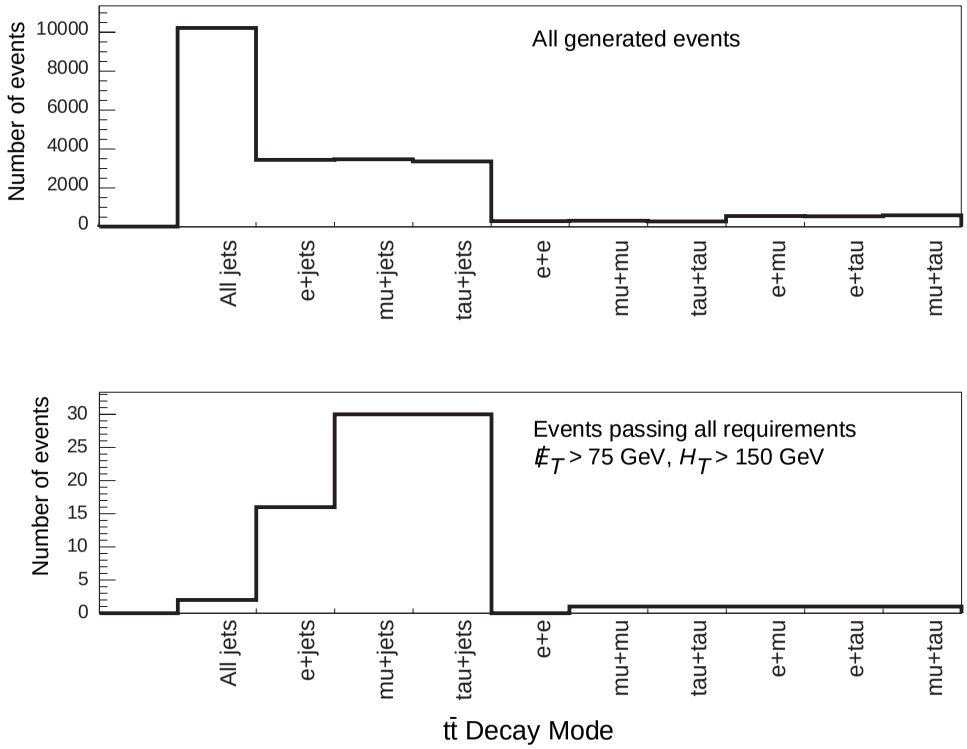

Figure 6.21: $t\bar{t}$ decay modes. The top plots shows the number of events generated in an `isajet` top quark to everything Monte Carlo sample ($M_{\rm top} = 170$ GeV/c^2). The bottom plot shows the number of events passing all of the analysis requirements ($\not\!\!E_T > 75$ GeV and $H_T > 150$ GeV).

6.3.1.1 $t\bar{t}$ decays

Production and decays of top quarks is the most significant Standard Model background, because the process of two heavy objects decaying through W bosons is very similar to squark and gluino cascade decays. The most prevalent $t\bar{t}$ decay mode that passes the analysis requirements is $t\bar{t} \to \ell$ + jets[§], since the many jets may have large E_T and there is significant $\not\!\!E_T$ due to the neutrino from the W decay. The fact that the lepton must not be found can also act to enhance the $\not\!\!E_T$. The $t\bar{t} \to$ all jets type events have little intrinsic $\not\!\!E_T$ and very rarely pass the analysis requirements.

[§]Top quarks decay to a b quark and a W. For lepton plus jets events, the W from one top decays to jets, and the W from the other decays to a lepton plus a neutrino.

The $t\bar{t}$ background is estimated from a 40,000 event Monte Carlo sample produced by the `herwig`[102] event generator[¶] with the top quark mass set at 170 GeV/c^2, close to the DØ measured value of 172 GeV/c^2.[103] The DØ measured cross section at that mass is 5.77 $\pm$ 1.82 pb.[90] So that errors are not applied twice, luminosity and energy scale errors are removed from the uncertainty on the cross section, resulting in a value of 5.77 $\pm$ 1.72 pb used for estimating the $t\bar{t}$ background.

Figure 6.21 displays the number of events from different $t\bar{t}$ decay modes passing the analysis requirements. The sample used there is from `isajet` instead of `herwig`, because the `herwig` events do not contain enough information to determine the parents of all of the daughter particles.

Single top

Although single top quark production has not been observed, one may imagine that such events can mimic the squark and gluino jets and missing energy signature. However, single top events typically do not have enough high E_T jets to pass the analysis requirements. With the low theoretical cross section for single top production, there is zero contribution to this analysis.

6.3.1.2 W $\rightarrow \ell\nu$

W boson decays can be an important background since the neutrino can produce substantial $\not\!\!E_T$ in the event. Though the leading jet produced in initial or final state radiation may have substantial E_T, the other jets are typically soft. By excluding the leading jet from the H_T calculation as described in Section 6.1.8, the H_T requirement severely reduces the contribution from these sources to the analysis background.

Large W + jets `vecbos`[104] Monte Carlo samples produced by the Top group (~20,000 events per decay type) and hadronized by `isajet` are used. For all W decays except

[¶] Event generators such as `herwig`, `pythia`, `vecbos`, and `isajet` are Monte Carlo programs that simulate desired physics processes. They determine that particles that are produced with their energies and directions. The detector simulation, `showerlibrary geant`,[100,101] simulates the detector response to those particles. Note that `vecbos` only generates quarks in the final state. `vecbos` is thus married with `isajet` or `herwig` which hadronize the quarks into jets.

for hadronic decays of the tau, a $W \rightarrow \ell\nu + \geq 3$ jets sample is used. Since a tau decaying to hadrons will look like a jet, a $W \rightarrow \ell\nu + \geq 2$ jets sample is used to get the $W \rightarrow \tau\nu$, $\tau \rightarrow$ hadrons estimate (only W's decaying to taus decaying to hadrons are examined).

The `vecbos` cross sections are used with a 30% error applied for the 3 jet samples and 20% for the two jet sample (10% per generated jet).[45]

6.3.1.3 WW and WZ

Events with vector boson pairs are considered because the final states are somewhat close to those of top decays though with fewer jets produced. Although the cross section for production of WW is close that of $t\bar{t}$, there are not enough high E_T jets for events to pass the analysis requirements.

Two `isajet` samples with ~50,000 events each produced by the Top group are used for this estimate: one for pair $W \rightarrow \ell\nu$, $W \rightarrow qq'$ events and another for $W \rightarrow \ell\nu$, $Z \rightarrow X$ pair events. The WW pair production cross section is 5.54 ± 1.66 pb and the WZ cross section is 0.32 ± 0.10 pb. Only a handful of Monte Carlo events pass the analysis requirements, yielding no significant contribution to the background.

6.3.1.4 $Z \rightarrow \nu\nu$ and $Z \rightarrow \tau\tau$

Decays of the Z boson do not normally involve large missing energy except perhaps in the invisible mode ($Z \rightarrow \nu\nu$) but even then, the neutrinos are back to back if the Z is not boosted. Therefore, for Z events to mimic the SUSY signal, the Z must be heavily boosted and a lepton must be lost for the visible modes. The H_T requirement severely reduces the amount of these backgrounds, since the secondary jets are typically soft like the W backgrounds.

The $Z \rightarrow \nu\nu$ and $Z \rightarrow \tau\tau$ backgrounds are estimated with `pythia`.[105] As seen in Table 6.7, several large samples of such events with varying Zp_T were produced. In order to reduce the number of events requiring processing with `geant` and `RECO`, events were required to have three generator level jets (jet cones drawn around the particles) with

$E_T > 7$ GeV and generator $\not\!\!E_T > 40$ GeV (imbalance of the particle E_T). The larger the Zp_T, the more events that pass, but the cross section also drops. For $Zp_T > 400$ GeV, the cross section is so small that the contribution to this analysis is negligible. The cross sections are determined by `pythia` with an assumed error of 30%.

6.3.2 Instrumental Backgrounds

Instrumental backgrounds arise from events where the $\not\!\!E_T$ is solely due to mismeasurements. Examples of possible sources are:

- QCD multijet events with mismeasured jets
- $t\bar{t} \rightarrow$ all jets events with mismeasured jets
- $Z \rightarrow ee$ + jets, $Z \rightarrow \mu\mu$ + jets events where both leptons are lost or mismeasured.

The Z sources yield little contribution (< 0.04 event for the loose requirements of $\not\!\!E_T > 75$ GeV and $H_T > 100$ GeV). A 12,000 event $Z \rightarrow \mu\mu + \geq 3$ jets `vecbos` Monte Carlo sample was used to check the estimate. Although such events could rarely have substantial $\not\!\!E_T$ when a muon is lost, the H_T requirement eliminates them.

The $t\bar{t} \rightarrow$ all jets source is essentially identical to mismeasured QCD multijet events. QCD has a huge cross section, however, so it is expected that the $t\bar{t} \rightarrow$ all jets contribution is small compared to QCD.

6.3.2.1 Mismeasured QCD Multijet Events

QCD multijet events can be a background when one or more jets fluctuate and are mismeasured, potentially generating $\not\!\!E_T$ in what should be a balanced event. The jet – $\not\!\!E_T$ direction correlation requirements described in Section 6.1.4 eliminate much of this background, but there is still some left over. The background is difficult to estimate, since one does not expect a Monte Carlo to model correctly the extreme tails of the QCD multijet $\not\!\!E_T$ spectrum where the jet fluctuations are large. Therefore, collider data is used to estimate the QCD multijet background.

One cannot use QCD multijet data with very large $\not\!\!E_T$, since that overlaps with the signal region and the events would be the same as those passing the analysis `missing_et` trigger. In order to stay in the region where the QCD cross section dominates over SUSY, some characteristic of low $\not\!\!E_T$ QCD data must be extrapolated into the signal region to estimate the background. Two procedures are used: a shape fit and an extrapolation of the QCD multijet $\not\!\!E_T$ spectrum.

The shape fit is the primary method used for this analysis. The procedure involves taking histograms of a certain distribution from data and background/signal sources and then use a histogram shape fitter to estimate the contribution of each source to the data. The histogram shape fitter itself is described in and References 106 and 107. The distribution that is fit is derived from the two dimensional plot of $\phi_{\text{2nd jet}} - \phi_{\not\!\!E_T}$ vs. $\phi_{\text{Leading jet}} - \phi_{\not\!\!E_T}$ shown in Figure 6.6 on page 115. The distance of each point from the upper right hand corner at (π, π) is histogrammed for the data, QCD multijet events, $t\bar{t}$ Monte Carlo, and a squark and gluino signal sample as shown in Figure 6.22. Note that the histograms have variable sized bins so that when random angles are plotted, the resulting histogram is flat. This rather peculiar distribution (henceforth referred to as "distance from (π, π)") was chosen because the histograms from QCD multijet events and $t\bar{t}$/ SUSY events are markedly different. Since the QCD multijet background is the goal of the fit, it is important to use a distribution where the QCD events are distinct. The fact that $t\bar{t}$ and SUSY histograms appear very similar (as expected since $t\bar{t}$ decays are similar to squark and gluino decays) will mean that the fitter will attribute left over data to both $t\bar{t}$ and SUSY about evenly. That is of no concern, since $t\bar{t}$ background and SUSY efficiencies are determined by other means.

The QCD multijet data used in the shape fit are from the `jet85` trigger. In order for the extrapolating methods to work well, there must be a large amount of multijet data in various $\not\!\!E_T$ bins. A sample taken by the `jet85` trigger, which was only prescaled at the highest luminosities, provides the largest amount of data. The trigger with the next lower jet threshold, `jet50` yields a sample with less than one tenth the size of the `jet85` sample. The lower threshold jet triggers were either severely prescaled, eliminated

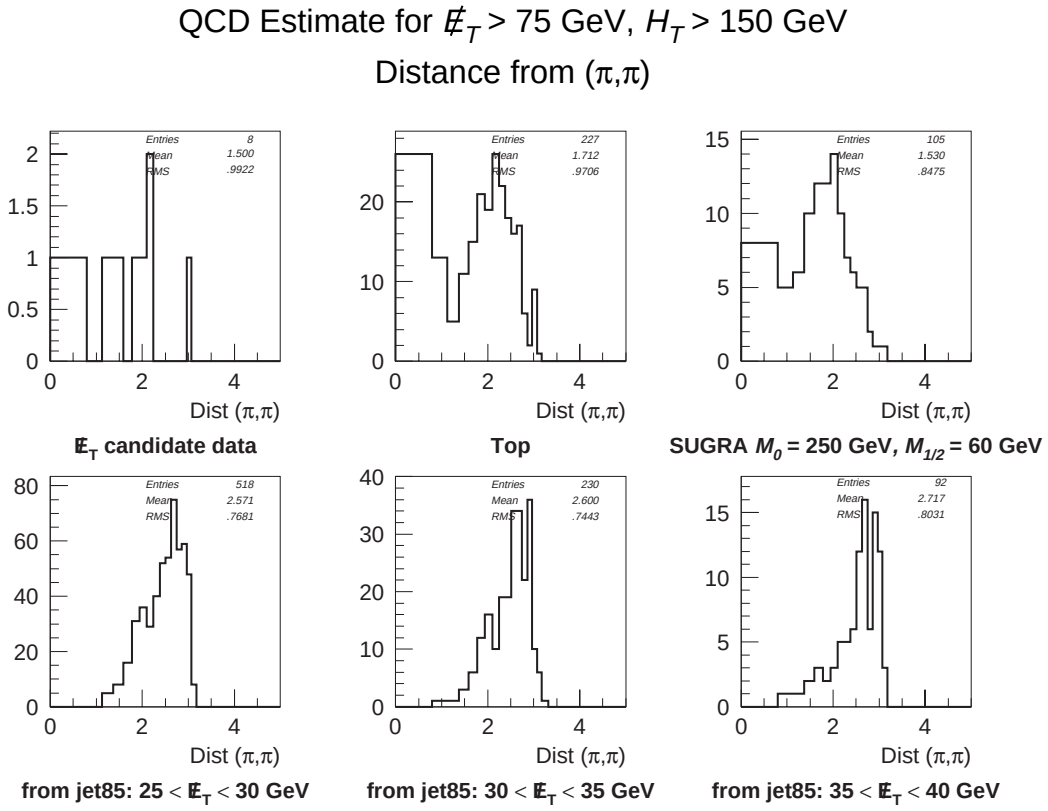

Figure 6.22: The "Distance from (π, π)" distributions.

altogether after a fraction of the run, or had some additional unwanted requirements such as single interactions. The sample from `jet85` is the only viable option. In order for the `jet85` sample to be a proper model of the background, the leading jet requirement of $E_T > 115$ GeV is made in the analysis as described in Section 6.1.9.[‖]

All of the analysis requirements except for $\not\!\!E_T$ are made on events from the `jet85` trigger. The events are then binned by $\not\!\!E_T$, and histograms of the distance from (π, π) distribution are made. A good feature of the distance from (π, π) distribution for QCD multijet events is that it only changes slightly as $\not\!\!E_T$ is increased, thus the shape most likely holds for large $\not\!\!E_T$. Three or four $\not\!\!E_T$ bins are used: $25 < \not\!\!E_T < 30$ GeV, $30 < \not\!\!E_T < 35$ GeV, $35 < \not\!\!E_T < 40$ GeV, and for some samples $40 < \not\!\!E_T < 45$ GeV. The last sample is omitted if it is populated with fewer than 30 events.

Each of the QCD multijet histograms are independently fed into the histogram shape fitter along with histograms from `missing_et` stream data (the data histogram) , $t\bar{t}$ Monte Carlo and a SUSY signal Monte Carlo sample. The latter three samples also have all analysis requirements applied including the various $\not\!\!E_T$ and H_T requirements.

The result of this procedure is a posterior probability distribution of the expected QCD multijet contribution to the data done for each of the QCD multijet $\not\!\!E_T$ bins. The distributions shown in Figure 6.23 are all similar. They are peaked at or near zero with large tails. The estimate for the expected number of QCD multijet events is taken to be the average of the means of the three (or four) distributions with the error given by the average of the RMS values. The means of the distributions are all within errors of each other.

The histogram fitter can only handle three source histograms plus the data histogram. Though one would like to include all of the backgrounds in the fit, that is difficult to do since there must be a more events in the histograms than the number of bins. For most

[‖]In order to generate a very large sample of low threshold jets in next run of the Tevatron with the upgraded detector, it may be feasible to produce distributions in the level 3 trigger system (the software filter) instead of collecting and writing out each event. That procedure will work so long as complicated event-by-event information and corrections are not needed. For the 1993-1995 run, events that are misvertexed contaminate the jet samples and are removed by the primary vertex confirmation method described in Section 6.1.10. This procedure is too complex to run in the level 2 filter nodes.

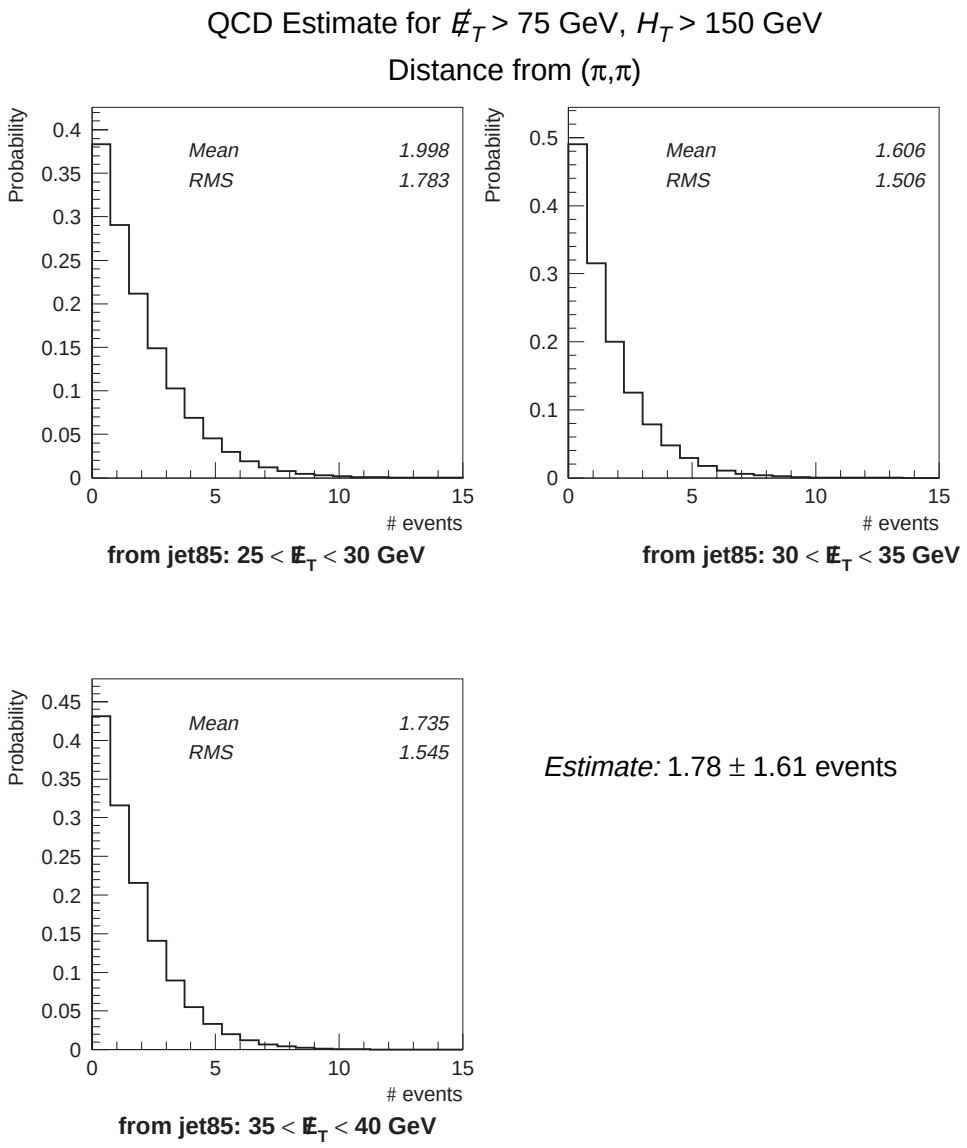

Figure 6.23: Posterior probability distributions for the QCD estimate.

of the backgrounds determined from Monte Carlo other than $t\bar{t}$, very few events pass. Since $t\bar{t}$ is the dominant physics background, adding in the others would have little affect. In fact, replacing the SUSY signal sample with the $W \rightarrow e\nu + \geq 3$ jets histogram only changes the result by 0.1 event. Replacing the SUSY histogram with ones from other mSUGRA points also has little affect on the QCD estimate, since the distance from (π, π) distributions are similar.

To verify that the QCD multijet background estimate is valid, an extrapolation of the QCD multijet $\not\!\!E_T$ spectrum is also performed, again using `jet85` data with all the requirements except $\not\!\!E_T$ applied. Figure 6.24 shows a $\not\!\!E_T$ spectrum and a fit with the function,

$$f(\not\!\!E_T) = \frac{N\beta e^{-\left(\sqrt{\beta \not\!\!E_T} - \sqrt{\beta \not\!\!E_{T\,\mathrm{cut}}}\right)}}{2\left(1 + \sqrt{\beta \not\!\!E_{T\,\mathrm{cut}}}\right)} \tag{6.4}$$

This function is essentially $f(x) = e^{-\sqrt{x}}$ with extra constants so that for a value of $\not\!\!E_{T\,\mathrm{cut}}$, the fit parameter N is almost the number of events expected for $\not\!\!E_T > \not\!\!E_{T\,\mathrm{cut}}$ (N is $f(\not\!\!E_T)$ integrated from $\not\!\!E_{T\,\mathrm{cut}}$ to infinity). The estimate is obtained by dividing N by the bin width (5 GeV) and then multiplying by the ratio of the `missing_et` luminosity to the `jet85` luminosity (79.2/55.9). The estimate for the extrapolation in Figure 6.24 is 1.7 ± 0.3 events for $\not\!\!E_T > 75$ GeV. One has no evidence that the very small errors are correct.

The fit region is $25 < \not\!\!E_T < 45$ GeV and is chosen to avoid using points in the possible signal region ($\not\!\!E_T > 50$ GeV). If the next point beyond the fit region is used (at $\not\!\!E_T = 50$ GeV), the estimate from Figure 6.24 changes from 1.7 events to 2.1 ± 0.9 events with $\chi^2/\mathrm{ndf} = 7.8/4$.

The QCD estimates from the shape fit shown in Figures 6.22 and 6.23 agree well with the $\not\!\!E_T$ extrapolation in Figure 6.24. Table 6.8 compares the estimates for some other $\not\!\!E_T$/ H_T requirements.

For the QCD multijet background prediction at $\not\!\!E_T > 50$ GeV, the histogram shape fitting procedure cannot be used, because it is not designed to handle accounting for the `missing_et` turn on curve (the trigger is inefficient for $\not\!\!E_T < 75$ GeV). Therefore, the

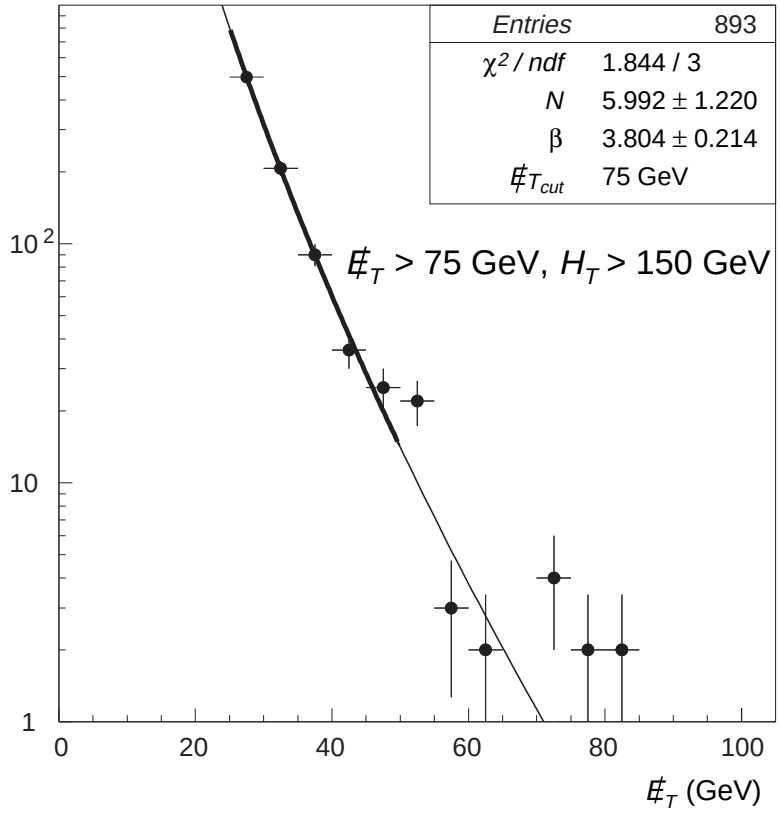

Figure 6.24: Extrapolation of the QCD multijet $\not\!\!E_T$ spectrum from `jet85`. The fit region is $25 < \not\!\!E_T < 45$ GeV. The parameters for the expected QCD background at $\not\!\!E_T > 75$ GeV are described in the text.

$\not\!\!E_T >$ (GeV)	$H_T >$ (GeV)	Shape fit Estimate	Extrapolation Estimate
75	100	3.5 ± 2.6	2.8 ± 0.9
75	150	1.8 ± 1.6	1.7 ± 0.3
100	100	1.7 ± 1.6	0.6 ± 0.1

Table 6.8: QCD background estimates from the shape fit and $\not\!\!E_T$ spectrum extrapolation.

extrapolation of the $\not\!\!E_T$ spectrum with the turn on curve folded in is used to obtain that background estimate. The estimates are displayed in Tables 6.9 and 6.10.

6.3.3 Background Estimates

The background estimates for all the analysis requirements and varying $\not\!\!E_T$ and H_T thresholds are shown in Tables 6.9 through 6.18. The expected background, $< N >$, is given for 79.2 pb^{-1} of data. E–scale indicates the error due to the energy scale described in Section 5.6.5. $\delta\mathcal{L}$ is the error due to the luminosity and $\delta\sigma$ is the error due to the cross section. Only the backgrounds that contribute events are shown. The total background expected without QCD is given at the bottom of the first block. The QCD background with its error is then shown.

The bottom block shows the total background. The first error is the total statistical error. The upper and lower errors are the sum of the upper and lower systematic errors. The systematic errors are added in the following manner:

- Energy scale errors are added linearly.
- Luminosity errors are added linearly.
- All `vecbos` and `pythia` cross section errors are added linearly. The $t\bar{t}$ cross section error is then added in quadrature to form the cross section error.
- The energy scale, luminosity, cross section, and error on the QCD estimate are added in quadrature to form the final error.

There are many background sources where no Monte Carlo events pass the analysis requirements. Such backgrounds are not included in the total background estimate. The "95% CL No Pass" value indicates the 95% upper limit on the number of events that

could be contributed from those sources. This value is calculated in the following manner,

$$N_{95\%\text{ CL No Pass}} = \frac{3}{\sum(\#\text{ MC events generated})_i} \left(\sum \sigma_i\right) \mathcal{L} \tag{6.5}$$

where the sums are over those backgrounds with zero efficiency.

The last number in each table is the number of events seen in the data passing the analysis requirements with the specified $\not\!\!E_T$ and H_T thresholds. It is clear from these tables that no significant excess over Standard Model backgrounds is observed. Plots comparing the background estimates to the data are shown in Figure 6.25.

6.4 Summary

As mentioned at the beginning of this chapter, event requirements beyond those of the trigger and filter are necessary to pick out the events that could be signal and reject those that are probably background. The main event criteria for this analysis are large $\not\!\!E_T$, at least three jets meeting good quality criteria, large H_T, and high E_T leading jet. Events with isolated electrons and muons are rejected since they do not fit the desired jets and $\not\!\!E_T$ signature. With these requirements, the data can be examined and the backgrounds estimated. Most of the background estimates are based on Monte Carlo simulation predictions. The most difficult background to estimate is the QCD multijet background. Fortunately, the excellent DØ calorimetry allows use of a jet – $\not\!\!E_T$ direction correlation requirement to eliminate most of those events. However, some background remains and it is estimated using collider data.

To be discussed in the next chapter, the $\not\!\!E_T$ and H_T thresholds are optimized for each mSUGRA Monte Carlo point. Thus, there are actually 10 sets of cuts that are used. When the number of events in the data passing the requirements are compared to the estimates from Standard Model backgrounds, it is clear that no excess of events is seen. Therefore, all of the collider data is consistent with being produced by SM processes, and thus no new particles are observed.

Background	$< N >$	$\pm$ Stat	$+$ E–scale	$-$ E–scale	$\pm$ $\delta\mathcal{L}$	$\pm$ $\delta\sigma$
$t\bar{t} \to X$	4.67	$\pm$ 0.21	$+$ 1.69	$-$ 1.10	$\pm$ 0.25	$\pm$ 1.41
$W \to e\nu + \geq 3$ jets	1.35	$\pm$ 0.67	$+$ 0.03	$-$ 0.03	$\pm$ 0.07	$\pm$ 0.40
pair $W \to \ell\nu$, $W \to qq'$	0.29	$\pm$ 0.05	$+$ 0.11	$-$ 0.12	$\pm$ 0.02	$\pm$ 0.09
$Z \to \mu\mu + \geq 3$ jets	0.04	$\pm$ 0.03	$+$ 0.04	$-$ 0.01	$\pm$ 0.00	$\pm$ 0.01
$Z \to \tau\tau$	0.22	$\pm$ 0.08	$+$ 0.01	$-$ 0.09	$\pm$ 0.01	$\pm$ 0.07
$Z \to \nu\nu$	1.02	$\pm$ 0.34	$+$ 0.55	$-$ 0.03	$\pm$ 0.05	$\pm$ 0.30
Total (w/o QCD)	7.59	$\pm$ 0.79	$+$ 2.45	$-$ 1.39	$\pm$ 0.40	$\pm$ 1.49

$< N_{QCD} >$ $\quad 36.4 \pm 7.9$

Total $< N >$	95% CL No Pass	Events in Data
$44.0 \pm 0.8\ ^{+8.5}_{-8.2}$	0.8	49

Table 6.9: Backgrounds for $\not\!\!E_T > 50$ GeV and $H_T > 100$ GeV. The QCD background is from extrapolating the `jet85` $\not\!\!E_T$ spectrum. $< N >$ indicates the number of events expected in 79.2 pb^{-1} of data.

Background	$< N >$	$\pm$ Stat	$+$ E–scale	$-$ E–scale	$\pm$ $\delta\mathcal{L}$	$\pm$ $\delta\sigma$
$t\bar{t} \to X$	3.13	$\pm$ 0.17	$+$ 1.17	$-$ 0.81	$\pm$ 0.17	$\pm$ 0.95
pair $W \to \ell\nu$, $W \to qq'$	0.09	$\pm$ 0.03	$+$ 0.08	$-$ 0.03	$\pm$ 0.00	$\pm$ 0.03
$Z \to \nu\nu$	0.09	$\pm$ 0.02	$+$ 0.01	$-$ 0.02	$\pm$ 0.01	$\pm$ 0.03
Total (w/o QCD)	3.35	$\pm$ 0.17	$+$ 1.29	$-$ 0.86	$\pm$ 0.18	$\pm$ 0.95

$< N_{QCD} >$ 21.9 $\pm$ 5.14

Total $< N >$	95% CL No Pass	Events in Data
$25.2 \pm 0.2\ ^{+5.4}_{-5.3}$	0.8	31

Table 6.10: Backgrounds for $\not\!\!E_T > 50$ GeV and $H_T > 150$ GeV. The QCD background is from extrapolating the `jet85` $\not\!\!E_T$ spectrum. $< N >$ indicates the number of events expected in 79.2 pb^{-1} of data.

Background	$< N >$	$\pm$ Stat	$+$ E–scale	$-$ E–scale	$\pm$ $\delta\mathcal{L}$	$\pm$ $\delta\sigma$
$t\bar{t} \to X$	3.11	$\pm$ 0.17	$+$ 1.08	$-$ 0.84	$\pm$ 0.17	$\pm$ 0.94
$W \to e\nu +$ ≥ 3 jets	1.35	$\pm$ 0.67	$+$ 0.03	$-$ 0.03	$\pm$ 0.07	$\pm$ 0.40
pair $W \to \ell\nu$, $W \to qq'$	0.21	$\pm$ 0.04	$+$ 0.09	$-$ 0.09	$\pm$ 0.01	$\pm$ 0.06
$Z \to \mu\mu +$ ≥ 3 jets	0.04	$\pm$ 0.02	$+$ 0.03	$-$ 0.01	$\pm$ 0.00	$\pm$ 0.01
$Z \to \tau\tau$	0.14	$\pm$ 0.06	$+$ 0.01	$-$ 0.06	$\pm$ 0.01	$\pm$ 0.05
$Z \to \nu\nu$	0.93	$\pm$ 0.33	$+$ 0.42	$-$ 0.03	$\pm$ 0.04	$\pm$ 0.28
Total (w/o QCD)	5.79	$\pm$ 0.77	$+$ 1.67	$-$ 1.08	$\pm$ 0.31	$\pm$ 1.04

$< N_{QCD} >$ $\quad 3.54 \pm 2.64$

Total $< N >$	95% CL No Pass	Events in Data
$9.3 \pm 0.8\ ^{+3.4}_{-3.2}$	0.8	15

Table 6.11: Backgrounds for $\not\!\!E_T > 75$ GeV and $H_T > 100$ GeV. $< N >$ indicates the number of events expected in 79.2 pb^{-1} of data.

Background	$< N >$	$\pm$ Stat	$+$ E–scale	$-$ E–scale	$\pm$ $\delta\mathcal{L}$	$\pm$ $\delta\sigma$
$t\bar{t} \to X$	2.65	$\pm$ 0.16	$+$ 1.02	$-$ 0.71	$\pm$ 0.14	$\pm$ 0.80
$W \to e\nu +$ ≥ 3 jets	0.34	$\pm$ 0.34	$+$ 0.03	$-$ 0.03	$\pm$ 0.02	$\pm$ 0.10
pair $W \to \ell\nu$, $W \to qq'$	0.13	$\pm$ 0.03	$+$ 0.05	$-$ 0.06	$\pm$ 0.01	$\pm$ 0.04
$Z \to \mu\mu +$ ≥ 3 jets	0.02	$\pm$ 0.02	$+$ 0.01	$-$ 0.02	$\pm$ 0.00	$\pm$ 0.01
$Z \to \tau\tau$	0.05	$\pm$ 0.03	$+$ 0.00	$-$ 0.00	$\pm$ 0.00	$\pm$ 0.02
$Z \to \nu\nu$	0.61	$\pm$ 0.27	$+$ 0.02	$-$ 0.02	$\pm$ 0.03	$\pm$ 0.18
Total (w/o QCD)	3.81	$\pm$ 0.46	$+$ 1.14	$-$ 0.84	$\pm$ 0.20	$\pm$ 0.82

$< N_{QCD} >$ $\quad 2.68 \pm 2.23$

Total $< N >$	95% CL No Pass	Events in Data
$6.5 \pm 0.5\ ^{+2.7}_{-2.6}$	0.8	12

Table 6.12: Backgrounds for $\not\!\!E_T > 75$ GeV and $H_T > 120$ GeV. $< N >$ indicates the number of events expected in 79.2 pb^{-1} of data.

Background	$< N >$	$\pm$ Stat	+ E–scale	− E–scale	$\pm$ $\delta\mathcal{L}$	$\pm$ $\delta\sigma$
$t\bar{t} \to X$	2.19	$\pm$ 0.14	+ 0.78	− 0.58	$\pm$ 0.12	$\pm$ 0.66
pair $W \to \ell\nu$, $W \to qq'$	0.08	$\pm$ 0.02	+ 0.03	− 0.04	$\pm$ 0.00	$\pm$ 0.03
$Z \to \tau\tau$	0.02	$\pm$ 0.00	+ 0.00	− 0.00	$\pm$ 0.00	$\pm$ 0.01
$Z \to \nu\nu$	0.25	$\pm$ 0.15	+ 0.05	− 0.10	$\pm$ 0.01	$\pm$ 0.07
Total (w/o QCD)	2.54	$\pm$ 0.21	+ 0.86	− 0.72	$\pm$ 0.13	$\pm$ 0.67

$< N_{QCD} >$ $\quad 2.05 \pm 1.82$

Total $< N >$	95% CL No Pass	Events in Data
$4.6 \pm 0.2\ ^{+2.1}_{-2.1}$	0.7	11

Table 6.13: Backgrounds for $\not\!\!E_T > 75$ GeV and $H_T > 140$ GeV. $< N >$ indicates the number of events expected in 79.2 pb^{-1} of data.

Background	$< N >$	$\pm$ Stat	$+$ E–scale	$-$ E–scale	$\pm$ $\delta\mathcal{L}$	$\pm$ $\delta\sigma$
$t\bar{t} \to X$	2.03	$\pm$ 0.14	$+$ 0.65	$-$ 0.67	$\pm$ 0.11	$\pm$ 0.62
pair $W \to \ell\nu$, $W \to qq'$	0.06	$\pm$ 0.02	$+$ 0.04	$-$ 0.02	$\pm$ 0.00	$\pm$ 0.02
$Z \to \tau\tau$	0.02	$\pm$ 0.00	$+$ 0.00	$-$ 0.00	$\pm$ 0.00	$\pm$ 0.01
$Z \to \nu\nu$	0.09	$\pm$ 0.02	$+$ 0.01	$-$ 0.02	$\pm$ 0.01	$\pm$ 0.03
Total (w/o QCD)	2.21	$\pm$ 0.14	$+$ 0.70	$-$ 0.71	$\pm$ 0.12	$\pm$ 0.62

$< N_{QCD} >$ $\quad 1.78 \pm 1.61$

Total $< N >$	95% CL No Pass	Events in Data
$4.0 \pm 0.1\ ^{+1.9}_{-1.9}$	0.7	8

Table 6.14: Backgrounds for $\not\!\!E_T > 75$ GeV and $H_T > 150$ GeV. $< N >$ indicates the number of events expected in 79.2 pb^{-1} of data.

Background	$< N >$	$\pm$ Stat	$+$ E–scale	$-$ E–scale	$\pm$ $\delta\mathcal{L}$	$\pm$ $\delta\sigma$
$t\bar{t} \to X$	1.73	$\pm$ 0.13	$+$ 0.72	$-$ 0.53	$\pm$ 0.09	$\pm$ 0.53
pair $W \to \ell\nu$, $W \to qq'$	0.06	$\pm$ 0.02	$+$ 0.01	$-$ 0.03	$\pm$ 0.00	$\pm$ 0.02
$Z \to \tau\tau$	0.02	$\pm$ 0.00	$+$ 0.00	$-$ 0.00	$\pm$ 0.00	$\pm$ 0.00
$Z \to \nu\nu$	0.08	$\pm$ 0.02	$+$ 0.01	$-$ 0.01	$\pm$ 0.00	$\pm$ 0.02
Total (w/o QCD)	1.89	$\pm$ 0.13	$+$ 0.74	$-$ 0.58	$\pm$ 0.10	$\pm$ 0.53

$< N_{QCD} >$ $\quad 1.72 \pm 1.54$

Total $< N >$	95% CL No Pass	Events in Data
$3.6 \pm 0.1\ ^{+1.8}_{-1.7}$	0.7	6

Table 6.15: Backgrounds for $\not\!\!E_T > 75$ GeV and $H_T > 160$ GeV. $< N >$ indicates the number of events expected in 79.2 pb^{-1} of data.

Background	$< N >$	$\pm$ Stat	$+$ E–scale	$-$ E–scale	$\pm$ $\delta\mathcal{L}$	$\pm$ $\delta\sigma$
$t\bar{t} \to X$	2.22	$\pm$ 0.14	$+$ 0.94	$-$ 0.64	$\pm$ 0.12	$\pm$ 0.67
$W \to e\nu +$ ≥ 3 jets	1.01	$\pm$ 0.58	$+$ 0.03	$-$ 0.03	$\pm$ 0.05	$\pm$ 0.30
pair $W \to \ell\nu$, $W \to qq'$	0.18	$\pm$ 0.04	$+$ 0.08	$-$ 0.08	$\pm$ 0.01	$\pm$ 0.05
$Z \to \mu\mu +$ ≥ 3 jets	0.03	$\pm$ 0.02	$+$ 0.02	$-$ 0.01	$\pm$ 0.00	$\pm$ 0.01
$Z \to \tau\tau$	0.11	$\pm$ 0.05	$+$ 0.01	$-$ 0.03	$\pm$ 0.01	$\pm$ 0.03
$Z \to \nu\nu$	0.93	$\pm$ 0.33	$+$ 0.43	$-$ 0.16	$\pm$ 0.05	$\pm$ 0.28
Total (w/o QCD)	4.47	$\pm$ 0.69	$+$ 1.51	$-$ 0.96	$\pm$ 0.24	$\pm$ 0.76

$< N_{QCD} >$ $\quad 2.48 \pm 2.01$

Total $< N >$	95% CL No Pass	Events in Data
$7.0 \pm 0.7\ ^{+2.7}_{-2.5}$	0.8	8

Table 6.16: Backgrounds for $\not\!\!E_T > 90$ GeV and $H_T > 100$ GeV. $< N >$ indicates the number of events expected in 79.2 pb^{-1} of data.

Background	$< N >$	$\pm$ Stat	$+$ E–scale	$-$ E–scale	$\pm$ $\delta\mathcal{L}$	$\pm$ $\delta\sigma$
$t\bar{t} \to X$	1.75	$\pm$ 0.13	$+$ 0.73	$-$ 0.54	$\pm$ 0.09	$\pm$ 0.53
$W \to e\nu + \geq 3$ jets	1.01	$\pm$ 0.58	$+$ 0.03	$-$ 0.03	$\pm$ 0.05	$\pm$ 0.30
pair $W \to \ell\nu$, $W \to qq'$	0.16	$\pm$ 0.03	$+$ 0.06	$-$ 0.08	$\pm$ 0.01	$\pm$ 0.05
$Z \to \mu\mu + \geq 3$ jets	0.02	$\pm$ 0.02	$+$ 0.02	$-$ 0.00	$\pm$ 0.00	$\pm$ 0.01
$Z \to \tau\tau$	0.08	$\pm$ 0.04	$+$ 0.00	$-$ 0.00	$\pm$ 0.00	$\pm$ 0.02
$Z \to \nu\nu$	0.79	$\pm$ 0.30	$+$ 0.28	$-$ 0.03	$\pm$ 0.04	$\pm$ 0.24
Total (w/o QCD)	3.81	$\pm$ 0.67	$+$ 1.15	$-$ 0.69	$\pm$ 0.20	$\pm$ 0.63

$< N_{QCD} >$ $\quad 1.77 \pm 1.59$

Total $< N >$	95% CL No Pass	Events in Data
$5.6 \pm 0.7\ ^{+2.2}_{-2.0}$	0.8	7

Table 6.17: Backgrounds for $\not\!\!E_T > 100$ GeV and $H_T > 100$ GeV. $< N >$ indicates the number of events expected in 79.2 pb^{-1} of data.

Background	$< N >$	$\pm$ Stat	+ E–scale	− E–scale	$\pm$ $\delta\mathcal{L}$	$\pm$ $\delta\sigma$
$t\bar{t} \to X$	1.04	$\pm$ 0.10	+ 0.44	− 0.40	$\pm$ 0.06	$\pm$ 0.32
pair $W \to \ell\nu$, $W \to qq'$	0.03	$\pm$ 0.02	+ 0.03	− 0.01	$\pm$ 0.00	$\pm$ 0.01
$Z \to \nu\nu$	0.09	$\pm$ 0.02	+ 0.02	− 0.02	$\pm$ 0.00	$\pm$ 0.03
Total (w/o QCD)	1.18	$\pm$ 0.10	+ 0.49	− 0.43	$\pm$ 0.06	$\pm$ 0.32

$< N_{QCD} >$ $\quad 1.15 \pm 1.08$

Total $< N >$	95% CL No Pass	Events in Data
$2.3 \pm 0.1\ ^{+1.2}_{-1.2}$	0.7	3

Table 6.18: Backgrounds for $\not\!\!E_T > 100$ GeV and $H_T > 150$ GeV. $< N >$ indicates the number of events expected in 79.2 pb^{-1} of data.

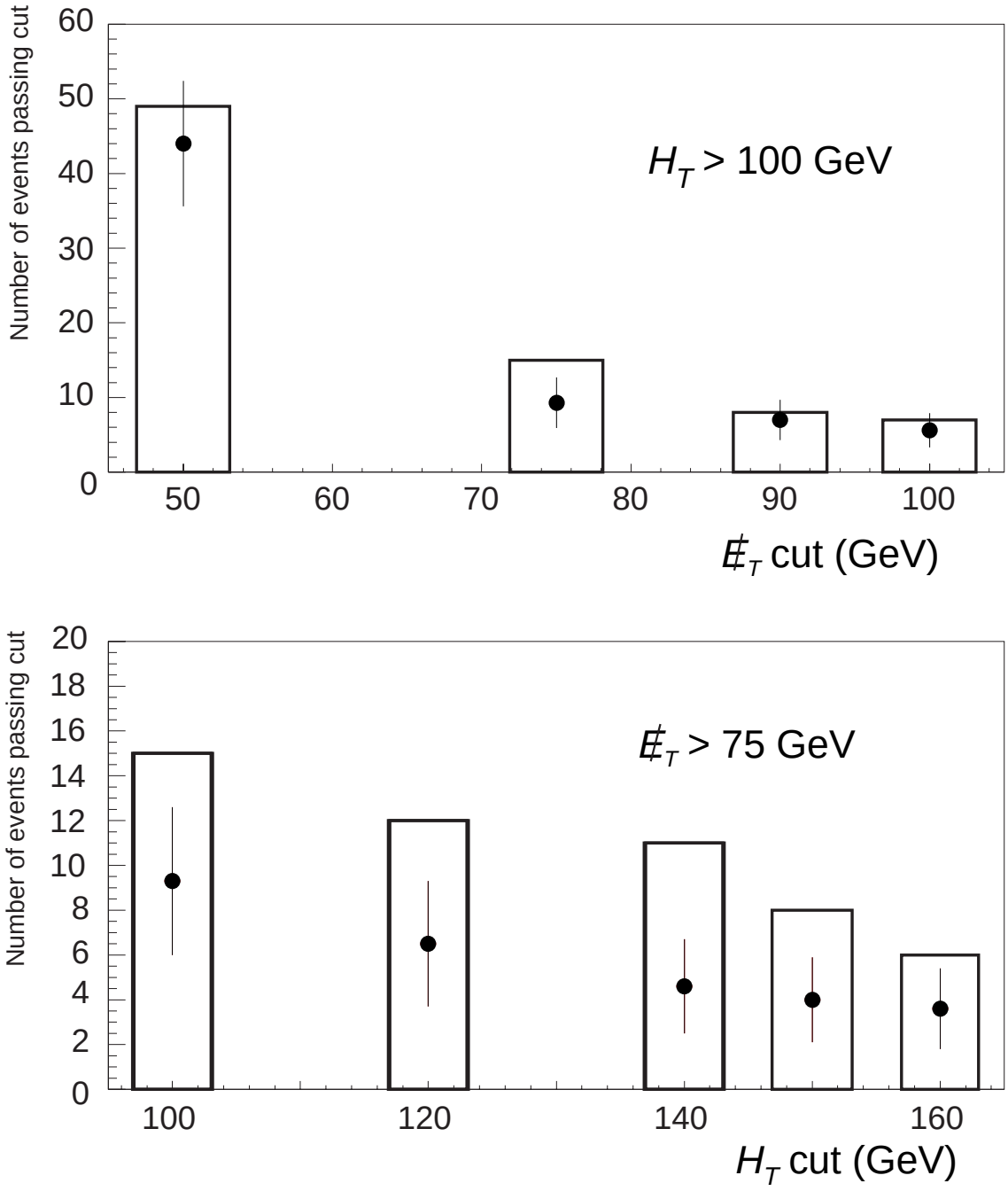

Figure 6.25: Comparison of background estimates to the data. The points with the error bars are the background estimates. The bars are the number of events observed in the data. The top plot shows the comparisons for $H_T > 100$ GeV and varying $\not\!\!E_T$ threshold. The lower plot is comparisons for $\not\!\!E_T > 75$ GeV and varying H_T threshold.

Chapter 7

Results

No significant excess over Standard Model backgrounds is observed for any of the analysis requirement sets. Since no new physics will be discovered with this analysis, the result will be interpreted as cross section and mass limits on squarks and gluinos.

7.1 Sensitivity to the Signal

The sensitivity of a search depends on the production cross section (σ), the total integrated luminosity of the data observed ($\mathcal{L}$), and the fraction of signal events passed by the analysis requirements, which is signal efficiency (ϵ). The number of signal events one would expect to observe is then given by,

$$<N> = \sigma \mathcal{L} \epsilon \tag{7.1}$$

Generally, one needs $<N> \geq 3$ events to be able to state that particles of some model would have been discovered by the analysis if those particles actually existed, and so that model can be ruled out. For this search, the cross sections are determined by `prospino` and the total integrated luminosity of the data is 79.2 pb^{-1}. The efficiencies of the models (each M_0, $M_{1/2}$ value is considered to be a different model) are determined by applying the analysis requirements to simulated events.

To determine the sensitivity of this analysis, production and decays of squarks and gluinos are simulated using `isajet` v7.13.[29] Events are produced according to the

mSUGRA parameters described in Section 2.3. Three mSUGRA parameters and the top quark mass are fixed to the following values:

- $\tan\beta = 2$,
- $A_0 = 0$,
- $\mu < 0$,
- $M_{top} = 170$ GeV/c^2.

A_0 only affects the decay of SUSY light scalar top quarks. Since jets from the top squarks are soft, this analysis is not sensitive to them and so the value of A_0 has little effect. For $\mu < 0$, the gluino mass is typically three times the LSP mass. For $\mu > 0$, the gluino is more than $6M_{\rm LSP}$. The analysis is not attempted for $\mu > 0$ since most of the region below the resulting exclusion contour is already ruled out by the LEP limits. Changing $\tan\beta$ alters the gauge and Higgs content of the charginos and neutralinos, thus changing the branching ratios in cascade decays. $\tan\beta = 2$ is a popular value among theorists and the analysis is insensitive to small changes of this parameter. Altering $\tan\beta$ may be done as an extension of this analysis. The M_0 and $M_{1/2}$ parameters are allowed to vary.

With those mSUGRA parameters set, events are generated at 49 various points in the M_0 – $M_{1/2}$ plane as shown in Figure 7.1. The MC samples are processed by `showerlibrary geant` v3.14 and `reco` v12.15. All of the analysis requirements are applied to these samples. The few events that have an isolated hot cell are defective and are not counted (see Section 6.1.3).

Although in principle all sparticles can contribute to this analysis, squarks and gluinos by far dominate the types of events that pass the requirements and also have the largest production cross sections. Therefore, only squark and gluino type events are produced by `isajet`. All decay modes are allowed.

Next-to-leading order cross sections are calculated by the `prospino` program discussed in Section 3.1. `prospino` does not include scalar tops in its calculation (that will be available in the near future from the program's authors). Therefore, any scalar tops

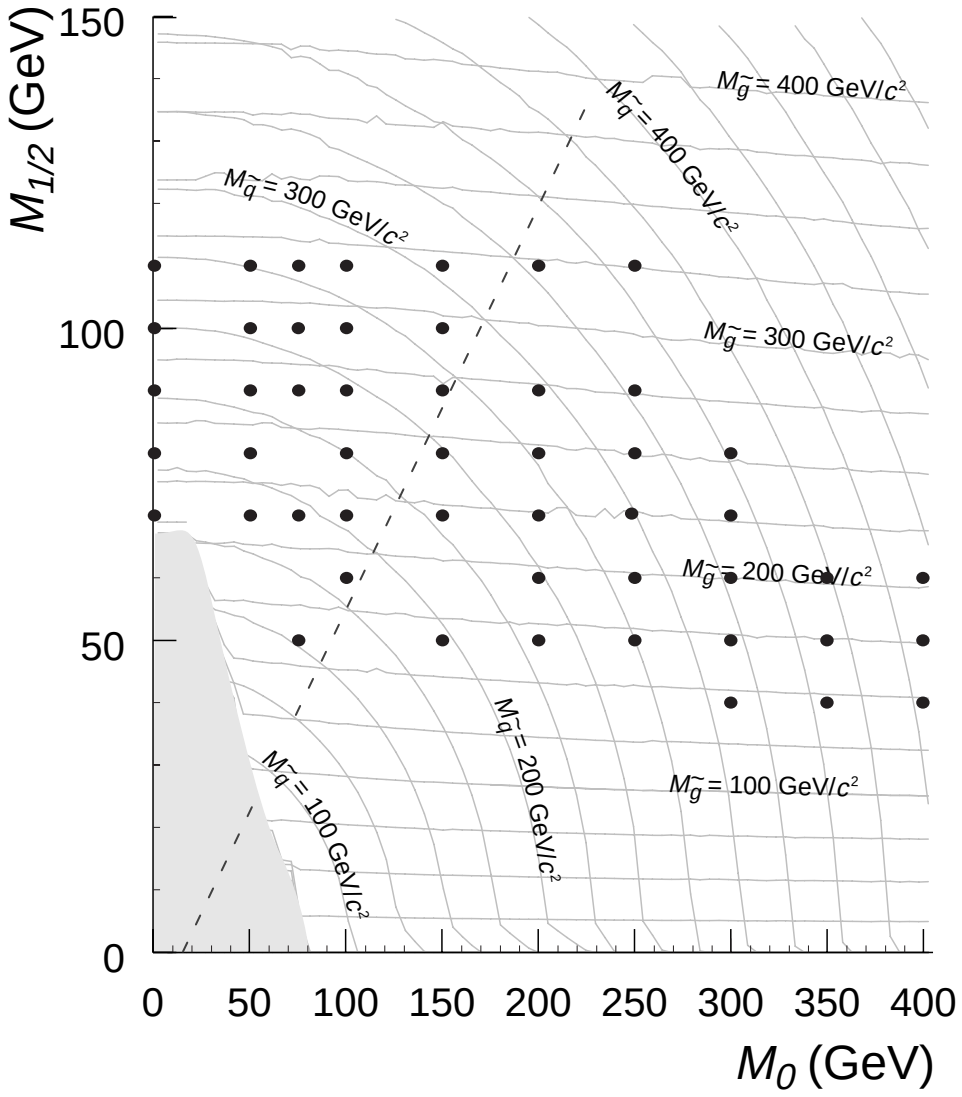

Figure 7.1: Monte Carlo signal points in the M_0 – $M_{1/2}$ plane. The light grey lines are contours of gluino and squark masses. The dashed line indicates where squarks and gluinos have equal mass. The shaded region is where mSUGRA does not produce electroweak symmetry breaking.

produced by `isajet` are not counted. Typically, fewer than 1% of squark and gluino events produced contain scalar tops, and only up to a percent or two of them will pass the analysis requirements since jets and $\not\!\!E_T$ from scalar tops are soft.

As mentioned, the NLO cross sections from `prospino` are anywhere from equal to double the cross sections returned by `isajet`. For a given value of M_0 and $M_{1/2}$, the ratios of the NLO squark and gluino production process cross sections (gluino–gluino, squark–squark, etc.) match ratios of the types of squark and gluino events that `isajet` produces to within 10%. A list of total production cross sections for the MC points is given in Tables 7.1 through 7.3.

7.2 Optimization of the $\not\!\!E_T$ and H_T requirements

As seen in the figures of Sections 3.3 and 6.1, the characteristics of the signal change as M_0 and $M_{1/2}$ are varied. Therefore, more than one set of analysis requirements will help maximize signal efficiency and background rejection for each mSUGRA point. The two requirements that can be easily varied within some limits are $\not\!\!E_T$ and H_T.

For a given signal point, the efficiencies for passing the analysis requirements with $\not\!\!E_T$ ranging from 50 GeV to 150 GeV and H_T varying from 100 GeV to 250 GeV (both with 5 GeV steps) are recorded. A similar procedure is performed for all of the background efficiencies along with keeping track of their energy scale errors (or the QCD estimate error for the QCD background).

An "optimizing figure of merit" (F) is calculated for each tested $\not\!\!E_T - H_T$ point,

$$F(\not\!\!E_T,\, H_T) = S/\sqrt{B + (\delta B)^2} \tag{7.2}$$

where S is the number of signal events expected, B is the number of background events expected, and δB is the average of the sum high and low energy scale errors for all of the backgrounds added in quadrature with the QCD background estimate error. The optimal $\not\!\!E_T - H_T$ thresholds are found by looking near the peak of the 2-D F distribution. Typically, the maximum of F is the center of a plateau in the $\not\!\!E_T - H_T$ plane where F only

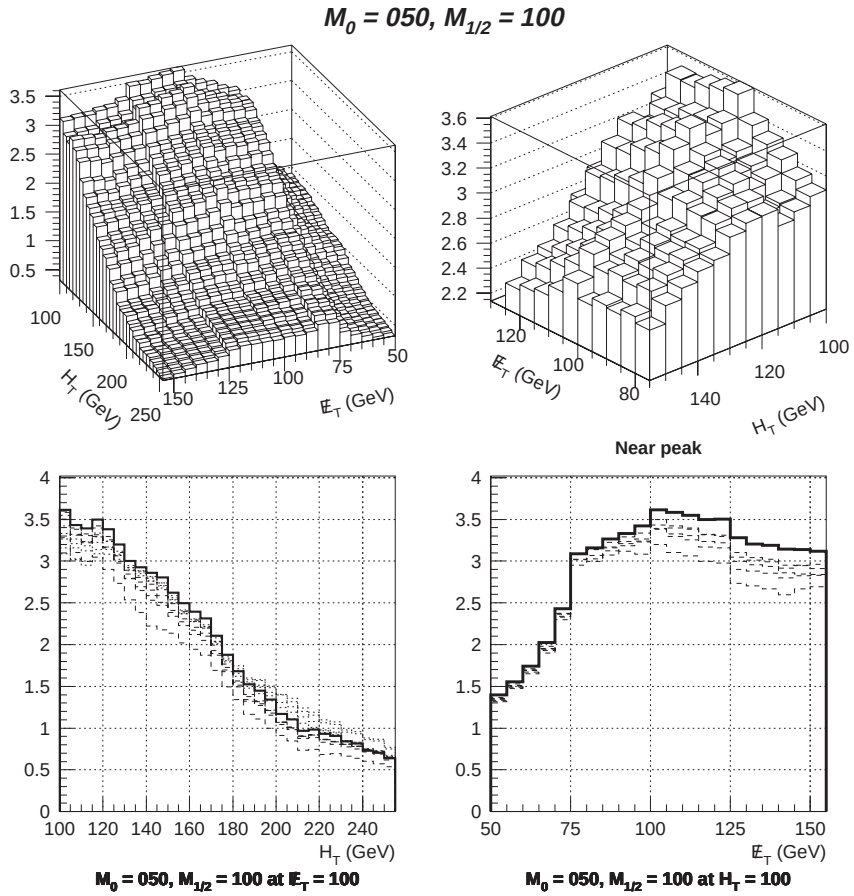

Figure 7.2: Optimizing figure of merit (F) for $M_0 = 50$ GeV and $M_{1/2} = 100$ GeV. The upper left plot shows F for the entire $\not\!\!E_T - H_T$ plane. The region around the peak of F is displayed in the upper right hand plot (note the different orientation of the plot). The lower two plots show the projection of F on the H_T axis (lower left) and the $\not\!\!E_T$ axis (lower right). The heavy solid line indicates the F trace for the $\not\!\!E_T$ or H_T slice that corresponds to the peak (and shown in the plot caption). The long dashed lines show F traces when the $\not\!\!E_T$ or H_T slice is moved higher the peak in five steps of 5 GeV each. The dotted lines are for moving lower than the peak (obviously, there will be no dotted lines on the $\not\!\!E_T$ plot when the peak H_T value is at the lower limit of 100 GeV). For this signal point, the optimal thresholds are $\not\!\!E_T = 100$ GeV and $H_T = 100$ GeV.

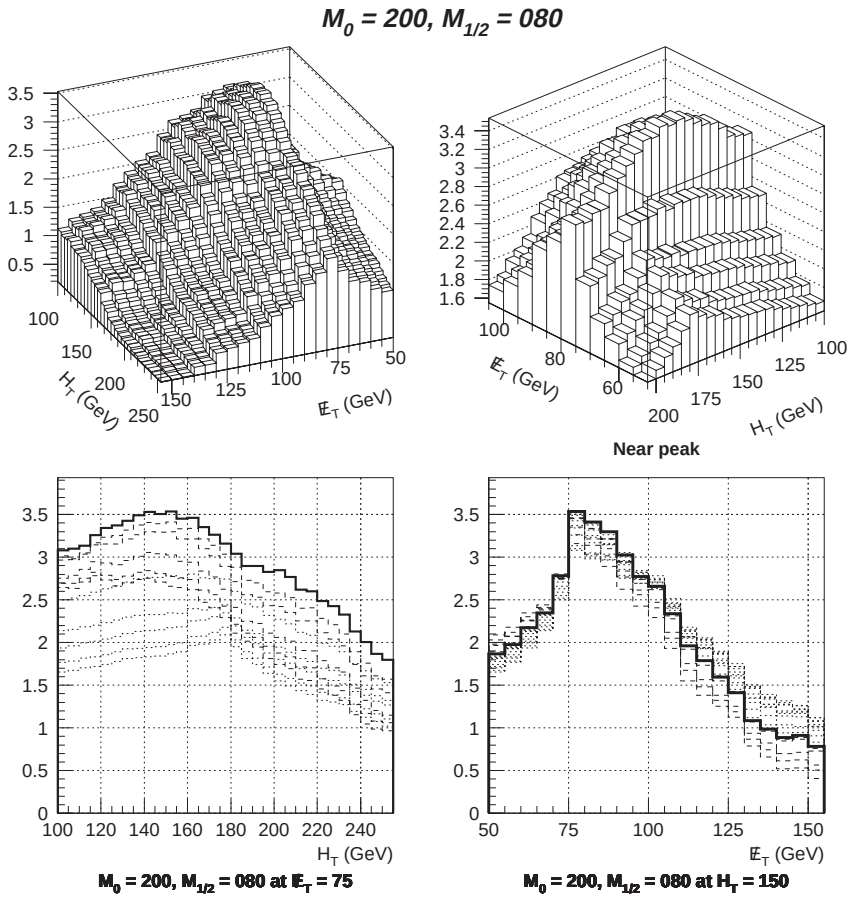

Figure 7.3: Optimizing figure of merit for $M_0 = 200$ GeV and $M_{1/2} = 80$ GeV. For this signal point, the optimal thresholds are $\not\!\!E_T = 75$ GeV and $H_T = 140$ GeV.

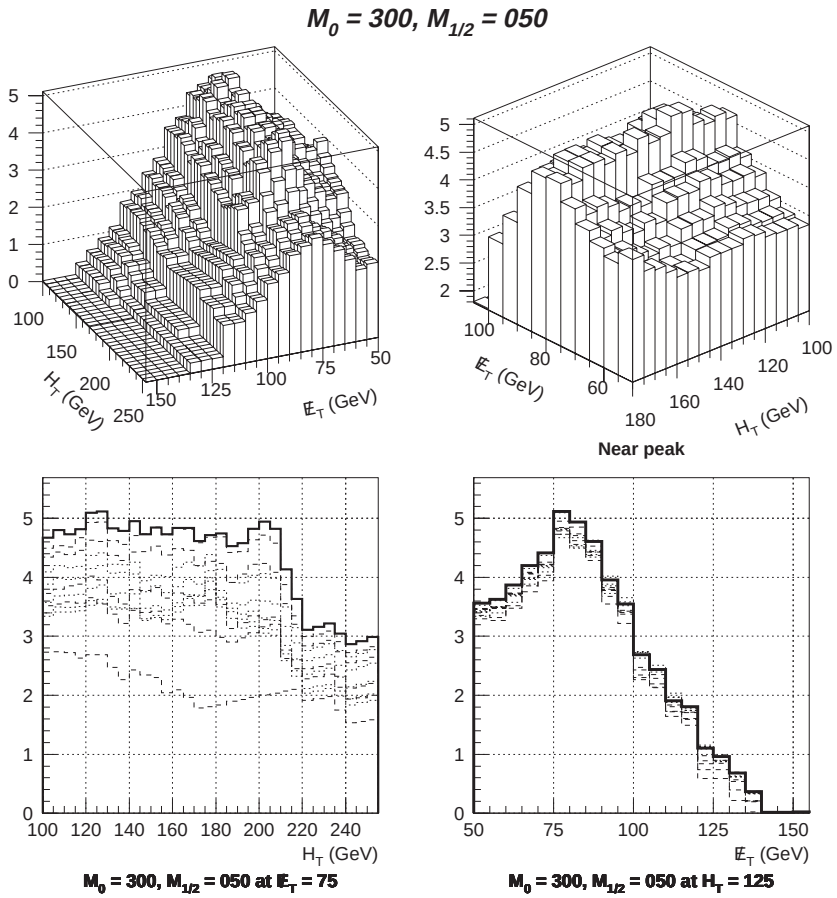

Figure 7.4: Optimizing figure of merit for $M_0 = 300$ GeV and $M_{1/2} = 50$ GeV. For this signal point, the optimal thresholds are $\not\!\!E_T = 75$ GeV and $H_T = 120$ GeV.

changes slightly. One chooses the lower edge of the plateau for greater signal efficiency to facilitate a discovery.

$\not\!\!E_T - H_T$ are optimized for all signal samples. Three example optimization plots are shown in Figures 7.2 through 7.4. As seen in the figures, the F value falls rapidly as $\not\!\!E_T$ drops below 75 GeV due to the rapidly increasing QCD background. An explanation of the general trends of the optimization is given in Section 7.5. Note that many signal samples have an optimized H_T of 100 GeV, the lower H_T limit. All of the mSUGRA samples have H_T peaked beyond 100 GeV, so decreasing H_T will soon start the fall of the F parameter as little signal is being added while the backgrounds are increasing. The value of 100 GeV H_T is probably very near true optimal for those signal points where F in H_T does not show a full plateau.

7.3 Signal Efficiency

Tables 7.1 through 7.3 include the optimized $\not\!\!E_T$ and H_T thresholds as well as the efficiency (ϵ) and number of events expected for each signal point ($< N >$). The errors on the efficiencies are the statistical and the high and low energy scale errors. The energy scale errors are calculated in the same manner as the backgrounds. The error on the expected number of events is the statistical and average of the energy scale errors added in quadrature. The `prospino` NLO cross sections (σ_{NLO}) are also shown along with the number of MC events generated not including events with scalar tops and isolated hot cells as discussed previously.

7.4 Calculation of the limit

With no excess of events over Standard Model backgrounds, upper limits on the cross section for production of squarks and gluinos are calculated. These limits indicate the reach of the experiment. Models that predict cross sections greater than the upper limit can be ruled out, since the resulting squarks and gluinos would have been observed in the analysis. Lower limits on the M_0 and $M_{1/2}$ mSUGRA parameters and the squark and

M_0 (GeV)	$M_{1/2}$ (GeV)	MC Events	$\not{E}_T >$ (GeV)	$H_T >$ (GeV)	σ_{NLO} (pb)	ϵ (%)	$< N >$
0	70	2468	75	100	30.1	$2.1 \pm 0.3 \,^{+0.5}_{-0.4}$	50.9 ± 13.2
0	80	2451	100	100	11.7	$2.8 \pm 0.3 \,^{+0.6}_{-0.5}$	25.7 ± 5.9
0	90	2428	100	100	5.8	$4.6 \pm 0.4 \,^{+0.8}_{-0.8}$	21.1 ± 3.9
0	100	2407	100	100	2.8	$4.9 \pm 0.4 \,^{+1.0}_{-1.1}$	10.8 ± 2.5
0	110	2389	100	100	1.3	$6.5 \pm 0.4 \,^{+0.5}_{-0.9}$	6.9 ± 0.9
50	70	2448	75	100	25.6	$2.7 \pm 0.3 \,^{+1.0}_{-0.6}$	54.5 ± 16.4
50	80	2454	100	100	11.3	$3.4 \pm 0.3 \,^{+1.1}_{-0.7}$	30.4 ± 8.5
50	90	2429	100	100	5.1	$4.3 \pm 0.4 \,^{+0.9}_{-1.0}$	17.3 ± 4.2
50	100	2406	100	100	2.5	$5.8 \pm 0.4 \,^{+0.9}_{-1.2}$	11.3 ± 2.2
50	110	2385	100	100	1.2	$6.7 \pm 0.5 \,^{+1.3}_{-1.2}$	6.5 ± 1.3
75	50	991	75	100	121.5	$1.1 \pm 0.3 \,^{+0.4}_{-0.4}$	107.5 ± 47.5
75	70	983	100	100	21.2	$2.2 \pm 0.4 \,^{+0.7}_{-0.5}$	37.7 ± 12.6
75	90	966	75	120	4.3	$5.9 \pm 0.7 \,^{+1.2}_{-0.9}$	19.9 ± 4.1
75	100	2408	100	100	2.2	$6.4 \pm 0.4 \,^{+1.3}_{-1.0}$	11.1 ± 2.1
75	110	963	100	100	1.1	$5.8 \pm 0.7 \,^{+1.8}_{-0.8}$	4.9 ± 1.2
100	60	2468	75	100	36.1	$2.2 \pm 0.3 \,^{+0.8}_{-0.5}$	62.2 ± 19.7
100	70	2438	75	100	16.7	$3.7 \pm 0.3 \,^{+1.3}_{-0.9}$	49.6 ± 14.9
100	80	2418	100	100	7.7	$4.1 \pm 0.4 \,^{+1.3}_{-1.1}$	24.9 ± 7.5
100	90	2425	90	100	3.7	$6.2 \pm 0.4 \,^{+0.9}_{-1.2}$	18.1 ± 3.3
100	100	2417	90	100	1.8	$7.7 \pm 0.5 \,^{+1.4}_{-1.5}$	11.1 ± 2.2
100	110	2358	100	100	0.9	$8.8 \pm 0.5 \,^{+1.3}_{-1.5}$	6.4 ± 1.1

Table 7.1: Signal information (small M_0). Details of the errors are given in the text. The cross sections are calculated by `prospino`, also discussed in the text.

M_0 (GeV)	$M_{1/2}$ (GeV)	MC Events	$\not{E}_T >$ (GeV)	$H_T >$ (GeV)	σ_{NLO} (pb)	ϵ (%)	$< N >$
150	50	2120	75	100	48.6	$1.5 \pm 0.2\,^{+0.6}_{-0.1}$	58.5 ± 16.3
150	70	2438	75	120	8.7	$4.4 \pm 0.4\,^{+1.3}_{-0.7}$	30.6 ± 7.3
150	80	2036	75	100	4.4	$5.8 \pm 0.5\,^{+1.7}_{-1.4}$	20.2 ± 5.8
150	90	2400	75	100	2.2	$8.5 \pm 0.5\,^{+1.3}_{-1.5}$	14.5 ± 2.5
150	100	2390	75	120	1.1	$8.8 \pm 0.5\,^{+1.1}_{-1.4}$	7.6 ± 1.1
150	110	2334	100	100	0.6	$10.2 \pm 0.6\,^{+0.9}_{-1.8}$	4.6 ± 0.7
200	50	2478	75	100	27.6	$1.5 \pm 0.2\,^{+0.5}_{-0.4}$	33.2 ± 11.7
200	60	2470	75	120	11.4	$2.5 \pm 0.3\,^{+0.9}_{-0.6}$	22.8 ± 7.0
200	70	2427	75	120	4.7	$4.8 \pm 0.4\,^{+0.8}_{-1.0}$	17.8 ± 3.6
200	80	2407	75	140	2.4	$5.8 \pm 0.4\,^{+1.0}_{-1.6}$	11.0 ± 2.6
200	90	2374	75	140	1.2	$8.8 \pm 0.5\,^{+1.1}_{-1.4}$	8.3 ± 1.3
200	110	2316	100	150	0.3	$9.2 \pm 0.5\,^{+0.6}_{-1.3}$	2.4 ± 0.3

Table 7.2: Signal information (intermediate M_0). Details of the errors are given in the text. The cross sections are calculated by `prospino`, also discussed in the text.

M_0 (GeV)	$M_{1/2}$ (GeV)	MC Events	$\not{E}_T >$ (GeV)	$H_T >$ (GeV)	σ_{NLO} (pb)	ϵ (%)	$< N >$
250	50	2475	75	120	19.7	$1.5 \pm 0.2\,^{+0.4}_{-0.4}$	22.9 ± 6.5
250	60	2461	75	150	7.1	$3.1 \pm 0.3\,^{+0.4}_{-0.9}$	17.3 ± 4.1
250	70	2443	75	160	3.1	$3.6 \pm 0.3\,^{+0.9}_{-0.5}$	8.6 ± 1.8
250	80	2370	75	150	1.3	$6.4 \pm 0.4\,^{+1.2}_{-1.1}$	6.6 ± 1.2
250	90	2332	75	150	0.6	$8.8 \pm 0.5\,^{+1.0}_{-1.6}$	4.3 ± 0.7
250	110	2228	75	160	0.2	$10.7 \pm 0.6\,^{+1.0}_{-0.9}$	1.4 ± 0.1
300	50	2488	75	120	15.7	$1.5 \pm 0.2\,^{+0.3}_{-0.2}$	18.5 ± 4.4
300	60	2444	75	120	5.3	$3.1 \pm 0.3\,^{+0.5}_{-0.4}$	13.1 ± 2.3
300	70	2406	75	160	2.0 2	$4.2 \pm 0.4\,^{+0.7}_{-0.8}$	6.7 ± 1.4
300	80	2362	75	160	0.9	$6.0 \pm 0.4\,^{+1.1}_{-1.2}$	4.0 ± 0.8
350	40	2491	75	100	48.3	$0.5 \pm 0.1\,^{+0.1}_{-0.2}$	20.6 ± 7.3
350	50	2479	75	120	14.1	$1.5 \pm 0.2\,^{+0.2}_{-0.4}$	16.5 ± 4.5
350	60	2468	75	120	4.6	$2.8 \pm 0.3\,^{+0.5}_{-0.8}$	10.0 ± 2.6
400	40	2494	75	100	46.3	$0.7 \pm 0.1\,^{+0.1}_{-0.4}$	25.8 ± 10.7
400	50	2480	75	120	13.4	$1.0 \pm 0.2\,^{+0.4}_{-0.2}$	10.7 ± 3.6
400	60	2461	75	120	4.4	$2.5 \pm 0.3\,^{+0.8}_{-0.5}$	8.7 ± 2.4

Table 7.3: Signal information (large M_0). Details of the errors are given in the text. The cross sections are calculated by `prospino`, also discussed in the text.

gluino masses can then be inferred from the upper cross section limits (a lower mass limit states that the masses of squarks and gluinos must be greater than the lower limit, or else they would have been observed). A 95% CL cross section limit is calculated within Bayesian statistics* and is described in Reference 110. A brief outline of the calculation for the cross section limit is given here.

The expression that drives this calculation is from Bayes Theorem†,

$$P(h \mid d, I) \propto P(d \mid h, I) P(h \mid I) \tag{7.3}$$

This equation states that probability that a hypothesis h is true given the data d and other information I is proportional to the *likelihood* of observing the data given the hypothesis times the *prior probability* of hypothesis being true without considering the data. The probability that hypothesis h is true is thus inferred from the data and the prior information. The constant of proportionality is determined from normalizing $P(h \mid d, I)$.

For this analysis, the model or hypothesis for the expected number of events (μ) in terms of the signal cross section (σ), the signal efficiency (ϵ), the integrated luminosity ($\mathcal{L}$), and the expected background (b) is given by

$$\mu = b + \mathcal{L}\epsilon\sigma \tag{7.4}$$

The likelihood function for observing the data is a Poisson distribution; the probability or likelihood of observing k events in the data given an expectation value of μ is,

$$P(k \mid \mu, I) = \frac{e^{-\mu}\mu^k}{k!} \tag{7.5}$$

*For more information on Bayesian statistics, see the definitive 3000 page "Bible of all things Bayesian" by Jaynes.[108] A superb introductory article is one by Loredo.[109]

†The notation for probabilities reflects the fact that all probabilities are conditional in the Bayesian framework; they must depend on some knowledge about the problem. For example, the probability that a tossed coin will come up heads would be written Prob(Heads$|\,I$) where I indicates the known information relevant to the problem, such as knowledge about the initial conditions of the flip and whether or not the coin is two headed. Assuming the coin is ordinary, the 50% probability of the coin coming up heads is derived from the fact that one does has little knowledge of the initial conditions (for if one knew the initial conditions exactly, the outcome of the flip could be predicted with certainty). P represents probability distributions. For example, the probability distribution for observing k events as a function of k given that the true expectation value is μ would be written as $P(k \mid \mu, I)$. I symbolizes relevant information about the problem (such as how the k events were obtained, whether the process is governed by Poisson statistics, etc.) that need not be shown explicitly. The expression is, in fact, the likelihood function for k given μ. $P(A\,B \mid I)$ indicates a joint probability distribution, or the probability for A and B given information I.

With the model of Equation (7.4), Equation (7.5) becomes

$$P(k \mid \sigma, \mathcal{L}, \epsilon, b, I) = \frac{e^{-(b+\mathcal{L}\epsilon\sigma)}(b + \mathcal{L}\epsilon\sigma)^k}{k!} \tag{7.6}$$

This expression is the probability of observing k events given σ, $\mathcal{L}$, ϵ, and b.

The other needed part of Equation (7.3) is the prior probabilities for the parameters. Since one has no knowledge about the true cross section for production of squarks and gluinos, the prior probability is taken to be flat (all values are equally likely),

$$P(\sigma \mid I) = \begin{cases} 1/\sigma_{\max} & \text{if } 0 \leq \sigma \leq \sigma_{\max}, \\ 0 & \text{otherwise.} \end{cases} \tag{7.7}$$

$\sigma_{\max}$ is chosen to be large enough so that the likelihood that the true signal cross section is greater than $\sigma_{\max}$ is negligible. The prior probabilities for the luminosity, background, and signal efficiencies are represented by truncated Gaussians with mean of the parameter value and standard deviation the parameter 1σ error. The correlations of errors is explained below.

With these parts, Bayes Theorem gives,

$$P(\sigma\, \mathcal{L}\, \epsilon\, b \mid k, I) \propto \frac{e^{-(b+\mathcal{L}\epsilon\sigma)}(b + \mathcal{L}\epsilon\sigma)^k}{k!}\, P(\sigma \mid I)\, P(\mathcal{L}\, \epsilon\, b \mid I) \tag{7.8}$$

This equation is the joint probability distribution for the signal cross section, luminosity, signal efficiency, and the background estimation. The desired result is the probability distribution for the signal cross section (σ), and so the other *nuisance parameters* are *marginalized* by integrating them out,

$$P(\sigma \mid k, I) = \int_0^\infty d\mathcal{L} \int_0^1 d\epsilon \int_0^\infty db\, P(\sigma\, \mathcal{L}\, \epsilon\, b \mid k, I) \tag{7.9}$$

$P(\sigma \mid k, I)$ is the probability distribution for the signal cross section given the data observed. The relevant result to report from a search is an upper limit on the signal cross section. The standard limit is at the 95% confidence level (CL) which can be determined by solving,

$$0.95 = \int_0^{\sigma_{\mathrm{UL}}} P(\sigma \mid k, I) d\sigma \tag{7.10}$$

for $\sigma_{\rm UL}$, the sought 95% CL upper limit.

The cross section upper limit is calculated with the `limit` program.[111] The program performs Monte Carlo integration to solve the integrals and takes into account correlations between the errors. The Gaussian priors are also truncated, which means that if a choice of a Gaussian random variable yields a negative, unphysical value for its parameter, then those results are discarded. The truncated Gaussians can create a problem if the signal efficiency (ϵ is small with a large error). The cross section is given by

$$\sigma = \frac{k - b}{\mathcal{L}\epsilon} \tag{7.11}$$

Though ϵ will never go negative since the Gaussian is truncated, if the Gaussian is peaked near zero, very small values of ϵ will be sampled in the course of the MC integration. Since the signal efficiency is in the denominator, the signal cross section can blow up. A remedy to this problem is under study.

The output of the `limit` program is the posterior probability distribution for the signal cross section. Two example distributions are shown in Figure 7.5. Note that the posterior probabilities are peaked near zero cross section. If the cross section has a negligible probability at zero, then perhaps a discovery could be at hand. The fact that no excess of events was found over backgrounds is reflected by the large probability for zero cross section for every signal point.

7.5 Exclusion Contour

A 95% CL cross section limit is calculated in the manner described in the previous section for each of the mSUGRA Monte Carlo points in the M_0 – $M_{1/2}$ plane. The problem with small signal efficiencies with large errors comes in for points with $M_0 > 300$ GeV, and so the limit beyond there is not known as of yet for this analysis. However, the DØ squark and gluino dielectron analysis covers that region. The appropriate background estimate and signal efficiency associated with an M_0, $M_{1/2}$ point are used by the limit calculator, along with the number of events seen in the data and the luminosity. The limit calculator accounts for the correlated energy scale, luminosity, and cross section errors (the $t\bar{t}$ cross

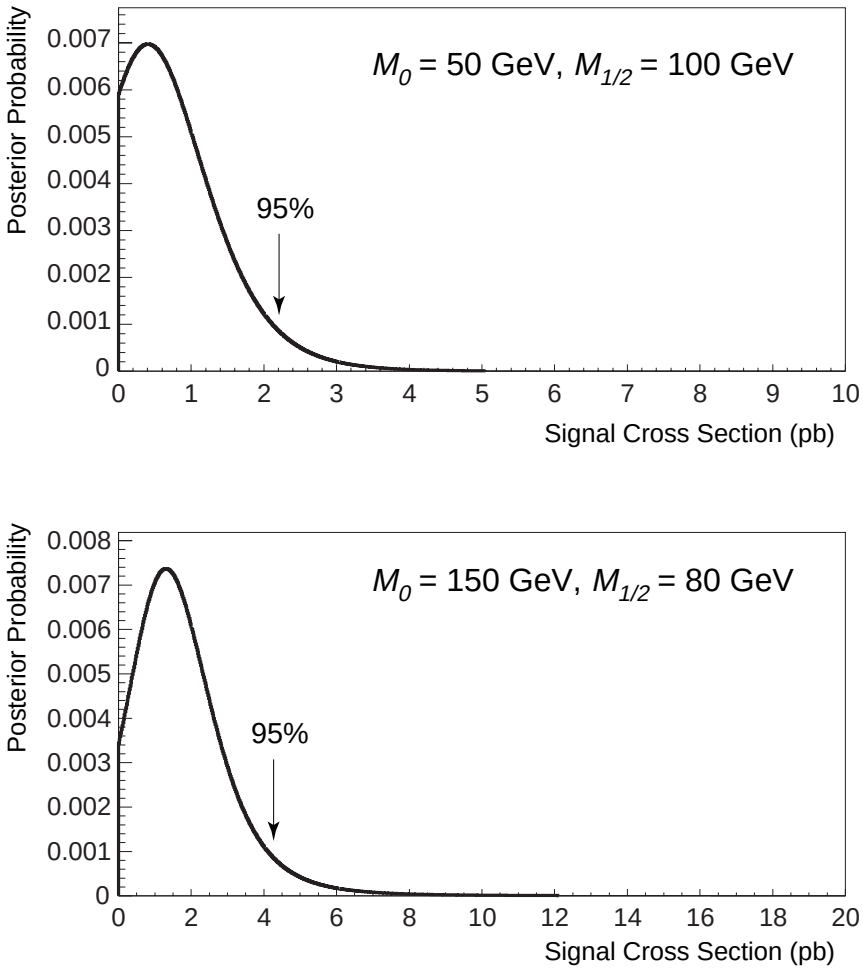

Figure 7.5: Posterior probability distributions for the signal cross section. The arrow indicates integrating out to 95% of the total area under the curve.

section error is uncorrelated with the others). Backgrounds where no events in the Monte Carlo pass the analysis requirements are not included in the limit calculation. The 95% CL upper limit on the total number of events that could contribute from those sources is 0.8 events.

The 95% CL upper cross section limits, σ_{UL}, are shown in Tables 7.4 through 7.5. Figure 7.6 shows which mSUGRA points are ruled out by this analysis when comparing σ_{UL} to the NLO theoretical cross section (σ_{NLO}). Points where $\sigma_{UL} < \sigma_{NLO}$ are excluded by this analysis, because the theoretical signal cross section at that point exceeds the upper limit. Theoretical and 95% CL cross sections for intermediate points are determined by interpolating.[112]

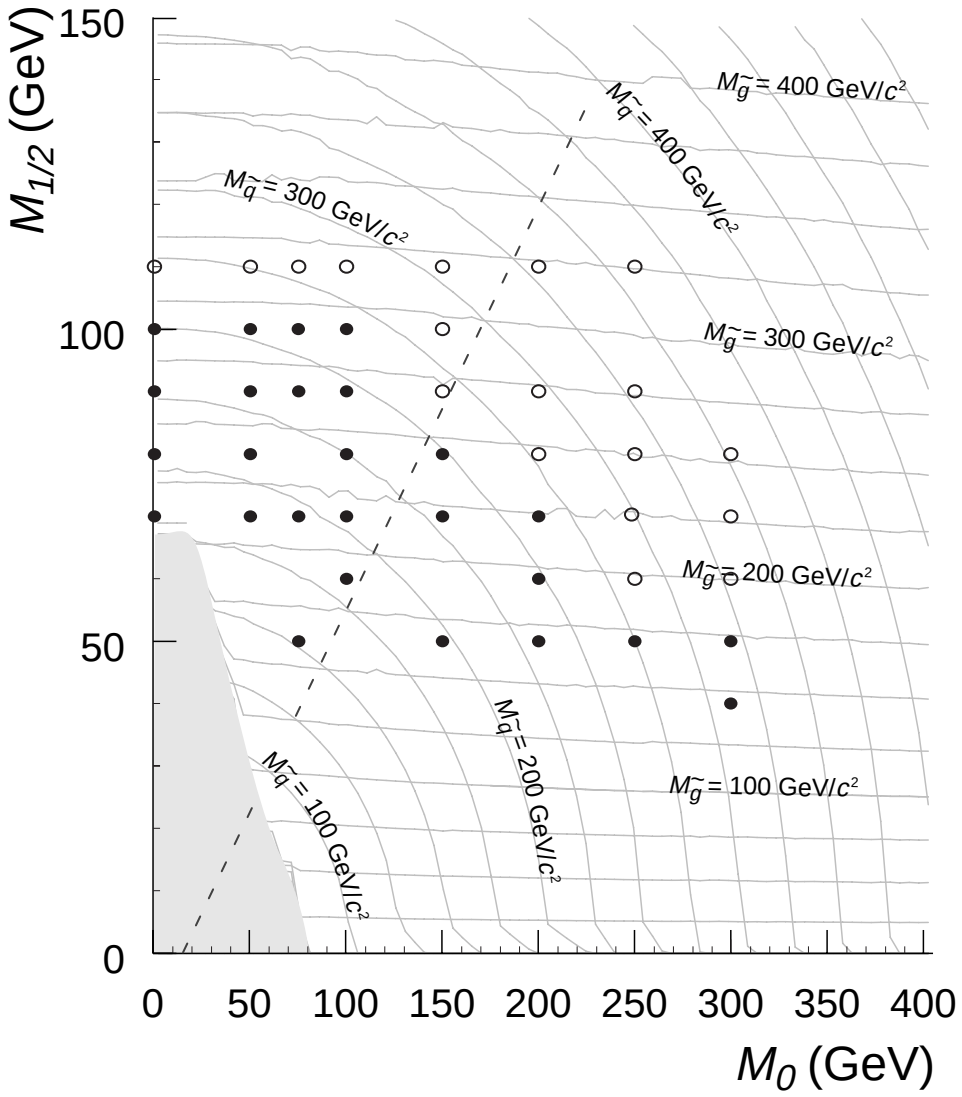

Figure 7.6: Excluded Monte Carlo signal points. Points excluded at 95% CL are filled. Points that cannot be ruled out are open. The other lines on the plot are described in the caption of Figure 7.1.

M_0	$M_{1/2}$	$M_{\tilde{g}}$	$M_{\tilde{q}}$	$\not\!\!E_T >$	$H_T >$	σ_{NLO}	σ_{LO}	σ_{UL}
0	70	209	182	75	100	30.1	20.0	**10.8**
0	80	240	207	100	100	11.7	7.6	**4.4**
0	90	262	228	100	100	5.8	3.7	**2.6**
0	100	288	250	100	100	2.8	1.8	**2.6**
0	110	314	272	100	100	1.3	0.8	1.8
50	70	211	188	75	100	25.6	17.0	**8.6**
50	80	237	210	100	100	11.3	7.3	**5.8**
50	90	263	232	100	100	5.1	3.3	**3.2**
50	100	288	254	100	100	2.5	1.6	**2.2**
50	110	315	276	100	100	1.2	0.7	1.8
75	50	161	153	75	100	121.5	81.4	**43.2**
75	70	212	195	100	100	21.2	13.9	**7.4**
75	90	266	239	75	120	4.3	2.7	**3.4**
75	100	289	259	100	100	2.2	1.4	**1.8**
75	110	315	281	100	100	1.1	0.7	2.0
100	60	190	185	75	100	36.1	23.6	**11.1**
100	70	214	205	75	100	16.7	10.8	**6.2**
100	80	240	225	100	100	7.7	4.9	**3.5**
100	90	266	246	90	100	3.7	2.3	**2.0**
100	100	290	266	90	100	1.8	1.1	**1.6**
100	110	316	287	100	100	0.9	0.6	1.3

Table 7.4: 95% CL cross section upper limits (σ_{UL}) for small M_0. All cross sections are in pb. Masses and energies are GeV/c^2 and GeV respectively. Points that are ruled out ($\sigma_{UL} < \sigma_{NLO}$) have the 95% CL cross section in bold.

M_0	$M_{1/2}$	$M_{\tilde{g}}$	$M_{\tilde{q}}$	$\not\!\!E_T >$	$H_T >$	σ_{NLO}	σ_{LO}	σ_{UL}
150	50	165	196	75	100	48.6	30.0	**12.0**
150	70	221	231	75	120	8.7	5.4	**4.4**
150	80	243	249	75	100	4.4	2.7	**4.2**
150	90	269	268	75	100	2.2	1.3	2.5
150	100	294	287	75	120	1.1	0.7	2.2
150	110	319	305	100	100	0.6	0.3	1.2
200	50	169	234	75	100	27.6	16.0	**14.7**
200	60	195	247	75	120	11.4	6.7	**8.8**
200	70	224	263	75	120	4.7	2.8	**4.4**
200	80	246	278	75	140	2.4	1.4	4.8
200	90	272	295	75	140	1.2	0.7	2.3
200	110	322	330	100	150	0.3	0.2	0.9
250	50	170	274	75	120	19.7	10.9	**14.6**
250	60	198	286	75	150	7.1	3.9	7.6
250	70	223	299	75	160	3.1	1.7	3.5
250	80	251	313	75	150	1.3	0.7	2.5
250	90	277	328	75	150	0.6	0.4	1.8
250	110	326	359	75	160	0.2	0.1	1.1
300	50	172	318	75	120	15.7	8.6	**14.2**
300	60	200	328	75	120	5.3	2.8	6.1
300	70	228	339	75	160	2.0	1.1	3.2

Table 7.5: 95% CL cross section upper limits (σ_{UL}) for intermediate and large M_0. All cross sections are in pb. Masses and energies are GeV/c^2 and GeV respectively. Points that are ruled out ($\sigma_{UL} < \sigma_{NLO}$) have the 95% CL cross section in bold.

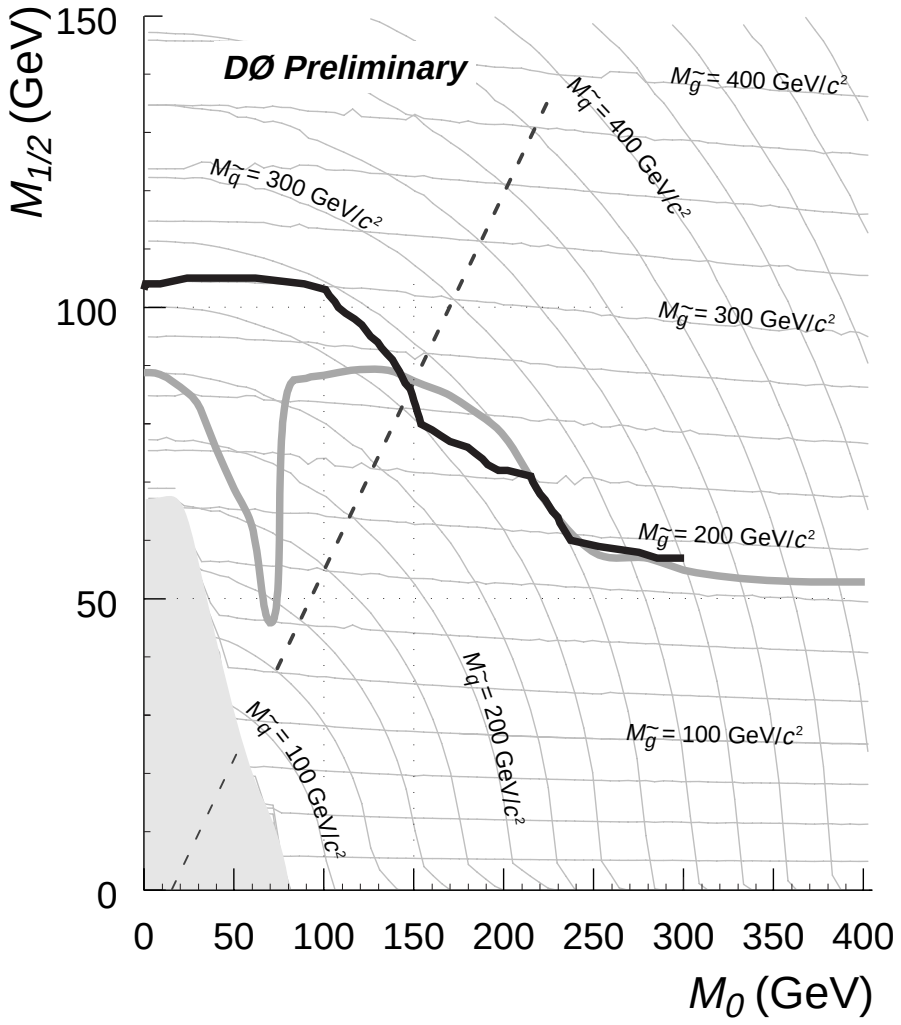

Figure 7.7: Exclusion contour in the M_0 – $M_{1/2}$ plane. This analysis rules out M_0 and $M_{1/2}$ points below the solid black line. The dielectron squark and gluino analysis contour[36] is shown in grey (note that analysis uses cross sections from `isajet`). The grey lines are contours of gluino and squark masses so marked. The shaded region is where mSUGRA yields some unphysical condition (such as no electroweak symmetry breaking). The dashed line indicates where squarks and gluinos have equal mass.

An exclusion region in the M_0 – $M_{1/2}$ plane is determined by again comparing the theoretical next-to-leading order cross sections to σ_{UL}. The exclusion contour is shown in Figure 7.7. For $M_0 < 100$ GeV, points with $M_{1/2} < \sim$103 GeV are ruled out. Note that the dip in the dielectron limit (shown in grey in the figure) is not present in this analysis. The dip is due to sneutrinos becoming lighter than the second lightest neutralino as $M_{1/2}$ is decreased, spoiling the dielectron signature. Since this analysis is only concerned with jets, changes in the lepton branching fractions produces no effect.

Beyond M_0 of 100 GeV, the limit falls quickly. Figure 3.3 on page 33 indicates why that happens. As seen in the figure, for small M_0 and large $M_{1/2}$ mostly squarks are being produced. Directly decaying squarks tend to produce larger E_T jets and $\not\!\!E_T$ than cascade decaying gluinos, and so the efficiencies for the signals samples there are large. Accordingly, in that region the optimization tends to choose large $\not\!\!E_T$ and lower H_T, since while the jets have large E_T, there are fewer of them produced (compare the signal plots in Figure 3.7 on page 39) than in gluino decays. As M_0 is increased, the squarks become heavier and so the gluinos processes start to dominate the production. Gluino cascade decays yield more jets, but they are softer and less $\not\!\!E_T$ is produced (compare the signal plots in Figure 3.6 on page 38). The optimization tends to choose less $\not\!\!E_T$ and then larger H_T to gain advantage over the large backgrounds.

The limit contour is quite robust. Altering the background estimates by ± 1 event shifts the limit by only 3–4 GeV, and none of the ruled out Monte Carlo points move out of the excluded region.

The limit on the M_0 – $M_{1/2}$ plane can be translated into limits on the physical squark and gluino masses as shown in Figure 7.8. Note that there are squark and gluino masses that have no corresponding model in mSUGRA. The excluded region includes all mSUGRA models with $m_{\tilde{q}} < 250$ GeV/c^2. For small M_0, gluinos with mass less than 300 GeV/c^2 are excluded. If squarks and gluinos have the same mass, that common mass must be greater than 260 GeV/c^2 to not be ruled out.

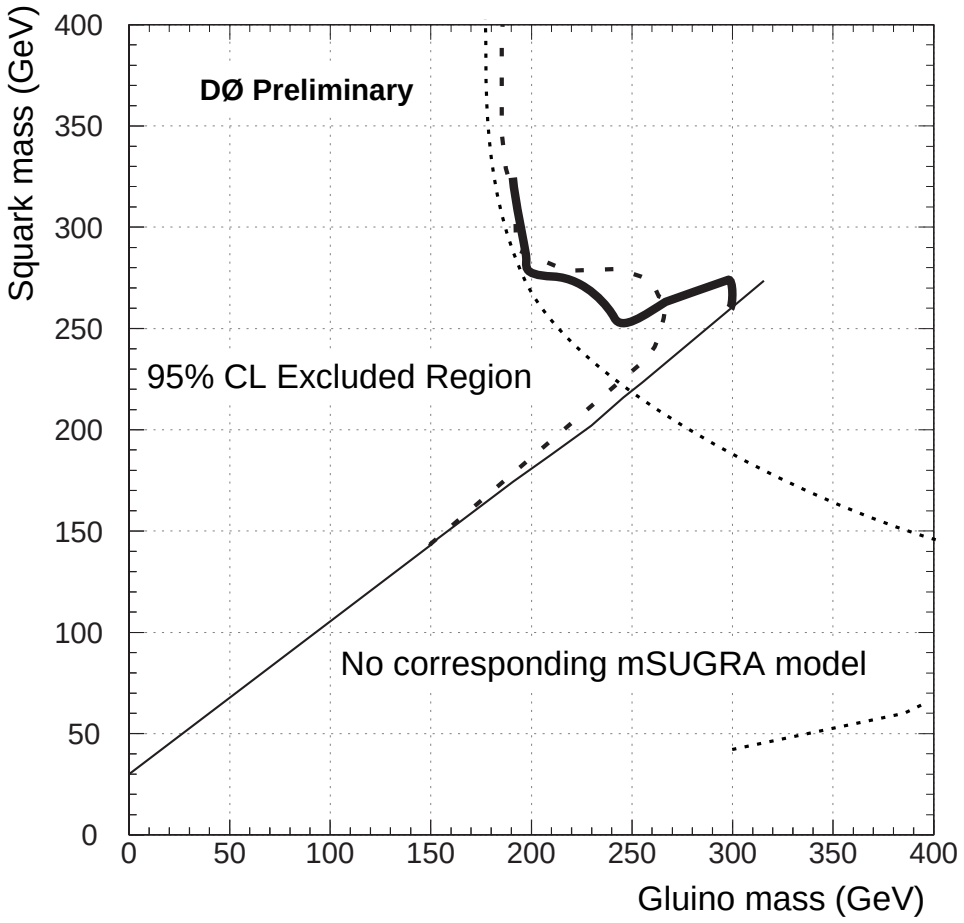

Figure 7.8: Limits in the $M_{\tilde{q}} - M_{\tilde{g}}$ plane. The heavy solid line is the exclusion contour from this analysis. The long dashed line is the contour from the DØ dielectron analysis.[36] The short dashed line is part of the previous DØ limit from the 1992–1993 run.[37,38] Masses below and right of the thin diagonal line have no corresponding mSUGRA models.

7.6 Summary

This analysis gives no evidence for physics beyond the Standard Model, since no excess of events beyond the backgrounds are seen. This result is interpreted in the mSUGRA framework. The sensitivity of the analysis to mSUGRA models needs to be determined, since seeing no excess does not in and of itself rule out Supersymmetry. The analysis can only rule out models that predict a significant excess of events in the amount of data analyzed. For example, some mSUGRA models (those with large M_0 and $M_{1/2}$) predict that squarks and gluinos are produced at such a small rate that one would not expect to see them unless much more data are collected. Furthermore, not all squark and gluino events will pass the analysis requirements, so the signal efficiency of the analysis also determines which models can be excluded.

This analysis can exclude a large part of the Supergravity parameter space as shown in Figure 7.7. Any theorist favoring a model with M_0 and $M_{1/2}$ below the solid black line in that figure (and the solid grey line for large M_0) will have to search for a new model, for models in that region are ruled out by this search.

Chapter 8

Conclusions

This analysis searched for squarks and gluinos within the minimal Supergravity framework through their hadronic decays. The desired signal events are those with many jets and large missing energy. No significant excess over Standard Model backgrounds is observed, and so the results are in the form of cross section limits at 95% CL and corresponding limits on the mSUGRA parameters of M_0 and $M_{1/2}$. Those limits can be translated for limits on squark and gluino masses.

Section 3.6 discussed the naturalness of Supersymmetry, or when one gets worried that the sparticles are too much heavier than their SM partners. Figure 8.1 shows the limit from this analysis and the dielectron search superimposed on contours of a naturalness measure[50, 113] labeled $\tilde{\gamma}_2$. A model with a smaller naturalness measure is more natural than models with larger $\tilde{\gamma}_2$. One sees that a large part of the most natural region is excluded by these analyses.

Strong limits are set for low M_0. To set strong limits in the region of large M_0, it is necessary to increase dramatically the signal efficiency. In order to do so, the $\not\!\!E_T$ requirement must be lowered. To avoid the rapidly increasing backgrounds, one may consider raising the number of jets required. To drop $\not\!\!E_T$ lower to gain enough efficiency, it may be necessary to use another trigger with a lower $\not\!\!E_T$ requirement than `missing_et`. The leptonic searches also win in that region, since though branching fractions to leptons are small, the backgrounds are also small and are more easily understood.

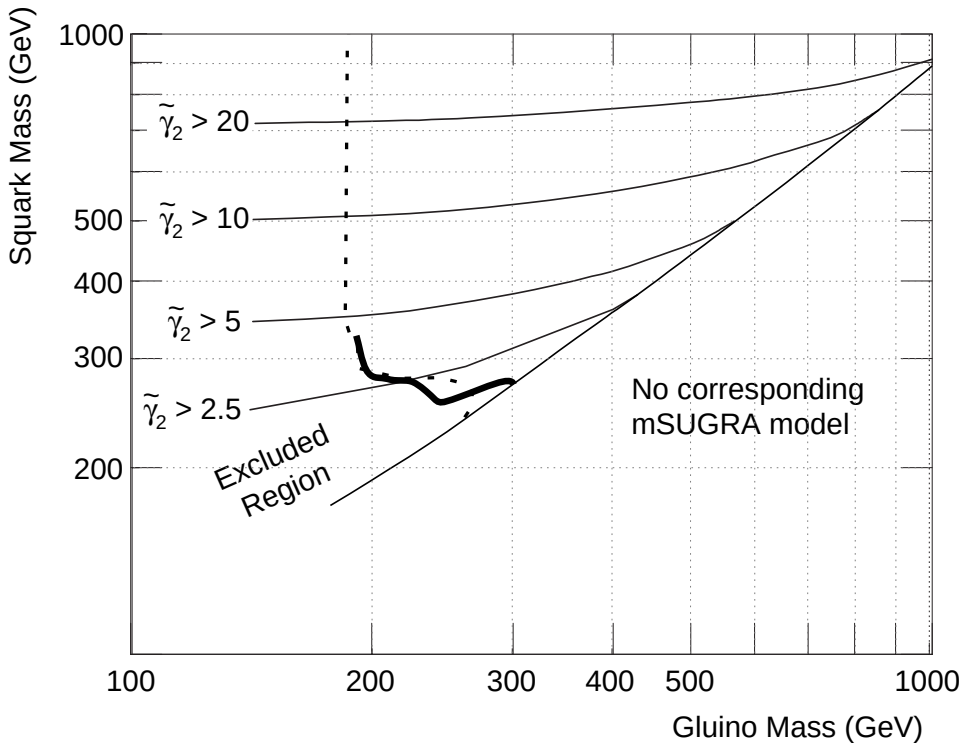

Figure 8.1: Exclusion of most natural SUSY. The $\tilde{\gamma}_2$ contours are described in the text. The heavy solid line is the limit from this jets and $\not\!\!E_T$ analysis. The dashed line is the DØ dielectron limit (assumed to be asymptotic for large squark mass). Note that a log–log plot is shown.

For the future, more SUSY models will be tested to expand the range of the analysis. In the next run of the Tevatron (Run II) to begin in 1999, the instantaneous luminosity will increase by an order of magnitude. Therefore, data corresponding to inverse femtobarns (1000s of pb^{-1}) will be collected within a few years, allowing searches to extend into regions of heavier squark and gluino mass. For example, with 2 fb^{-1} of data, gluinos up to $\sim$400 GeV/c^2 can be probed.[114] The effectiveness of the jets and $\not\!\!E_T$ signature for the next run is uncertain, since the backgrounds will be huge and estimating the background due to QCD multijet events will be even more difficult than for this analysis.

For the next Tevatron run, the DØ detector will undergo a substantial upgrade. The central detectors will be replaced with a silicon vertex detector and a scintillating fiber tracker within a superconducting magnet (2 T field). Since the p_T of tracks will be measured, there should be little contamination from misvertexed events. While the calorimeter will remain the same, its electronics will be upgraded to handle the faster crossing times (132 ns). The muon system will be improved as well, increasing the acceptance and resolution for measuring muons. All of these changes will greatly improve identification and measurement of leptons, allowing the leptonic SUSY searches to probe more parameter space. With the silicon vertex detector, b–quarks are easily observable. Requiring events with a "b–tag" will help to improve the jets and $\not\!\!E_T$ search for squarks and gluinos, since more of the QCD multijet background can be rejected.

In the farther future, the Large Hadron Collider (LHC) at CERN will collide beams sometime in the next decade. With a center of mass energy of 14 TeV, squarks and gluinos with TeV/c^2 masses can be probed. If no evidence of sparticles at the LHC is observed, then the mass splittings are so large that SUSY will probably no longer be a viable theory.

Of course, the hope is that someday a new particle will be observed. There are still plenty of chances with the Tevatron Run II and the LHC. Until that day, the SUSY parameter space will be further constrained by other SUSY searches. With the Minimal Supergravity models, the results from many searches for sparticles can be easily combined, improving limits obtained by any one analysis. DØ searches for squarks and gluinos in

the dimuon and electron–muon channels are underway as are searches for charginos and neutralinos, scalar tops, and R–parity violating SUSY processes. The work is still not finished if a sparticle is discovered, for the correct SUSY model must still be determined. Theorists and experimentalists will worry about that exciting problem if that time comes.

Appendix A

How particles interact with matter

This appendix gives some background on how particles interact with matter, the physics behind particle detectors.[115, 116]

A.1 Heavy Charged Particles

When particles pass through materials, there are two effects: they will lose energy and may be deflected from their original direction. Charged particles will lose energy primarily from inelastic collisions with atomic electrons in the medium or at high energies (above 100s of MeV) from scattering with nuclei. More rarely, energy loss can also occur from emitting bremsstrahlung radiation, Cherenkov radiation, or even nuclear fission. For charged particles heavier than the electron, the predominant means of energy loss is inelastic collisions with atomic electrons. A soft collision occurs when the energy imparted to the atomic electron only results in the electron's excitation. Hard collisions are those where the passing particle loses enough energy to ionize the electron, thus freeing it from the atom. It is possible for so much energy to be given to the liberated electron that it will cause secondary ionizations of other atomic electrons. Such high energy electrons are called δ-rays or knock–on electrons. Although each interaction with an atomic electron or nuclei is statistical in nature, so many interactions occur as the heavy charged particle passes through a material that the macroscopic average energy loss per unit path length, dE/dx, can be predicted and measured.

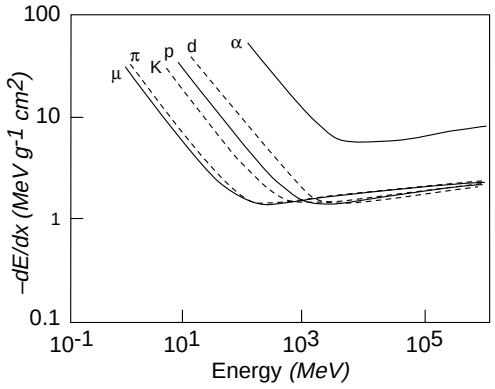

Figure A.1: dE/dx for several particles in some material vs. their energy. A log–log plot is displayed[115]

A classical formula for dE/dx for heavy charged particles was first determined by Bohr. One must assume that the atomic electron is initially at rest and is free, and that the charged particle is not deflected from its original path as a result of the interaction, implying $M \gg m_e$. Therefore, a different treatment is necessary for electrons passing through the medium. Relativistic effects are also important, and so the Bethe-Bloch formula[4, 115] is used rather than Bohr's classical equation.

Rather than write out the complicated Bethe-Bloch formula (see page 24 of Reference 115) its implications will be briefly discussed. A plot of the average energy loss for several particles traversing a block of some material as predicted by the Bethe-Bloch formula is shown in Figure A.1. For low energy particles, dE/dx falls as $1/\beta^2$, where β is v/c, until $v \approx 0.96c$ when a minimum is reached. At that point, the particles lose the minimum amount of energy as they traverse the medium and are called minimum ionizing particles. The last feature to note in Figure A.1 is the relativistic rise where dE/dx increases slowly past the minimum. The rise is less than logarithmic due to the density effect. A high energy particle traversing the medium will polarize atoms along its path, so electrons far from the particle are shielded from the full electric field and contribute less to the dE/dx than they would otherwise. Since more energy is lost at slow velocity, more energy is deposited into the material towards the end of a particle's path than at the beginning.

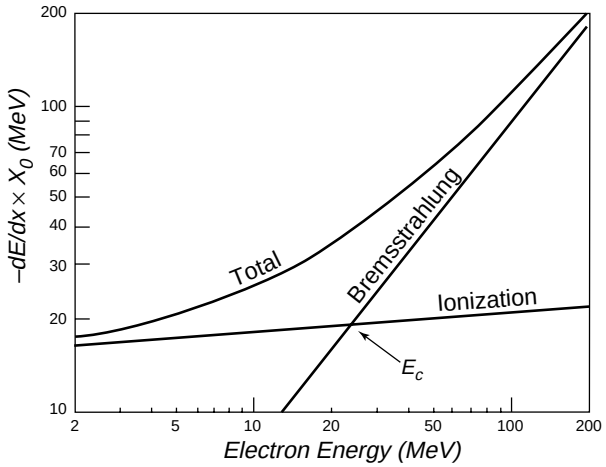

Figure A.2: Energy loss for electrons in copper. $X_0 = 12.86$ g/cm^2, $E_c = 24.8$ MeV.[4, 115] Note the log-log axes.

The minimum ionizing point and relativistic rise are very similar for particles of the same charge traversing the same material, as evident from Figure A.1, but some of the $1/\beta^2$ parts of the curves are different and can be used for particle identification. In addition, particles of the same velocity have similar dE/dx in different media.

A.2 Electrons

The description of the standard Bethe-Bloch formula is not applicable to electrons and positrons, because they are so light. $e^{\pm}$ will not only suffer collisions with other atomic collisions but can also radiate photons due to scattering in the electric field of a nucleus (bremsstrahlung radiation). Since the cross section for bremsstrahlung goes as $1/M^2$, heavier particles radiate much less often than electrons (e.g. 40,000 times less for muons).

The energy loss for electrons traversing material is split into two parts,

$$\left(\frac{dE}{dx}\right)_{\text{total}} = \left(\frac{dE}{dx}\right)_{\text{collisions}} + \left(\frac{dE}{dx}\right)_{\text{radiation}} \tag{A.1}$$

For electrons with energy of a few MeV and below, collision (ionization) losses dominate. At energies of tens of MeV and more, the radiation term of the total dE/dx takes over as seen in Figure A.2. The point at which the average loss due to collisions equals that due to bremsstrahlung radiation is the critical energy, E_c, as shown in the figure. In

Material	A	Z	X_0 [g/cm^2]	λ [g/cm^2]	density [g/cm^3]
Air at STP	–	–	36.66	90	273
NaI Crystal	–	–	9.49	152	3.67
Liquid Argon	40	18	19.55	117	1.40
Iron	56	26	13.84	132	7.87
Lead	207	82	6.37	194	11.35
Uranium	238	92	6.00	199	$\sim$19

Table A.1: Properties of some materials.[4, 115]

general, dE/dx from collisions increases logarithmically with the energy of the electron and linearly with the Z of the material. dE/dx due to radiation increases linearly with E and quadratically with Z.

In order to refer to energy loss without explicitly stating the material, a quantity called radiation length (X_0) is used. A radiation length is related to the distance an electron travels before its energy is reduced by a factor of $1/e$ due to losses. X_0/ρ, where ρ is the density of the material, gives the actual distance. A listing of such quantities for a few materials is given in Table A.1.

Positrons will undergo one more type of interaction: annihilation with electrons. When that happens, two photons with energy of at least 0.511 MeV are released.

A.3 Photons

Neutral particles interact differently with matter. Without an electric field, neutral particles rarely interact through ionization of atomic electrons. Depending on the mass and type of neutral particle, different interactions are possible.

Photons have zero mass and interact with matter electromagnetically through the photoelectric effect, compton scattering and pair production. For the photoelectric effect, an incident photon is completely absorbed by an atomic electron which is ejected from the atom if the photon has enough energy. This process can only occur with atomic electrons, since the nucleus must be present to absorb the recoil momentum. Compton scattering is the scattering of photons with free electrons (or atomic e if the photon energy exceeds

the ionization energy), such that the photon gives up some energy to the electron. Both the photon and the electron survive the scattering, and the photon is deflected.

If a photon's energy exceeds 1.012 MeV ($E_\gamma > 2m_e$), it can transform into an electron-positron pair. A third body must also be present, such as a nucleus, to conserve momentum. This process occurs with the largest cross section for photons with energy greater than a few MeV to tens of MeV, depending on the material.

For electrons and photons at high energy, an interesting consequence of the dominating cross sections for bremsstrahlung and pair production is the production of electromagnetic showers. Imagine a high energy electron entering some material. It will produce bremsstrahlung radiation, releasing many high energy photons. Each of these photons with enough energy will pair produce, creating more high energy electron and positron pairs. The electrons can undergo bremsstrahlung again, creating more photons and so on. This shower of electrons and photons continues to multiply until the average electron energy falls below E_c, and each electron interaction with the material produces one or no photons. Such showers are crucial for operation of a calorimeter.

A.4 Neutrons

Neutrons interact with nuclei through the strong force and are non-ionizing. Neutrons can elastically scatter off nuclei, inelastically scatter leaving the nucleus in an excited state, be radiatively captured by a nucleus where the nucleus absorbs the neutron and radiates a photon, and undergo reactions where the nucleus absorbs the neutron and emits a charged particle (proton, deuteron, alpha, or combinations of those). Finally, when traversing certain materials like Uranium, neutrons can cause a nucleus to undergo fission.

A.5 Hadronic Showers

Hadrons are particles that feel the strong force, such as neutrons, protons, pions and kaons. Like electrons, hadrons with enough energy can also create showers in materials.

High energy hadrons (over hundreds of MeV) will interact with nuclei, exciting them and producing mesons (hadrons made up of a quark and an antiquark, such as pions and kaons). Highly excited nuclei will emit protons and neutrons. Photons and ionized electrons will be released from atoms with nuclei excited to a lesser extent. All of these particles will interact with the material as well, and, like electromagnetic showers, will create a cascade of particles. Since electrons and photons are released in hadronic showers, electromagnetic showers are also produced.

Somewhat similar to the radiation length, the nuclear interaction length λ is the distance a high energy hadron travels before interacting with a nucleus. A radiation length is much shorter than an interaction length for the same material. Some example interaction lengths are given in Table A.1.

A.6 Multiple Scattering

With every interaction in a material that a particle survives, there is a chance that the particle's direction will be altered. The degree of deflection depends on the particle's energy and the nature of the interaction. Though each deflection is statistical in nature, the outcome of a particle passing through some medium, if it survives, is a net change in direction due to multiple scattering. A Gaussian approximation for small angle multiple scattering of charged particles gives,[4]

$$\theta_{rms} = \frac{0.015\,\mathrm{GeV}/c}{\beta p}\sqrt{\frac{X}{X_0}} \tag{A.2}$$

where θ_{rms} is the r.m.s. deflection in the plane containing the particle, p is the particle momentum, β is v/c, X is the material thickness, and X_0 is one radiation length for that material.

Appendix B

Principles of Drift Chambers

Drift chambers are an important tool for measuring the properties of particles emanating from collisions. Some details on the principles and the operation of drift chambers[115, 117, 118] are given in this appendix.

The DØ VTX chamber, CDC, and FDC are drift chambers that measure the direction of a particle by collecting electrons and ions released as the particle passes through some tracking medium. Since the particle's direction should remain as undisturbed as possible, gases are the optimal choice for the tracking medium, though liquids can also be used as well.

A simplified *drift cell* is shown in Figure B.1. It consists of a very thin sense or anode wire, usually in the middle of the cell, a cathode at the edge of the cell, and electric field shaping wires. The wires form a constant electric field so that electrons liberated by an ionizing particle travel along the field lines towards the anode that is at a high positive voltage. The liberated ions drift towards the cathode. At about one wire radius away from the anode wire, the electric field strength increases very quickly. An electron in this region becomes accelerated to a high energy and causes further ionizations of the gas. The electrons liberated in those secondary ionizations will produce tertiary ionizations and so on. Thus, an avalanche of electrons will occur just outside of the wire with their positive ions moving away towards the cathode. This avalanche amplifies the resulting signal by several orders of magnitude. Such amplification is called *gas gain*. Contrary to intuition, the signal pulse on the anode wire is produced by induction due to the motion

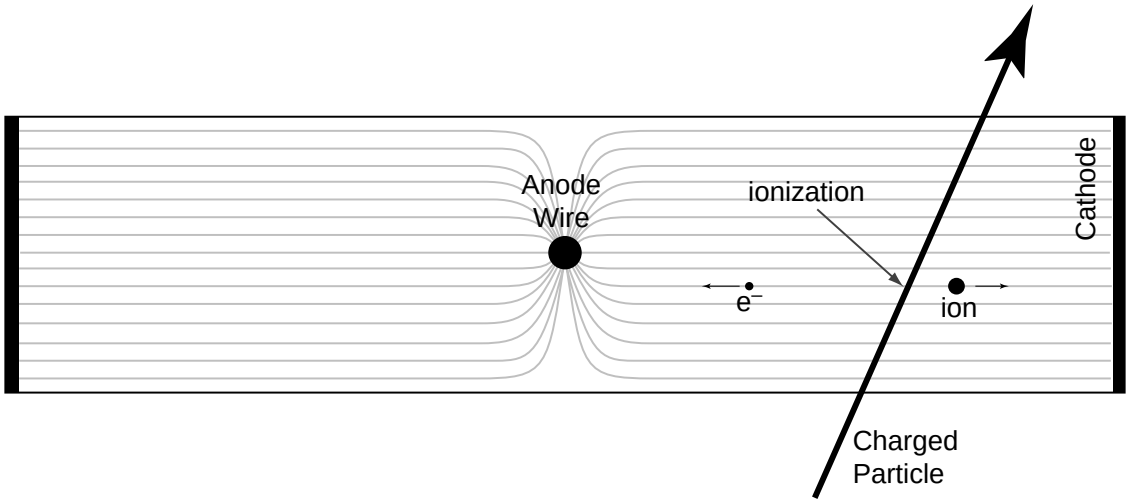

Figure B.1: An example drift cell, viewed looking down the anode wire. Shown in grey are the electric field lines. Field shaping wires are not displayed.

of the positive ions. The movement of the electrons gives only a small contribution, and even though the ions move very slowly compared to electrons, the rise time of the signal is very fast.

As the liberated ions travel through the drift volume along the electric field lines, they collide with gas molecules along the way. These very soft collisions slow the accelerating electrons and ions so that, in effect, they travel at a constant *drift velocity*. The drift velocity depends on the gas mixture in the drift volume. If one knows the drift velocity and the time difference between the particle entering the chamber and the pulse on the anode wire, the position of the primary ionization, and thus the position of the passing particle at the time of ionization, can be determined. In DØ, the first time marker, t_0, is given by the beam crossing time. For the VTX chamber, drift distances are up to 12 mm and the position resolution is 40-60 μm for drift distance greater than 4 mm. For the CDC, typical drift distances are a few centimeters with position resolution from about 150 mm to 260 mm as measured from test beam data.[52, 53]

Although the distance of the primary ionization from the anode wire can be determined, one does now know which side of the wire the ionization occurred, because the only information one has is the drift time. This confusion is called *left-right ambiguity*. Drift cells are therefore usually stacked in layers, with each layer offset from the others

by some fraction of the cell width. By connecting the *hits* from several cells in two or three layers, the correct sides of each wire can be determined by the sides that form a contiguous *track* through the detector.

To measure the position where the avalanche occurs *along* the anode wire, DØ tracking detectors use either charge division or delay lines. The method of charge division involves collecting charge at both ends of the anode wire. The ratio of the charge collected from one end to the total is equal to the ratio of the distance the charge was injected from that end to the total wire length. The use of delay lines is a more accurate technique. A delay line is an additional wire running the length of the cell parallel to the anode and is capacitively coupled to the cathode planes. Given a t_0, the position of the avalanche along the wire can be calculated from the time difference between the arrival of signals from each end of the delay line. The VTX chamber and the CDC have their sense wires running parallel to the z axis. To measure the z coordinate of a hit, the VTX chamber uses charge division while the CDC uses delay lines.

Since the signal from a drift cell is proportional to the energy given to the ionized electron and the ion, the dE/dx of the passing particle can also be measured. A frequent particle identification problem is to determine if a track was produced from one electron alone or an electron and positron close together and following the same path (a magnetic field would separate the particles, but, since DØ has none, the e^+e^- pair will be unresolved). Photons and neutral pions converting to e^+e^- pairs will create such situations. By measuring dE/dx, single particle tracks can be distinguished from doubly-ionizing tracks produced by two particles following the same path.

Appendix C

Principles of Calorimeters

Calorimeters[116, 117, 119] measure energy by total absorption of incident particles. Remember from the discussions of Appendix A that high energy electrons and hadrons shower as a result of inelastic collisions. Each collision degrades the original particle's incident energy. The number of particles produced in a shower, N, is proportional to the incident energy, $N \sim E$. The cascades are statistical in nature, so fluctuations in the number of particles from shower to shower determine the energy resolution,

$$\frac{\sigma(E)}{E} \sim \frac{\sigma(N)}{N} \sim \frac{1}{\sqrt{N}} \sim \frac{1}{\sqrt{E}} \tag{C.1}$$

A good feature of well designed calorimeters is that the resolution improves by $1/\sqrt{E}$ as the energy of particles increase.

The shower energy is measured by its particles traversing some active region. The DØ calorimeters use liquid argon (LAr) as the active medium which is ionized by the particles in the shower. The ionization is collected by read out boards with copper pads at high voltage (similar to the anode wires of a drift chamber). In this case, there is no avalanche effect, and so LAr has unit gain. Unit gain is a desired property, since the energy lost to the ionization needs to be measured very accurately.

C.1 Sampling Calorimeters

The entire shower must be contained for calorimeters to measure the correct energy. Since the depth of showers increase as $\ln E_{incident}$, containing higher energy electrons and

hadrons does not mean adding enormous amounts of extra material. Because electromagnetic and hadronic particles interact with different path lengths, (radiation length for electromagnetic and the much longer nuclear interaction length for hadrons), calorimeters are split into separate electromagnetic (EM) and hadronic sections. The EM calorimeters are much shorter in depth than their hadronic counterparts, since much less material is necessary to contain an EM cascade.

When the incident energies are very high, it is often impractical to make a calorimeter completely out of active material due to size and expense in material and read out electronics. For example, the DØ EM and hadronic calorimeters amount to $\sim$20 X_0 and $\sim$7 λ of material, respectively. If that were entirely LAr, the depths would be about 3 m for EM and 5 m for the hadronic calorimeters! Since DØ needs to be a compact detector, many plates of depleted uranium, copper, and stainless steel are inserted in the liquid argon. These uninstrumented high Z and high density absorbers help to contain the showers in a much shorter depth: 11 cm for EM and $\sim$1 m for the hadronic calorimeter. The showers are sampled by instrumented gaps between the absorber plates, and thus DØ and similar calorimeters are called sampling. A consequence of sampling the shower is that only a small fraction of the energy is read out, and thus the energy resolution can suffer. Through careful construction and calibration, the sampling fractions can be determined and the original incident energy can be calculated by applying sampling weights to the data.

C.2 Compensation

In Appendix A, some of the differences between hadronic and electromagnetic showers were discussed. Hadrons interacting with nuclei can produce electrons and photons, so a hadronic shower includes an electromagnetic part. π^0 and η mesons will also be absorbed electromagnetically since they quickly decay to two photons. A further difference is that excited nuclei releasing protons and neutrons will absorb much more energy than they release in order to overcome the nucleon binding energy. On average but with large fluctuations, 40% of the energy in the purely hadronic part of the shower is lost to

exceeding the nucleon binding energies.[116] The calorimeter response to electrons is thus greater than that compared to hadrons with the same energy; $e/h > 1$. This difference in response has disastrous effects on a hadron calorimeter's performance: the resolution will not improve as well as $1/\sqrt{E}$, the signal shape for monoenergetic hadrons will be nongaussian (and thus asymmetric), and the hadronic response will not be linear with incident energy. Fortunately, there are techniques in calorimeter construction and off-line analysis to make calorimeters compensating, forcing e/h to 1.

One method for compensation is to accurately determine the EM component of the hadronic shower event by event, since it does not suffer from binding energy losses. But EM showers are much shorter in depth than hadronic showers, so the calorimeter read out must be very finely segmented in depth to get many accurate measurements of the shower to identify the EM part. Weighting factors determined by the strength of the EM fraction are applied when the data are analyzed off-line to give compensation. Although the DØ calorimeters are finely segmented, the longitudinal segmentation is not enough to allow this technique.

Another method is careful choice of the absorber material and its thickness to increase the energy of the purely hadronic shower. By using uranium plates, extra energy with new photons and neutrons will be released when an uranium atom undergoes fission due to a colliding neutron. If the plates have the correct thickness relative to the read out material, the measured hadronic energy will be boosted by the correct factor and compensation can be achieved. DØ uses this technique and reaches near compensation. A disadvantage of uranium absorbers is the extra noise from uranium radioactivity, but that can be taken care of with careful calibration and recording of ADC pedestals.

REFERENCES

[1] S. Weinberg, Phys. Rev. Lett. **19**, 1264 (1967).

[2] S. L. Glashow, Nucl. Phys. **22**, 579 (1961).

[3] A. Salam, in *Elementary Particle Theory*, edited by N. Svartholm (Almquist and Wiksells, Stockhlom, 1968).

[4] Particle Data Group, R. M. Barnett *et al.*, Phys. Rev. **D54**, 1 (1996).

[5] O. W. Greenberg, Phys. Rev. Lett. **13**, 598 (1964).

[6] S. Abachi *et al.*, Phys. Rev. Lett. **74**, 2632 (1995).

[7] F. Abe *et al.*, Phys. Rev. Lett. **74**, 2626 (1995).

[8] ALEPH, DEPHI, L3, and OPAL Collaborations, Phys. Lett. **B276**, 247 (1992).

[9] V. Barger and R. Phillips, *Collider Physics* (Addison–Wesley, New York, 1987).

[10] R. Mohapatra, *Unification and Supersymmetry* (Springer–Verlag, New York, 1992).

[11] T. L. Barklow *et al.*, "Strong Coupling Electroweak Symmetry Breaking", Preprint hep-ph/9704217, 1997, to appear in Snowmass 1996 proceedings.

[12] K. Lane, "Non-Supersymmetric Extensions of the Standard Model", Preprint hep-ph/9610463, 1997, to appear in ICHEP 1996 proceedings.

[13] H. E. Haber and G. L. Kane, Phys. Rep. **117**, 75 (1985).

[14] H. P. Nilles, Phys. Rep. **110**, 1 (1984).

[15] X. Tata, in *The Standard Model and Beyond*, edited by J. Kim (World Scienfitic, Singapore, 1991), p. 304.

[16] J. Wess and B. Zumino, Nucl. Phys. **B70**, 39 (1974).

[17] J. Wess and B. Zumino, Phys. Lett. **B49**, 52 (1974).

[18] A. L. Lyon, "The Basics of Supersymmetry", DØ Internal Note 2523, 1994 (unpublished).

[19] S. Dimopolous and H. Georgi, Nucl. Phys. **B193**, 150 (1981).

[20] N. Sakai, Z. Phys. **C11**, 153 (1981).

[21] J. Amundson *et al.*, "Report of the Supersymmetry Theory Subgroup", Preprint hep-ph/9609374v2, 1996, to appear in Snowmass 1996 proceedings.

[22] G. L. Kane, C. Kolda, L. Roszkowski, and J. D. Wells, Phys. Rev. **D49**, 6173 (1994).

[23] J. L. Lopez, Rep. Prog. Phys. **59**, 819 (1996).

[24] J. Ellis *et al.*, Nucl. Phys. **B238**, 453 (1984).

[25] A. Chamseddine, R. Arnowitt, and P. Nath, Phys. Rev. Lett. **49**, 970 (1982).

[26] R. Barbieri, S. Ferrara, and C. Savoy, Phys. Lett. **B119**, 343 (1982).

[27] L. J. Hall, J. Lykken, and S. Weinberg, Phys. Rev. **D27**, 2359 (1983).

[28] H. Baer, C. Kao, and X. Tata, Phys. Rev. **D48**, 2978 (1993).

[29] H. Baer, F. E. Paige, S. Protopopescu, and X. Tata, Technical Report No. FSU-HEP-930329, UH-511-764-93, 1993 (unpublished).

[30] S. Park, in *10th Topical Workshop on Proton – Anti-proton Collider Physics*, edited by R. Raja and J. Yoh (AIP, Woodbury, NY, 1996).

[31] S. Dimopoulos, M. Dine, S. Raby, and S. Thomas, Phys. Rev. Lett. **76**, 3494 (1996).

[32] S. Ambrosanio *et al.*, Phys. Rev. Lett. **76**, 3498 (1996).

[33] W. Beenakker, R. Höpker, M. Spira, and P. M. Zerwas, "Squark and Gluino Production at Hadron Colliders", Preprint hep-ph/9610490, DESY 96-150, CERN-TH/96-215, 1996 (unpublished).

[34] W. Beenakker, R. Höpker, and M. Spira, "PROSPINO: A Program for the Production of Supersymmetric Particles in Next to Leading Order QCD", Preprint hep-ph/9611232, 1996 (unpublished).

[35] DØ Collaboration, S. Abachi *et al.*, Phys. Rev. Lett. **76**, 2222 (1996).

[36] N. K. Mondal, V. S. Narasimham, H. C. Shankar, and K. De, "Supergravity Inspired SUSY Search in the Dielectron Channel", DØ Internal Note 2763, 1995 (unpublished).

[37] DØ Collaboration, S. Abachi *et al.*, Phys. Rev. Lett. **75**, 618 (1995).

[38] D. Claes, in *10th Topical Workshop on Proton – Anti-proton Collider Physics*, edited by R. Raja and J. Yoh (AIP, Woodbury, New York, 1996).

[39] CDF Collaboration, F. Abe *et al.*, FERMILAB–PUB 97/031–E, 1997, submitted to Phys. Rev. D Rapid Communications.

[40] F. Abe *et al.*, Phys. Rev. Lett. **76**, 2006 (1996).

[41] Mark II Collaboration, T. Barklow *et al.*, Phys. Rev. Lett. **64**, 2984 (1990).

[42] DELPHI Collaboration, P. Abreu *et al.*, Phys. Lett. **B247**, 148 (1990).

[43] UA1 Collaboration, C. Albajar *et al.*, Phys. Lett. **B198**, 261 (1987).

[44] UA2 Collaboration, J. Alitti *et al.*, Phys. Lett. **B235**, 363 (1990).

[45] M. Paterno, *A Search for Squarks and Gluinos in $p\bar{p}$ Collisions at $\sqrt{s} = 1.8$ TeV with the DØ Detector*, Ph.D. Thesis, State Universtity of New York at Stony Brook, 1994 (unpublished).

[46] M. Goforth, *Search for Squarks and Gluinos with the DØ Detector*, Ph.D. Thesis, Florida State University, 1995 (unpublished).

[47] ALEPH Collaboration, D. Decamp *et al.*, Phys. Rep. **216**, 253 (1992).

[48] L3 Collaboration, M. Acciarri *et al.*, Phys. Lett. **B350**, 109 (1995).

[49] OPAL Collaboration, K. Ackerstaff *et al.*, Phys. Lett. **3389**, 616 (1996).

[50] G. W. Anderson and D. J. Castaño, Phys. Rev. **D52**, 1693 (1995).

[51] J. Thompson, "Introduction to the Accelerator", FERMILAB–TM 1909, 1994 (unpublished).

[52] DØ Collaboration, S. Abachi *et al.*, Nucl. Instrum. Meth. **A338**, 185 (1994), and references therein.

[53] A. Clark *et al.*, Nucl. Instrum. Meth. **A279**, 243 (1989).

[54] A. Clark *et al.*, Nucl. Instrum. Meth. **A315**, 193 (1992).

[55] J. Thompson, *Search for the Top Quark in Muon + Jets Channel at DØ*, Ph.D. Thesis, State University of New York at Stony Brook, 1994 (unpublished).

[56] J. W. Bantly, *The DØ Detector Forward Drift Chamber Performance and Physics Capability in the 1990 FNAL Testbeam Run*, Ph.D. Thesis, Northwestern University, 1992 (unpublished).

[57] J. F. Detoeuf *et al.*, Nucl. Instrum. Meth. **A279**, 310 (1989).

[58] D. Buchholz *et al.*, Nucl. Instrum. Meth. **A257**, 556 (1987).

[59] S. Wimpenny *et al.*, Nucl. Instrum. Meth. **A279**, 107 (1989).

[60] P. Franzini *et al.*, Nucl. Instrum. Meth. **A289**, 438 (1990).

[61] A. Spadafora *et al.*, Nucl. Instrum. Meth. **A315**, 279 (1992).

[62] J. Yu, *Determination of the Strong Coupling Constant and a Test of Perturbative QCD using W + jets Processes in the DØ Detector*, Ph.D. Thesis, State University of New York at Stony Brook, 1993 (unpublished).

[63] S. Snyder, *Measurement of the Top Quark Mass at DØ*, Ph.D. Thesis, State University of New York at Stony Brook, 1995 (unpublished).

[64] A. Ito and W. Cooper, Fermilab, private communication.

[65] D. Norman, *A Search for First Generation Leptoquarks at* $\sqrt{s}$ *= 1.8 TeV with the DØ Detector*, Ph.D. Thesis, University of Maryland, College Park, 1993 (unpublished).

[66] C. Brown *et al.*, Nucl. Instrum. Meth. **A279**, 121 (1990).

[67] M. Abolins *et al.*, IEEE Trans. Nucl. Sci. **36**(1), 384 (1989).

[68] M. Abolins *et al.*, Nucl. Instrum. Meth. **A289**, 543 (1990).

[69] G. S. Gao and R. Partridge, IEEE Trans. Nucl. Sci. **38**(2), 286 (1992).

[70] D. Edmunds, S. Gross, and P. Laurens, in *IEEE Nucl. Sci. Symp.* (IEEE, Norfolk, Va., 1994).

[71] M. Fortner *et al.*, IEEE Trans. Nucl. Sci. **38**(2), 480 (1991).

[72] J. Butler, "Main Ring Deadtime", DØ Internal Note 1682, 1993 (unpublished).

[73] N. Amos, "Main Ring Veto Counters for Run 1b", DØ Internal Note 2072, 1994 (unpublished).

[74] J. A. Wightman, "The DØ Data Acquisition System", DØ Internal Note 1541, 1992 (unpublished).

[75] D. Cutts *et al.*, IEEE Trans. Nucl. Sci. **36**(1), 738 (1989).

[76] CERN *ZEBRA*, CERN Program Library Number Q100, 1992 (unpublished).

[77] G. Manning *et al.*, "DØ Software Documentation", DØ internal note, in preparation.
(URL: `http://www-d0.fnal.gov/software/offline_document.ps`)

[78] C. Cretsinger, *Search for the Top Quark in the All–Jets Channel*, Ph.D. Thesis, University of Rochester, 1995 (unpublished).

[79] N. J. Hadley, "Cone Algorithm for Jet Finding", DØ Internal Note 904, 1989 (unpublished).

[80] A. R. Baden and N. J. Hadley, "Jets and Kinematics", DØ Internal Note 957, 1990 (unpublished).

[81] R. Hirosky, "A Data–based Estimate of Jet Reconstruction Efficiencies", DØ Internal Note 2369, 1994 (unpublished).

[82] M. Bhattacharjee *et al.*, "Jet Energy Resolutions", DØ Internal Note 2887, 1996 (unpublished).

[83] M. Paterno, "A Monte Carlo Study of the DØ Calorimeter Missing E_T Resolution", DØ Internal Note 1374, 1992 (unpublished).

[84] M. Paterno, "A Study of the DØ Calorimeter $\not\!\!E_T$ Resolution Using Low E_T Jet Triggers", DØ Internal Note 1782, 1993 (unpublished).

[85] R. Kehoe, *Search for the Top Quark in Dielectron Final States at* $\sqrt{s}$ *= 1.8 TeV and Measurement of the Response of the DØ U/LAr Calorimeter to Jets*, Ph.D. Thesis, University of Notre Dame, 1997 (unpublished).

[86] C. Gerber *et al.*, "Muon Momentum Determination", DØ Internal Note 2140, 1994 (unpublished).

[87] E. Gallas, "The MTC Package (Muon Tracking in the Calorimeter)", DØ Internal Note 2066, 1004 (unpublished).

[88] R. Kehoe and R. Astur, "Determination of the Hadronic Energy Scale of DØ Calorimetry (`cafix` version 5.0)", DØ Internal Note 2908, 1996 (unpublished).

[89] F. Hseih, R. Partridge, and S. Snyder, "Jet Energy Scale Uncertainty for Top Cross Section PRL", DØ internal note, in preparation.

[90] DØ Collaboration, S. Abachi *et al.*, "Measurement of the Top Quark Pair Production Cross Section in $p\bar{p}$ Collisions", FERMILAB–Pub 97/109, hep-ex/9704015, 1997, submitted to Phys. Rev. Lett.

[91] J. Butler *et al.*, "Measurement of the Top Quark Production Cross Section Using Lepton + Jets Events", DØ Internal Note 2978, 1995 (unpublished).

[92] J. Hobbs, Fermilab, private communication.

[93] T. Marshall and H. Haggerty, "Crud Removal from Muon Drift Chamber Wires Using *Zap* Cleaning", DØ Internal Note 2556, 1995 (unpublished).

[94] J. M. Butler, "EF Muon ID for b–Tagging in the Post-Zap Era", DØ Internal Note 2602, 1995 (unpublished).

[95] G. Blazey, M. Bhattacharjee, and D. Elvira, "Efficiencies of the Standard Jet Cuts for Cone Sizes: 0.3, 0.5 and 0.7", DØ Internal Note 2197, 1995 (unpublished).

[96] W. Carvalho and T. T. Thomas, "Multiple Interaction Tool Study for Run 1", DØ Internal Note 2798, 1995 (unpublished).

[97] B. Abbot, "Vertex Determination for Jets", DØ Internal Note 1990, 1993 (unpublished).

[98] A. Boehnlein and G. Wang, Fermilab, Florida State University, private communication.

[99] J. Bantly, D. Owen, and R. Partridge, "DØ Luminosity Monitor Constant for the 1994–1996 Tevatron Run", DØ Internal Note 3199, FERMILAB–TM–1995, 1997 (unpublished).

[100] R. Brun and F. Carminati, "*GEANT*", CERN Program Library Long Writeup W5013, 1993 (unpublished).

[101] W. Dharmaratna, R. Raja, and C. Stewart, "The DØ Shower Library – Version 2.0", DØ Internal Note 1730, 1993 (unpublished).

[102] G. Marchesini *et al.*, Comp. Phys. Comm. **67**, 465 (1992).

[103] DØ Collaboration, S. Abachi *et al.*, "Direct Measurement of the Top Quark Mass", FERMILAB–Pub 97/059, hep-ex/9703008, 1997, submitted to Phys. Rev. Lett.

[104] F. A. Berends, H. Kuijf, B. Tausk, and W. T. Giele, Nucl. Phys. **B357**, 32 (1991).

[105] T. Sjöstrand, Comp. Phys. Comm. **82**, 74 (1994).

[106] P. C. Bhat, H. B. Prosper, and S. S. Snyder, "Bayesian Analysis of Multi-Source Data", FERMILAB–Pub 96/397, 1997, submitted to Phys. Lett. B.

[107] A. L. Lyon and M. Paterno, "A Search for Squarks and Gluinos with the Jets and Missing Energy Signature in Run 1b", DØ internal note, in preparation.

[108] E. Jaynes, "Probability Theory: The Logic of Science", Book, in preparation. (URL: `ftp://bayes.wustl.edu/pub/Jaynes/book/probability.theory`)

[109] T. J. Loredo, in *Maximum Entropy and Bayesian Methods*, edited by P. F. Fougère (Kluwer Academic Publishers, Dordrecht, The Netherlands, 1990). (URL: `ftp://bayes.wustl.edu/pub/Loredo`)

[110] I. Bertram *et al.*, "A Recipe for the Construction of Confidence Limits", DØ Internal Note 2775A, 1995 (unpublished). (URL: `http://www-d0.fnal.gov/d0notes/2775A.html`)

[111] M. Paterno, Unversity of Rochester, private communication.

[112] A. L. Lyon and M. Paterno, "Two–Dimensional Interpolation on an Irregular Grid", DØ Internal Note 2378, 1995 (unpublished). (URL: `http://www-d0.fnal.gov/physics_analysis/d0notes/source/note2378.ps`)

[113] G. W. Anderson and D. J. Castaño, Phys. Rev. **D53**, 2403 (1996).

[114] D. Amidei *et al.*, "Future Electroweak Physics at the Fermilab Tevatron: Report of the TEV_2000 Study Group", Fermilab–PUB 96/082, 1996 (unpublished).

[115] W. R. Leo, *Techniques for Nuclear and Particle Physics*, revised ed. (Springer–Verlag, New York, 1992).

[116] R. Wigmans, in *Techniques and Concepts of High Energy Physics VI*, edited by T. Ferbel (Plenum Press, New York, 1991).

[117] F. Fabjan, "Detectors for Elementary Particle Physics", CERN Yellow Book CERN-94-04, 1994 (unpublished).

[118] F. Sauli, in *Experimental Techniques in High Energy Physics*, edited by T. Ferbel (Addison-Wesley, Menlo Park, CA, 1987).

[119] R. Wigmans, Nucl. Instrum. Meth. **A279**, 107 (1988).